A NOVEL SPECTROSCOPIC INSTRUMENT FOR THE RAPID IDENTIFICATION OF LIVE AND DEAD BACTERIA

An Undergraduate Research Scholars Thesis

by

ARJUN KRISHNAMOORTHI

Submitted to the Undergraduate Research Scholars program at
Texas A&M University
in partial fulfillment of the requirements for the designation as an

UNDERGRADUATE RESEARCH SCHOLAR

Approved by Research Advisor: Dr. Peter Rentzepis

May 2020

Major: Electrical Engineering

TABLE OF CONTENTS

CHAPTER Page

ABSTRACT

A Novel Spectroscopic Instrument for the Rapid Identification of Live and Dead Bacteria

Arjun Krishnamoorthi
Department of Electrical and Computer Engineering
Texas A&M University

Research Advisor: Dr. Peter Rentzepis
Department of Electrical and Computer Engineering
Texas A&M University

The rapid detection and assessment of bacterial infections is of critical significance in various settings. Currently, the “gold standard” for the quantification of bacterial species is Colonies Forming Units (CFU) counting, which requires extensive equipment, personnel, and time (on the order of days). Such a procedure is rather unfeasible and detrimental in scenarios requiring prompt, *in-situ* diagnosis. To that effect, a rapid, portable means for detecting and assessing bacterial infections would prove invaluable. In this research, a novel spectroscopic instrument capable of fluorescence, synchronous fluorescence, and Raman spectroscopy was designed and constructed. This instrument was employed to record the fluorescence, synchronous fluorescence, and Raman spectra of bacteria, bacterial components, mixtures, and other molecules. We have utilized this instrument to determine the effects of ultraviolet (UV) irradiation on bacteria and bacterial components. Principal component analysis (PCA) was also applied to identify bacterial strains and distinguish live (viable) and dead (nonviable) bacteria within minutes. This novel, portable instrument may be used in hospitals, clinics, or the field for the rapid detection and identification of live and dead bacteria.

DEDICATION

I would like to dedicate this thesis to my loving parents, Dr. Ramaswamy Krishnamoorthi and Dr. Shyamala Rajagopalan.

ACKNOWLEDGMENTS

I would like to sincerely thank my professor and research advisor, Dr. Peter Rentzepis, for his guidance, support, kindness, and mentorship these past three years in his lab. His advice, wisdom, and enthusiasm were invaluable not only in the completion of this thesis, but also in regards to my own personal and professional development. It has been a privilege working in his lab, and I will certainly remember this experience in graduate school and beyond.

During my time at Texas A&M University, I have had the pleasure of working with several individuals who have positively impacted my research experience. Firstly, I would like to thank Umang Goswami for welcoming and training me my very first summer in the lab, which ultimately enabled me to pursue this project. Secondly, I would like to thank Dr. Runze Li for his advice and expertise, along with the many opportunities he provided in assisting with his computational and experimental work. Thirdly, I would like to thank Jocelyn Leon and Anushka Nagpal for their friendship and assistance in lab. Finally, I would like to thank Dinesh Dhankhar for his continuous advice, support, and insight in lab, along with our many discussions on research, science, graduate school, and life. Such interactions have largely shaped my research skills and interests, and I will be forever grateful to Dinesh for that.

Thanks also go to Dr. Kevin Nowka and Ping Wang for their further mentorship and support. I would also like to thank Dr. Christi Madsen for her optics courses, which provided a significant amount of theory and technical knowledge pertinent to this research.

Moreover, I thank Mr. Garrick Garza and the Physics Machine Shop for their expertise and assistance with the design and fabrication of various components utilized in this research.

Finally, I express my deepest gratitude to my family for their continual love and support.

CHAPTER I

INTRODUCTION

Bacterial infections present a significant threat to human life. It is estimated that at least 2 million people incur infections due to antibiotic-resistant bacteria, and in addition, at least 23,000 people die each year following such infections [1]. Furthermore, almost 1.7 million hospital-acquired infections, along with approximately 99,000 resulting deaths, occur annually [2]. Such health care-associated infection (HAI) was noted to be among the top 10 causes of death in the United States with an estimated $4.5 billion to $6.5 billion cost for treatment [3]. Growing antibiotic resistance, coupled with a decline in new antibiotics, has further worsened the effects of HAIs [2]. Additionally, the threat of bacterial infection is compounded by the fact that current detection and assessment methods are rather time-consuming and inefficient. The current "gold standard" for the quantification of bacterial species is Colonies Forming Units (CFU) counting, which consists of the isolation, culturing, and manual identification of the bacterial strain [4]. Such procedures require extensive time (1 to 3 days) and specialized equipment that are inappropriate for *in-situ* analyses and, therefore, may be detrimental to a patient's long-term health, especially in settings where such resources are not readily available. In addition, the ability to efficiently diagnose and assess bacterial infections has implications on the efficacy of the resulting antimicrobial therapy. Particularly, it has been noted that the inappropriate application of antibiotic drugs, in an attempt to treat HAI, has contributed to growing antibiotic resistance, toxic effects, and health care costs [2]. Certainly, a rapid means of identifying and assessing bacterial infections, *in-situ*, within minutes rather than days, would prove invaluable in

detecting and preventing the onset of infections, in addition to supporting more effective antimicrobial therapy for the patient.

Several studies have been documented in the literature which address such problems. Notably, optical spectroscopy, coupled with multivariate data analyses, has proven to be a key technique in detecting and identifying bacterial strains and concentrations [5–14]. In particular, vibrational spectroscopic techniques, such as Fourier-transform infrared (FTIR) and Raman spectroscopy, have been used to accomplish these tasks. FTIR spectroscopy, for example, has been applied to identify and classify several bacterial strains, including *Staphylococcus*, *Streptococcus*, and *Escherichia coli*, among others [8]. This was accomplished by comparing the sample spectra against a database of reference spectra. More recently, FTIR spectroscopy has been utilized for the identification and discrimination of bacteria at the genus, species, and clonal levels [9–10]. In addition, surface-enhanced Raman spectroscopy (SERS) was integrated with discriminant function analysis (DFA) and hierarchical cluster analysis (HCA) to identify and discriminate within a group of clinical bacterial samples responsible for urinary tract infections [11]. This study similarly demonstrated the ability to distinguish between bacteria within the same strain. Current efforts have focused on achieving single bacteria detection through Raman spectroscopy [12–13] and applying machine learning for rapid identification and classification [14].

Owing to the fact that bacterial components, such as amino acids (tryptophan and tyrosine) and nucleic acids (DNA), possess absorption and fluorescence bands in the ultraviolet (UV) spectral region [15], fluorescence spectroscopy has also been utilized for the detection and identification of bacteria [5–7]. When coupled with principal component analysis (PCA), this technique has provided discrimination at the associated genus, species, and strain levels [6]. In

addition, excitation-emission matrix (EEM) and synchronous fluorescence spectroscopy [16] have been employed to resolve the spectra of molecular components, such as tryptophan and tyrosine, in both bacterial and human tissue cells [5, 17–19]. Furthermore, such techniques have been utilized, along with PCA, to detect and classify pathogenic bacteria in foods [5], as well as clinically-important bacteria [17]. As an extension of these results, our previous studies [20–22] have demonstrated that the fluorescence and synchronous fluorescence spectra of bacteria, including its tryptophan and tyrosine components, undergo detectable changes following UV or antibiotic treatment. In particular, we found that the fluorescence of bacteria and its components decreases with increasing UV dosage or antibiotic treatment time and may be correlated with the number of inactivated bacteria. Subjecting these spectra to PCA allowed us to rapidly distinguish live and dead bacteria within minutes. In addition, our work with Raman spectroscopy [23] further elucidated the role of protein damage in the inactivation process and provided an additional means of determining the live-to-dead bacteria ratio as a function of UV dosage. The above results suggest that a portable spectroscopic instrument, capable of fluorescence and Raman spectroscopy, would offer a novel and important solution for the rapid detection and identification of live and dead bacteria. Such an instrument could be readily employed in hospitals, clinics, and the field, thereby providing practically instantaneous detection and assessment capabilities. In many of these studies, however, the benchtop instruments used were bulky and therefore unsuitable for usage *in-situ.*

To that effect, this thesis describes the design, construction, and operation of a novel, portable instrument capable of fluorescence, synchronous fluorescence, and Raman spectroscopy for the *in-situ* detection of live and dead bacteria. The additional, onboard capabilities of PCA and bacterial disinfection are integrated into the instrument. To that end, this instrument is

composed of several commercial, off-the-shelf components, including monochromators, a linear charge-coupled device (CCD) detector array, and light-emitting diodes (LEDs). This instrument is capable of recording the fluorescence, synchronous fluorescence, and Raman spectra of bacteria, bacterial components, and other molecules *in-situ* within minutes. We have employed this instrument to determine the effects of UV radiation on bacteria and bacterial components. In addition, live and dead bacteria were rapidly distinguished by means of PCA. These results support a novel, efficient, and portable means of identifying live and dead bacteria *in-situ*.

CHAPTER II

BACKGROUND

In this chapter, background information on bacteria, ultraviolet (UV) light, and principal component analysis (PCA) is provided. Additionally, the spectroscopic techniques (absorption, fluorescence, and Raman spectroscopy) and instrumentation employed for this research are described.

Bacteria

Bacteria are unicellular, prokaryotic microorganisms [24]. Despite being the most primitive form of life on Earth [25], bacteria have remained for over billions of years in a variety of harsh environments. As shown in Figure 1, bacteria generally consist of a cell wall, cell membrane, and cell interior (cytoplasm).

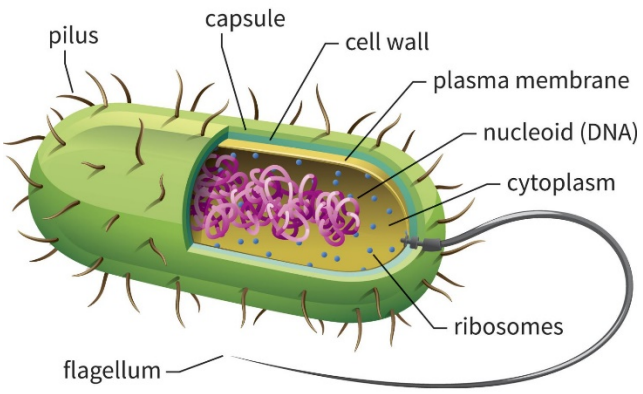

Figure 1: General structure of bacterial cell [26].

A distinction exists between Gram-positive and Gram-negative bacteria through a staining method developed in 1884 [24]. In this method, a crystal violet dye is applied to the bacterium;

Gram-positive bacteria retain the dye, while Gram-negative bacteria do not. This rather simple method elucidates key differences in the structure of each type of bacteria. To that effect, Figure 2 displays diagrams of the cell wall for both Gram-positive and Gram-negative bacteria.

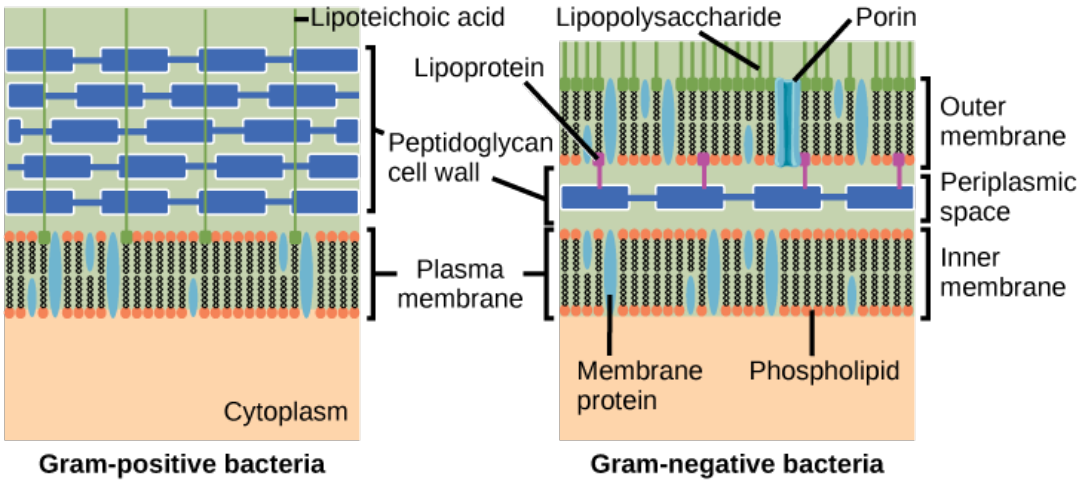

Figure 2: Structure of cell wall for Gram-positive and Gram-negative bacteria [27].

It may be observed that Gram-positive bacteria possess a thicker peptidoglycan layer than Gram-negative bacteria, which results in the retention of the crystal violet dye. Additionally, Gram-negative bacteria possess an outer membrane, in addition to the inner membrane, while Gram-positive bacteria simply consist of a single, inner membrane. Due to its additional outer membrane, Gram-negative bacteria have been found to possess greater antibiotic resistance than Gram-positive bacteria. *Bacillus* and *E. coli* are examples of Gram-positive and Gram-negative bacteria, respectively. The structure of the cytoplasm is practically the same for both types of bacteria and contains the “naked” DNA, situated in a region known as the nucleoid, which is utilized and necessary for replication. Bacteria replicate asexually, in as short a time as 20 minutes, by means of binary fission [24], which results in an identical copy of a bacterium’s DNA and cell contents.

The major components of a bacterial cell are proteins and nucleic acids (DNA and RNA). Topically, proteins are primarily located in the cytoplasm and along the bacterial membrane [23]. Of particular spectroscopic relevance are the aromatic amino acids tryptophan and tyrosine, which compose the membrane proteins and serve vital “anchoring” functions [28–29]. Tryptophan and tyrosine possess rather intense absorption and fluorescence bands in the UV region and have been studied by means of both fluorescence spectroscopy and UV resonance Raman spectroscopy [5, 17, 20–21, 30]. In addition, DNA maximally absorbs and fluoresces in the UV region [15]. Owing to the fact that its quantum efficiency is orders of magnitude lower than that of tryptophan and tyrosine, however, DNA is generally rather difficult to detect spectroscopically. Some bacteria, such as *Micrococcus luteus* and *Serratia marcescens*, are additionally capable of producing colored pigments with absorption bands in the visible region. Numerous resonance Raman studies have been conducted in detecting and elucidating the functions of these pigments [31–33].

Ultraviolet (UV) Light

Ultraviolet (UV) light is generally defined as the region of the electromagnetic spectrum with wavelengths in the range of ~ 100–400 nm [34]. Further bands are identified within this range, namely vacuum UV (100–200 nm), UVC (200–280 nm), UVB (280–315 nm) and UVA (315–400 nm). UV light is typically generated through a mercury vapor lamp, which is a type of gas-discharge lamp, composed of an inert gas and mercury. In such lamps, a voltage is applied to ionize the inert gas and create an electrical discharge, or arc, which heats, vaporizes, and ionizes the mercury. The output light of the lamp, following excitation of the vaporized mercury, is the characteristic emission spectrum of the mercury atoms. Recently, however, UV LEDs have developed as a less expensive, safer, and more effective alternative for generating narrowband

and intense UVC, UVB, and UVA radiation. Such LEDs provide several benefits compared to gas-discharge lamps, including a smaller size, faster startup time, and greater energy efficiency.

Owing to the fact that the absorption band maxima of tryptophan, tyrosine, and DNA are in the UVC and UVB regions, UVC and UVB radiation is particularly effective in inactivating bacteria. Figure 3 displays the germicidal effectiveness curve and illustrates the utility of UVC and UVB LEDs for disinfection.

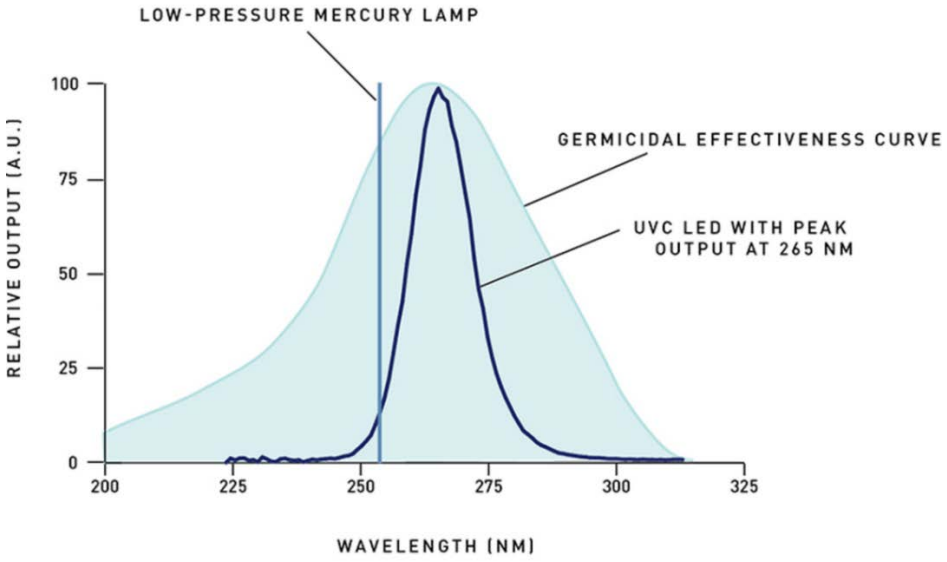

Figure 3: Germicidal effectiveness curve with mercury lamp and UVC LED outputs [35].

The inactivation of a bacterium is achieved through damage to its DNA, which prohibits the replication process [36]. A rather prominent mechanism by which this occurs is the direct absorption of UV light by the DNA nucleobases, particularly the pyrimidine bases, which results in the formation of lesions along the DNA strand, thereby preventing replication and inactivating the bacterium. Cyclobutane pyrimidine dimers, namely thymine dimers, have been shown to be the predominant UV photoproduct in both human and bacterial cells upon UV radiation [36–38].

It is worthy to mention that the maximum of the germicidal effectiveness curve occurs at ~ 265 nm, which corresponds to the absorption band maximum of thymine. Indirect damage to DNA may also occur through the generation of free radicals or reactive oxygen species (ROS), namely singlet oxygen and hydroxyl radicals, which are highly reactive and may introduce strand breaks in DNA [36]. Protein damage, in addition to nucleic damage, is a known deleterious effect of UV treatment. Our own studies have detailed the photodegradation of tryptophan and tyrosine and suggested that protein damage precedes DNA dimerization [20–21, 23, 39]. This is attributed to the higher absorption of UV light by proteins, as they exist in greater quantity, possess significantly higher absorption cross-sections, and, topically, envelope the DNA within the cytoplasm. It is rather interesting to note that the photoproducts of both tryptophan and tyrosine have been shown to promote the production of free radicals and ROS that induce further strand breaks in bacterial DNA [36, 40–42].

Principal Component Analysis (PCA)

Principal component analysis (PCA) is a multivariate analysis technique which enables the analysis of large, multidimensional datasets through the reduction of dimensionality [43]. This is accomplished by treating each dataset as a single object and representing the variation in the original data through principal components, which retain the dimensionality of the dataset. Typically, the outputs of PCA are a score plot and principal component plots. The score plot is a two-dimensional or three-dimensional plot of the objects in principal component space and serves as a means for identifying and distinguishing objects. Generally, objects are plotted against principal component 1 (PC1), principal component 2 (PC2), and/or principal component 3 (PC3), as these principal components account for the greatest variation in the original data.

Additionally, principal component plots provide detailed information regarding the principal components and regions of variation in the data.

The applications of PCA in spectroscopy and related fields are numerous and have been detailed thoroughly in the literature [44]. Our own studies [20–23] have utilized PCA as a means of processing fluorescence and Raman spectra for the identification of live and dead bacteria. This was achieved by subjecting the spectra of UV-irradiated bacteria to PCA and observing the separation of objects in the score plot as a function of the UV irradiation dose.

Absorption Spectroscopy

In molecules, electronic energy levels comprise broad energy bands that may correspond to either singlet (S_0, S_1, S_2, etc.) or triplet (T_0, T_1, T_2, etc.) electronic states [45]. Within these electronic states, further vibrational and rotational energy levels may be occupied by the molecule. A typical energy level diagram is shown in Figure 4.

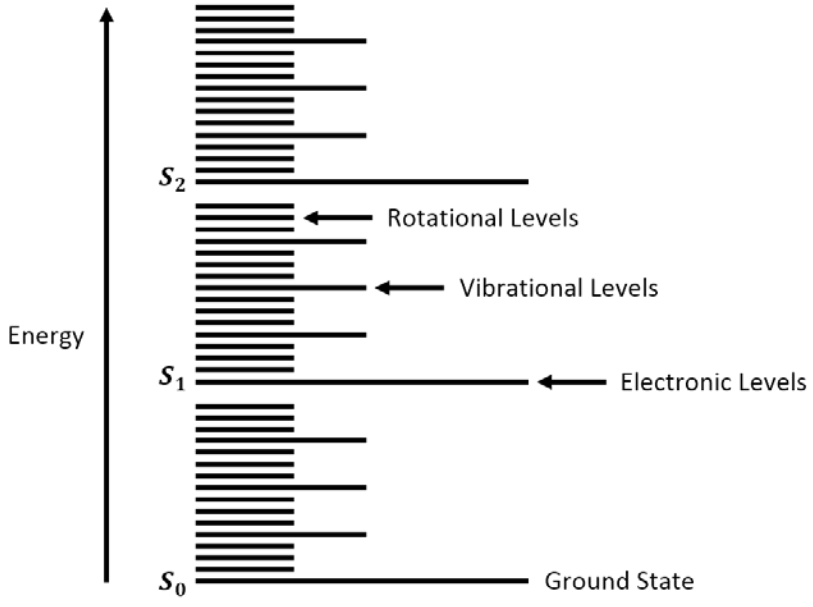

Figure 4: Energy level diagram of electronic, vibrational, and rotational energy levels.

Transitions between ground (lower-energy) states and excited (higher-energy) states may be induced through the absorption of light with a wavelength corresponding to a particular energy difference. The resulting distribution of transitions is the characteristic absorption spectrum of the molecule. Generally, transitions between electronic energy states occur in the UV and visible region, while transitions between vibrational and rotational energy levels occur in the infrared and microwave region, respectively, owing to the smaller spacing between energy levels. In this research, we are solely concerned with electronic absorption. A typical absorption spectrum plots the absorbance, A, as a function of wavelength, λ . This relation is governed by the Beer-Lambert Law:

$$A = \log_{10} \frac{I_0}{I} = \varepsilon l c \tag{1}$$

where I_0 is the intensity of light incident on the sample, I is the intensity of light exiting the sample, ε is the extinction coefficient $\left(\frac{1}{M \cdot cm}\right)$, l is the optical path length (cm), and c is the concentration of the sample (M). In general, ε is a function of λ and the Beer-Lambert Law may therefore be rewritten as follows:

$$A(\lambda) = \varepsilon(\lambda) l c \tag{2}$$

where $\varepsilon(\lambda)$ is dependent on the sample.

The design of a typical absorption spectrometer is provided in Figure 5.

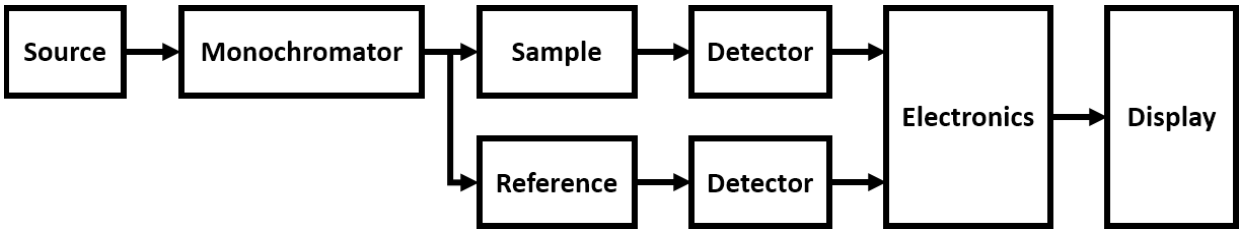

Figure 5: Simplified block diagram for an absorption spectrometer.

The light source is generally a broadband emitting source such as a tungsten or high-pressure mercury lamp. The broadband output of the lamp is then coupled to a monochromator, which disperses the light and transmits a single wavelength through a slit. The design of a typical monochromator is displayed in Figure 6.

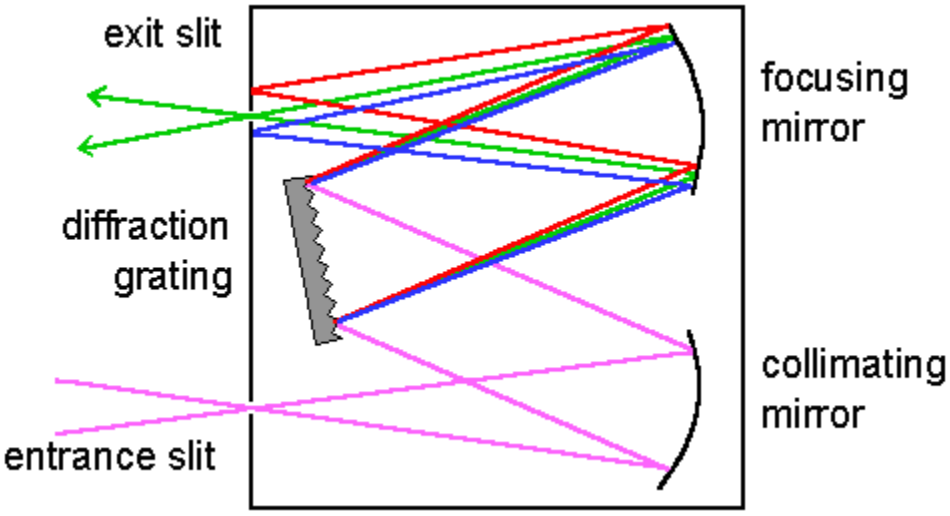

Figure 6: Design of a Czerny-Turner monochromator [46].

The angular positioning of the diffraction grating determines the wavelength of light that is focused at the exit slit. The excitation wavelength may therefore be scanned by rotating the diffraction grating by means of a stepper motor. Upon exiting the monochromator, the excitation light is redirected to both a sample and reference cell. A detector, such as a photomultiplier tube (PMT) or CCD, is situated behind the sample and reference cells to measure the transmitted intensity, I, and incident intensity, I_0, respectively. The reference cell is utilized to account for solvent absorption and scattering. Owing to its sensitivity to sample concentration, electronic absorption spectroscopy has been utilized to observe both protein and DNA damage through the decrease of their characteristic absorption band maxima.

Fluorescence Spectroscopy

Following excitation from a ground (lower-energy) electronic state to excited (higher-energy) electronic state, a molecule will decay through nonradiative and, usually, radiative transitions [15, 45]. The excitation of a molecule from the ground electronic state to excited electronic state is followed by a rapid, nonradiative decay, on the order of picoseconds, to the lowest vibrational level of the excited electronic state. This process is known as vibrational relaxation and occurs due to the comparatively smaller spacing between vibrational energy levels, resulting in the dissipation of energy as phonons (molecular vibrations). Following vibrational relaxation, a molecule will further decay through either nonradiative or radiative transitions to the ground electronic state. In addition to vibrational relaxation, nonradiative transitions may include internal conversion, in which excess energy is dissipated as heat. Radiative transitions involve the emission of photons, or light, in a process known as fluorescence. This process is depicted in Figure 7.

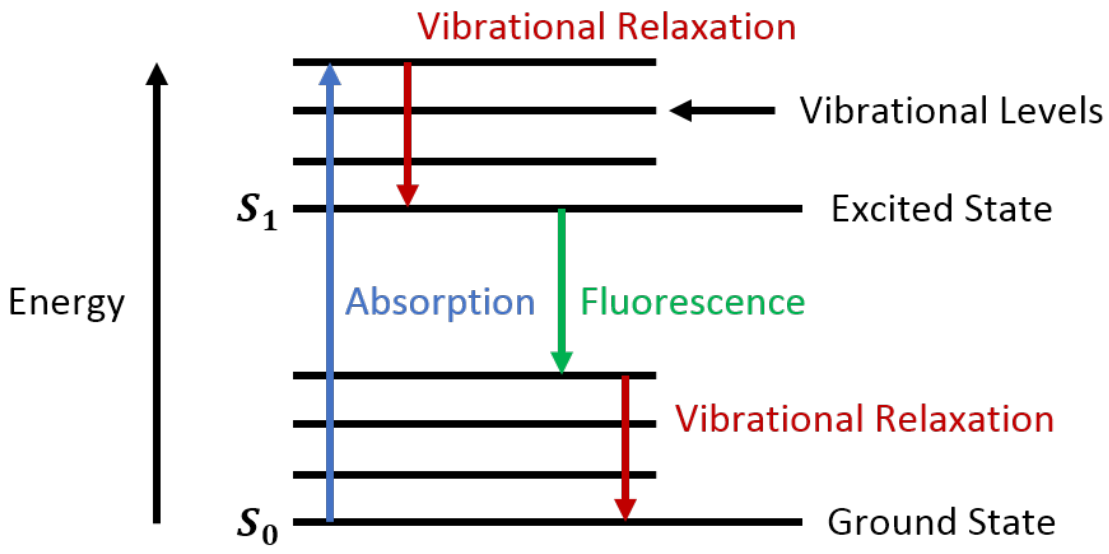

Figure 7: Energy level diagram for absorption, nonradiative decay, and fluorescence.

The resulting distribution of radiative transitions, from the ground vibrational level of the excited state to a vibrational level in the ground state, comprises the characteristic fluorescence spectrum of the molecule. Owing to the fact that fluorescence is preceded by vibrational relaxation, the fluorescence spectrum of a molecule is generally at longer wavelengths and may be considered a mirror image of the absorption spectrum. It is worthy to mention that the shape of the fluorescence spectrum is generally independent of the excitation wavelength due to radiative transitions mostly occurring from the ground vibrational level of the excited state; the intensity of the spectrum, however, depends on the absorption cross-section of the molecule at the excitation wavelength. The fraction of molecules undergoing radiative transitions additionally depends on the quantum yield of the sample. In bacteria, tryptophan possesses the highest absorption cross-section and quantum yield in the UV region.

The design of a typical fluorescence spectrometer is provided in Figure 8.

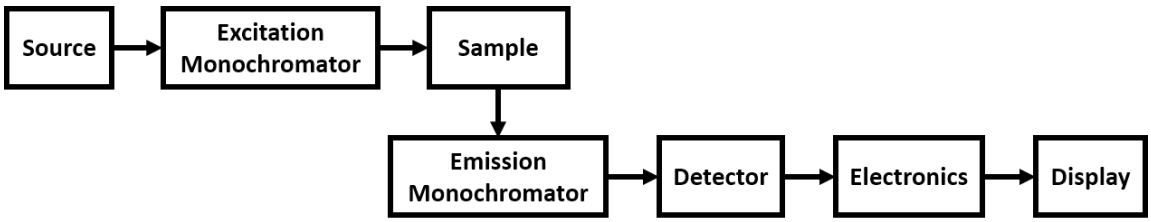

Figure 8: Simplified block diagram for a fluorescence spectrometer.

Fluorescence spectrometers are generally composed of a double monochromator, which includes both an excitation monochromator and emission monochromator. The excitation monochromator selects and transmits the excitation light to the sample, while the emission monochromator disperses and detects the emitted light from the sample. A stepper motor is attached to both the excitation and emission gratings for selection and scanning of the excitation and emission

wavelengths, respectively. To that effect, a fluorescence spectrum is achieved by selecting a particular excitation wavelength and scanning the emission monochromator. Alternatively, selecting a particular emission wavelength and scanning the excitation monochromator provides an excitation spectrum. In some spectrometers, a one-dimensional (linear) or two-dimensional (2D) CCD detector array, capable of detecting the entire fluorescence spectrum, is situated at the focal plane of the emission monochromator, which obviates the need for a second stepper motor.

Excitation-Emission Matrix (EEM)

An excitation-emission matrix (EEM) provides a detailed characterization of the absorption and fluorescence of a particular sample, where one axis is the excitation wavelength, the second axis is the emission wavelength, and the third axis is the intensity of the emitted light. This information may be provided in the form of a two-dimensional (2D) contour plot or three-dimensional (3D) surface plot. Generally, an EEM is achieved by scanning the excitation wavelength over an excitation range and measuring the fluorescence spectrum at each individual excitation wavelength. EEMs are particularly useful in the analysis of multicomponent samples because they may resolve the absorption and fluorescence band maxima of individual components. In our previous studies [20–22, 39], we have collected the EEM of bacteria to resolve the fluorescence of the tryptophan, tyrosine, and DNA components, which is not possible through fluorescence spectroscopy alone.

Synchronous Fluorescence Spectroscopy

Synchronous fluorescence spectroscopy is a useful technique for resolving the fluorescence of individual components in a mixture or multicomponent sample [16]. In commercial fluorescence spectrometers, this technique is generally achieved by synchronously

scanning both the excitation monochromator and emission monochromator such that the excitation wavelength, λ_{EX}, and emission wavelength, λ_{EM}, satisfy the following relationship:

$$\Delta\lambda = \lambda_{EM} - \lambda_{EX} \tag{3}$$

where $\Delta\lambda$ denotes the constant offset in wavelength maintained between the two monochromators. This quantity is a rather critical parameter in determining which fluorescence bands are resolved and is generally derived from the EEM of a sample. Alternatively, synchronous fluorescence spectra may simply be extracted from a sample's EEM by considering the following rewritten form of equation (3):

$$\lambda_{EM} = \lambda_{EX} + \Delta\lambda \tag{4}$$

which is simply a linear equation with a slope equal to unity and intercept equal to $\Delta\lambda$. Synchronous fluorescence spectra may therefore be considered as a set of parallel lines with varying intercepts that exist within a sample's EEM. To that end, once an EEM is acquired, synchronous fluorescence spectra of varying $\Delta\lambda$ may be immediately obtained. For bacteria, synchronous fluorescence spectroscopy is an especially useful technique for resolving the fluorescence of its cellular components, namely tryptophan and tyrosine. This is made possible due to the difference in the absorption and fluorescence band maxima of these components.

Raman Spectroscopy

A rather small fraction of incident light, $\sim$ 1 in 10^6 photons, is scattered upon interaction with a molecule [47]. Typically, the scattered radiation is at the same wavelength (energy) as the incident radiation, a phenomenon known as Rayleigh (elastic) scattering. Remarkably, an even smaller portion of incident light, $\sim$ 1 in 10^{10} photons, is inelastically scattered at a different wavelength (energy) than the incident radiation [47]. This phenomenon is known as the Raman effect, which describes Raman (inelastic) scattering. In general, Raman scattering involves an

exchange of energy between an incident photon and molecule, resulting in the excitation or relaxation of molecular vibrations. Stokes Raman scattering results in a molecule gaining energy, while anti-Stokes Raman scattering results in a molecule losing energy. The quantum mechanical models of Rayleigh, Stokes Raman, and anti-Stokes Raman scattering are provided in Figure 9.

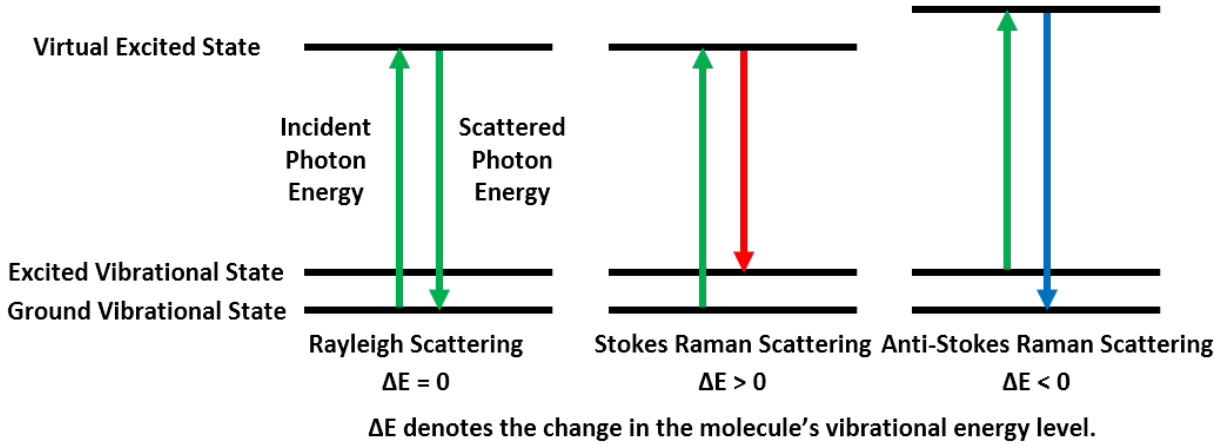

Figure 9: Quantum mechanical models of Rayleigh and Raman scattering.

Following excitation to a virtual (non-resonant) excited state, a molecule may remain in its vibrational state (Rayleigh scattering) or transition to a vibrational state of different energy (Raman scattering). Transitions to higher-energy vibrational states correspond to Stokes Raman bands, while transitions to lower-energy vibrational states correspond to anti-Stokes Raman bands. The resulting distribution of Stokes and anti-Stokes Raman bands, along with the orders of magnitude more intense Rayleigh line, is the Raman spectrum of the molecule. It is worthy to mention that at room temperature, practically all molecules will occupy the ground vibrational level, resulting in Stokes Raman bands being the predominant form of Raman scattering. A typical Raman spectrum displays the intensity of scattered light as a function of the Raman shift, $\Delta\nu$ (cm^{-1}), which is computed as follows:

$$\Delta\nu = 10^7 \left(\frac{1}{\lambda_{EX}} - \frac{1}{\lambda_{EM}}\right) \quad (5)$$

where λ_{EX} (nm) is the incident wavelength and λ_{EM} (nm) is the scattered wavelength. In general, the Raman shift is unique for different vibrational modes of a molecule, dependent on the atoms, bond energy, and bond type associated with the molecular vibration. In fact, specific motions, such as stretching, bending, and scissoring, can be associated with distinct Raman shifts. To that effect, Raman spectroscopy is a highly discriminating technique for the identification of specific functional groups in a molecule. When coupled with infrared absorption spectroscopy, Raman spectroscopy may offer a complete, detailed characterization of the vibrational modes of a molecule and may therefore aid in its identification.

Two common designs for a Raman spectrometer are depicted in Figure 10 and Figure 11.

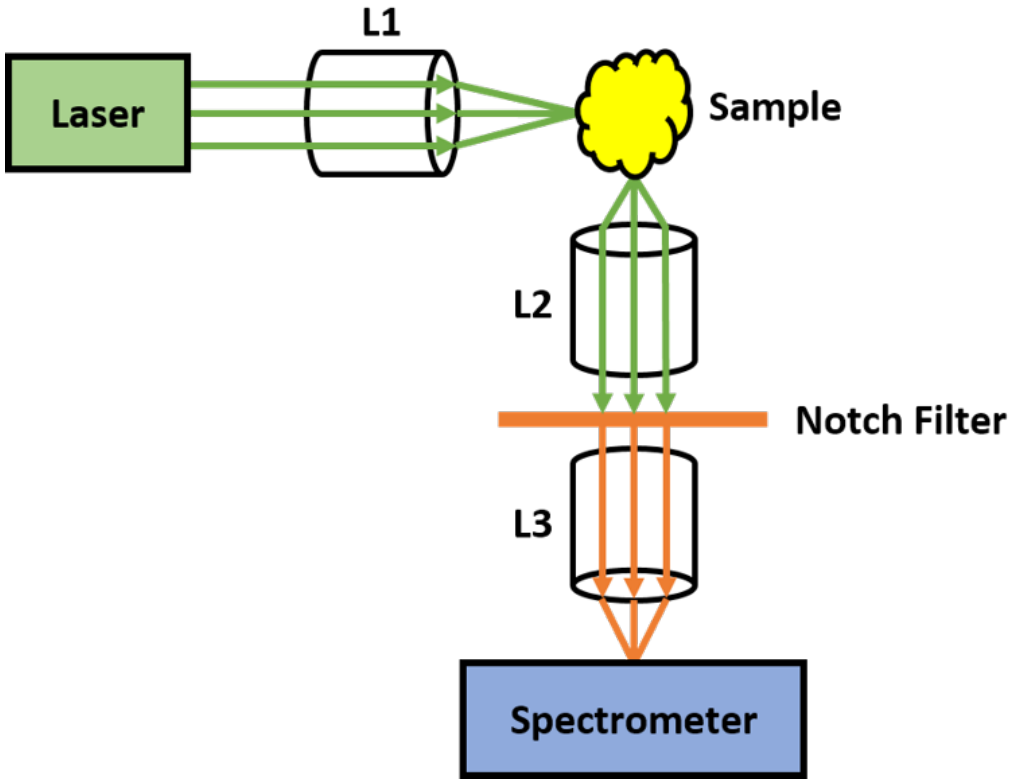

Figure 10: Design of Raman spectrometer using 90° configuration.

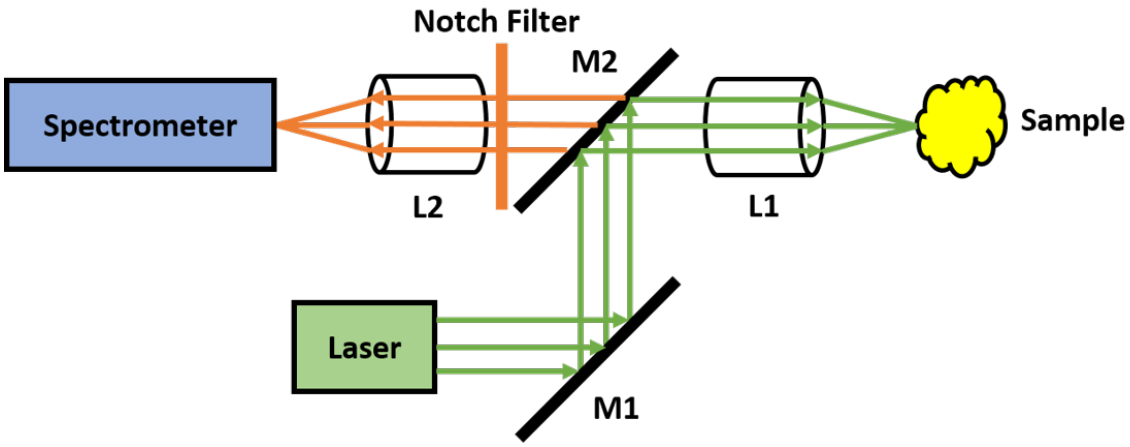

Figure 11: Design of Raman spectrometer using 180° (backscattering) configuration.

Due to the Raman effect being a rather weak phenomenon, a continuous-wave (CW) laser is generally employed as the excitation source. Selection of the proper excitation wavelength, λ_{EX}, is required to optimize the scattering intensity ($I_{scattering} \propto {\lambda_{EX}}^{-4}$) without either degrading the sample or inducing intense fluorescence which may mask the Raman signal. In both the 90° and 180° (backscattering) configurations, the excitation light is focused onto the sample by means of a lens or microscope objective with a high numerical aperture (NA), which further increases the excitation and scattering intensities. The scattered light is collected at a right angle in the 90° configuration, whereas the 180° configuration collects the backscattered light with the same microscope objective. One benefit of the backscattering configuration is that the signal collection is maximized; however, this often results in a rather intense Rayleigh line which must be removed in order to prevent saturation of the detector. This is generally accomplished through a dichroic mirror, $M2$, which functions as a longpass filter for transmitting only the Stokes Raman bands. While the 90° configuration inherently minimizes the intensity of the Rayleigh line, the Raman band intensity is also lower. Additional notch or color filters may be utilized in both

configurations for a stronger rejection of the Rayleigh line. Finally, a spectrometer is employed for dispersing and detecting the Raman spectrum.

Owing to the fact that the Raman effect is a non-resonant process, Raman bands can theoretically be generated at any excitation wavelength with the same Raman shifts. The consequence of this fact is that the scattered wavelength, and its spectral relation to the excitation wavelength, changes as well.

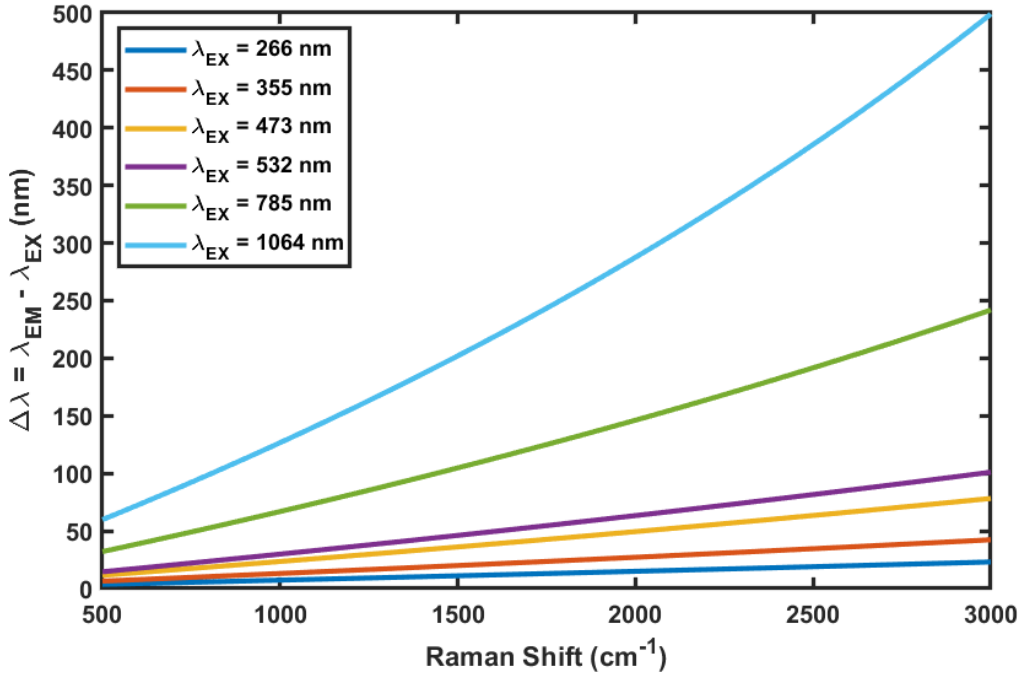

Figure 12: Effects of changing excitation wavelength on measurement of Raman bands.

In Figure 12, the wavelength shift between the excitation and scattered wavelength, $\Delta\lambda = \lambda_{EM} - \lambda_{EX}$, is plotted as a function of Raman shifts in the range of 500–3000 cm^{-1} for various excitation wavelengths. Five common laser output wavelengths in the UV, visible, and infrared regions were considered in this analysis. In general, Raman bands undergo spectral contraction

in the wavelength domain as the excitation wavelength decreases. In order to record Raman spectra in the UV region, for example, notch filters with extremely narrow bandwidths would be needed, in addition to spectrometers with high dispersion, resolution, and resolving power. These system requirements can be demanding and expensive in terms of equipment, but the tradeoff is that the Raman signals should be rather intense, owing to the lower excitation wavelength. For certain samples, the excitation wavelength may be chosen to coincide with the absorption band of the molecule, a technique known as resonance Raman spectroscopy. This technique has been shown to enhance the intensity of the Raman signals by a factor of $\sim 10^3$ to 10^6 [48]. This enhancement has been exploited for the detection of proteins and DNA in bacteria through their absorption bands in the UV region [49–50].

CHAPTER III

METHODS

Materials

The three bacteria studied in this research were *Bacillus thuringiensis* (*B. thuringiensis*), *Escherichia coli* (*E. coli*), and *Serratia marcescens* (*S. marcescens*). *B. thuringiensis* is a Gram-positive bacterium, whereas *E. coli* and *S. marcescens* are Gram-negative. *B. thuringiensis* suspensions were made by rehydrating *B. thuringiensis* spores in water for approximately an hour. *E. coli* bacteria were grown by suspending the bacteria in approximately 10 mL of Luria-Bertani (LB) broth overnight at 37 °C in a water bath. The solution was subsequently centrifuged at 3300 rpm (Fisher Scientific Centrific Model 228) for 5 minutes and washed with water. This procedure was repeated three times to ensure removal of the growth medium. The bacterial pellet was then resuspended in approximately 3 mL of water and stored at 4 °C, until usage, to minimize growth. *S. marcescens* bacteria were grown through similar procedures as those followed for *E. coli*, except that the incubation temperature was adjusted to room temperature to facilitate the growth of prodigiosin. All bacterial suspensions were diluted to a final concentration of $\sim 10^8 \frac{cells}{mL}$ for all experiments. The concentration was approximated by recording the absorption spectrum of the bacterial sample and measuring the absorbance at 600 nm, which is due to light scattering [51].

The bacterial components tryptophan and tyrosine were also studied in this research. Solutions of tryptophan and tyrosine were made in water with concentrations in the range of 2–400 $\frac{\mu g}{mL}$, depending on the experiment being performed.

UV Irradiation

Both bacteria and bacterial components were irradiated with UV light using both an Oriel mercury arc lamp and UV LED. The mercury lamp was coupled with a UV filter to block light in the visible region. The transmission spectrum of this filter is shown in Figure 13.

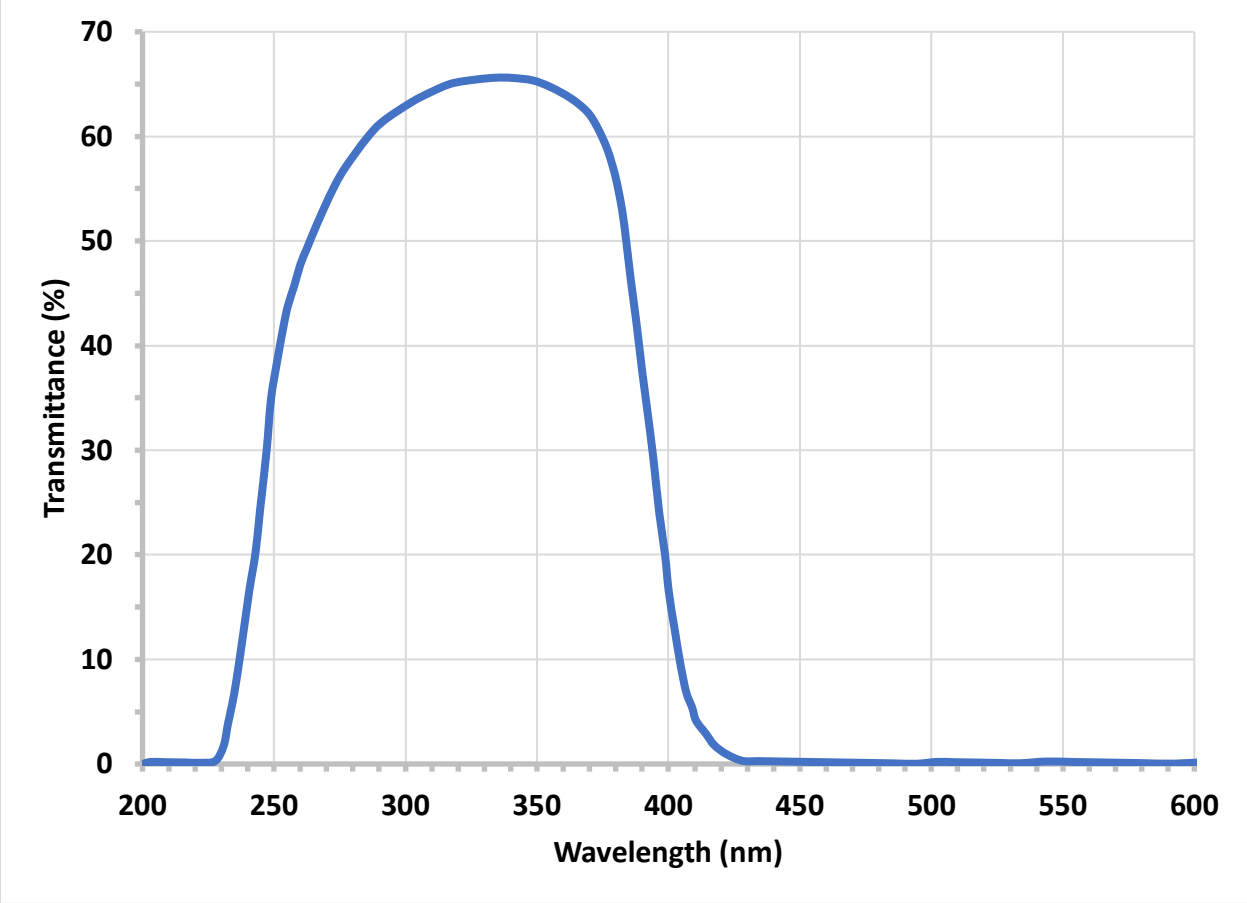

Figure 13: Transmission spectrum of UV filter.

Additionally, a UV lens was utilized to focus the beam onto the sample. The intensity of the incident light was measured with a Molectron detector (PM3Q with EPM1000) and generally varied between 5–7 $\frac{mW}{cm^2}$ for irradiation experiments.

The UV LED is a UVB LED (MTSM285UV-F1120S) with a nominal output wavelength of 285 nm. The relevant electrical and optical characteristics of this component are provided in Table 1.

Table 1: Nominal electrical and optical characteristics of UV LED [52].

Specification	Condition	Minimum	Maximum
Peak Wavelength (nm)	$I_F = 20$ mA	280	290
Power Output (mW)	$I_F = 20$ mA	1.0	2.0
Forward Voltage (V)	$I_F = 20$ mA	5.0	7.0
FWHM (nm)	$I_F = 20$ mA	10.0	15.0

The fluorescence spectra of bacteria and bacterial components, before and after UV irradiation by either the mercury lamp or UV LED, were collected for various irradiation times ranging from 0 to 240 minutes, depending on the experiment being performed.

Absorption Spectroscopy

Absorption spectroscopy was performed with a Shimadzu UV160U UV-visible recording spectrophotometer. Samples were placed in a quartz cuvette with an optical path length of 1 cm. The absorption spectra of all samples were recorded prior to UV irradiation. In addition, the transmission spectra of the filters employed in this research were also recorded with this instrument.

Fluorescence Spectroscopy

Fluorescence spectroscopy was performed using our portable instrument. Samples were placed in a quartz cuvette with an optical path length of 1 cm. The fluorescence spectra of all

samples were recorded before and after UV irradiation for various irradiation times ranging from 0 to 240 minutes, depending on the experiment being performed. Integration times were generally in the range of 1–5 seconds. Averaging and median filtering were performed for all spectra to improve the signal-to-noise ratio (SNR). To validate the operation of our portable instrument, a Shimadzu RF-5301PC fluorescence spectrometer was also utilized for performing fluorescence spectroscopy.

EEM and Synchronous Fluorescence Spectroscopy

The EEMs of bacteria, bacterial components, and mixtures were recorded with our portable instrument. Samples were placed in a quartz cuvette with an optical path length of 1 cm. Generally, EEMs were recorded over an excitation range of 260–310 nm with an excitation resolution varying from 1–10 nm, depending on the experiment being performed. Integration times were generally in the range of 5–30 seconds. Averaging and median filtering were performed for all spectra to improve the signal-to-noise ratio (SNR). Following acquisition of the EEM, synchronous fluorescence spectra of varying $\Delta\lambda$ were derived using our custom MATLAB software. To validate the operation of our portable instrument, a Shimadzu RF-5301PC fluorescence spectrometer was also utilized for performing synchronous fluorescence spectroscopy.

Principal Component Analysis (PCA)

PCA was performed on the fluorescence spectra of unirradiated (live) and irradiated (dead) bacteria using our custom MATLAB software to derive the score and principal component plots. Five fluorescence spectra were collected for each irradiation time interval. The data from at least three independent experiments were then normalized and combined for the

analysis. Generally, emission data in the range of ~ 300–500 nm resulted in the best variation between PCA objects.

In addition, PCA was also performed on the Raman spectra of various molecules. The data from at least ten independent measurements were background subtracted, normalized, and combined for the analysis. Generally, data in the range of ~ 500–4000 cm^{-1} resulted in the best variation between PCA objects.

Raman Spectroscopy

Raman spectroscopy was also performed with our portable instrument. Samples were typically placed in a quartz cuvette with an optical path length of 0.5 cm. For *S. marcescens*, the initial bacterial suspension was concentrated by centrifugation at 3300 rpm (Fisher Scientific Centrific Model 228) for 5 minutes. After discarding the supernatant, the bacterial pellet was resuspended in approximately 100 μL of water. A 2.5 μL aliquot of the suspension was then placed on an aluminum mirror. Once the suspension had dried, Raman spectra were recorded. Integration times were generally in the range of 1–5 seconds. Averaging was performed for all spectra to improve the signal-to-noise ratio (SNR). To validate the operation of our portable instrument, a Horiba XploRA PLUS Raman microscope was also utilized for performing Raman spectroscopy.

CHAPTER IV

DESIGN AND CONSTRUCTION OF PORTABLE INSTRUMENT

Overview

A block diagram of the portable instrument is provided in Figure 14.

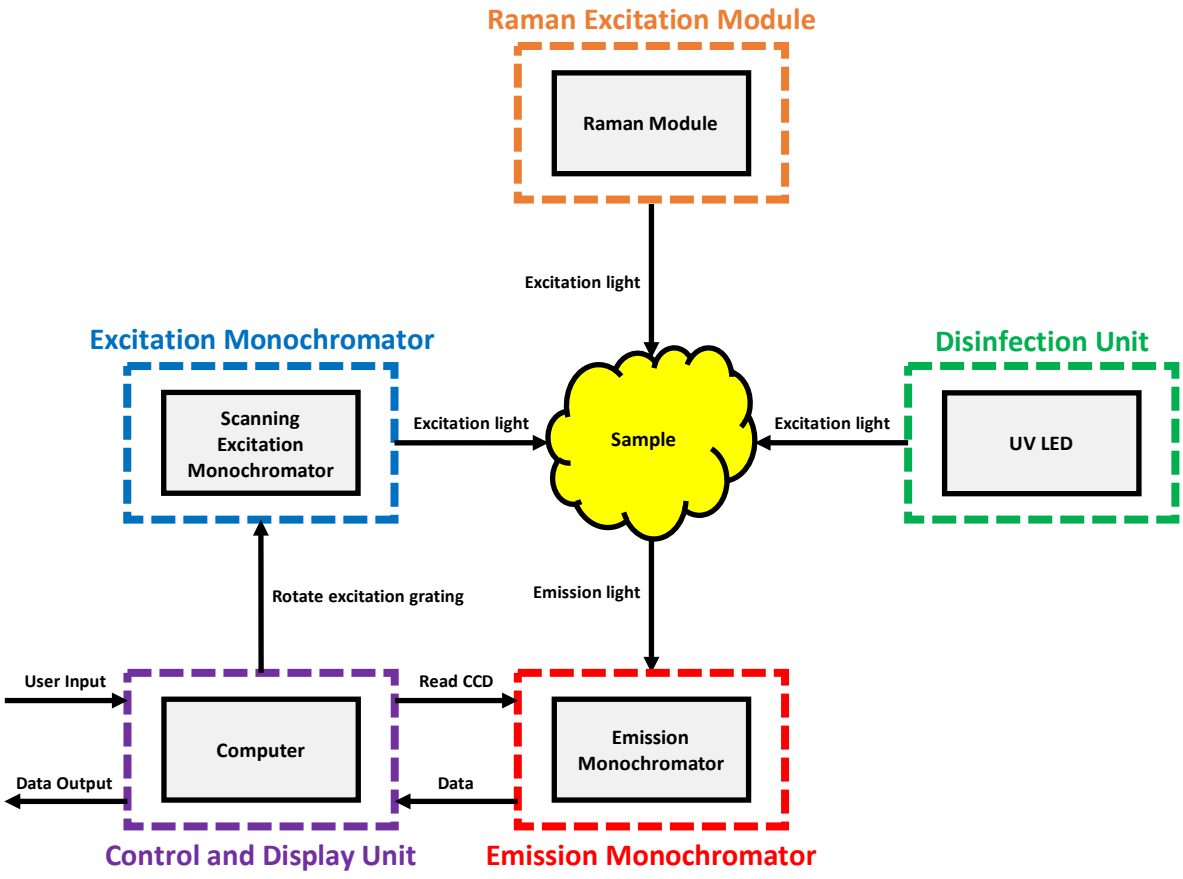

Figure 14: Block diagram of portable spectroscopic instrument.

The novel, portable instrument is composed of five subsystems: (1) a control and display unit, (2) disinfection unit, (3) excitation monochromator, (4) emission monochromator, and (5) Raman excitation module. The instrument is capable of performing fluorescence, synchronous

fluorescence, and Raman spectroscopy, in addition to its onboard capabilities of UV disinfection and PCA processing. The various modes of operation are summarized in Figure 15.

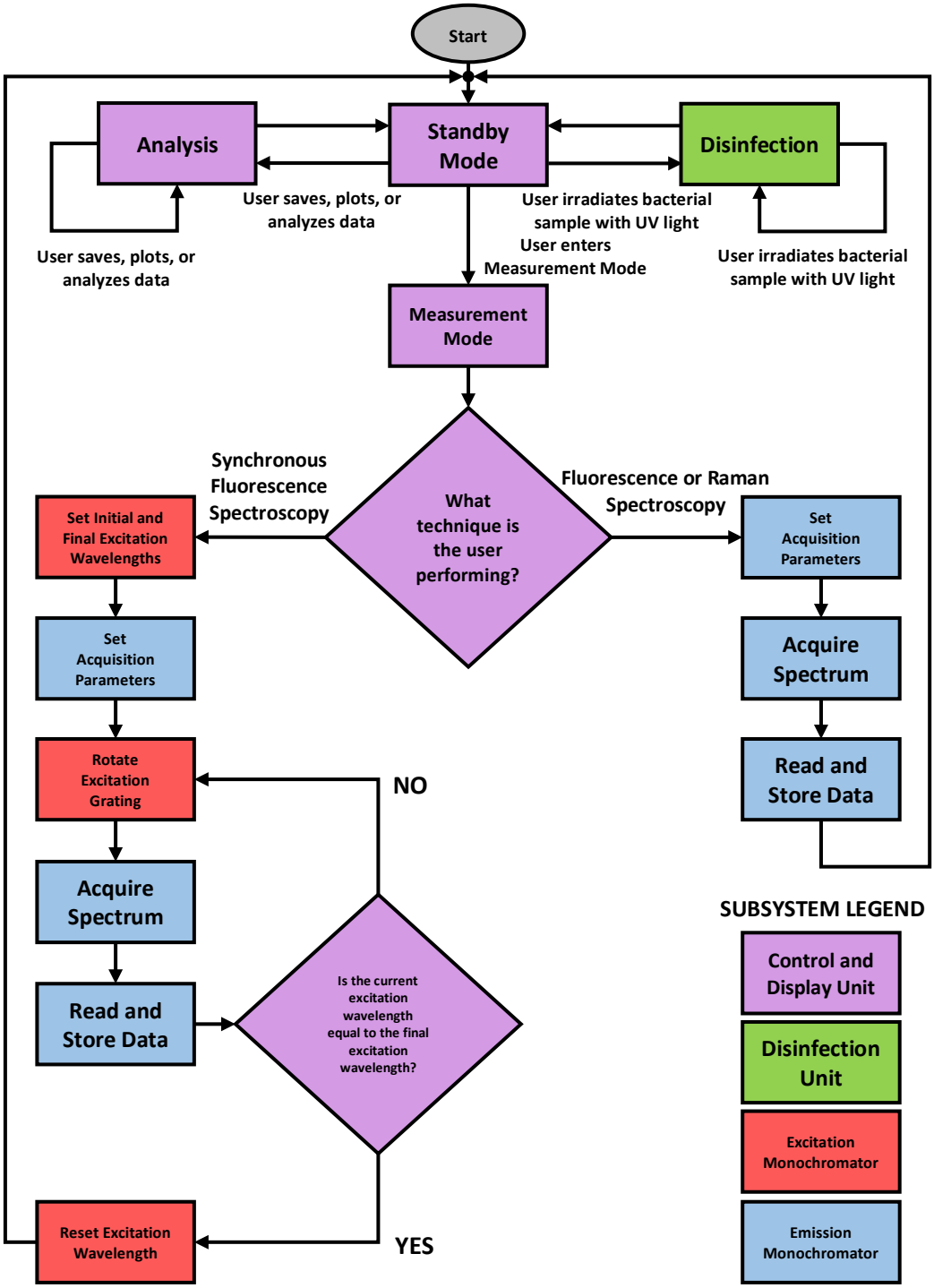

Figure 15: System flowchart detailing the various modes of operation.

To record fluorescence spectra, the excitation monochromator or disinfection unit may be utilized to excite the sample, thereby inducing fluorescence. Raman spectra may be similarly obtained by means of the Raman excitation module, which induces Raman scattering from the sample. The fluorescence or Raman spectrum is then collected, imaged, and recorded by the emission monochromator. Synchronous fluorescence spectroscopy may be achieved by rotating the excitation monochromator through a range of preselected excitation wavelengths, with the emission monochromator recording the sample's fluorescence spectrum at each excitation wavelength. The resulting dataset is a three-dimensional (3D) excitation-emission matrix (EEM) from which synchronous spectra may be easily derived. To perform UV disinfection, the disinfection unit may be utilized to irradiate bacterial samples with UV light. All commands issued to the excitation monochromator and emission monochromator, along with any recorded spectral data, are transmitted via a serial communication link. Finally, the processing and display of the recorded spectra, in addition to PCA, is performed by the control and display unit.

Control and Display Unit

MATLAB GUIs and Laptop

The current embodiment of the control and display unit subsystem is a compact laptop (Dell Precision 5510 Mobile Workstation Laptop) executing custom MATLAB software. The software currently consists of two coupled GUIs; one is an acquisition GUI for communicating with the excitation and emission monochromators, while the other is a processing GUI for performing PCA on recorded spectral data. The user may easily transition between these GUIs during execution of the software. These GUIs were designed using the App Designer feature of MATLAB to simplify the creation of the GUI layout and its various buttons, text fields, and checkboxes. To that effect, the majority of the programming involved implementing various

callbacks for each of the GUIs. The acquisition GUI and processing GUI are shown in Figure 16 and Figure 17, respectively.

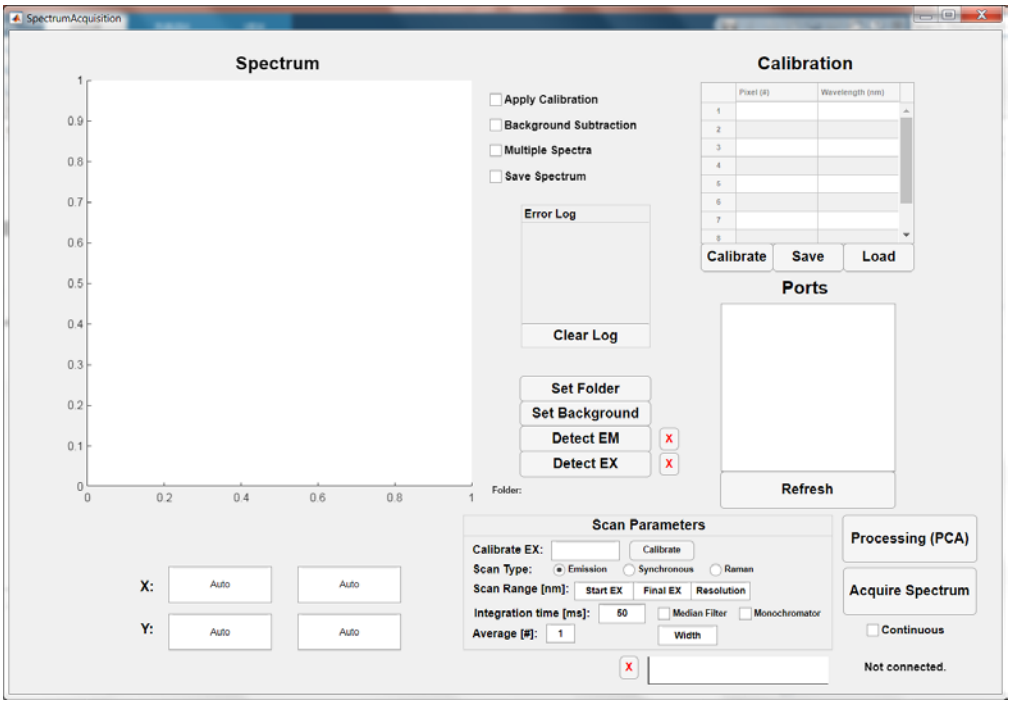

Figure 16: MATLAB acquisition GUI.

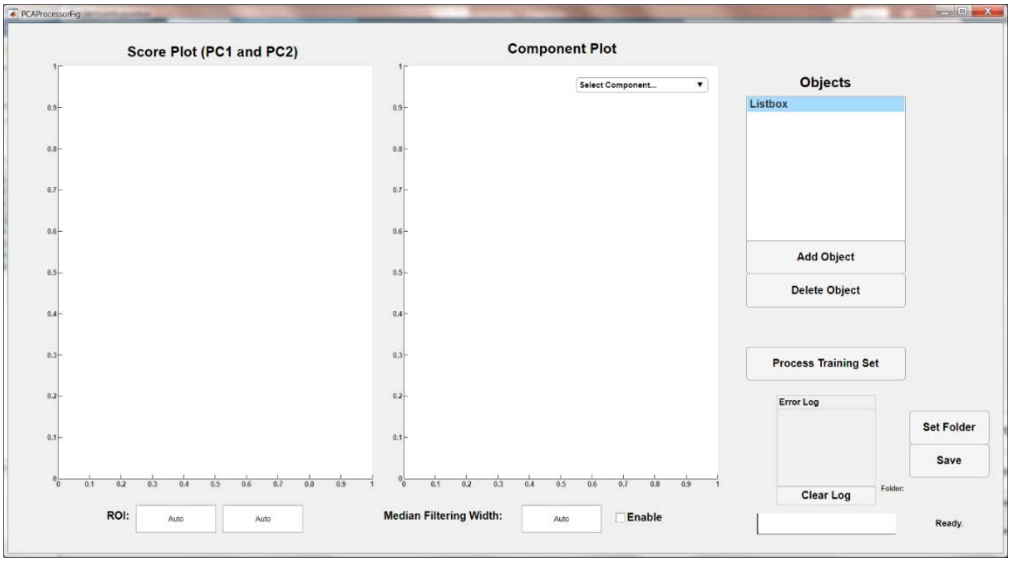

Figure 17: MATLAB processing GUI.

Various functionalities are currently available in the acquisition GUI, including the ability to record fluorescence, synchronous fluorescence, and Raman spectra, alter acquisition parameters, save spectra, calibrate the spectrometer and excitation monochromator, and perform background subtraction. In the processing GUI, the user may perform PCA on recorded spectral data and view the associated score and principal component plots. In addition, the user may also fine-tune the PCA processing by adjusting the region of interest (ROI), which essentially represents the range of fluorescence or Raman data subjected to PCA, or performing median filtering on the data to reduce noise and improve the separation of PCA objects in the score plot.

Communication with the excitation and emission monochromators is achieved through a common serial communication link, which allows commands to be issued to both subsystems, simultaneously, through separate serial ports. In particular, one serial cable connects to an RS-232 communication port integrated with the emission monochromator, while another serial cable feeds into the serial port of the microcontroller within the excitation monochromator. Figure 18 is the functional block diagram (FBD) of this setup, while Figure 19 shows its implementation.

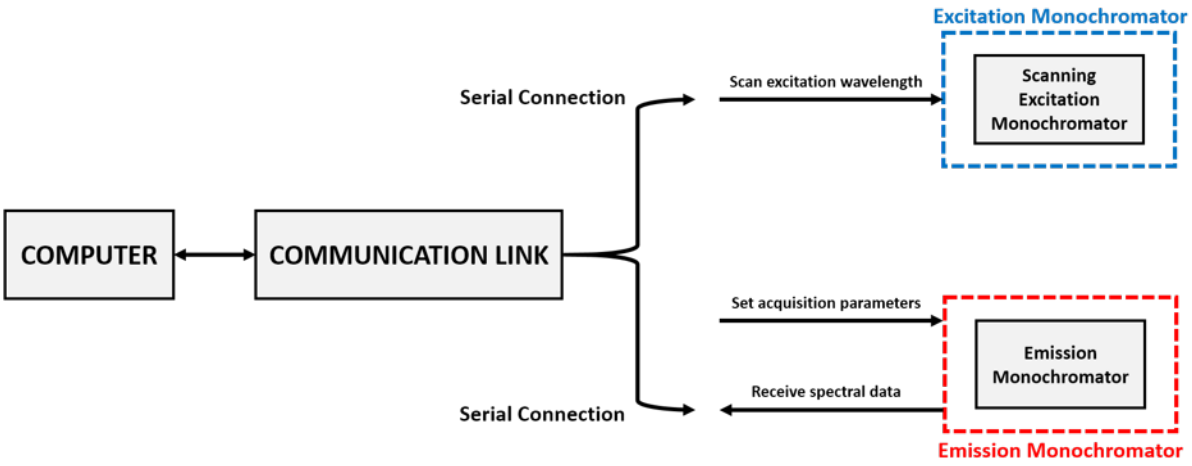

Figure 18: FBD for serial connection between computer and monochromator subsystems.

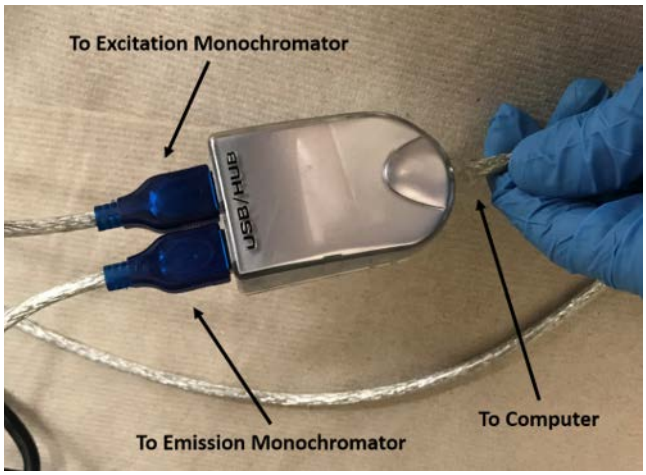

Figure 19: Serial connection between computer and monochromator subsystems.

To achieve communication with both subsystems simultaneously, individual serial port connections need to be established in MATLAB. The configurations of these serial port connections (e.g., baud rate, parity, data bits, etc.) are determined by the respective communication protocols associated with each subsystem.

Excitation Monochromator Communication

Communication with the excitation monochromator subsystem is achieved through the serial port of the microcontroller within the subsystem. The microcontroller is a DCB-241, which is an integrated stepper motor driver-controller board that operates on an RS-422 communication protocol. To simplify the software development, a SIN-11 intelligent serial adapter was utilized as a means of converting high-level, RS-232 commands from the computer into an RS-422 bus. The serial port configuration for this subsystem is provided in Table 2.

Table 2: Serial port configuration for excitation monochromator subsystem [53].

Specification	Value
Baud Rate (bps)	9600
Data Bits	8
Stop Bits	1
Parity	None
Flow Control	Hardware
Handshaking	None

The primary purpose of the DCB-241 microcontroller is to rotate the excitation grating located within the excitation monochromator subsystem by means of a stepper motor. To that effect, the serial port connection with the subsystem is utilized as a means of issuing high-level, ASCII commands for configuring and initiating the rotation of the stepper motor. A table of the most relevant commands is provided in Table 3. The full set of commands is available in the associated DCB-241 documentation [53].

Table 3: Relevant DCB-241 commands for rotating the stepper motor [53].

Command	Function	Value	Notes
I	Initial Velocity	18–23,000 SPS	The initial velocity specifies the start and stop speed, in steps per second (SPS), for the motor.
K	Ramp Slope	0–255	The ramp slope specifies the ramp acceleration and deceleration time.
V	Slew Velocity	18–23,000 SPS	The slew velocity is the final velocity following acceleration from the initial velocity.
+	Index in Plus Direction	0–16,777,215 Steps	This command steps the stepper motor in a positive direction for the specified number of steps.
-	Index in Minus Direction	0–16,777,215 Steps	This command steps the stepper motor in a negative direction for the specified number of steps.
S	Store Parameters	N/A	This command saves all operational parameters for recall during a power-on reset.

A picture of the communication setup is provided in Figure 20.

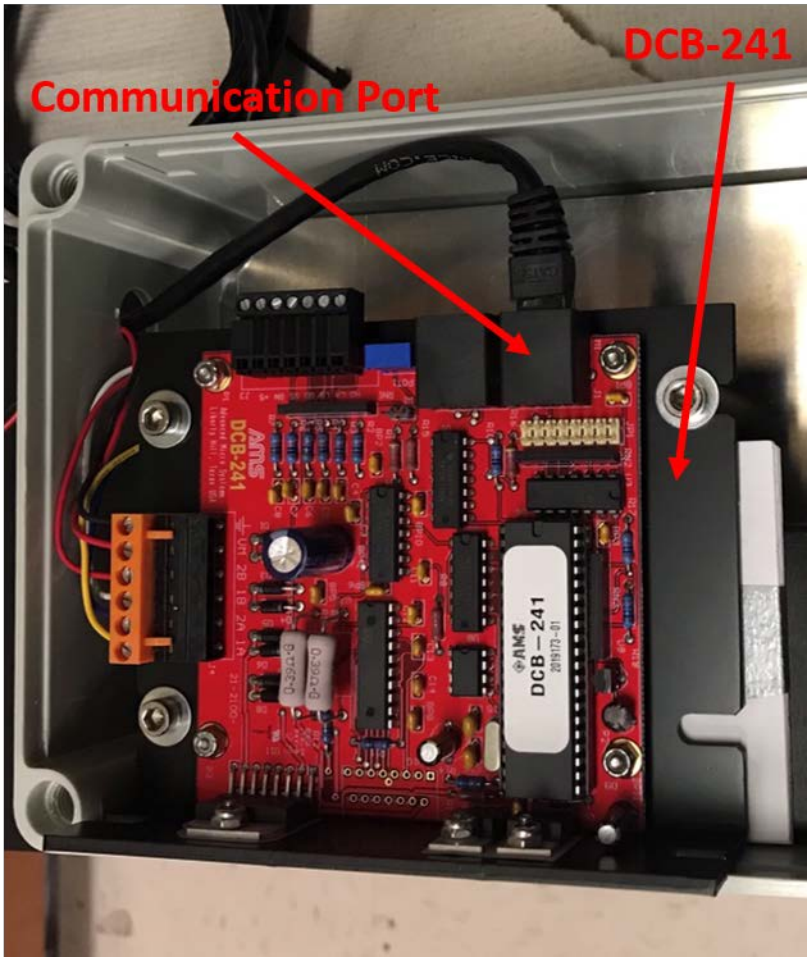

Figure 20: Overall communication setup for the excitation monochromator subsystem.

Emission Monochromator Communication

Communication with the emission monochromator subsystem is achieved through an RS-232 port integrated with the onboard control electronics. Owing to the onboard RS-232 port, a serial communication cable may be directly connected from the computer to the subsystem for communication. Details regarding the serial port configuration for the emission monochromator are noted in Table 4.

Table 4: Serial port configuration for emission monochromator subsystem [54].

Specification	Value
Baud Rate (bps)	9600
Data Bits	8
Stop Bits	1
Parity	None
Flow Control	Hardware
Handshaking	None

The primary purpose of the emission monochromator subsystem is to detect, digitize, and record the fluorescence and Raman spectra of samples. To that effect, the serial port connection with the subsystem is utilized as a means of issuing high-level, ASCII commands for configuring acquisition parameters (e.g., integration time, averaging, etc.) and receiving spectral data from the linear image sensor within the optical bench. A table of the most relevant commands is provided in Table 5. The full set of commands is available in the associated spectrometer documentation [54].

Table 5: Relevant commands for configuring and reading the spectrometer [54].

Command	Function	Value	Notes
K	Set Baud Rate	0	This command can be used to increase the baud rate (bps) to as high as 115,200 bps.
I	Set Integration Time	50–65535	This command can be used to set the integration time (milliseconds).
A	Set Averaging	1–1000000000	This command can be used to set the number of spectra to average in a given spectrum acquisition.
a	Set ASCII Mode	N/A	This command switches the communication into ASCII mode.
b	Set Binary Mode	N/A	This command switches the communication into binary mode.
S	Initiate Scan	N/A	This command initiates a scan and returns the spectrum in either ASCII or binary mode.

A picture of the communication setup is provided in Figure 21.

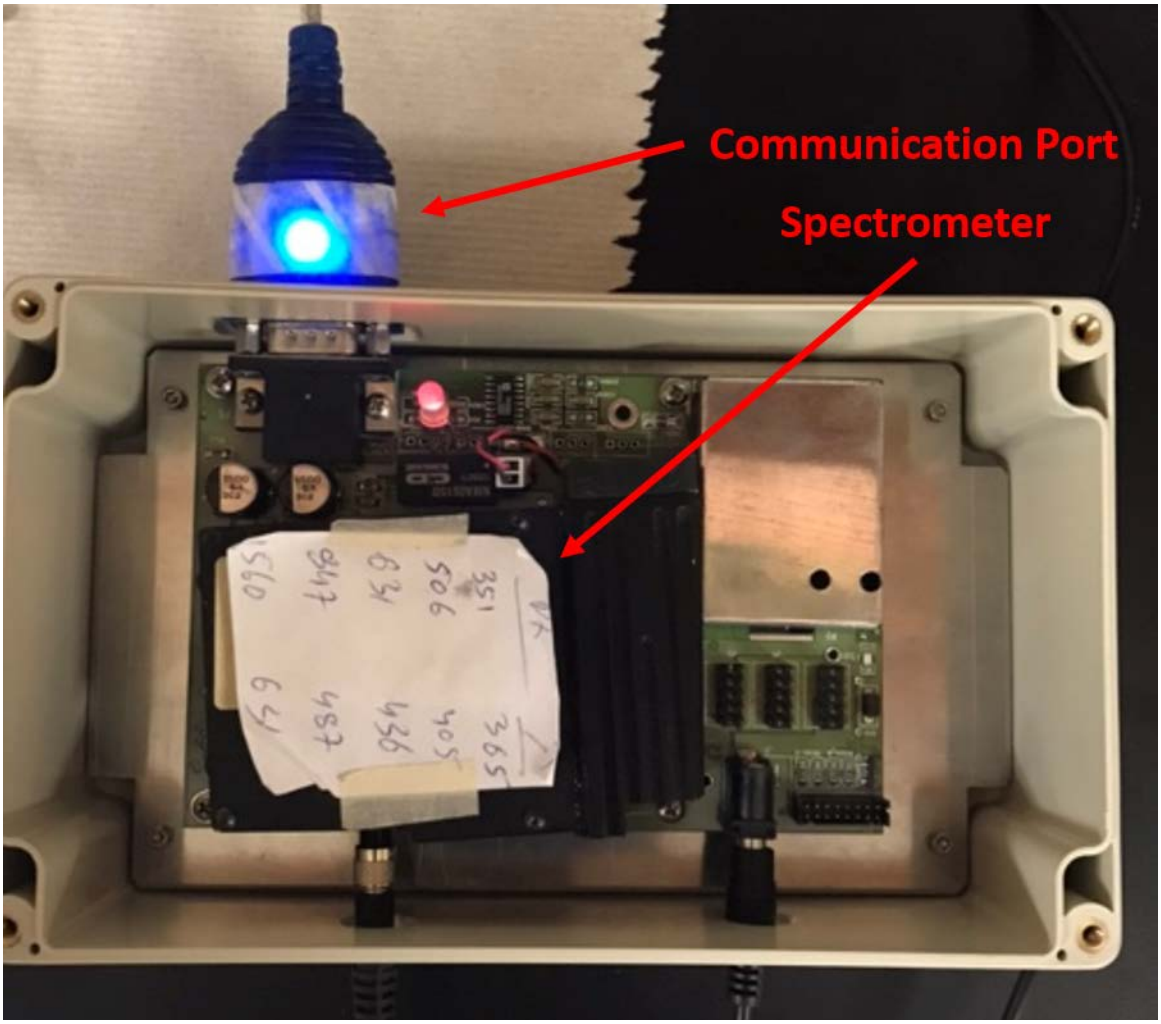

Figure 21: Overall communication setup for the emission monochromator subsystem.

Recording Fluorescence and Raman Spectra

Fluorescence spectra are recorded by utilizing either the disinfection unit or excitation monochromator as a fixed excitation source and subsequently measuring the fluorescence of the bacterial sample through the emission monochromator subsystem. Similarly, Raman spectra are acquired by coupling the Raman excitation module and emission monochromator for inducing,

and subsequently measuring, Raman scattering from the sample. Briefly, these measurements require selecting the scan type (i.e., fluorescence or Raman), identifying the excitation source (i.e., disinfection unit or excitation monochromator), configuring acquisition parameters, acquiring spectral data, processing the data, and outputting the data through a MATLAB figure and CSV file. The control logic for these measurements is provided in Figure 22.

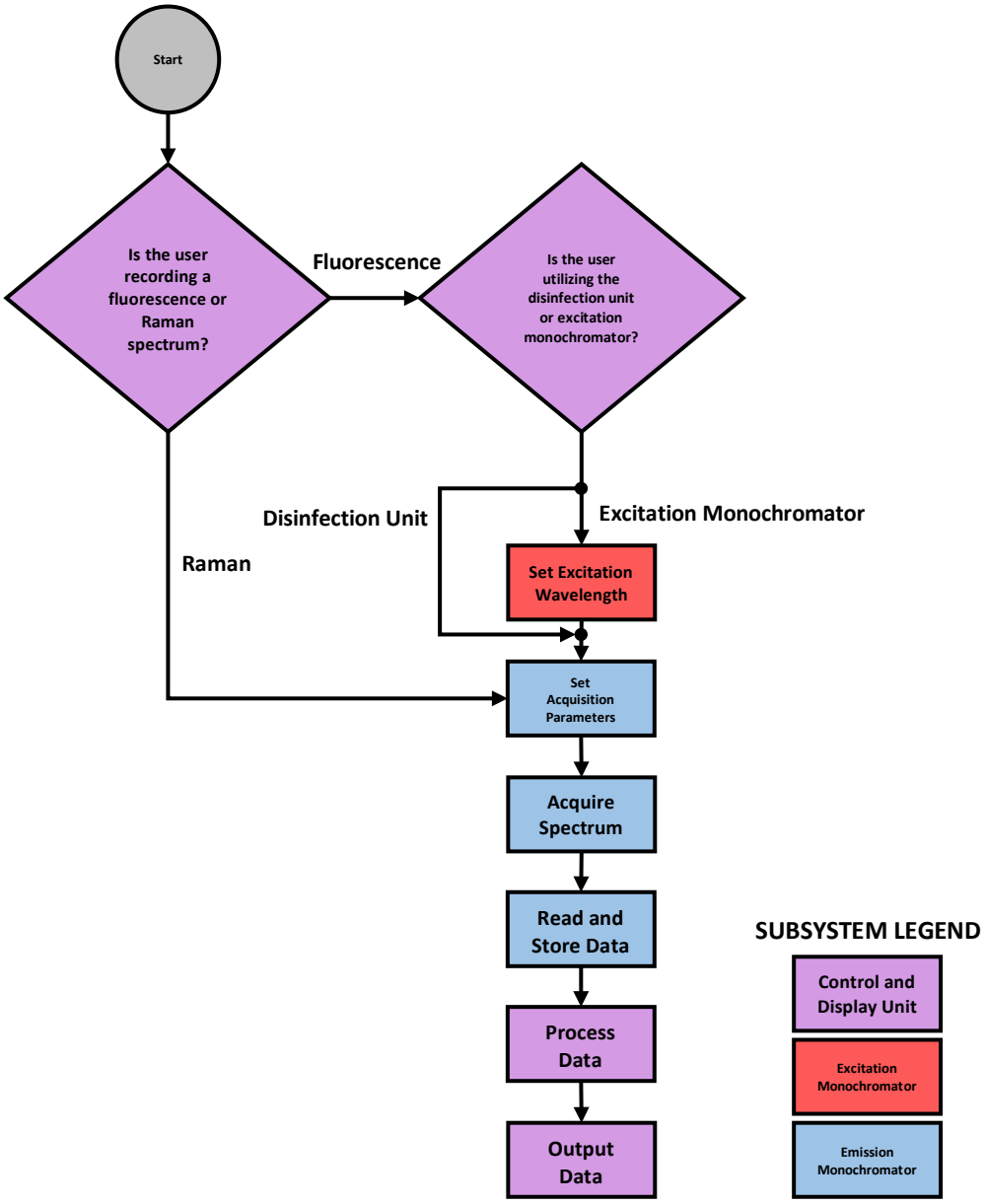

Figure 22: System flowchart detailing the fluorescence and Raman spectrum measurement.

Recording the Excitation-Emission Matrix (EEM) and Synchronous Fluorescence Spectra

The EEM of a sample is recorded by utilizing the excitation monochromator as a scanning excitation source and subsequently measuring the fluorescence of the sample over a range of excitation wavelengths. Briefly, this process requires calibrating and configuring the excitation monochromator, configuring acquisition parameters, acquiring spectral data over a range of scanned excitation wavelengths, processing the data, and outputting the data through MATLAB figures and CSV files. The EEM may be displayed as either a two-dimensional (2D) contour plot or three-dimensional (3D) surface plot. Once the EEM is acquired, synchronous fluorescence spectra of varying $\Delta\lambda$ may be efficiently acquired within the software itself. Currently, once an EEM is acquired, synchronous spectra across a range of $\Delta\lambda$ are automatically extracted and written to a separate CSV file. The control logic for this process is detailed in Figure 23.

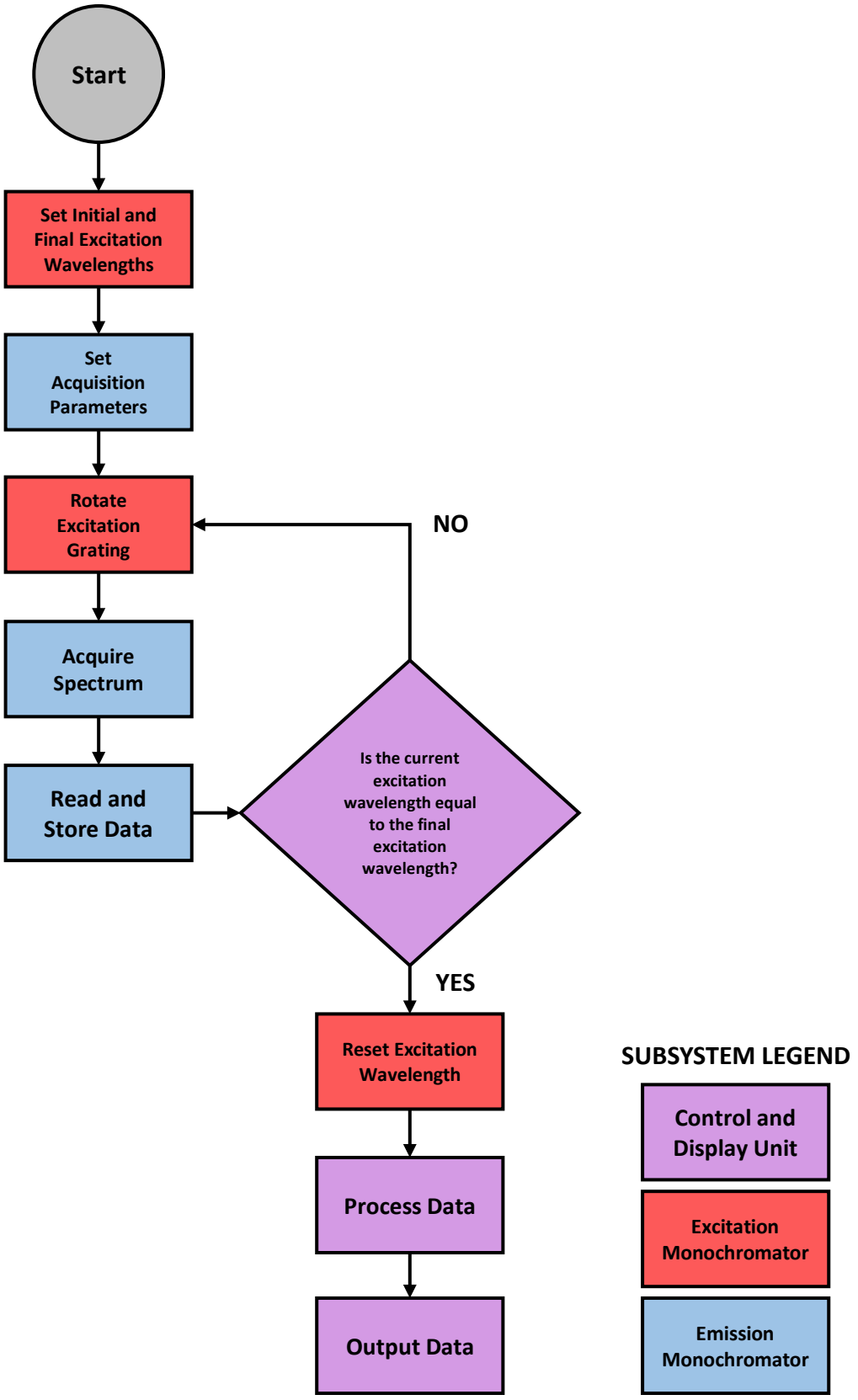

Figure 23: System flowchart detailing the EEM measurement.

Disinfection Unit

Components

Pictures of the disinfection unit subsystem, along with its major components, are shown in Figure 24 and Figure 25.

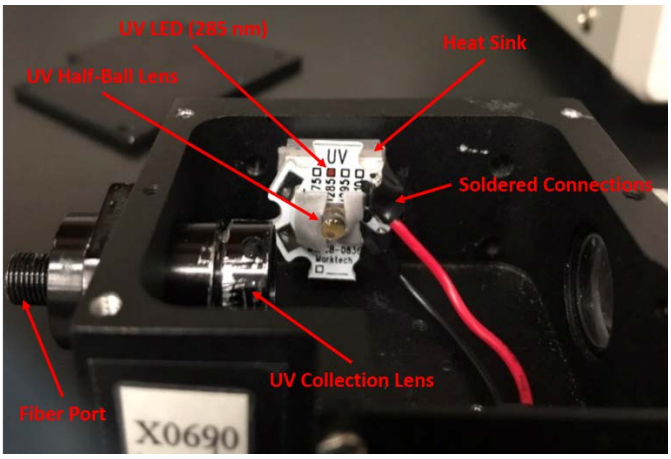

Figure 24: Disinfection unit subsystem and its major components.

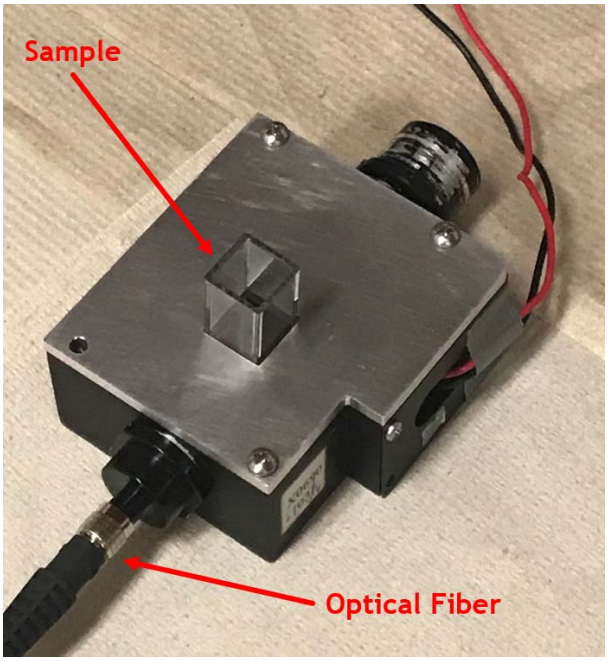

Figure 25: Excitation and disinfection setup.

The disinfection unit currently consists of a high-power, miniature UV LED (Marktech Optoelectronics MTSM285UV-F1120S) mounted on a heat sink and coupled with a UV half-ball lens (Edmund Optics #67-396). The UV LED is attached to the heat sink by means of a thermal adhesive to promote efficient heat dissipation, which is critical in ensuring stable LED operation. A UV half-ball lens is utilized as a means of collecting and focusing the diverging output of the LED. The effect of attaching a UV half-ball lens to the UV LED is shown in Figure 26.

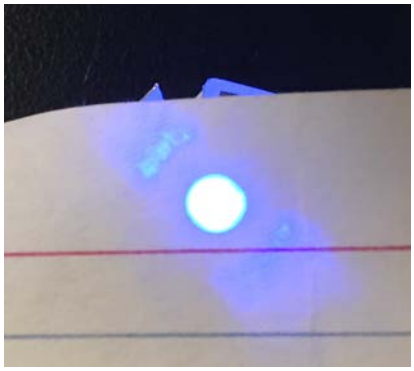

Figure 26: Effect of attaching a UV half-ball lens to the UV LED output.

Thus, the UV half-ball lens increases the excitation intensity and subsequent fluorescence intensity emitted by the bacterial sample. When it is coupled to the emission monochromator subsystem, the disinfection unit may simultaneously inactivate bacteria and serve as an excitation source for fluorescence measurements. This setup is a rather efficient means of monitoring changes in the fluorescence of a bacterial sample, which is indicative of the fraction of bacteria inactivated, as a function of the UV irradiation time. Owing to the fact that the fluorescence of the sample is rapidly diverging, a UV collection lens is utilized for collecting and focusing the fluorescence onto an optical fiber (Thorlabs M114L01) positioned at the fiber port. This optical fiber is coupled to the input port of the emission monochromator for recording the

sample fluorescence. The enclosure, fiber port, and collection lens holder are off-the-shelf components from B&W Tek, while the cover was designed and fabricated.

UV LED

Selection of the proper UV LED is particularly critical in ensuring that the functionalities of disinfection and excitation are both satisfied by a single LED. The maximum germicidal effectiveness is theoretically achieved at a UVC wavelength of ~ 265 nm [35], which corresponds to the absorption band of DNA. The fluorescence of bacteria, however, is primarily due to tryptophan and tyrosine residues, rather than DNA, which possess absorption bands at higher wavelengths in the UVB and UVC region (~ 270–290 nm). Tryptophan, in particular, is known to be the most intensely absorbing and fluorescing component of bacteria, with an absorption band maximum at ~ 280 nm. Therefore, a central wavelength of 285 nm was selected for the UV LED, which also provides a rather high germicidal effectiveness [35]. To that effect, the nominal output spectrum of the selected UV LED is shown in Figure 27. The nominal electrical and optical characteristics of this component were previously described in Chapter III.

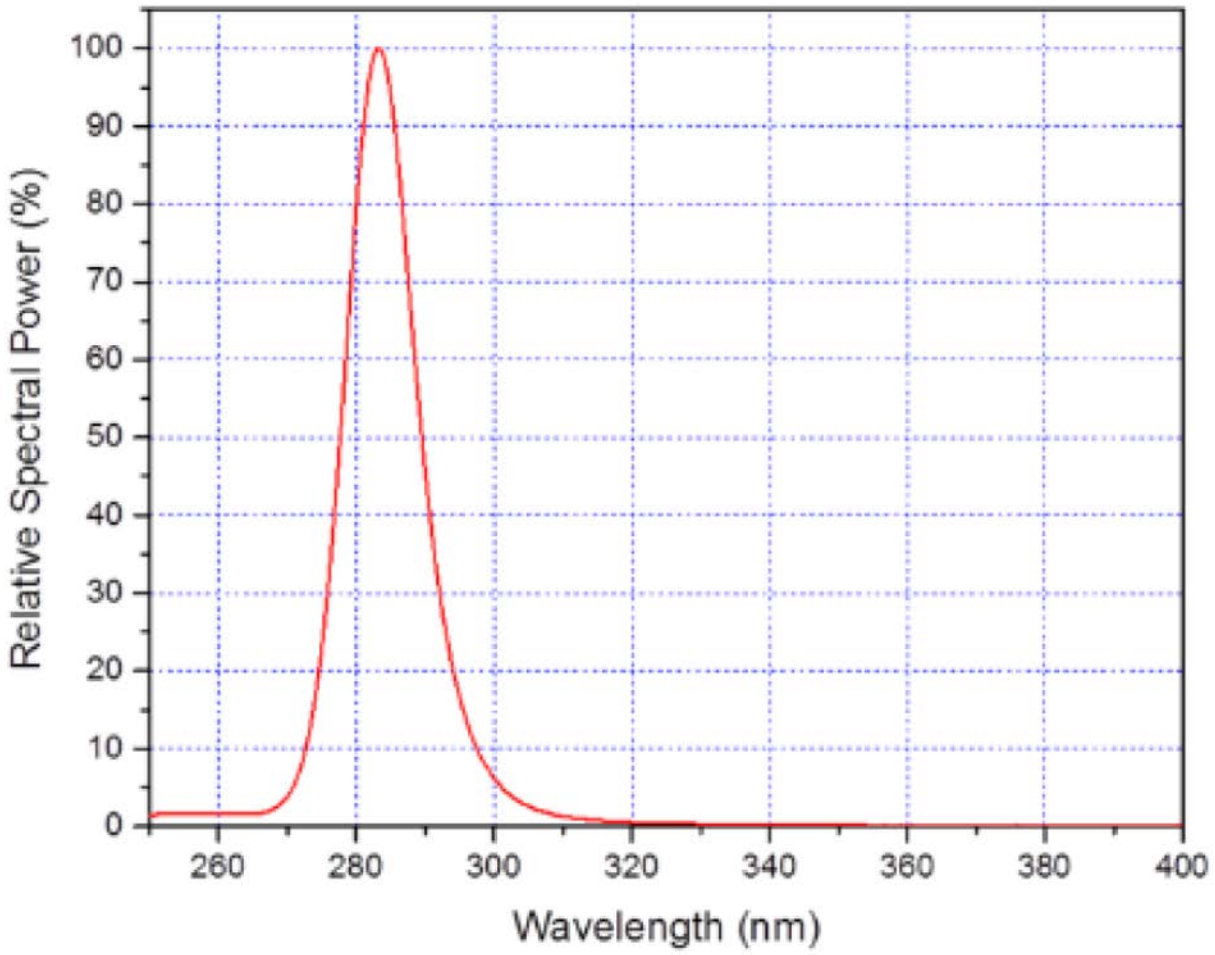

Figure 27: Output spectrum of UV LED for disinfection unit [52].

The specifications for the peak wavelength and full width at half maximum (FWHM) of the UV LED indicate that it is a suitable component for functioning as both a disinfection and excitation source, as its most intense emission wavelengths correspond to the absorption bands of tryptophan and tyrosine, in addition to providing high germicidal effectiveness. Owing to the fact that the absorption bands of tryptophan and tyrosine are rather broad, slight deviations in the exact peak emission wavelength do not significantly affect the excitation and disinfection capabilities of the UV LED.

Excitation Monochromator

Components

A picture of the excitation monochromator subsystem, along with its major components, is provided in Figure 28.

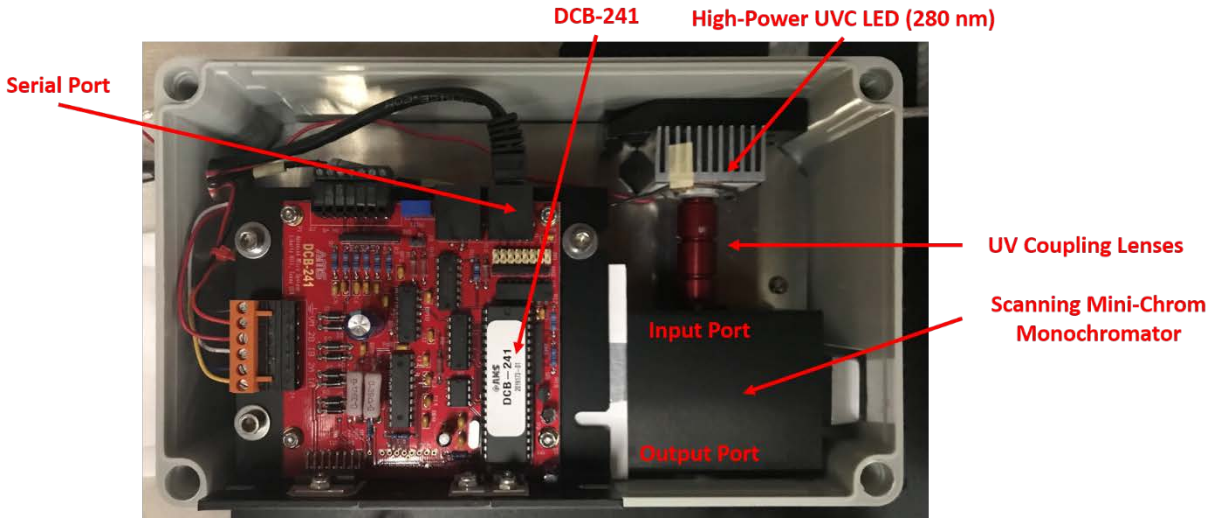

Figure 28: Excitation monochromator subsystem and its major components.

The excitation monochromator consists of a high-power, miniature UV LED (RayVio Corporation RVXP4-280-SM-077132) mounted on a heat sink and coupled with a set of three UV plano-convex lenses (Fiberguide Industries FSG012S0180). Similar to the disinfection unit, the UV LED is attached to the heat sink with a thermal adhesive to promote efficient heat dissipation. The three UV lenses are necessary for collecting and reducing the divergence of the LED output and ensuring that good coupling is achieved with the scanning monochromator, which determines the excitation intensity at the sample location and consequent fluorescence intensity. The effect of the coupling lenses is shown in Figure 29 and Figure 30.

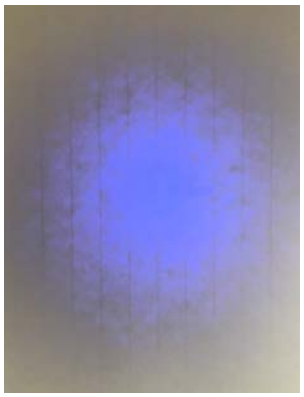

Figure 29: Image of UV LED output without coupling lenses.

Figure 30: Image of UV LED output with coupling lenses.

Thus, the UV coupling lenses are critical in capturing a large fraction of the rapidly diverging UV light from the LED. The use of three lenses increases the total optical power and results in a sharp image of the emitting surfaces within the LED. Alignment was manually performed between the UV LED and input slit of the excitation monochromator to maximize the coupling between the two components.

The scanning monochromator is an off-the-shelf component from Dynasil (SDMC1-02). The monochromator consists of two folding mirrors, a single curved mirror, and a reflective diffraction grating. The function of this component is to disperse the rather narrowband UV light from the LED and focus a particular wavelength of the dispersed light on the exit slit of the

monochromator. The particular wavelength of the dispersed light focused on the exit slit is dependent upon the angular positioning of the excitation grating and controlled by an onboard stepper motor. To that effect, the EEM of a sample may be acquired by rotating the excitation grating and consequently scanning a range of excitation wavelengths.

The integrated stepper motor controller and driver is the DCB-241, which was previously described in this chapter. The controller is wired to the stepper motor within the monochromator through an external DB-15 connector. Communication with the controller is achieved through the onboard serial port.

A mounting plate for this subsystem was designed and fabricated. In addition, an inexpensive, compact electronics project box was utilized as the enclosure.

UV LED

Selection of the UV LED wavelength was guided, mainly, by the same considerations noted with the UV LED in the disinfection unit subsystem. Owing to the fact that the LED output passes through a monochromator in this subsystem, however, an LED with a significantly higher output power was selected. This is necessary to account for both (a) coupling losses at the input of the monochromator and (b) diffraction losses within the monochromator itself, which will significantly reduce the excitation intensity at the sample location. To that effect, the nominal output spectrum of the selected UV LED is shown in Figure 31. The nominal electrical and optical characteristics of this component are also provided in Table 6.

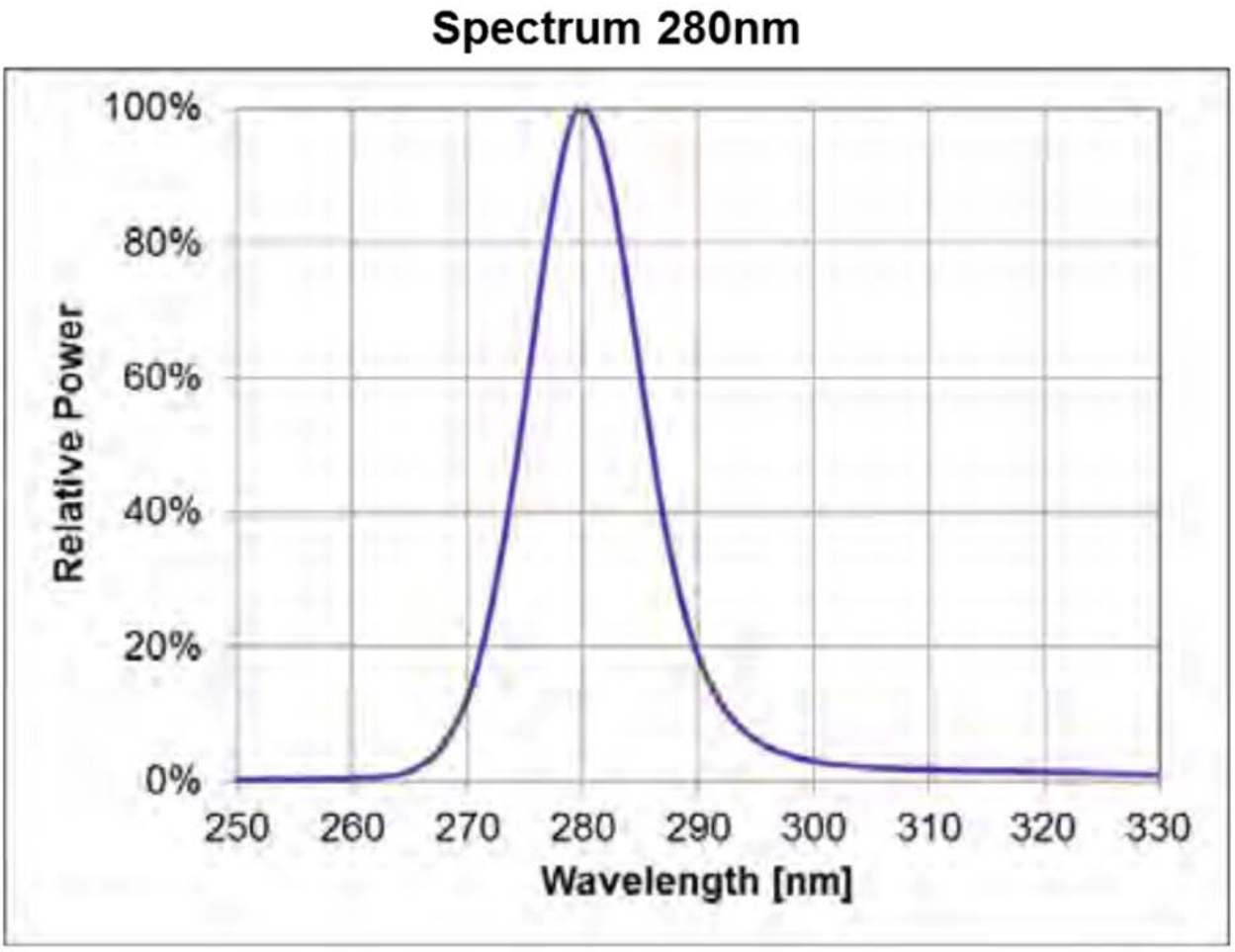

Figure 31: Output spectrum of UV LED for excitation monochromator [55].

Table 6: Nominal characteristics of UV LED for excitation monochromator [55].

Specification	Condition	Minimum	Typical	Maximum
Peak Wavelength (nm)	$I_F = 200$ mA	275	280	285
Power Output (mW)	$I_F = 200$ mA	30	50	70
Forward Voltage (V)	$I_F = 200$ mA	20	26	32
FWHM (nm)	$I_F = 200$ mA	Not given.	15	Not given.

Thus, the selected UV LED for the excitation monochromator has a significantly higher optical power, along with a larger bandwidth, than that used for the disinfection unit. This output power is among the highest available for current UV LED technology.

Scanning Monochromator

The scanning monochromator selected for this subsystem is the Scanning Digital Mini-Chrom Monochromator (SDMC1-02) sold by Dynasil. The optical layout for this component is provided in Figure 32.

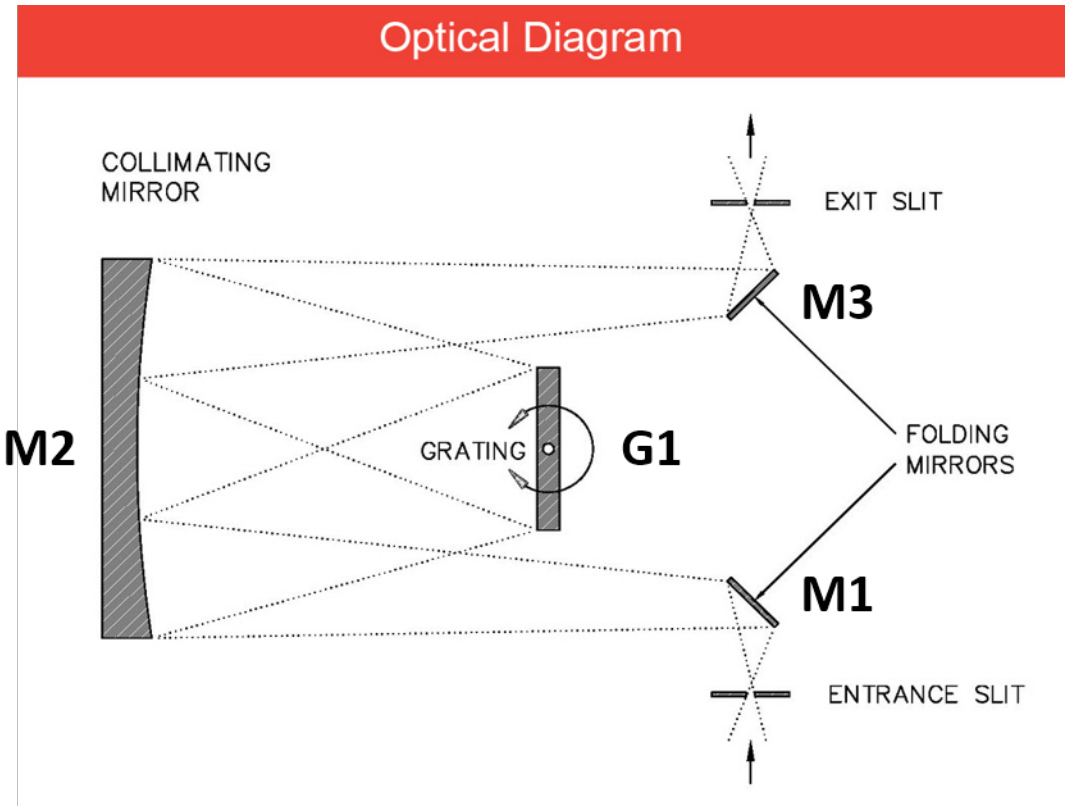

Figure 32: Optical layout of the scanning monochromator [56].

The monochromator optical bench houses a Fastie-Ebert configuration, consisting of two folding mirrors, $M1$ and $M3$, a single curved mirror, $M2$, and a reflective diffraction grating, $G1$. The

high-power, miniature UV LED is coupled to the monochromator at the entrance slit, whereupon the input UV light is reflected by $M1$ to $M2$. $M2$ then collimates and directs the light to the reflective diffraction grating, $G1$, which disperses and reflects the light to $M2$ again, which focuses the light to the exit slit by means of $M3$. The particular wavelength of the dispersed light focused on the exit slit depends upon the angular positioning of the excitation grating, $G1$. To that effect, the DCB-241 rotates a stepper motor within the monochromator connected to the excitation grating. This allows for rotation to a desired output wavelength or, alternatively, through a range of excitation wavelengths, as required in the acquisition of an EEM. An optical fiber may also be connected at the exit slit to transmit the excitation light to the sample. In order to maximize the excitation intensity, however, the sample should ideally be situated directly at the exit slit itself. The efficiency curve of the excitation grating, $G1$, is provided in Figure 33.

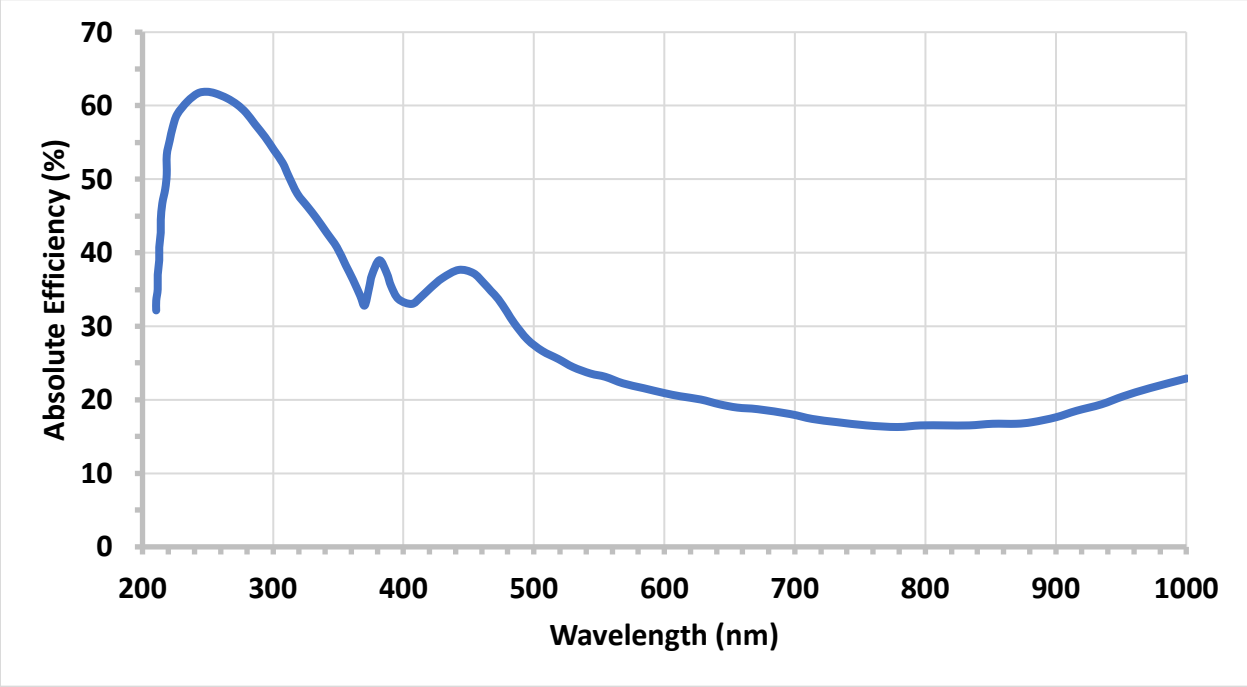

Figure 33: Absolute diffraction efficiency curve of excitation grating [57].

The excitation grating, $G1$, has a groove density $G = 1800\,\frac{lines}{mm}$, along with a blaze wavelength $\lambda_B = 250$ nm, which corresponds to its wavelength of maximum diffraction efficiency. In the excitation region of ~ 260–310 nm, the diffraction efficiency is as high as ~ 50–60%. Thus, the monochromator is optimized for performance in the UV region. Owing to its rather broad efficiency curve, though, this monochromator may also be coupled with visible light sources if needed.

DCB-241

The DCB-241 was described in detail earlier in this chapter. The commands provided in Table 3 were utilized to set the initial and final slew velocity of the stepper motor within the scanning monochromator, rotate the stepper motor and excitation grating, and thereby perform EEM acquisitions when coupled with the emission monochromator subsystem. The DCB-241 was biased through its onboard potentiometer to output a run current which resulted in stable rotation of the stepper motor within the monochromator. This process involved rotating the onboard potentiometer in small increments and observing the performance of the stepper motor in rotating the excitation grating. Once a minimum run current was established, it was increased by ~ 10%. This was done to ensure reliable operation of the stepper motor and minimize heating due to large run currents. The initial and final slew velocities of the stepper motor were then set to the lowest possible values and increased until the stepper motion was deemed sufficiently smooth. The operating parameters of the DCB-241 and stepper motor are summarized in Table 7.

Table 7: Operating parameters of the DCB-241 and stepper motor.

Specification	**Value**
Motor Step Resolution	$8\ \frac{steps}{nm}$
Initial Slew Velocity ($\frac{steps}{second}$)	20
Final Slew Velocity ($\frac{steps}{second}$)	20

Emission Monochromator

Components

A picture of the emission monochromator subsystem, along with its major components, is shown in Figure 34.

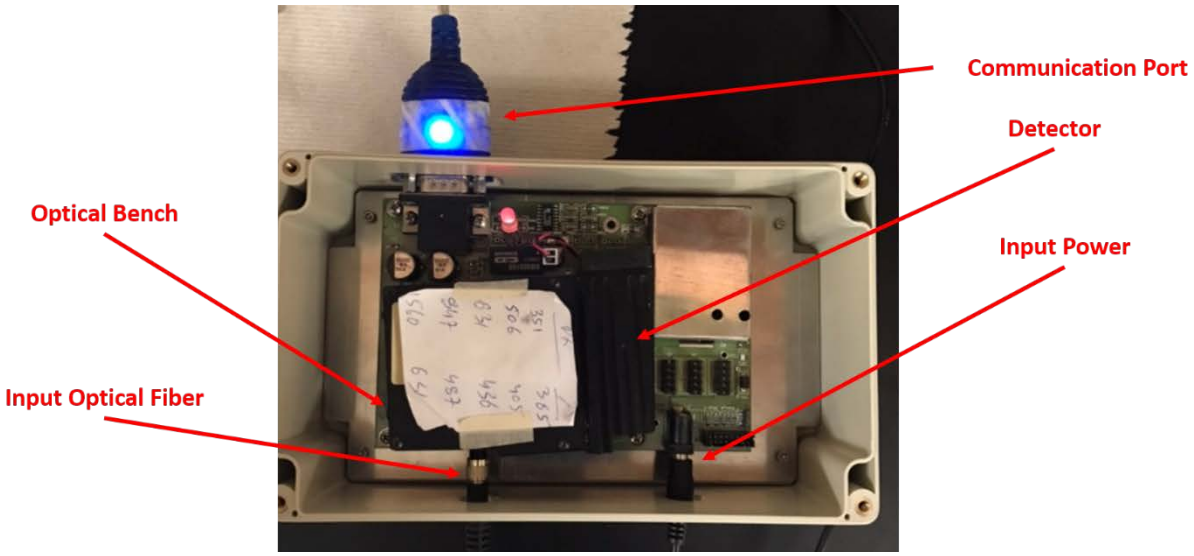

Figure 34: Emission monochromator subsystem and its major components.

The emission monochromator subsystem is an off-the-shelf spectrometer (BTC110-S) from B&W Tek. This spectrometer includes an optical bench, input fiber port, input power port, detector and cooling fan, and communication port for setting acquisition parameters (e.g., integration time, averaging, etc.) and acquiring spectral data. The optical bench may be easily configured and was modified with optical components, namely mirrors and a diffraction grating, with high efficiency in the UV region to increase the spectrometer's sensitivity to bacterial fluorescence. Details regarding the communication with the BTC110-S, and the associated procedures for setting acquisition parameters and receiving spectral data, were provided earlier

in this chapter. In addition, a mounting plate for this subsystem was designed and fabricated. An inexpensive, compact electronics project box was utilized as the enclosure.

Optical Bench

The design of the optical bench and its components is critical in determining the sensitivity and performance of the spectrometer in the UV and visible regions. A schematic of the optical bench and a picture of its components are shown in Figure 35 and Figure 36, respectively.

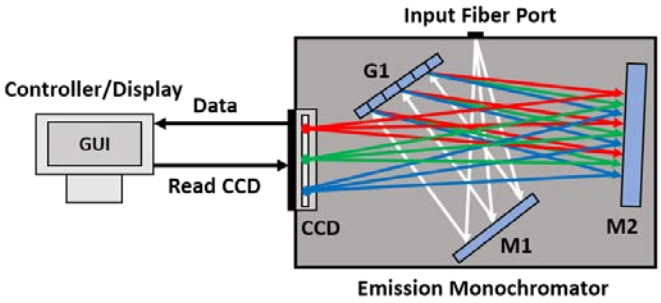

Figure 35: Schematic of optical bench for emission monochromator.

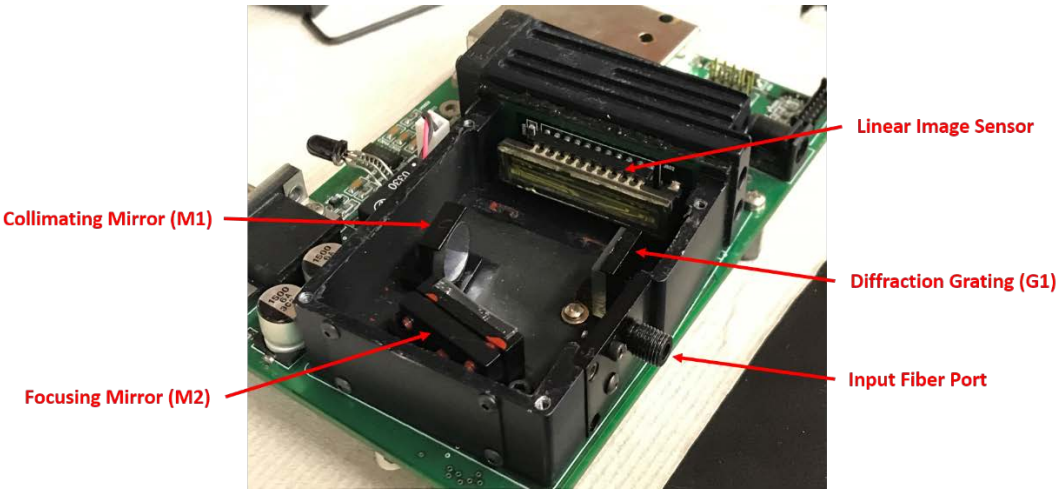

Figure 36: Optical bench and its major components.

The optical bench essentially utilizes the Czerny-Turner configuration, consisting of two concave aluminum mirrors, $M1$ and $M2$, and a reflective diffraction grating, $G1$. Briefly, fluorescence or Raman scattered light entering the input fiber port is collected and collimated by the collimating mirror, $M1$, dispersed by the diffraction grating, $G1$, and then focused onto the pixels of the linear CCD detector array, or linear image sensor, by $M2$, whereupon the spectrum is digitized, stored, and transmitted to the computer by means of control electronics and a serial communication cable. To achieve this, the optical components were properly aligned to maximize the intensity of light falling onto the detector pixels in the focal plane of the spectrometer. This was accomplished by performing horizontal and vertical adjustments on the mirrors and grating through the set screws in the optical bench.

To increase the UV sensitivity of the spectrometer, the visible diffraction grating provided by B&W Tek was replaced with a UV-visible, ruled diffraction grating with a maximum diffraction efficiency as high as $\sim$ 75% in the UV region (Newport Corporation 33025FL01-060R). This grating is mounted in the Littrow configuration [58] at its associated blaze angle $\theta_B \sim 8.6°$. The usage of this grating ensures that the fluorescence of bacteria and its components is not significantly attenuated within the optical bench. In addition to the diffraction grating, the collimating mirror was replaced with a UV-enhanced mirror of the same size to further increase the efficiency of the spectrometer in the UV region.

The detector is the Sony ILX511B linear image sensor [59], which is a CCD detector with 2048 pixels. This detector inherently has peak sensitivity in the visible region, but rather low UV sensitivity. Therefore, this detector was ordered with an additional dye coating known as Lumogen F Violet 570 [60–61]. This dye absorbs strongly in the UV region and fluoresces in the visible region, thereby increasing the UV sensitivity of the detector. Owing to its enhanced and

broad sensitivity, this detector is suitable for acquiring fluorescence and Raman spectra in the UV and visible regions. The efficiency curve of the diffraction grating $G1$ and sensitivity curve of the detector are provided in Figure 37 and Figure 38, respectively.

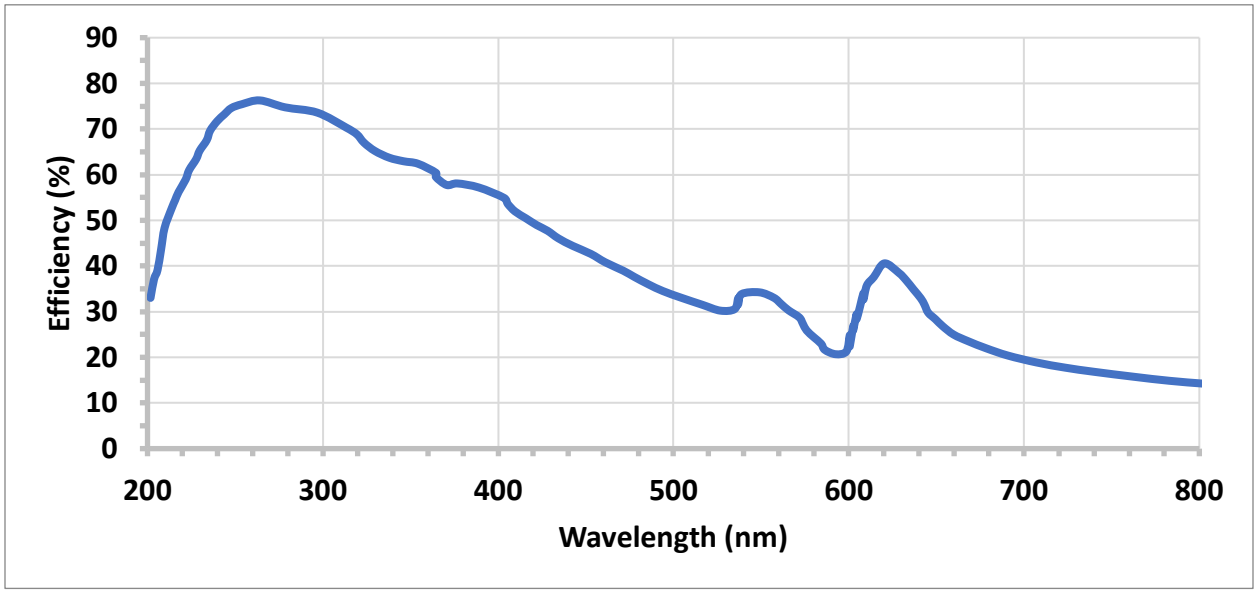

Figure 37: Diffraction efficiency curve of emission grating $G1$ [62].

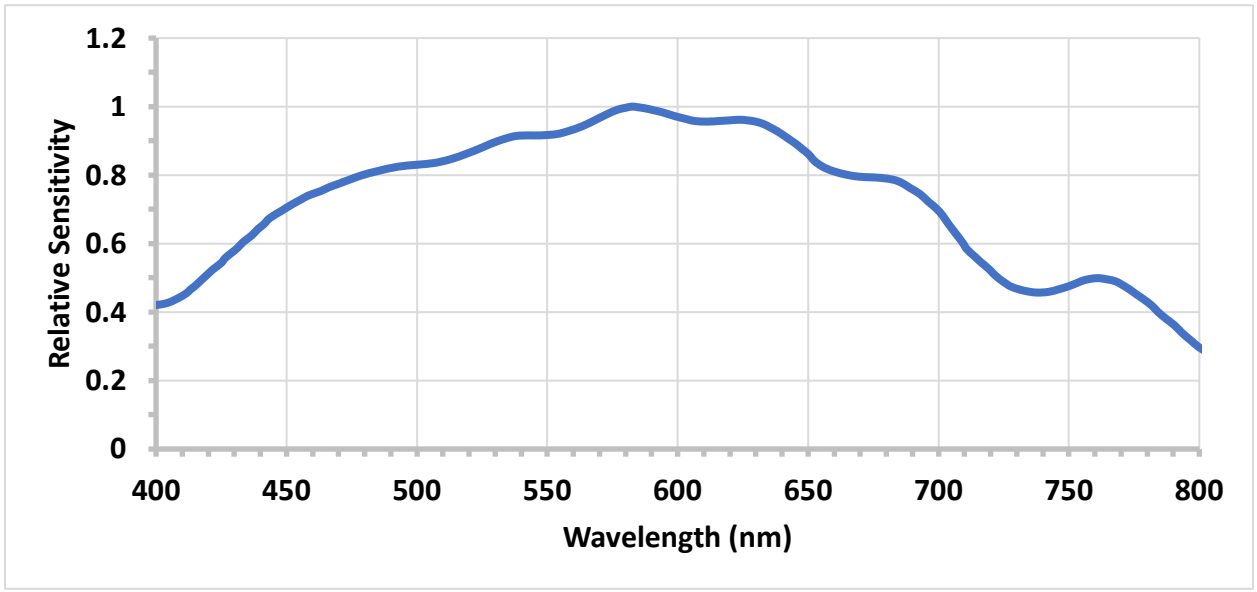

Figure 38: Sensitivity curve of detector (Sony ILX511B) [59].

The emission grating, $G1$, which has a groove density $G = 1200\,\frac{lines}{mm}$ and a designated blaze wavelength $\lambda_B = 250$ nm, is a rather critical component in determining the performance of the spectrometer. Considering the grating equation for a reflective diffraction grating [63],

$$d[\sin(\theta_i) + \sin(\theta_m)] = m\lambda \tag{6}$$

where d represents the grating pitch, θ_i is the incident angle, θ_m is the diffracted angle, m is the diffraction order, and λ is the wavelength. Note that θ_i and θ_m are expressed with respect to the grating normal. Differentiating with respect to wavelength,

$$d\cos(\theta_m)\frac{d\theta_m}{d\lambda} = m \tag{7}$$

Observe that while θ_i is constant for the incident beam, θ_m varies for each component wavelength. Consequently,

$$\frac{d\theta_m}{d\lambda} = \frac{m}{d\cos(\theta_m)} \tag{8}$$

where $\frac{d\theta_m}{d\lambda}$ represents the angular dispersion of the grating. This angular dispersion corresponds to a linear dispersion, $\frac{dx}{d\lambda}$, and reciprocal linear dispersion, $\frac{d\lambda}{dx}$, in the focal plane:

$$\frac{dx}{d\lambda} = \frac{d\theta_m}{d\lambda} \times f = \frac{m}{d\cos(\theta_m)} \times f \tag{9}$$

$$\frac{d\lambda}{dx} = \left(\frac{dx}{d\lambda}\right)^{-1} = \frac{d\cos(\theta_m)}{m \times f} \tag{10}$$

where f is the focal length of the focusing mirror $M2$. The theoretical wavelength spread, $\Delta\lambda$, across the detector plane may then be computed:

$$\Delta\lambda = \int_{\lambda_1}^{\lambda_2} d\lambda = \int_{x_1}^{x_2} \frac{d\cos(\theta_m)}{m \times f}\,dx = \frac{d}{m \times f}\int_0^L \cos(\theta_m)\,dx = \frac{d}{m \times f}\int_0^L \cos\left(\frac{x}{f}\right)dx \tag{11}$$

where $d = \frac{1}{G} \sim 833.333$ nm (grating pitch) and $f \sim 42$ mm (focal length of $M2$). In addition, for a detector pitch $W_P = 14\ \mu$m and $n = 2048$ pixels, $L = W_P \times n = 28672\ \mu$m (detector length). Assuming first-order diffraction ($m = 1$), we obtain the following:

$$\Delta\lambda \sim 525.72 \text{ nm}$$

which is larger than the experimentally observed spread $\Delta\lambda \sim 438.066$ nm. The reduced experimental spread is most probably due to a mismatch in the detector pitch and slit width, which limits the individual resolution of each pixel, along with nonidealities such as astigmatism and imperfect alignment between the beam profile, grating plane, and detector plane. The rather large wavelength spread nevertheless allows the spectrometer to detect both UV and visible region fluorescence and Raman bands. We may similarly compute the theoretical resolution, $d\lambda$, of the spectrometer [64]:

$$d\lambda = \frac{RF \times \Delta\lambda \times W_S}{L} \tag{12}$$

where $RF \sim 1.7145$ is a resolution factor determined by the relationship between the slit width and pixel width [64], $\Delta\lambda \sim 525.72$ nm is the theoretical wavelength spread across the detector plane, $L = 28672\ \mu$m is the detector length, and $W_S = 50\ \mu$m is the slit width. Consequently,

$$d\lambda \sim 1.572 \text{ nm}.$$

For Raman measurements, this corresponds to the following resolution in wavenumbers:

$$dR = 10^7 \times \left(\frac{1}{\lambda_{EX}} - \frac{1}{\lambda_{EX} + d\lambda}\right) \tag{13}$$

where $\lambda_{EX} = 532$ nm represents the excitation wavelength. Thus,

$$dR \sim 55.386 \text{ cm}^{-1}.$$

These values are also in good agreement with the experimentally observed values of $d\lambda \sim 2$ nm and $dR \sim 70.4$ cm^{-1}. This resolution may be improved, at the expense of the wavelength spread

at the detector plane, by increasing the grating density. The current resolution is sufficient for resolving the fluorescence bands, in addition to the most prominent Raman bands, of bacteria, bacterial components, and other molecules of interest in this research. The relevant optical characteristics of the spectrometer are summarized in Table 8.

Table 8: Optical characteristics of spectrometer.

Specification	**Theoretical**	**Measured**
Wavelength Spread $\Delta\lambda$ (nm)	525.72	438.066
Resolution (nm)	1.572	2
Resolution (cm^{-1})	55.386	70.4

Calibration

Calibration of the spectrometer is performed by recording the spectrum of a light source with distinct emission lines and subsequently deriving a fitting which provides the wavelength as a function of the detector pixel. This calibration is utilized, in software, to convert the pixel-dependent intensity read out by the detector into a wavelength-dependent spectrum. A rather simple source to use in this process is the mercury-vapor lamp, also known as the compact fluorescent lamp (CFL), which is the same lamp typically used for overhead lighting. Figure 39 shows the CFL spectrum recorded by the emission monochromator.

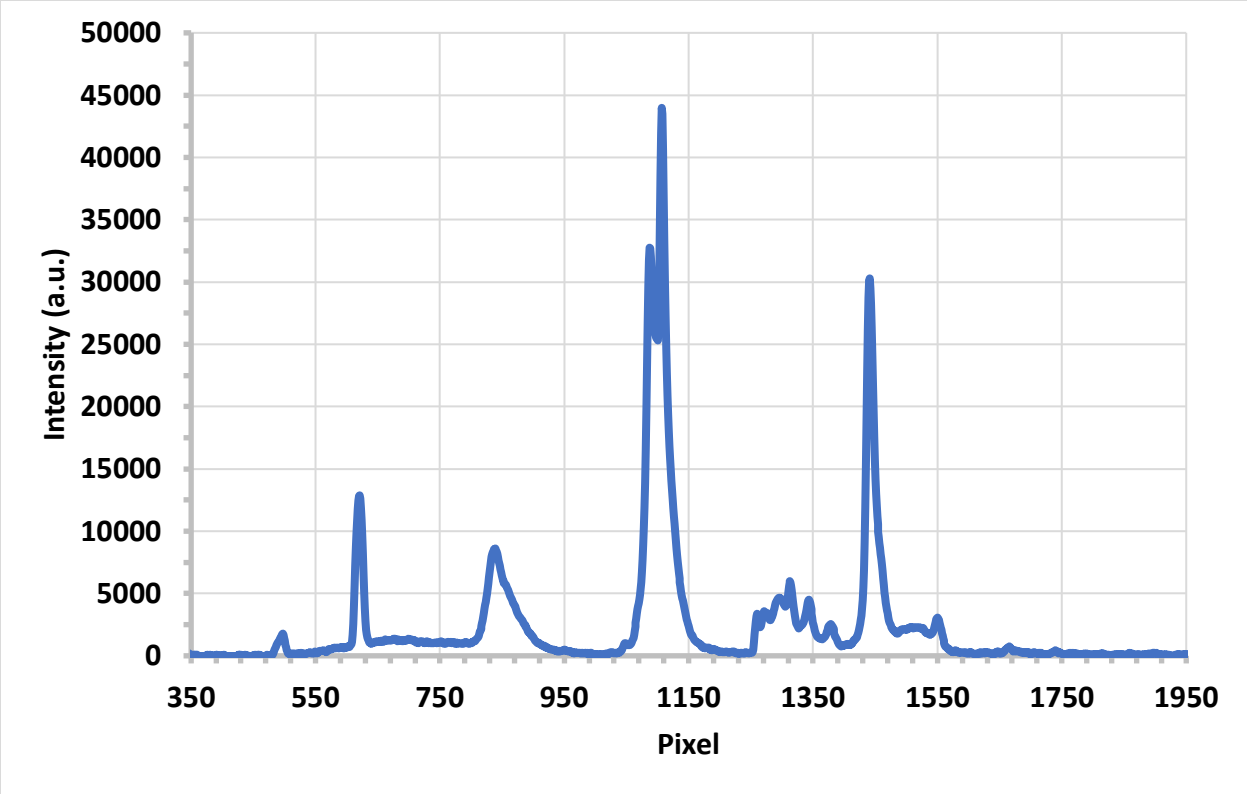

Figure 39: CFL spectrum recorded by the emission monochromator as a function of pixel.

From the data shown above, distinct emission lines of the CFL spectrum [65–66] in the UV and visible region could be identified at certain pixels. Recall Equation (10):

$$\frac{d\lambda}{dx} = \left(\frac{dx}{d\lambda}\right)^{-1} = \frac{d\cos(\theta_m)}{m \times f} \tag{10}$$

The above equation suggests that for small diffraction angles θ_m, where $\cos(\theta_m) \sim 1$, $\lambda = f(x)$ is a purely linear function of the position, and hence pixel number, in the focal plane of the spectrometer. For large diffraction angles which correspond to the edges of the detector in the focal plane, however, $\lambda = f(x)$ will be nonlinear. Thus, the pixel-wavelength pairs were utilized to derive a third-order polynomial, which accounts for this nonlinearity, using the least squares method. Table 9 provides the pixel-wavelength pairs utilized in deriving this fitting.

Table 9: Pixel-wavelength pairs for calibrating spectrometer.

Pixel	Wavelength (nm)
341	365
496	405.4
620	436.6
838	487.7
1086	542.4
1106	546.5
1260	577.7
1271	580.2
1294	584
1313	587.6
1343	593.4
1378	599.7
1440	611.6
1549	631.1
1666	650.8
1739	662.6
1900	687.7
1948	693.7

Based on the data presented in Table 9, the following third-order polynomial was derived for the pixel-wavelength relation:

$$\lambda(p) = C_0 + C_1 p + C_2 p^2 + C_3 p^3 \qquad (14)$$

where p represents the pixel number (0 to 2047), $C_0 \sim 269.8408968$ nm, $C_1 \sim 0.2921248$ nm, $C_2 \sim -3.7816804 \times 10^{-5}$ nm, and $C_3 \sim -1.6947201 \times 10^{-10}$ nm. This polynomial is graphed in Figure 40 and illustrates the nonlinear behavior predicted by Equation (10) for large diffraction angles.

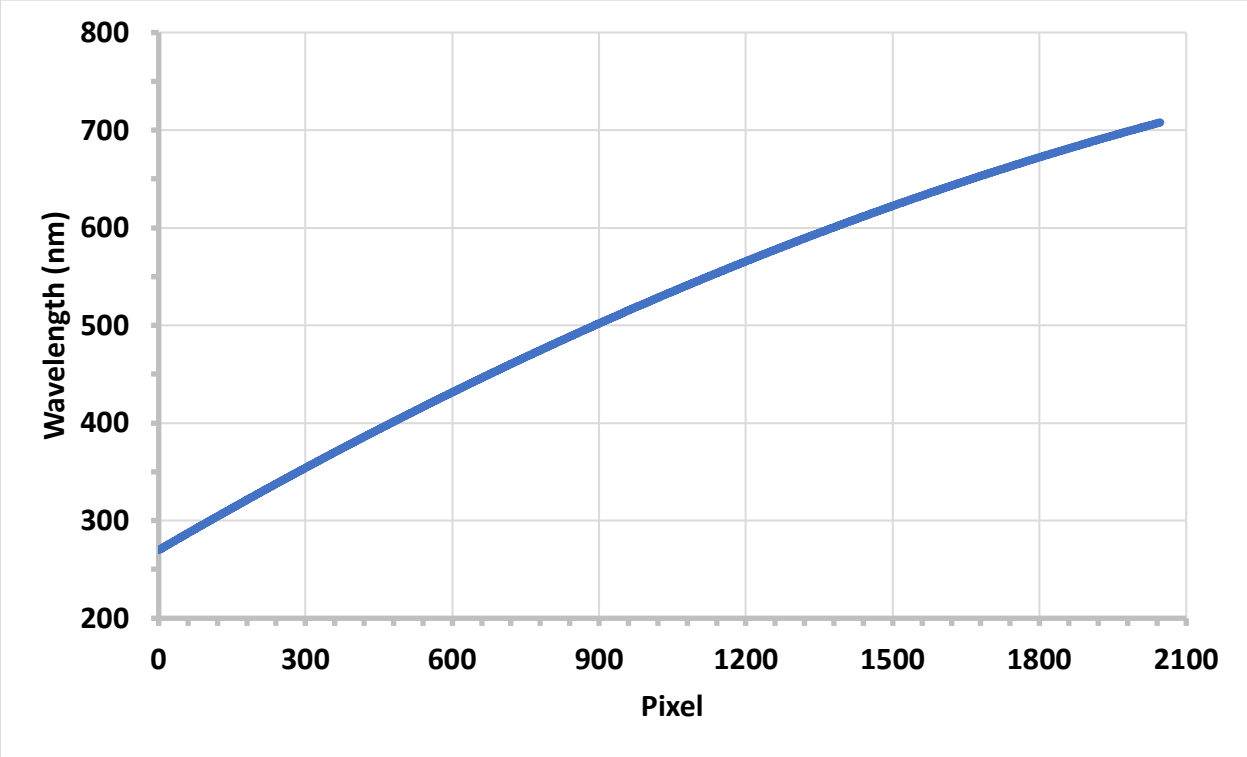

Figure 40: Pixel-wavelength relation $\lambda(p)$.

The resulting fitting was empirically adjusted based on the measured fluorescence and Raman spectra of bacteria and bacterial components to achieve reasonable agreement with those provided in the literature and measured by a benchtop spectrometer.

Raman Excitation Module

Components

A schematic and picture of the Raman excitation module subsystem, along with its major components, are shown in Figure 41 and Figure 42, respectively.

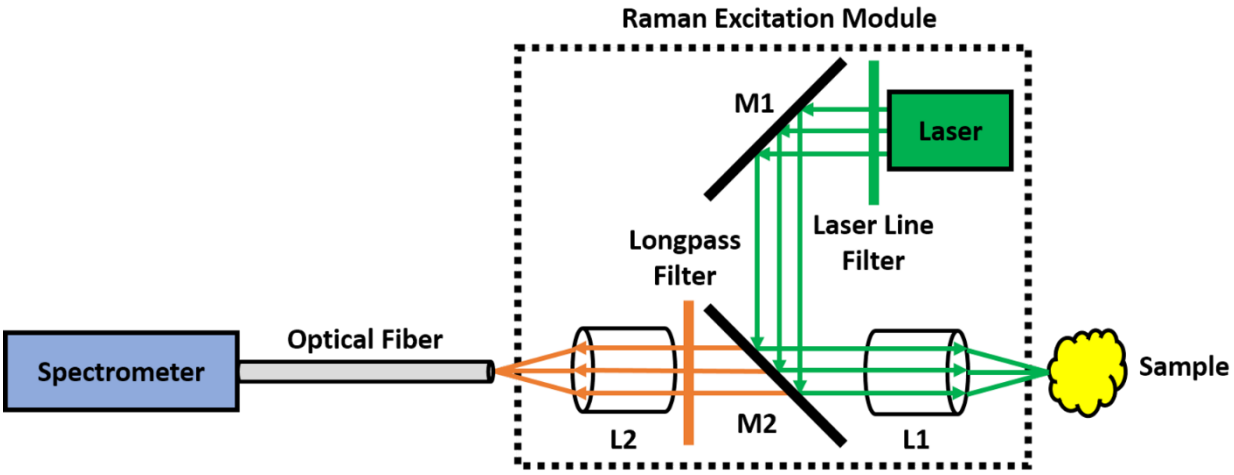

Figure 41: Schematic of the Raman excitation module and its major components.

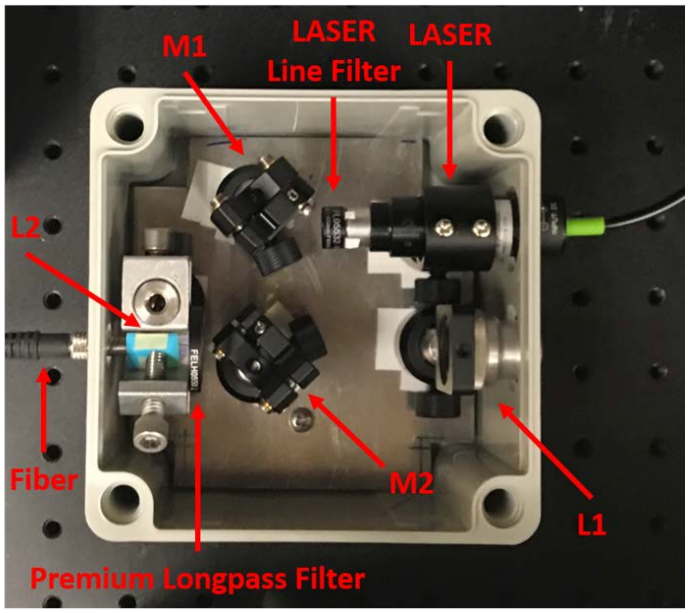

Figure 42: Picture of the Raman excitation module and its major components.

The Raman excitation module essentially utilizes a backscattering optical configuration. The excitation light, which is practically collimated at the laser output, passes through a laser line, "clean-up" filter and is redirected by a plane aluminum mirror, $M1$, and dichroic filter, $M2$, to the microscope objective, $L1$. Owing to the fact that the laser wavelength is below the cutoff wavelength of the dichroic filter for transmission, $M2$ essentially functions as an ideal mirror for 90° reflection. Upon being redirected to $L1$, the laser beam is focused to its diffraction-limited spot size at the focal point of the microscope objective. To maximize the scattering intensity, the sample should ideally be located directly at the focal point of $L1$. Following excitation of the sample, $L1$ collects and collimates the scattered light, which diverges from the focal point of $L1$. The Rayleigh scattered light, which is more intense than the Raman lines by orders of magnitude, is filtered to prevent saturation of the detector. This is achieved through the same dichroic filter, $M2$, which transmits the Stokes-shifted Raman lines, which lie in the passband of the filter, and reflect the Rayleigh line, which lies below the associated cutoff wavelength. An additional longpass filter is utilized to further reduce the Rayleigh line intensity, while enabling the detection of low-frequency Raman bands. The collimated, filtered scattered light is then collected and focused by a coupling lens, $L2$, onto an optical fiber coupled with the emission monochromator subsystem.

Laser Source

The laser source is a continuous-wave (CW) laser diode module (Laserland 1875-532D) with a nominal wavelength of 532 nm and output power of 50 mW. In addition to not possessing any deleterious effects for either chemical or biological samples, this wavelength of light also coincides with the absorption band of various natural pigments, including prodigiosin [67], which exist in living organisms such as bacteria [68]. This suggests that the proposed system is

capable of recording the resonance Raman spectra of such pigments, in addition to the Raman spectra of other biomolecules and chemicals in the solid, liquid, or gas phase. The output of the laser diode module is coupled to a laser line, “clean-up” filter (Thorlabs FL05532-10) which removes additional, undesirable longitudinal modes that reduce the purity of the excitation light and may result in spurious signal or saturation of the detector. To that effect, the transmission spectrum of the filter is plotted in Figure 43.

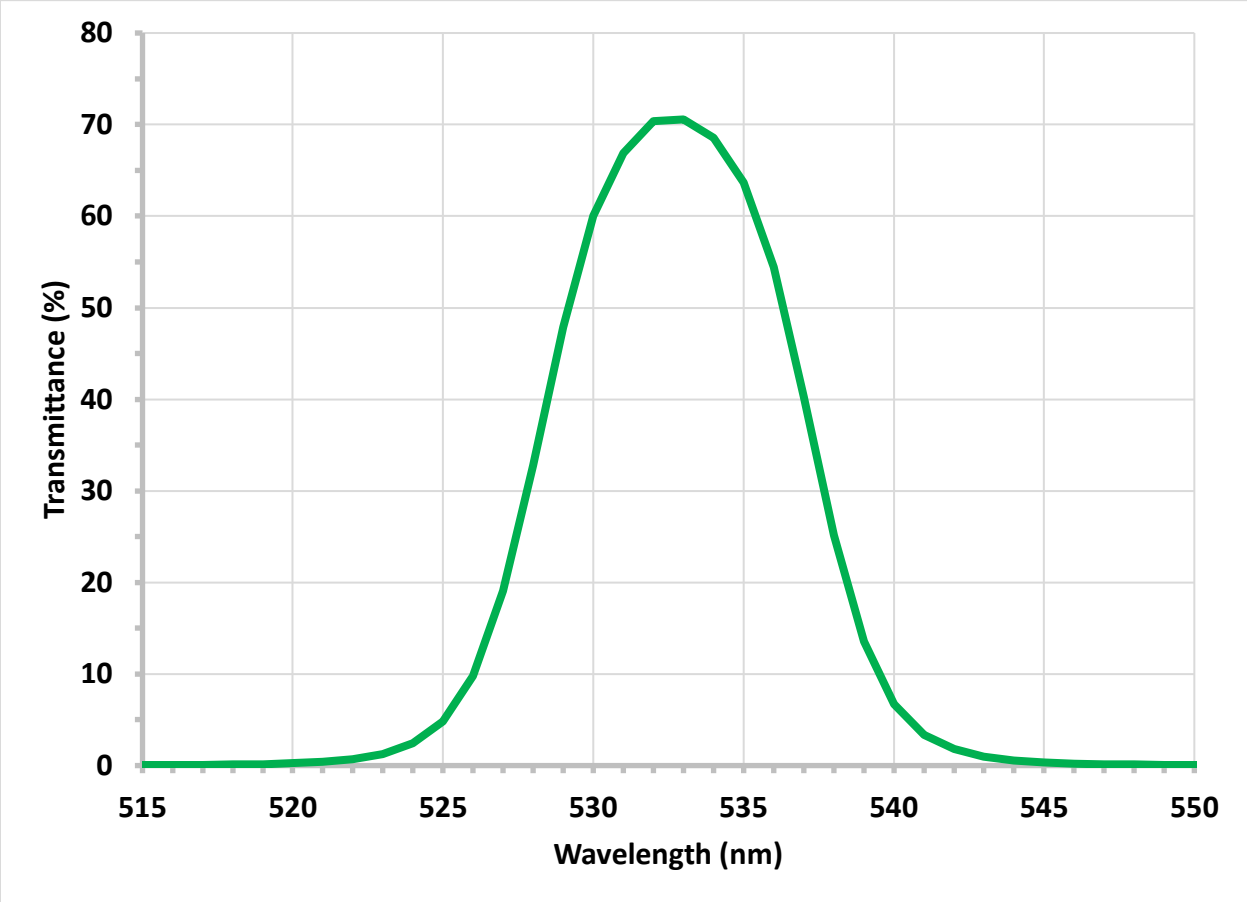

Figure 43: Transmission spectrum of the laser clean-up filter [69].

Clearly, the laser line filter produces a rather pure output at the nominal laser wavelength of 532 nm.

Optical Path Components

In regards to the excitation and collection optics, the optical path components include a plane aluminum mirror, $M1$, dichroic filter, $M2$, microscope objective, $L1$, longpass filter, and coupling lens, $L2$. $M1$ is a protected aluminum mirror (Thorlabs PF05-03-G01) with high broadband reflectivity (> 90%) in the visible region without the usage of any additional coatings. In addition, the placement of $M1$ allows for a simplified alignment of the laser beam in scenarios where the laser source is modified.

Following $M1$, $M2$ is a dichroic filter (Thorlabs DMLP550T) with a cutoff wavelength, 550 nm, that is well above the laser output wavelength in order to minimize transmission of the beam during its incident propagation, in addition to filtering the Rayleigh scattered light from the sample. The transmission and reflectance spectra of the filter are provided in Figure 44.

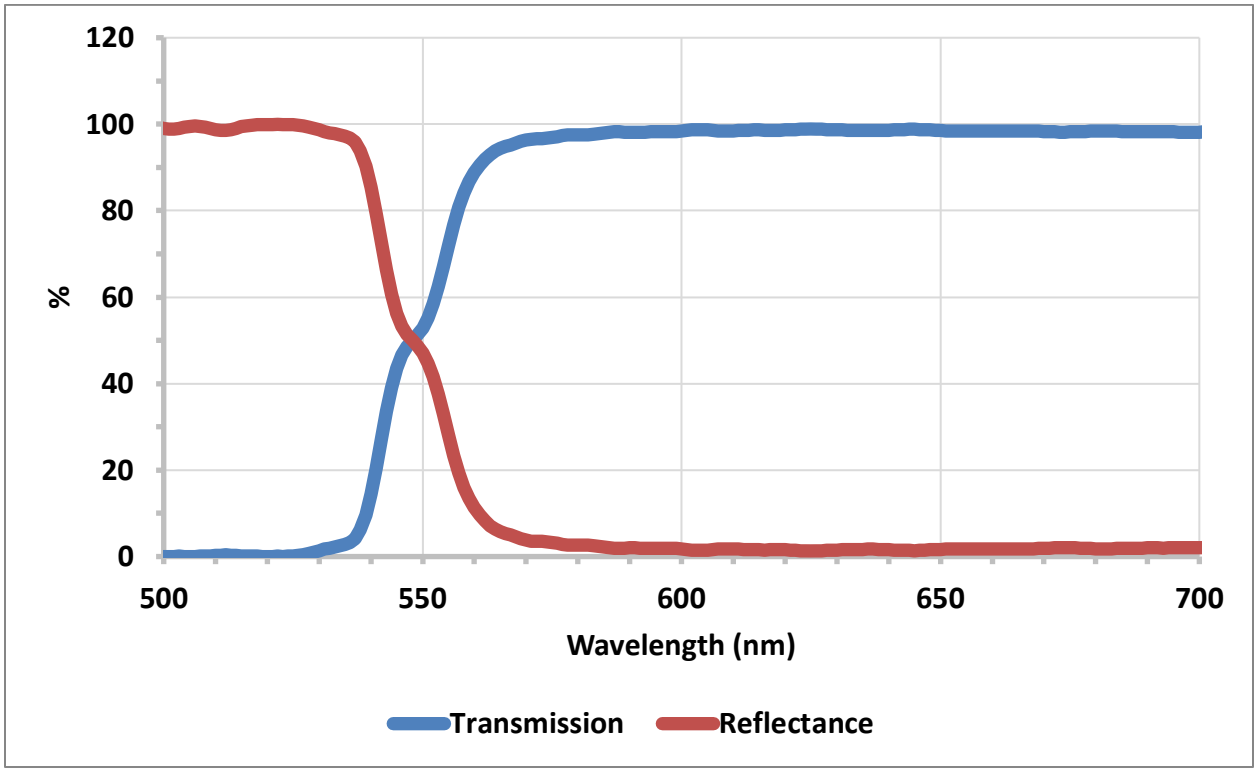

Figure 44: Transmission and reflectance spectra of dichroic filter $M2$ [70].

Following $M2$, $L1$ is a Bausch & Lomb divisible $10X$ microscope objective with high, broadband transmission in the visible region. Considering the focal length of the microscope objective, f, and collimated waist radius of the incident laser beam, w_0, the diffraction-limited spot size may be computed [71]:

$$w_f = \frac{\lambda f}{\pi w_0} \tag{15}$$

where $\lambda = 532$ nm, $f = 16$ mm, and $w_0 \sim 1.6934$ mm. The values for f and w_0 were obtained from the datasheets for the microscope objective and laser source, respectively. Consequently,

$$w_f \sim 1.6\ \mu\text{m}.$$

In general, the diffraction-limited spot size is inversely proportional to the magnification of the microscope objective. Larger magnifications would theoretically increase the scattering intensity owing to the higher numerical aperture and smaller beam diameter at the focal point of $L1$. To that effect, microscope objectives of larger magnification, and consequently smaller focal lengths, may be easily substituted at the lens holder as needed.

The longpass filter (Thorlabs FELH0550) is a premium filter with an optical density (OD) greater than 5 in the stopband (rejection region), along with a transmission higher than 90% in the passband (transmission region). The transmission spectra of the longpass filter and a standard color filter, as a function of the Raman shift, are provided for comparison in Figure 45.

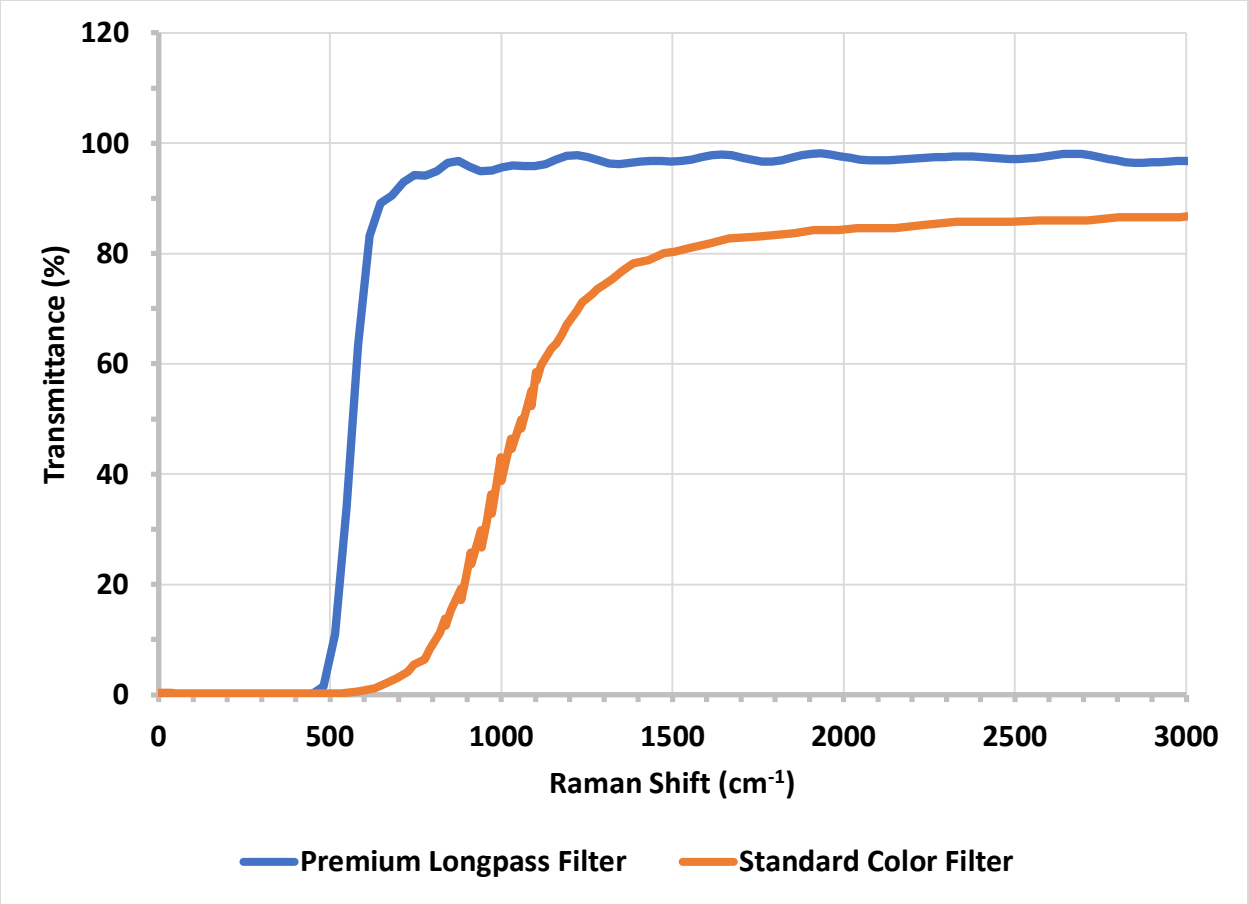

Figure 45: Transmission spectra of longpass filter [72] and color filter.

The above data show that the longpass filter provides a superior rejection of the Rayleigh scattered light, in addition to a higher passband transmission and a faster, steeper transition between the stopband and passband. We have successfully recorded Raman spectra with both the premium longpass filter and a standard color filter in the Raman excitation module. While both filters enable the detection of Stokes Raman bands, the longpass filter provides greater sensitivity, especially at lower frequencies. Such low-frequency bands often differentiate structurally similar, yet distinct, molecules, thus enabling accurate and rapid materials identification.

Following the filter, $L2$ is a coupling lens (Fiberguide Industries COL005S0101) that is roughly similar in diameter to $L1$, thus maximizing the throughput of the scattered light. Additionally, the numerical aperture of $L2$ is matched to the input numerical aperture of the attached optical fiber.

CHAPTER V

RESULTS AND DISCUSSION

Tryptophan

Absorption Spectrum

The normalized absorption spectrum of tryptophan in water is displayed in Figure 46.

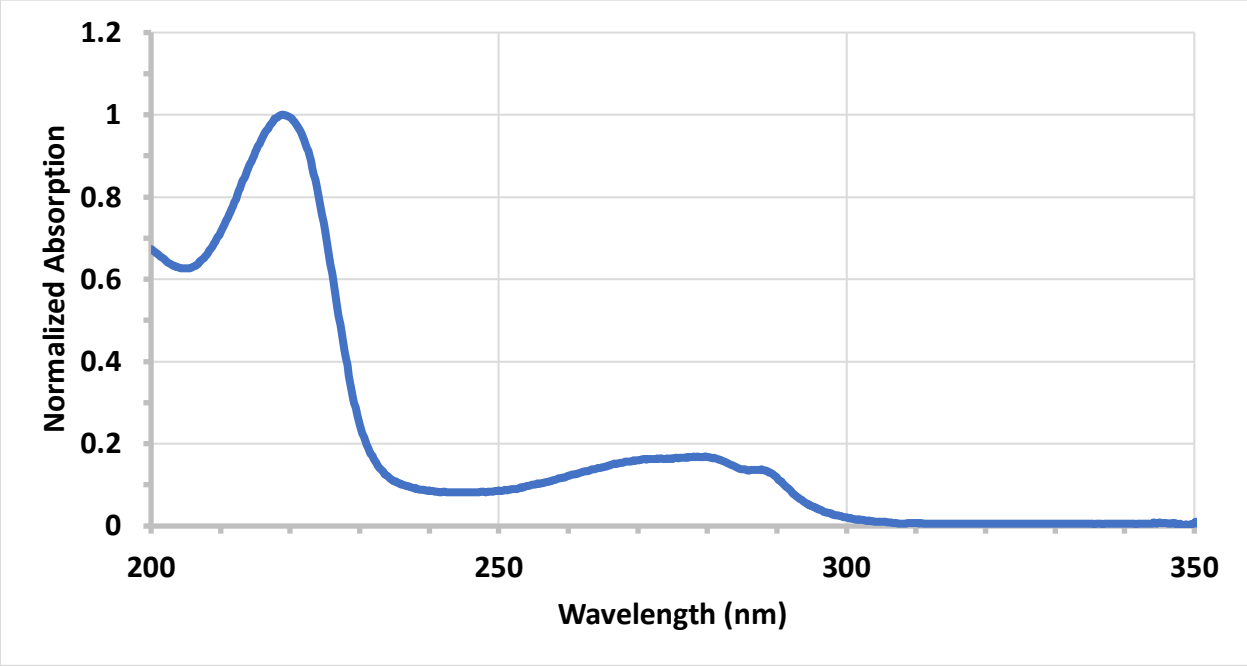

Figure 46: Normalized absorption spectrum of tryptophan in water.

Tryptophan possesses two rather broad absorption bands with peaks at ~ 280 nm and 220 nm, corresponding to the $S_0 \rightarrow S_1$ and $S_0 \rightarrow S_2$ electronic transitions, respectively. It may be noted that the $S_0 \rightarrow S_2$ absorption band is considerably more intense than the $S_0 \rightarrow S_1$ band, owing to the higher extinction coefficient of tryptophan at shorter wavelengths. These absorption bands are due to the indole group of tryptophan [39, 73].

Fluorescence Spectrum

The fluorescence spectrum of tryptophan in water (2 $\frac{\mu g}{mL}$) recorded by the portable instrument (integration time: 3 seconds; averaging: 10 scans; median filter width: 20 points) is depicted in Figure 47. The fluorescence spectrum recorded by the benchtop instrument is also shown in Figure 48 for reference.

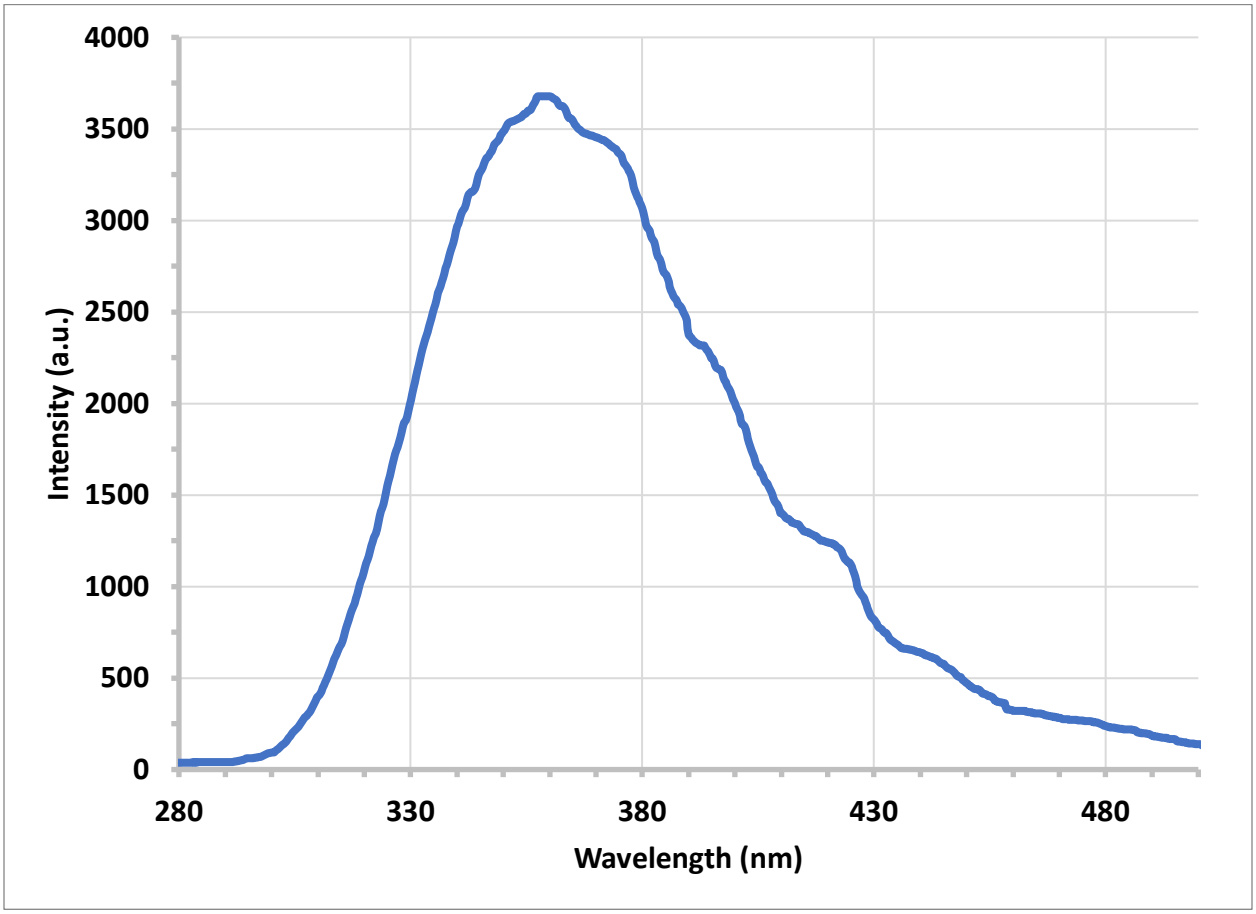

Figure 47: Fluorescence spectrum of tryptophan recorded by portable instrument.

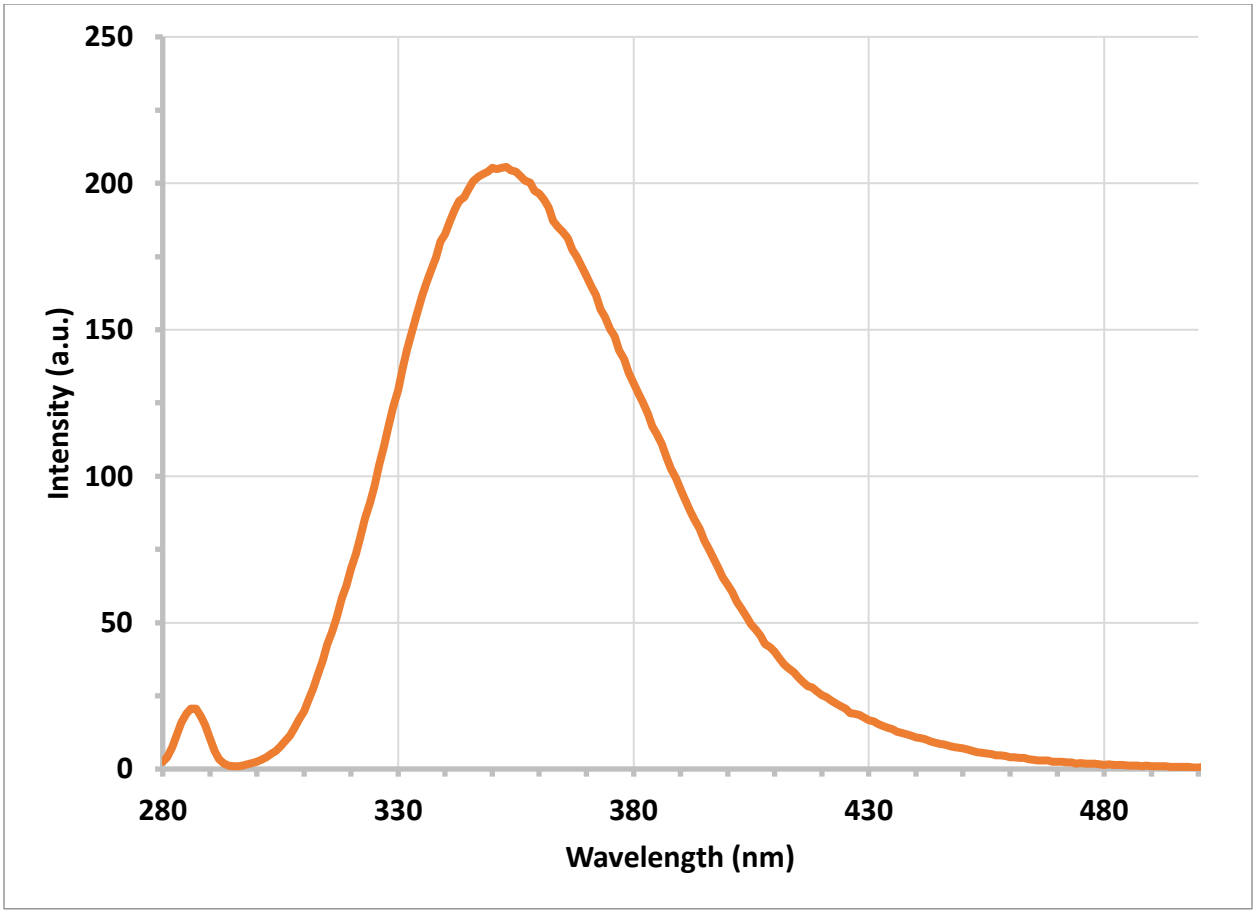

Figure 48: Fluorescence spectrum of tryptophan recorded by benchtop instrument.

The fluorescence spectrum recorded by the portable instrument was achieved by coupling the emission monochromator and disinfection unit subsystems. It may be observed that the recorded spectra are practically identical with respect to the fluorescence band shape and wavelength of peak intensity. The spectrum recorded by the portable instrument was additionally compared against the literature [73–75] for further validation of its accuracy.

Excitation-Emission Matrix (EEM)

The excitation-emission matrix (EEM) of tryptophan in water (100 $\frac{\mu g}{mL}$) was recorded over the excitation range of 260–310 nm with an excitation resolution of 1 nm (integration time:

5 seconds; averaging: 1 scan; median filter width: 20 points). The EEM is provided as a three-dimensional (3D) surface plot and two-dimensional (2D) contour plot in Figure 49 and Figure 50, respectively. The 2D contour plot is simply a projection of the 3D surface plot in the excitation-emission plane.

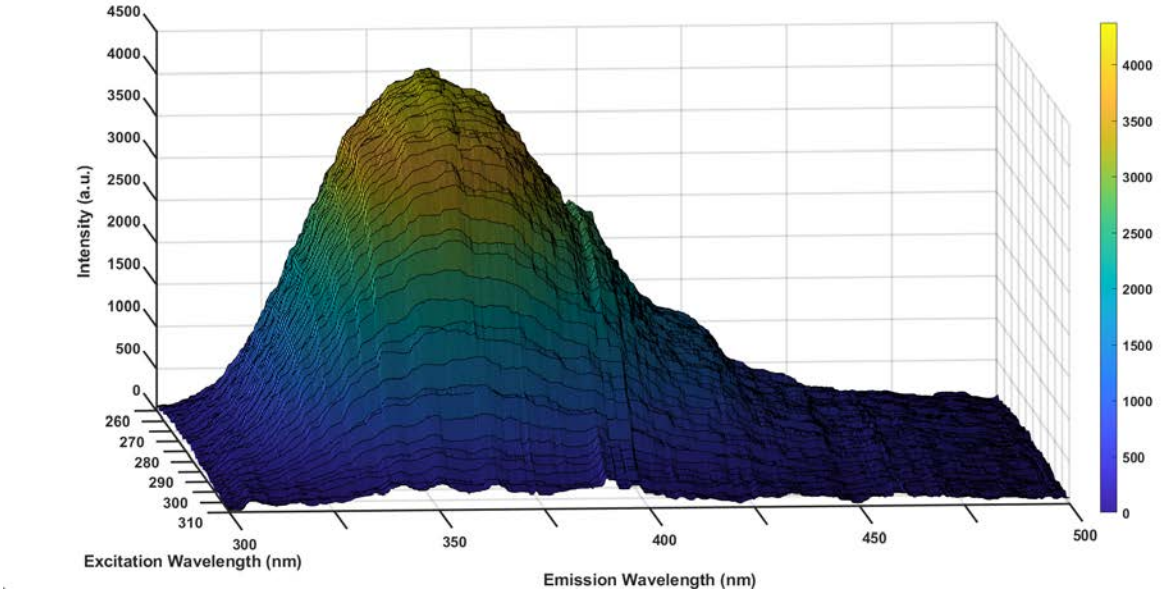

Figure 49: 3D surface plot of EEM for tryptophan recorded by portable instrument.

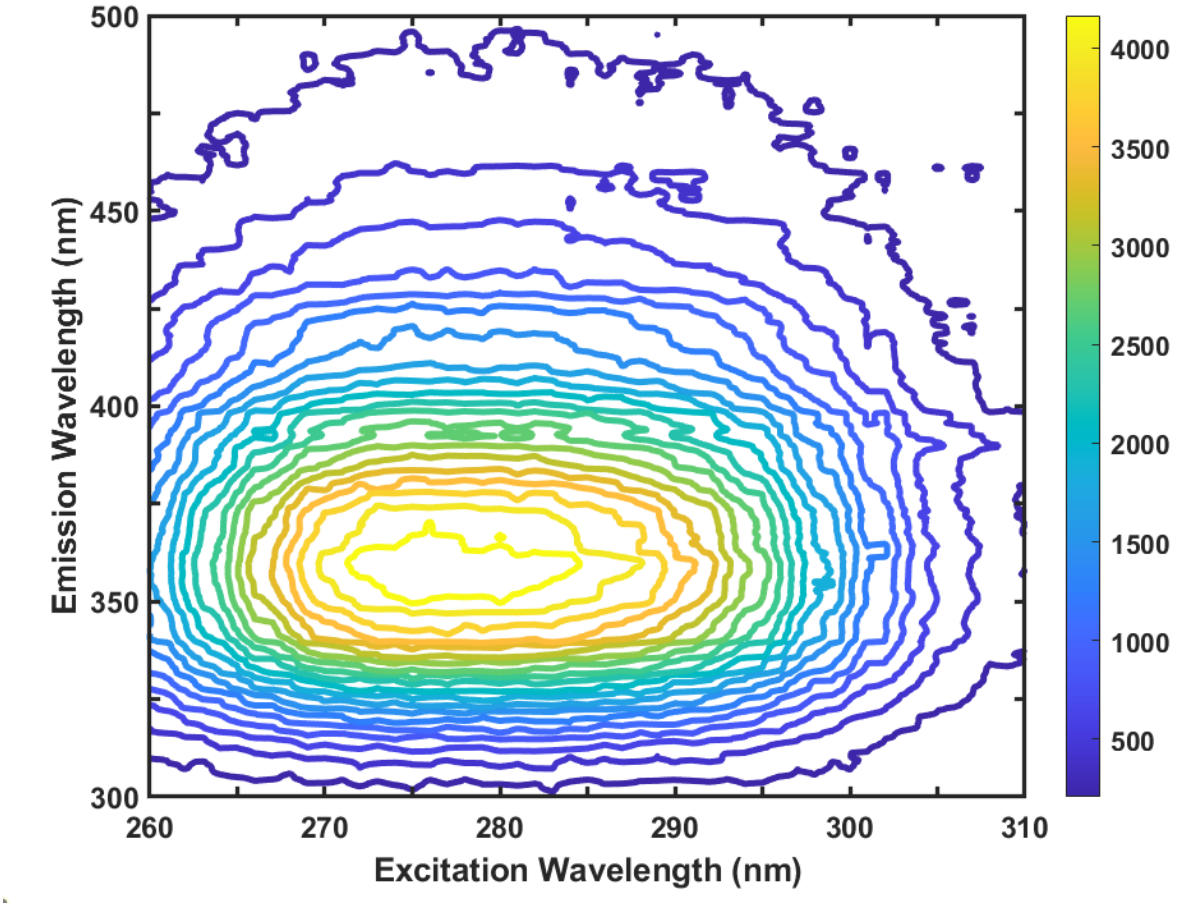

Figure 50: 2D contour plot of EEM for tryptophan recorded by portable instrument.

The EEM of tryptophan provides a detailed characterization of its most intense excitation and emission bands. For tryptophan, peak excitation occurs at ~ 280 nm with peak emission at ~ 350 nm, which is in good agreement with the literature [75]. The difference in the peak excitation and emission wavelength is, in general, characteristic of a given molecule and may be obtained through the EEM.

Fluorescence Decay

Solutions of tryptophan in water (2 $\frac{\mu g}{mL}$) were irradiated by means of a mercury arc lamp and UV LED, integrated with our portable instrument in the disinfection unit, for various irradiation times ranging from 0 to 240 minutes. Fluorescence spectra were recorded by the portable instrument (integration time: 3 seconds; averaging: 10 scans; median filter width: 20 points) following each interval of irradiation. The peak fluorescence intensity was then plotted as a function of the irradiation time, or dosage, for each irradiation source. To that effect, Figure 51 and Figure 52 display the fluorescence spectra and peak fluorescence intensity of tryptophan as a function of the irradiation time, respectively, using the mercury arc lamp.

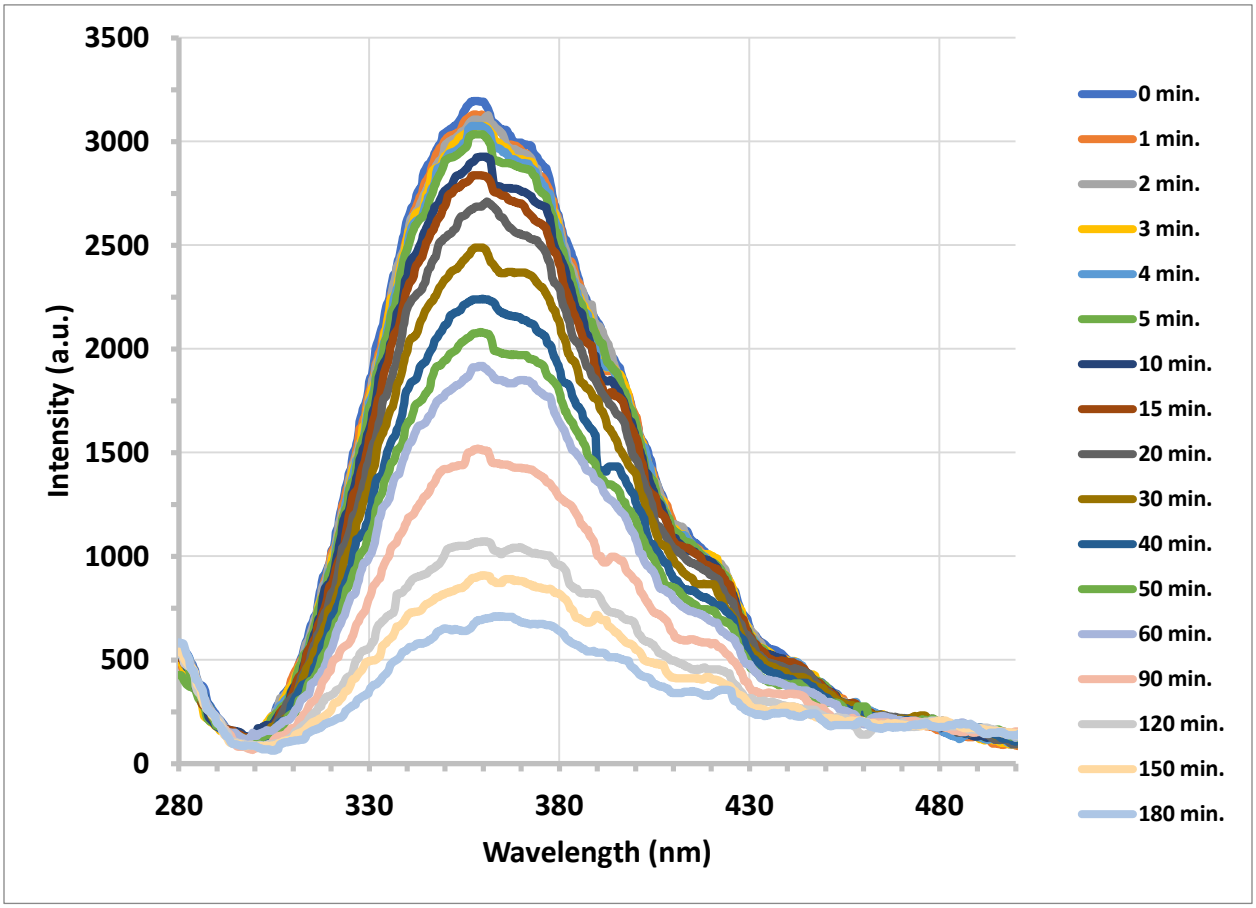

Figure 51: Fluorescence spectra of tryptophan as a function of irradiation time using arc lamp.

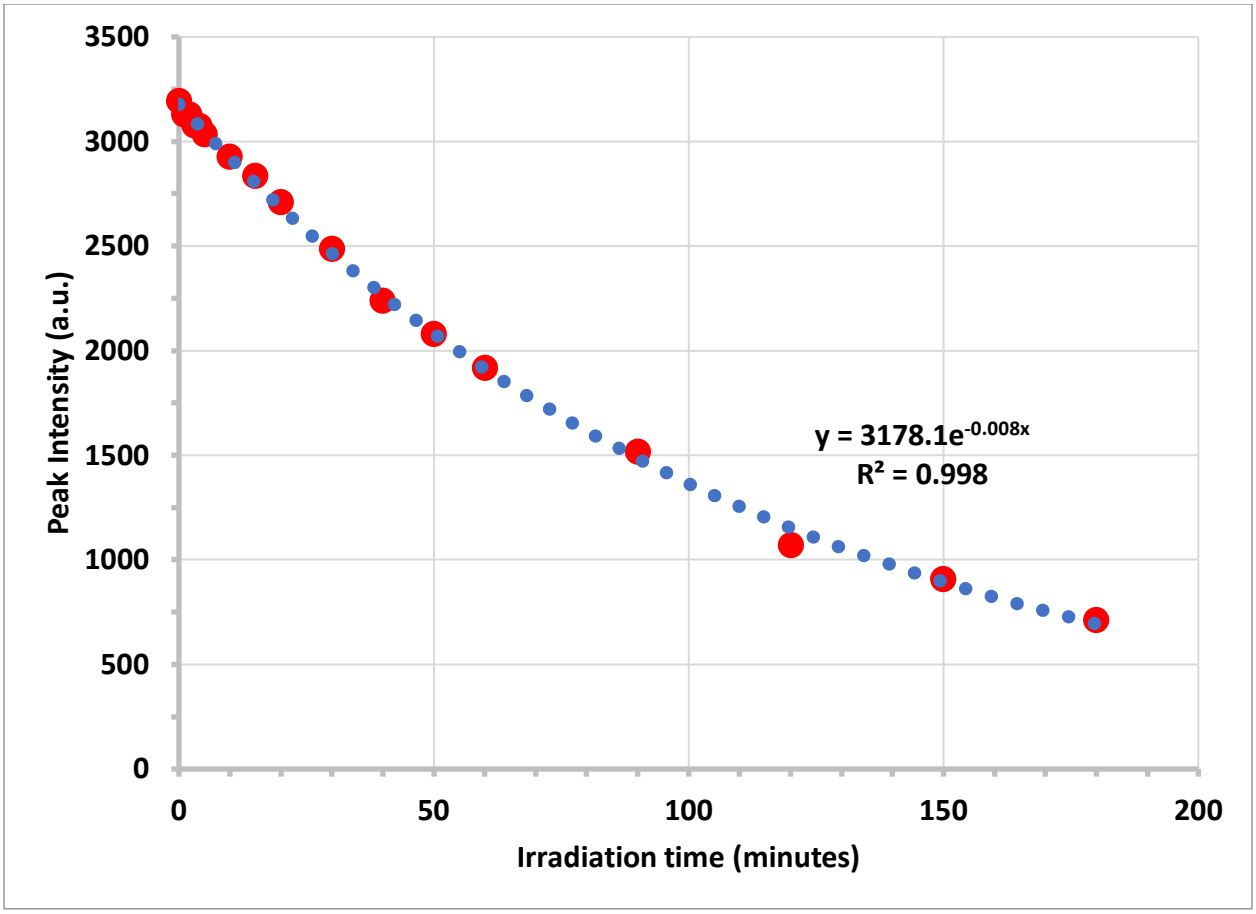

Figure 52: Peak intensity of tryptophan as a function of irradiation time using arc lamp.

The above data clearly show that the fluorescence spectrum and peak fluorescence intensity of tryptophan decrease as a function of irradiation time by the mercury arc lamp. In general, this decrease may be modeled by an exponential distribution of the following form:

$$I(t) = I_0 e^{-\alpha t} \tag{16}$$

where $I(t)$ is the fluorescence intensity (a.u.) at time t (minutes), I_0 is the initial fluorescence intensity at $t = 0$ minutes of irradiation, and α is a rate constant (minutes^{-1}) proportional to the UV irradiance and extinction coefficient of the sample. Figure 53 and Figure 54 similarly display the fluorescence spectra and peak fluorescence intensity of tryptophan as a function of the

irradiation time, respectively, using the UV LED in the disinfection unit of the portable instrument.

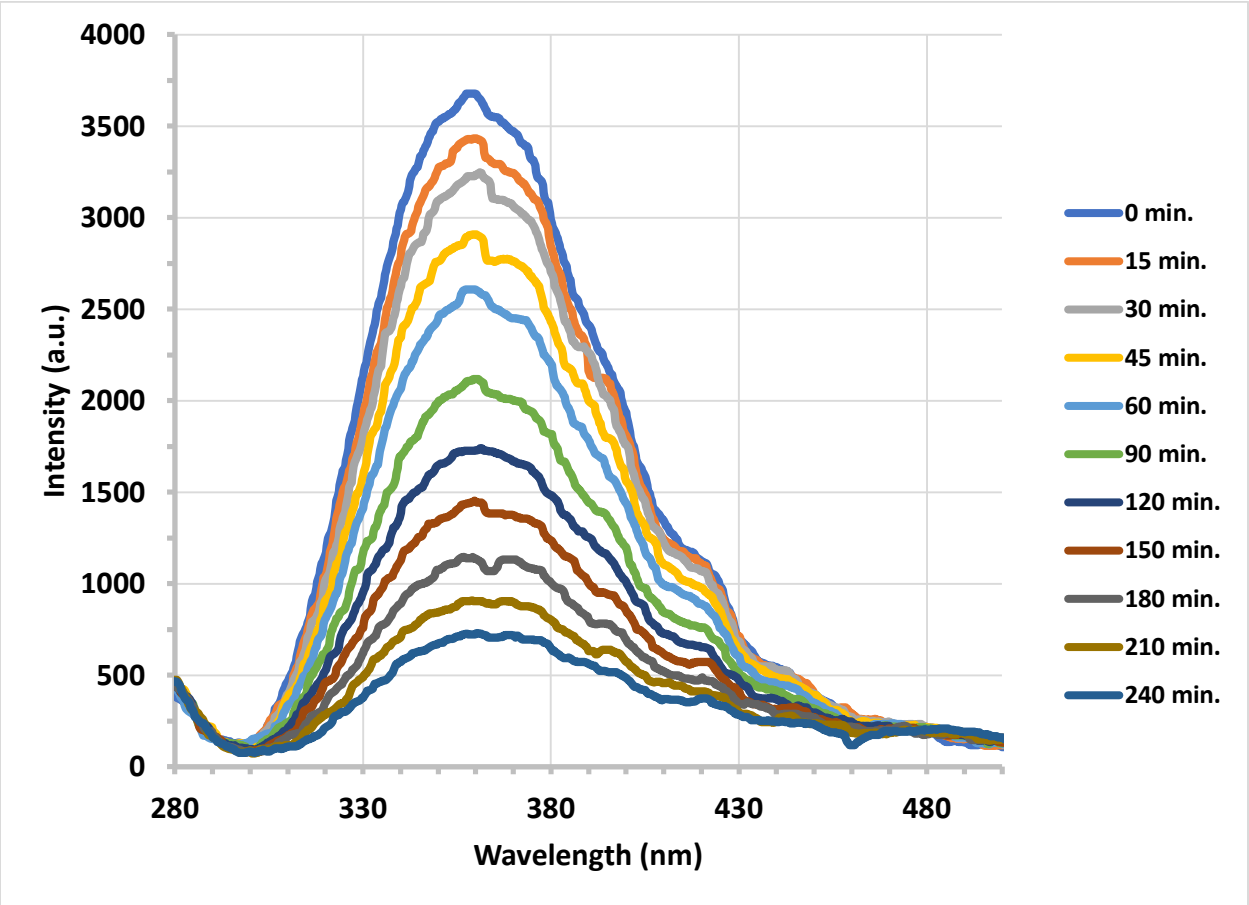

Figure 53: Fluorescence spectra of tryptophan as a function of irradiation time using UV LED.

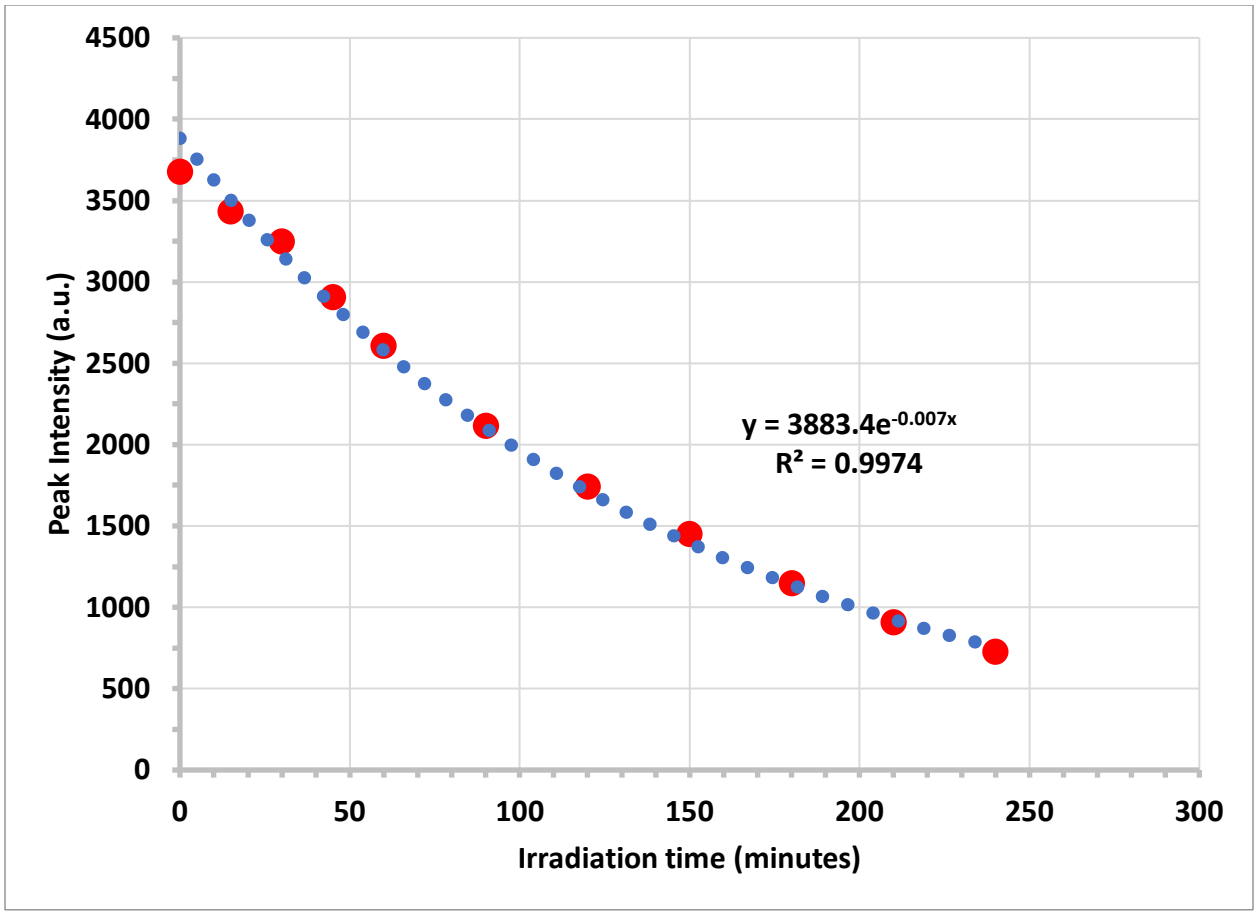

Figure 54: Peak intensity of tryptophan as a function of irradiation time using UV LED.

A similar phenomenon is observed following the irradiation of tryptophan by the UV LED. In particular, as the irradiation time, or dosage, increases, the peak fluorescence intensity of tryptophan decreases. Owing to the fact that the fluorescence intensity is proportional to the absorption and, therefore, concentration of the sample, the decreasing fluorescence may be correlated with a decrease in the concentration of tryptophan molecules. We have observed this decrease in fluorescence previously with a benchtop instrument [20–22], which may essentially be attributed to the photooxidation, or degradation, of tryptophan upon UV exposure [39, 76–77]. It is rather interesting to note that the predominant photoproducts of tryptophan, namely kynurenine and N-formylkynurenine, fluoresce maximally in the visible region [78–79]

following UVA excitation and may therefore provide an additional means of monitoring the oxidation of tryptophan molecules.

Tyrosine

Absorption Spectrum

The normalized absorption spectrum of tyrosine in water is provided in Figure 55.

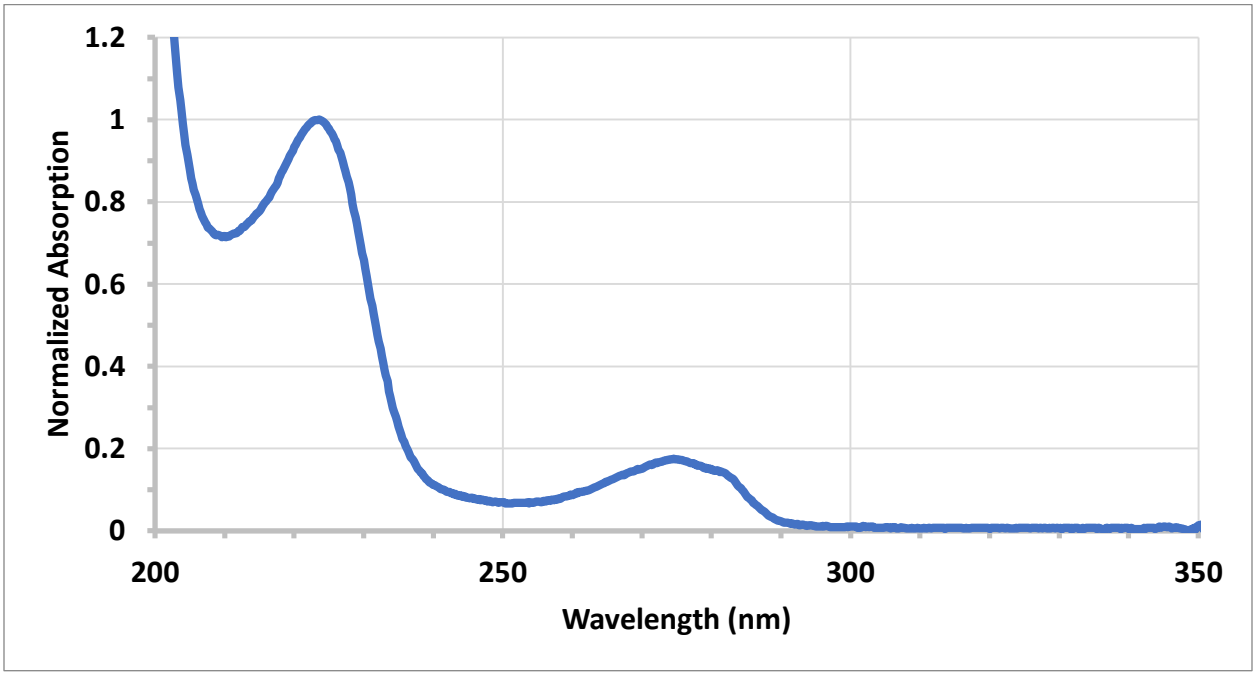

Figure 55: Normalized absorption spectrum of tyrosine in water.

Tyrosine possesses two rather broad absorption bands with peaks at ~ 275 nm and 225 nm, corresponding to the $S_0 \rightarrow S_1$ and $S_0 \rightarrow S_2$ electronic transitions, respectively. These absorption bands are due to the aromatic side-chain of the tyrosine molecule [15]. Similar to tryptophan, tyrosine possesses a higher extinction coefficient and absorption at shorter wavelengths. It is worth mentioning, however, that tyrosine has a considerably lower extinction coefficient than tryptophan at these wavelengths [15, 73].

Fluorescence Spectrum

The fluorescence spectrum of tyrosine in water (10 $\frac{\mu g}{mL}$) recorded by the portable instrument (integration time: 3 seconds; averaging: 10 scans; median filter width: 20 points) is provided in Figure 56. The fluorescence spectrum recorded by the benchtop instrument is shown in Figure 57 for reference.

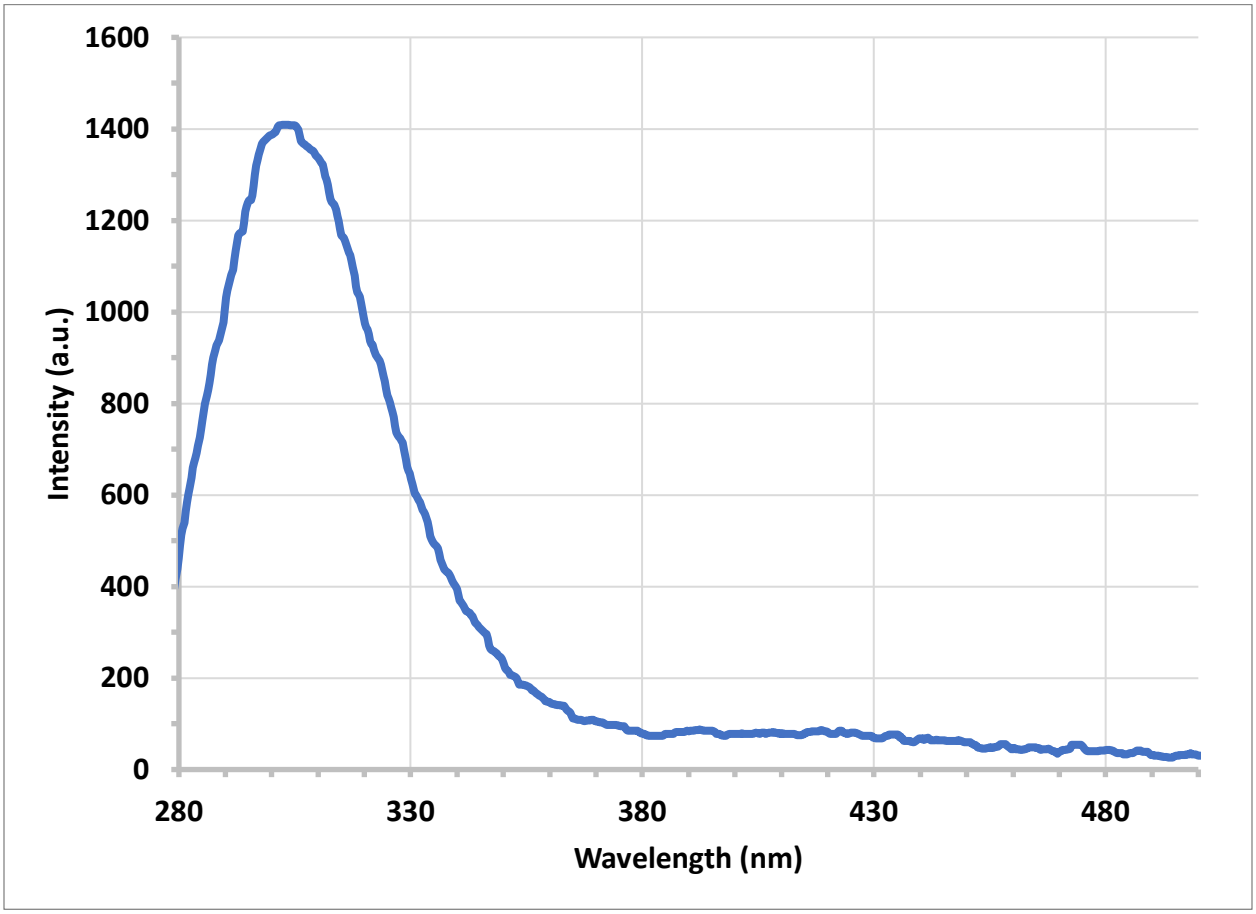

Figure 56: Fluorescence spectrum of tyrosine recorded by portable instrument.

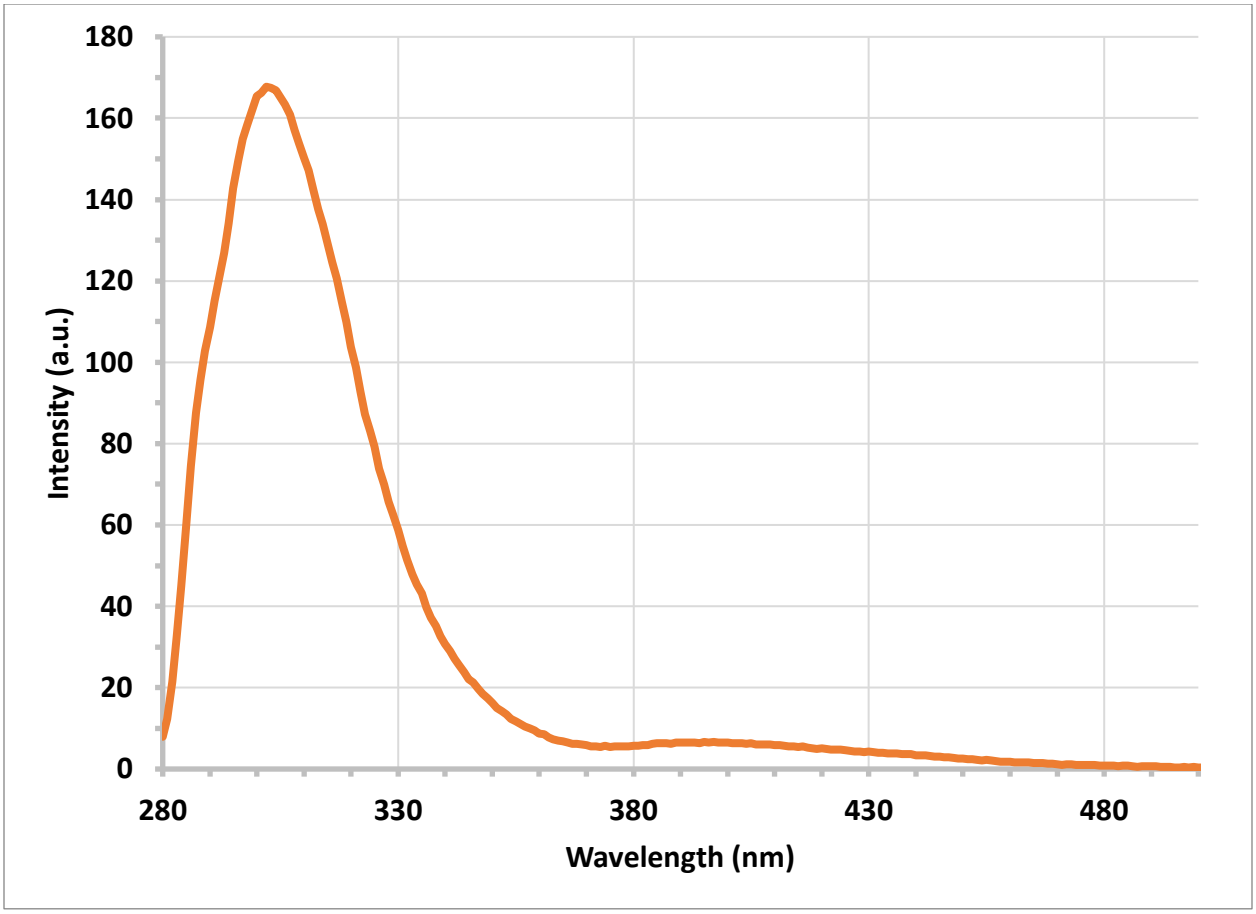

Figure 57: Fluorescence spectrum of tyrosine recorded by benchtop instrument.

The recorded spectra of tyrosine are practically identical with respect to the fluorescence band shape and wavelength of peak intensity. The spectrum recorded by the portable instrument was additionally compared against the literature [73–75] for further validation of its accuracy.

Excitation-Emission Matrix (EEM)

The excitation-emission matrix (EEM) of tyrosine in water (400 $\frac{\mu g}{mL}$) was recorded over the excitation range of 260–310 nm with an excitation resolution of 1 nm (integration time: 5 seconds; averaging: 1 scan; median filter width: 20 points). The EEM is provided as a three-

dimensional (3D) surface plot and two-dimensional (2D) contour plot in Figure 58 and Figure 59, respectively.

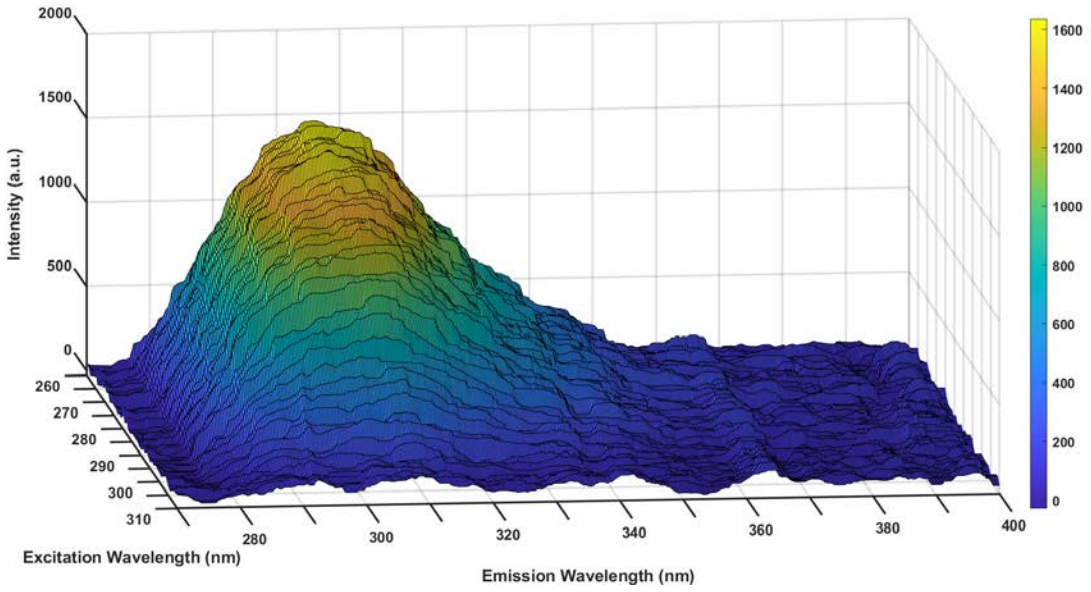

Figure 58: 3D surface plot of EEM for tyrosine recorded by portable instrument.

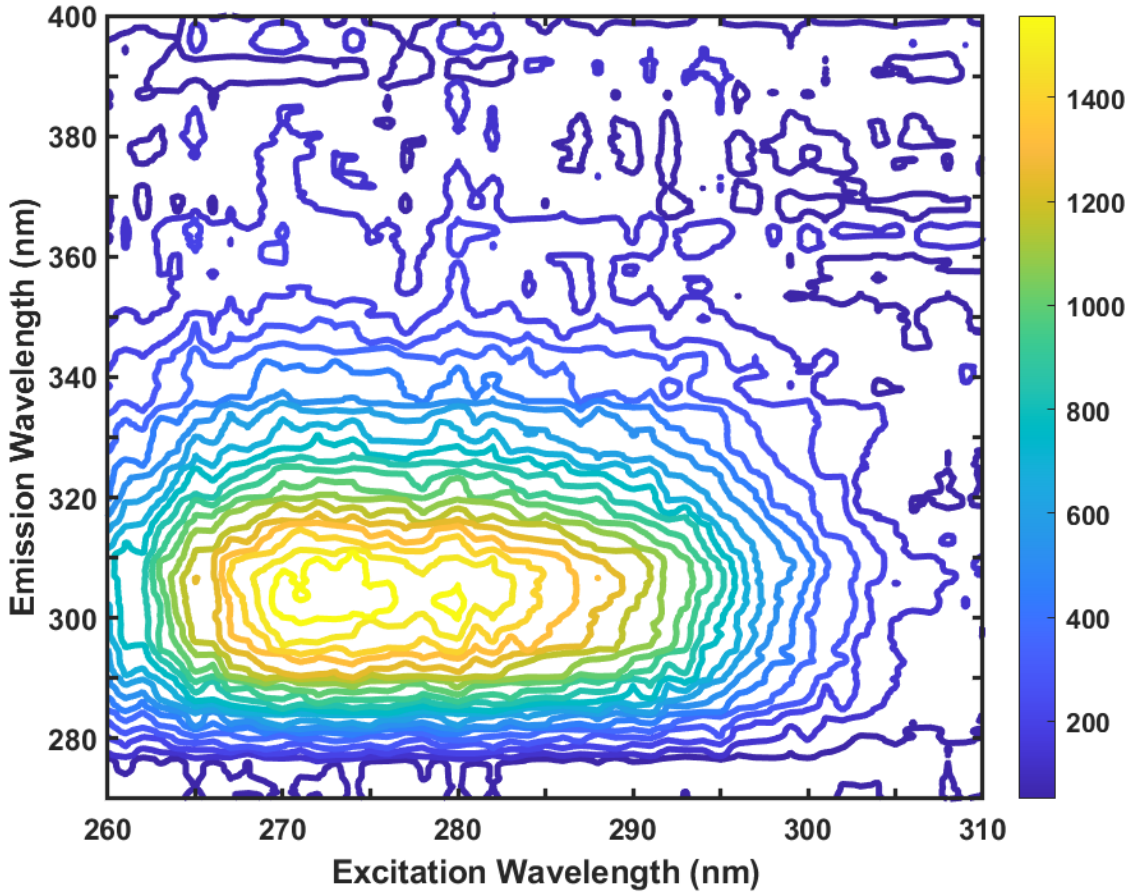

Figure 59: 2D contour plot of EEM for tyrosine recorded by portable instrument.

In contrast to tryptophan, the peak excitation of tyrosine occurs at ~ 275 nm with peak emission at ~ 305 nm, which is also in good agreement with the literature [75]. Owing to its lower extinction coefficient and quantum yield [73], the fluorescence intensity of tyrosine at these excitation and emission wavelengths is comparatively lower than that observed with a tryptophan solution of similar concentration.

Fluorescence Decay

Solutions of tyrosine in water (10 $\frac{\mu g}{mL}$) were irradiated by means of a mercury arc lamp and UV LED, integrated with our portable instrument in the disinfection unit, for various irradiation times ranging from 0 to 240 minutes. Fluorescence spectra were recorded by the portable instrument (integration time: 3 seconds; averaging: 10 scans; median filter width: 20 points) following each interval of irradiation. To that effect, Figure 60 and Figure 61 display the fluorescence spectra and peak fluorescence intensity of tyrosine as a function of the irradiation time, respectively, using the mercury arc lamp.

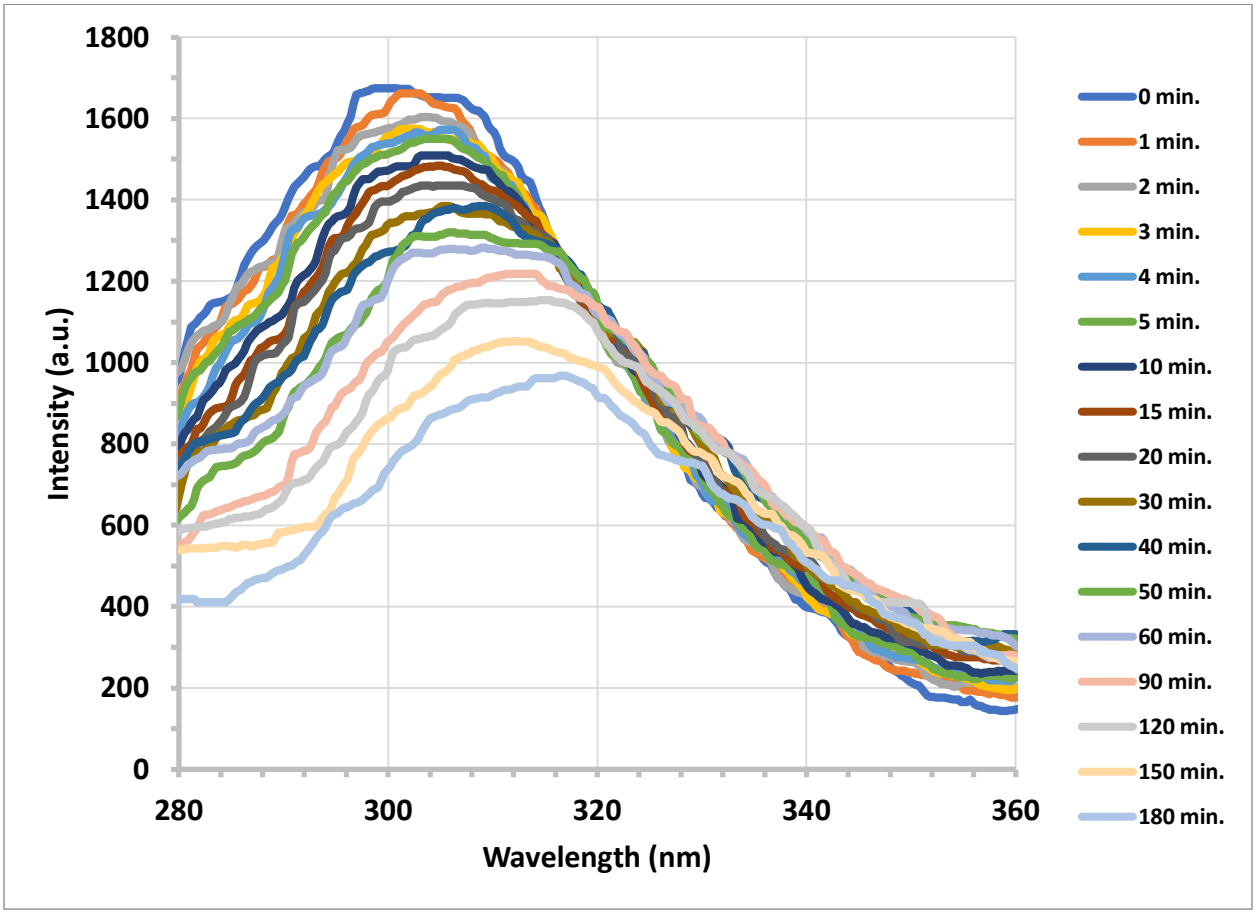

Figure 60: Fluorescence spectra of tyrosine as a function of irradiation time using arc lamp.

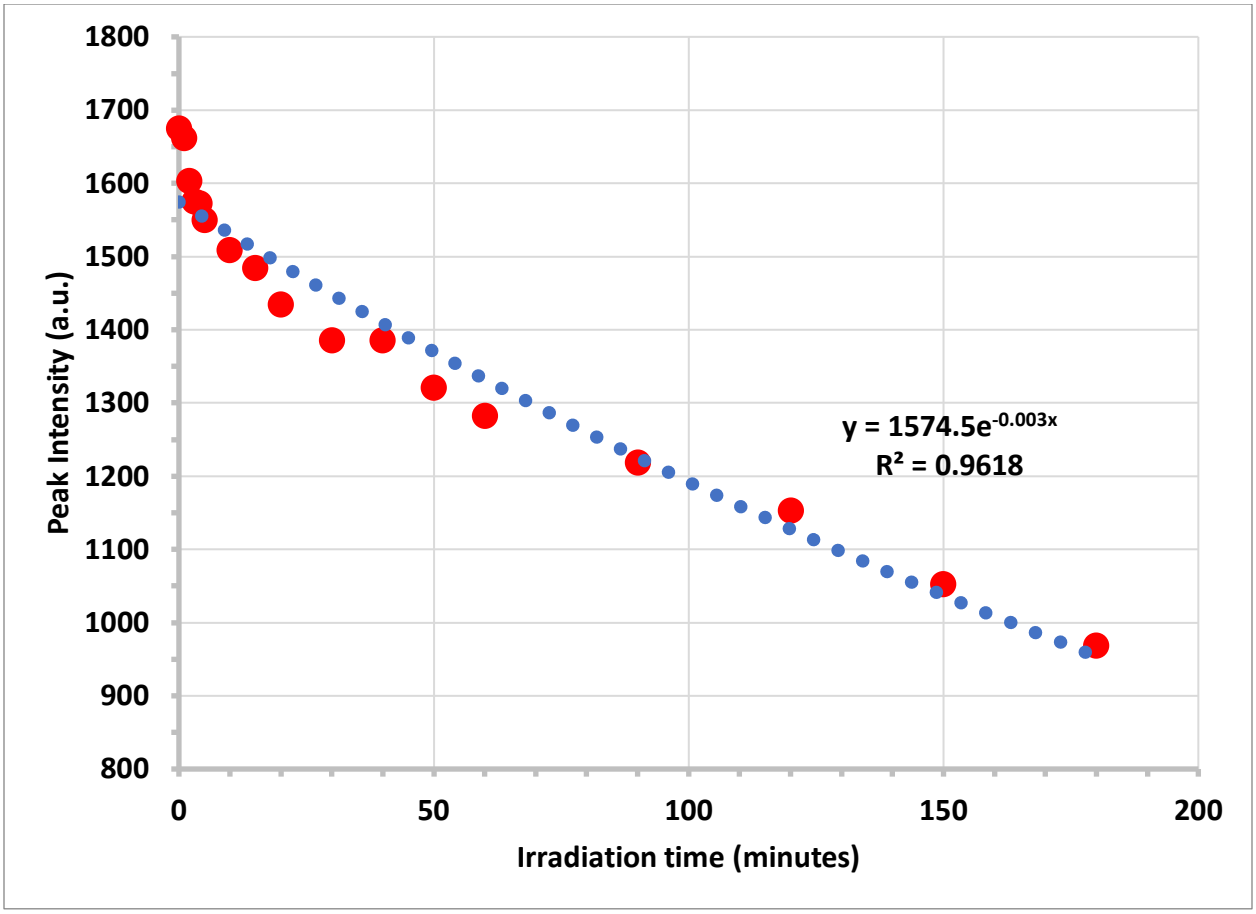

Figure 61: Peak intensity of tyrosine as a function of irradiation time using arc lamp.

Figure 62 and Figure 63 similarly display the fluorescence spectra and peak fluorescence intensity of tyrosine as a function of the irradiation time, respectively, using the UV LED in the disinfection unit of the portable instrument.

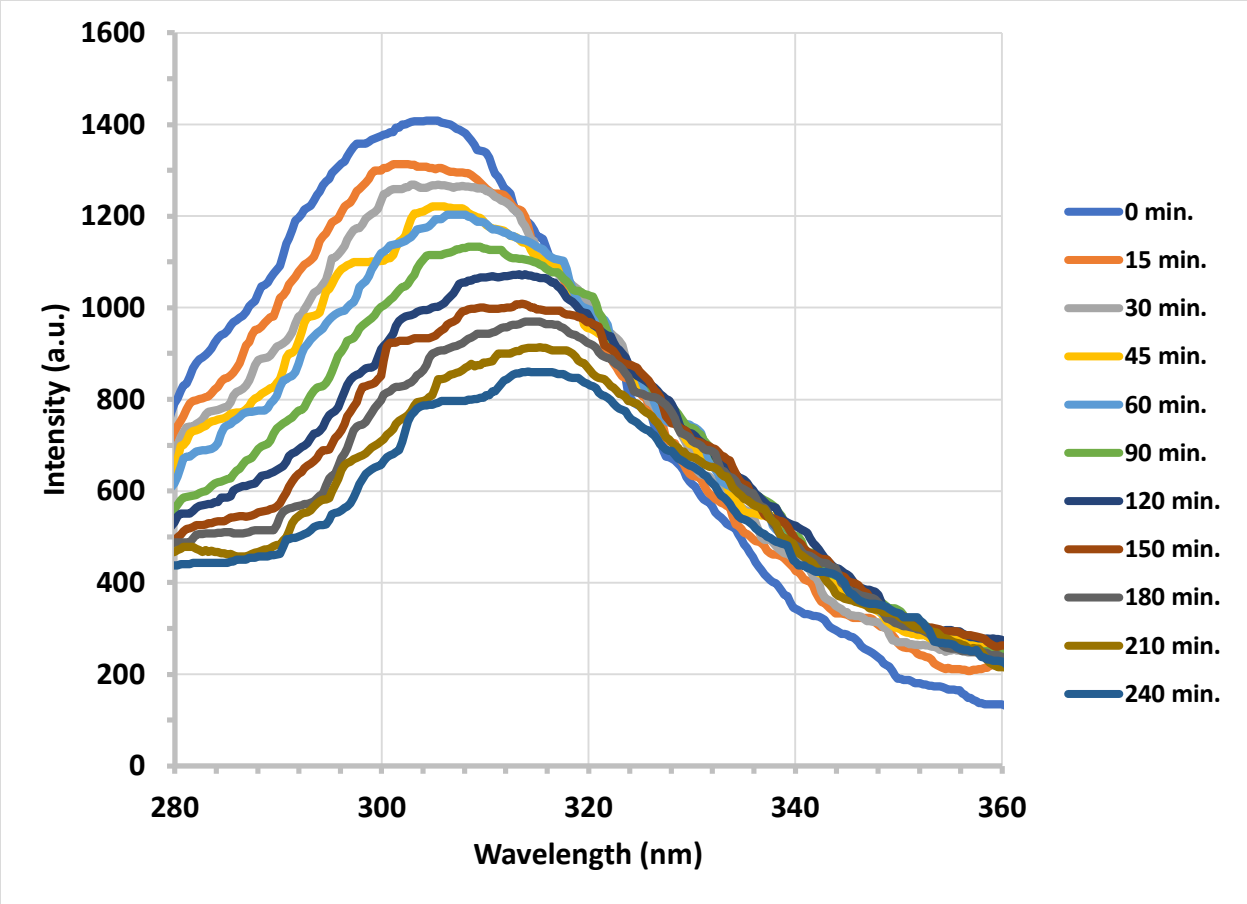

Figure 62: Fluorescence spectra of tyrosine as a function of irradiation time using UV LED.

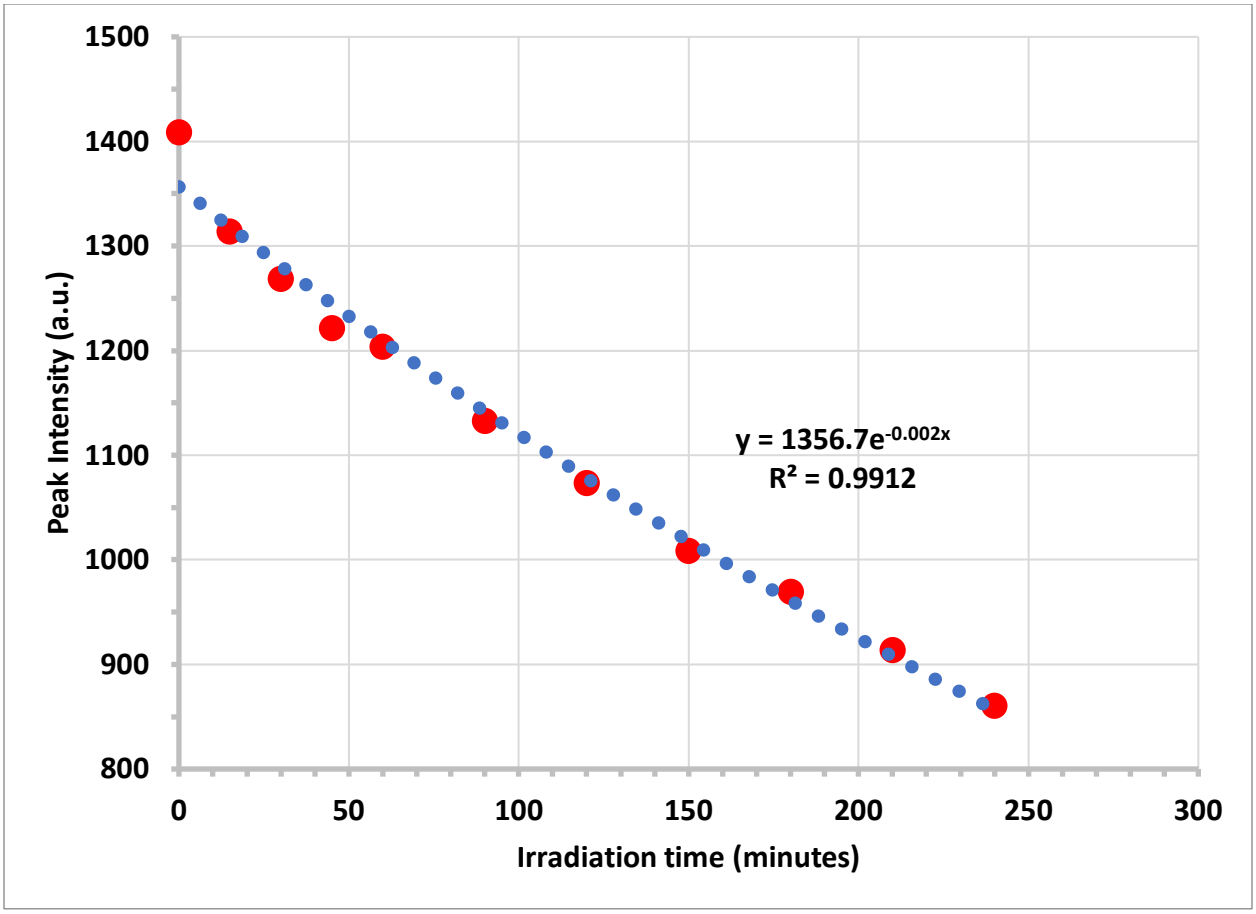

Figure 63: Peak intensity of tyrosine as a function of irradiation time using UV LED.

As observed with tryptophan, the peak fluorescence intensity of tyrosine decreases with increasing UV irradiation time, or dosage, using both the mercury arc lamp and UV LED. It may be observed that the rate constant, α, is smaller for tyrosine compared to tryptophan, indicating a slower decrease in the fluorescence intensity for the same irradiance, which may essentially be attributed to the lower absorption of tyrosine in the UV region. The decrease in the fluorescence intensity corresponds to the photooxidation of tyrosine molecules [80–81] following the absorption of UV light. Interestingly, it has been reported that tyrosine photoproducts, such as dityrosine, possess rather intense fluorescence bands in the visible region that may serve as an

indicator of oxidative stress in proteins that are present in both bacterial and human tissue cells [80, 82–83].

Tryptophan and Tyrosine Mixture

Absorption Spectrum

The normalized absorption spectrum of a tryptophan and tyrosine mixture in water is shown in Figure 64.

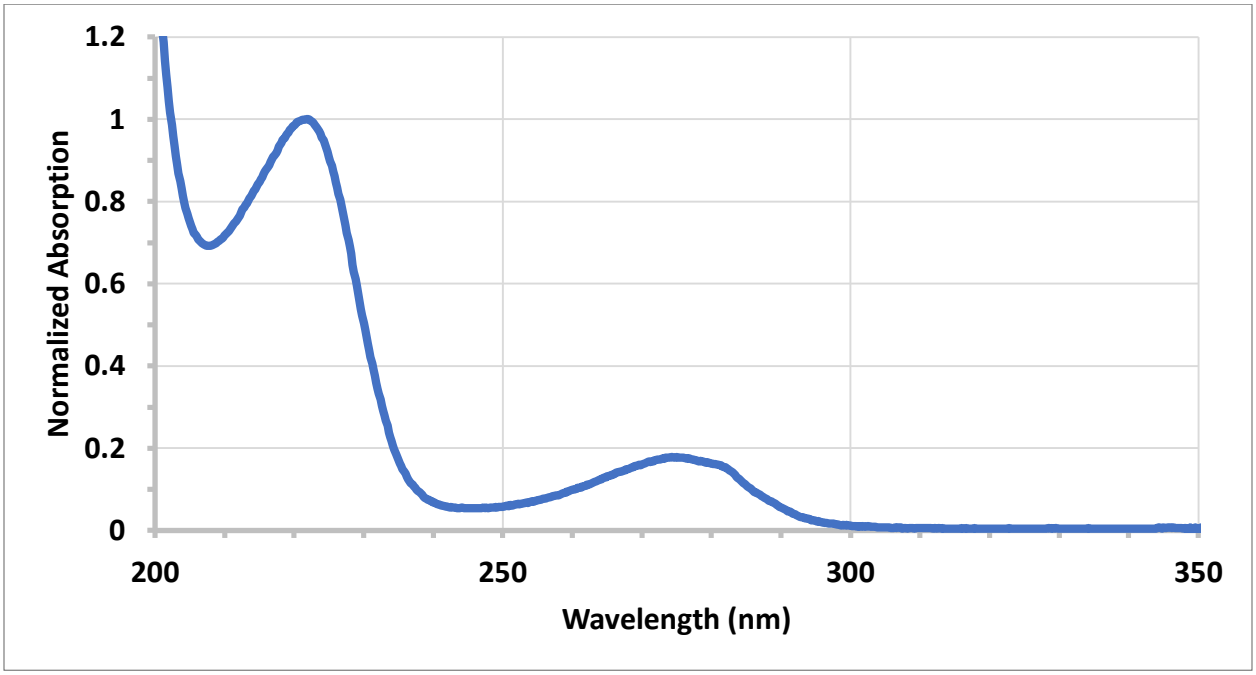

Figure 64: Normalized absorption spectrum of tryptophan and tyrosine mixture in water.

The absorption spectrum of the mixture displays two broad absorption bands corresponding to the absorption of the tryptophan and tyrosine components. Due to the overlapping absorption bands of each component, however, it is practically impossible to spectroscopically separate the tryptophan and tyrosine components, in mixture, by recording the absorption spectrum alone.

Excitation-Emission Matrix (EEM)

The excitation-emission matrix (EEM) of a tryptophan (100 $\frac{\mu g}{mL}$) and tyrosine (400 $\frac{\mu g}{mL}$) mixture in water was recorded over the excitation range of 260–310 nm with an excitation resolution of 1 nm (integration time: 5 seconds; averaging: 1 scan; median filter width: 20 points). The EEM is displayed as a three-dimensional (3D) surface plot and two-dimensional (2D) contour plot in Figure 65 and Figure 66, respectively.

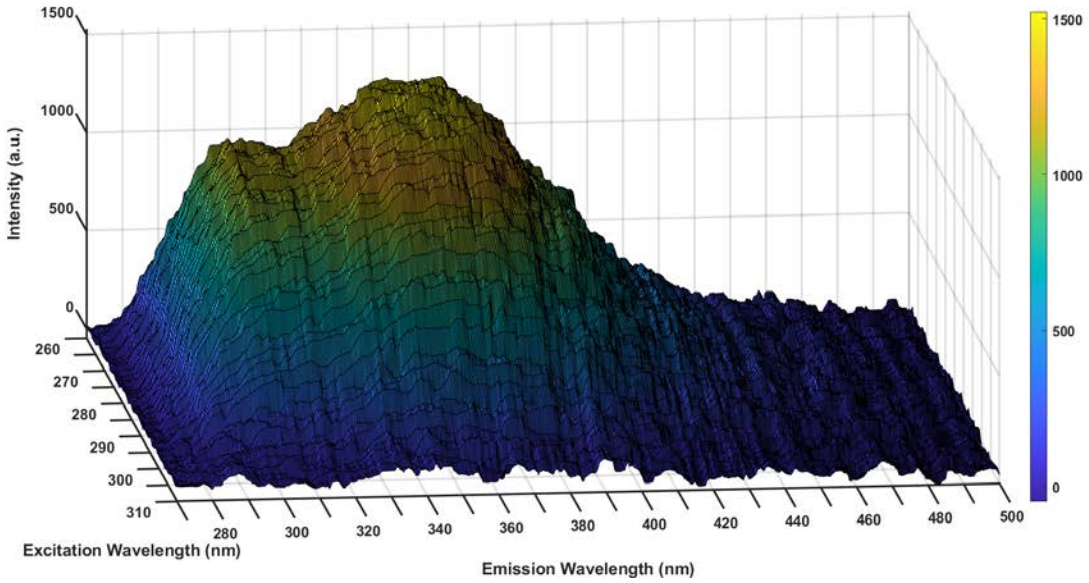

Figure 65: 3D surface plot of EEM for mixture recorded by portable instrument.

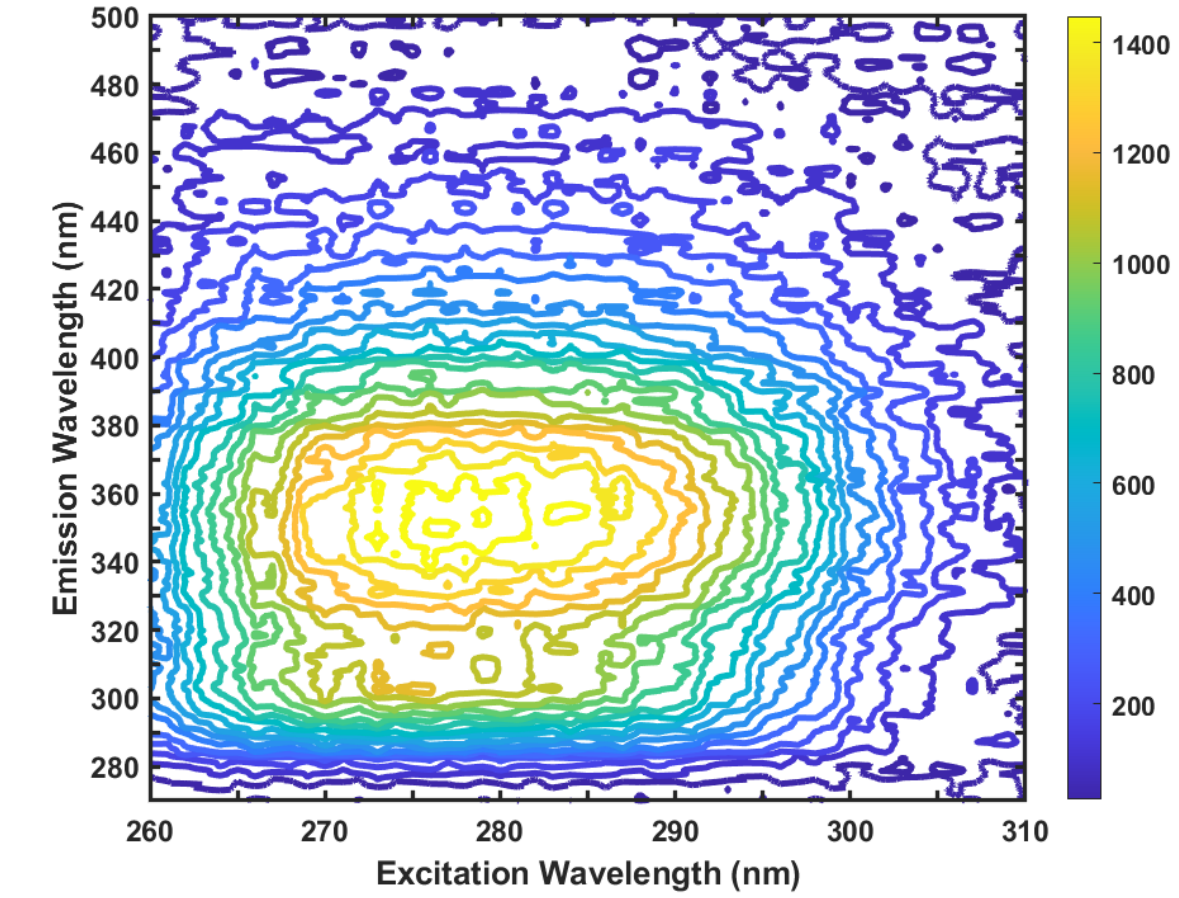

Figure 66: 2D contour plot of EEM for mixture recorded by portable instrument.

Two rather intense fluorescence bands may be observed in the EEM of the mixture, corresponding to the tryptophan and tyrosine fluorescing components. A primary band is present with peak excitation at ~ 280 nm and peak emission at ~ 350 nm, which is essentially due to tryptophan, in addition to a secondary, less intense band with peak excitation at ~ 275 nm and peak emission at ~ 305 nm, which may be assigned to tyrosine. Thus, while both components absorb at similar excitation wavelengths, the characteristic fluorescence band maximum of each component occurs at a distinct emission wavelength. Moreover, the difference between the absorption and fluorescence band maxima of each component may be utilized, through the

synchronous fluorescence technique [16], for the spectroscopic identification of each molecule in mixture.

Fluorescence and Synchronous Fluorescence Spectra

The fluorescence spectra of the tryptophan and tyrosine mixture at various excitation wavelengths, along with the synchronous fluorescence spectra of the tryptophan and tyrosine components, were extracted from the EEM of the mixture. It was determined that for $\Delta\lambda$ in the range of $\sim$ 20 to 30 nm, the tyrosine component of the mixture could be spectroscopically isolated, whereas $\Delta\lambda$ in the range of $\sim$ 60 to 80 nm were necessary for resolving and distinguishing tryptophan fluorescence. These results are consistent with the data reported in studies utilizing benchtop monochromators [84–86], including our own [20–22]. To that effect, the fluorescence spectrum of the mixture at an excitation wavelength $\lambda_{EX} = 270$ nm, along with the synchronous fluorescence spectra of the tyrosine and tryptophan components extracted using $\Delta\lambda = 25$ nm and $\Delta\lambda = 65$ nm, respectively, are provided in Figure 67.

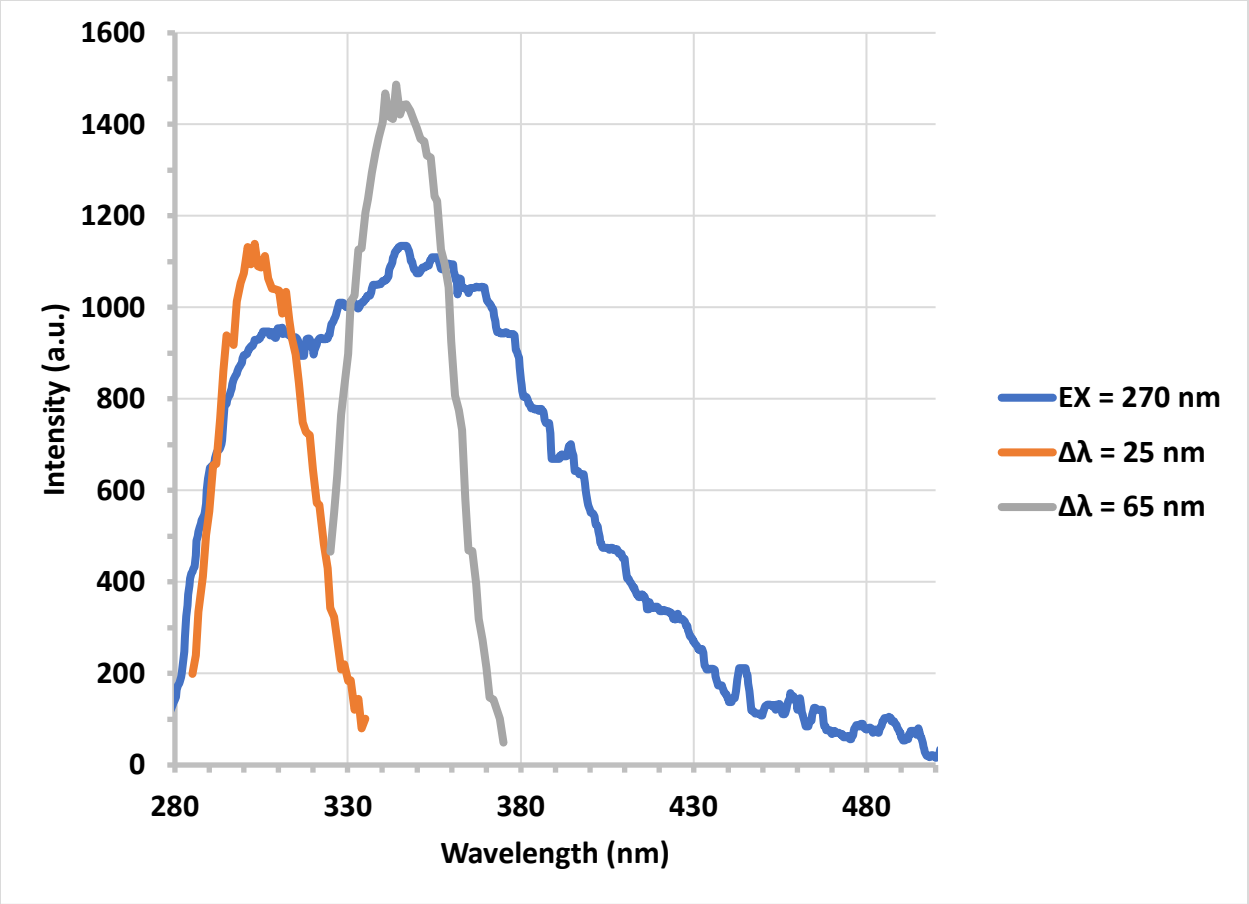

Figure 67: Fluorescence and synchronous fluorescence spectra of tryptophan and tyrosine mixture recorded by portable instrument.

The data displayed in Figure 67 show that while the fluorescence spectrum of the mixture consists of a rather broad, structureless, and diffuse band that cannot be uniquely assigned to either tyrosine or tryptophan, the synchronous spectra display narrow, resolved peaks of both the tyrosine and tryptophan components, which display characteristic maxima at ~ 305 nm and 350 nm, respectively. This is made possible through the selectivity of the synchronous fluorescence technique provided by the $\Delta\lambda$ parameter. It is rather important to note that the optimum $\Delta\lambda$, which provides the greatest SNR and smallest bandwidth of the desired fluorescence band, may vary slightly between instruments depending on the spectral characteristics of the excitation

source, in addition to the sensitivity and calibration of the spectrometer. We find that the data recorded by our portable instrument is practically identical to that provided in the literature and recorded by benchtop instruments [20–22, 84–86]. In contrast to benchtop spectrometers, which typically permit the recording of a synchronous fluorescence spectrum at a single Δλ, our portable instrument enables the direct, and practically instantaneous, computation of synchronous fluorescence spectra of any arbitrary Δλ following the acquisition of the EEM. This technique may therefore be employed for more complex chemical mixtures in order to resolve the fluorescence spectra of each individual component based on the appropriate set of Δλ derived from the EEM.

EEM Parameters

It is of practical relevance to consider the effects of the EEM parameters on the total acquisition time. Considering the excitation range, $\Delta\lambda$, excitation resolution, $d\lambda$, integration time, $\tau_{integration}$, number of scans to average, S, and total stepper motor delay, τ_{motor}, in addition to neglecting any communication delays between the computer and instrument, a lower bound on the total acquisition time, $\tau_{acquisition}$, for a given EEM may be obtained:

$$\tau_{acquisition} \geq \left(\left[\frac{\Delta\lambda}{d\lambda} + 1\right] \times \tau_{integration} \times S\right) + \tau_{motor} \tag{17}$$

which may be rewritten as

$$\tau_{acquisition} \geq \left(N \times \tau_{integration} \times S\right) + \tau_{motor} \tag{18}$$

where $N = \left(\frac{\Delta\lambda}{d\lambda} + 1\right)$ denotes the total number of spectra recorded in an EEM acquisition. Of particular importance in Equation (17) is the fact that $\tau_{acquisition} \propto \left(\tau_{integration} \times S\right)$ and $\tau_{acquisition} \propto \Delta\lambda$, as expected, yet $\tau_{acquisition} \propto \frac{1}{d\lambda}$. Thus, in acquisitions where the SNR is low and higher integration times or averaging is required, a smaller excitation range $\Delta\lambda$ and/or larger

excitation resolution $d\lambda$ may be employed as a means of maintaining a reasonable acquisition time. This is particularly important in scenarios where the sample concentration is low or a large background interference is present. To investigate the effects of increasing the excitation resolution $d\lambda$, the EEM of the tryptophan and tyrosine mixture was obtained with $d\lambda = 1$, 2, 5, and 10 nm. The synchronous fluorescence spectra of the tryptophan and tyrosine components were then computed from the EEM with $\Delta\lambda = 25$ nm and $\Delta\lambda = 65$ nm, respectively, for each excitation resolution and compared. The results of this comparison are provided in Figure 68.

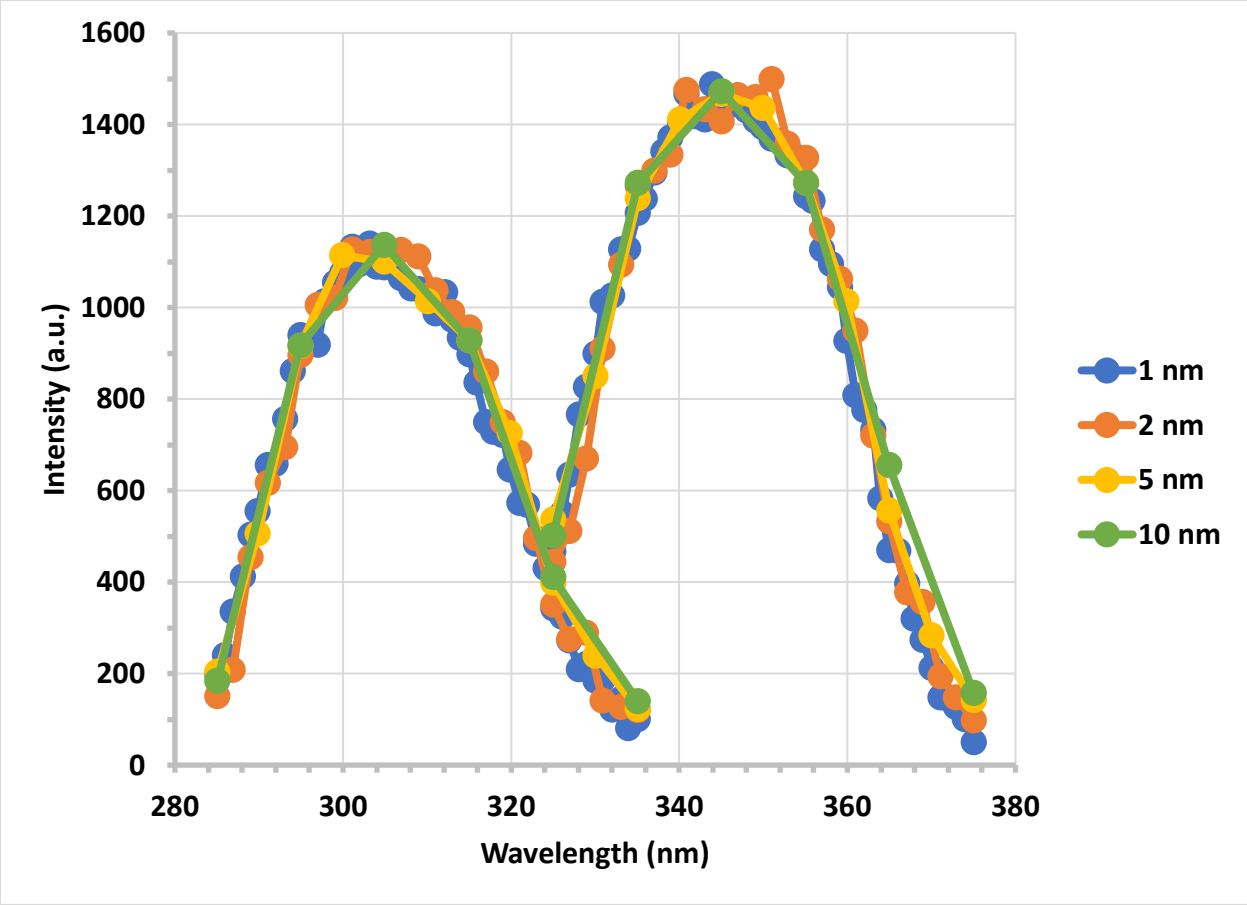

Figure 68: Synchronous fluorescence spectra of tryptophan and tyrosine mixture for various excitation resolutions.

The computed synchronous fluorescence spectra are practically identical for each excitation resolution, with respect to both band shape and fluorescence intensity, and successfully resolve the tryptophan and tyrosine components of the mixture. These results suggest that increasing the excitation resolution, to as high as ~ 10 nm, is a rather viable means of reducing the total acquisition time, particularly in circumstances where higher integration times or averaging is required, such as when the sample concentration is low or the fluorescence signal is inherently weak. Additional algorithms, such as interpolation of the fluorescence intensity between excitation wavelengths, may also be implemented as needed.

Bacteria

Absorption Spectra

The normalized absorption spectra of *B. thuringiensis* and *E. coli* suspensions in water are depicted in Figure 69 and Figure 70, respectively.

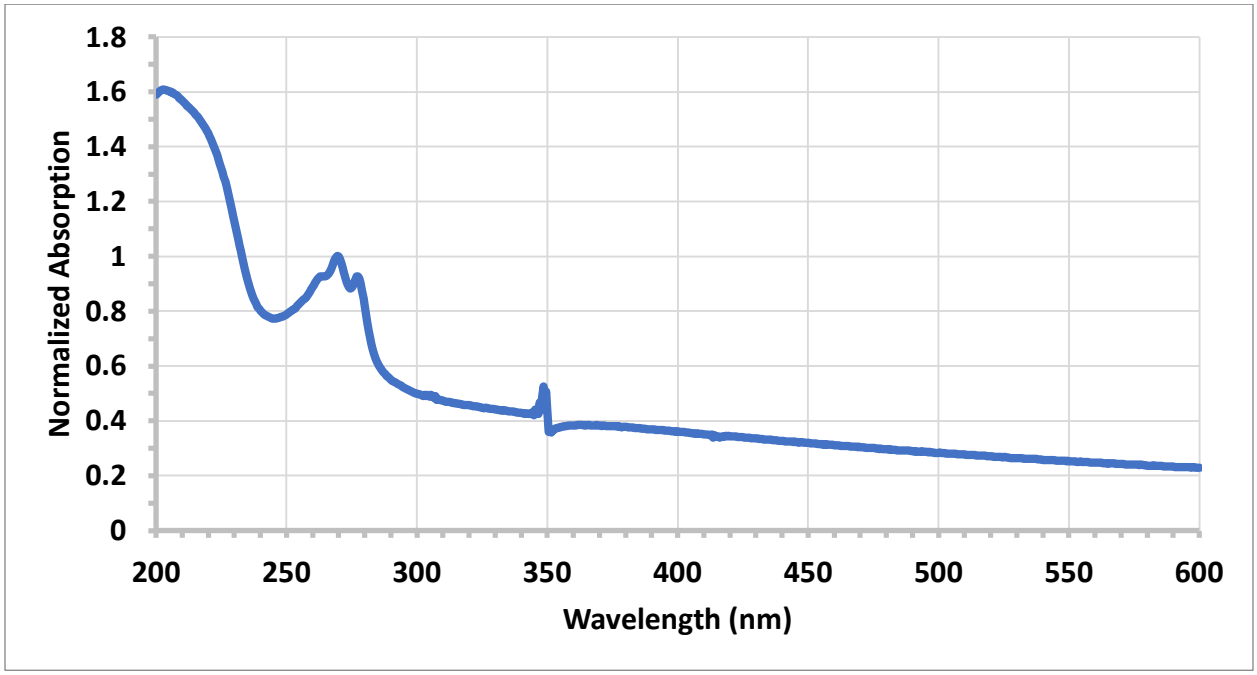

Figure 69: Normalized absorption spectrum of *B. thuringiensis* in water.

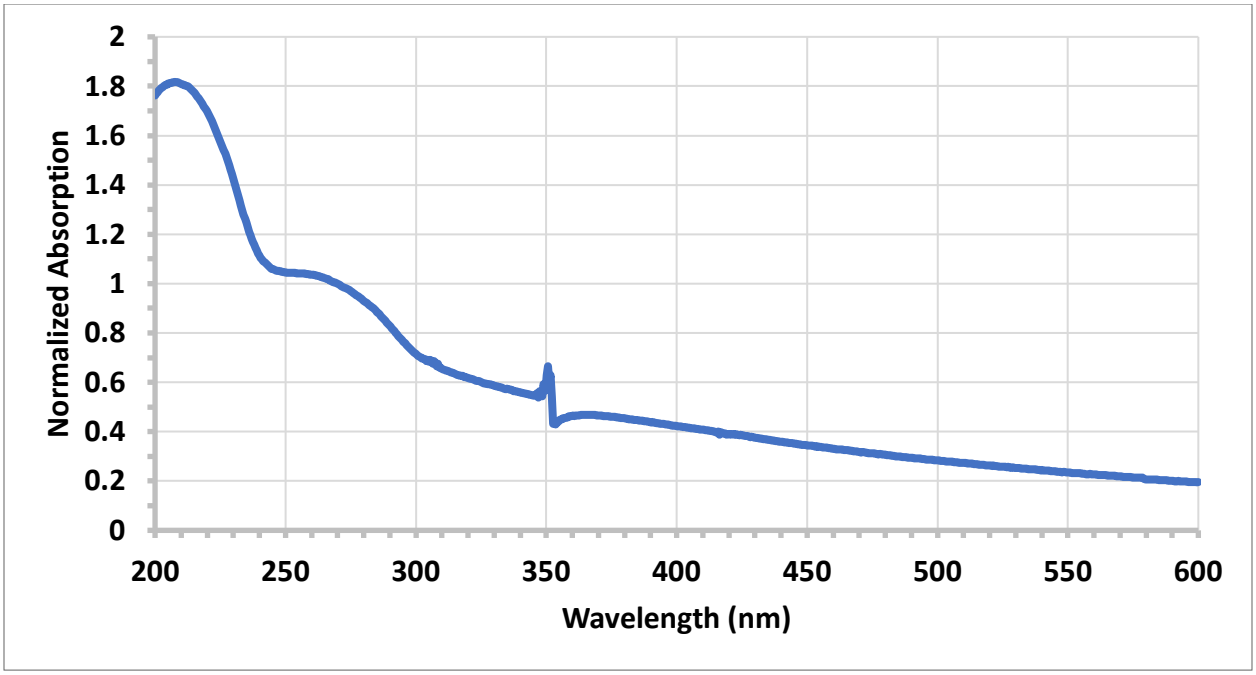

Figure 70: Normalized absorption spectrum of *E. coli* in water.

Both bacteria display a rather broad absorption band with maximum absorption at ~ 270 nm. This absorption band is primarily due to proteins situated along the cell membrane and within the cytoplasm, which consist of tryptophan and tyrosine residues, in addition to DNA, which is located in the cell interior. Owing to the fact that DNA is, topically, enveloped by proteins, which exist in greater quantity and display much higher absorption, by orders of magnitude, in the UV region [15, 39], the observed absorption bands may essentially be attributed to proteins, namely tryptophan and tyrosine residues, in the bacterial cell. The recorded absorption at longer wavelengths in the visible region, ~ 600 nm, is primarily due to light scattering and may be used to estimate the bacterial concentration [51].

Fluorescence Spectra

The fluorescence spectra of *B. thuringiensis* and *E. coli* suspensions in water ($\sim 10^8 \frac{cells}{mL}$) recorded by the portable instrument (integration time: 5 seconds; averaging: 5 scans; median

filter width: 20 points) are provided in Figure 71 and Figure 72, respectively. The corresponding fluorescence spectra recorded by the benchtop instrument are shown in Figure 73 and Figure 74 for reference.

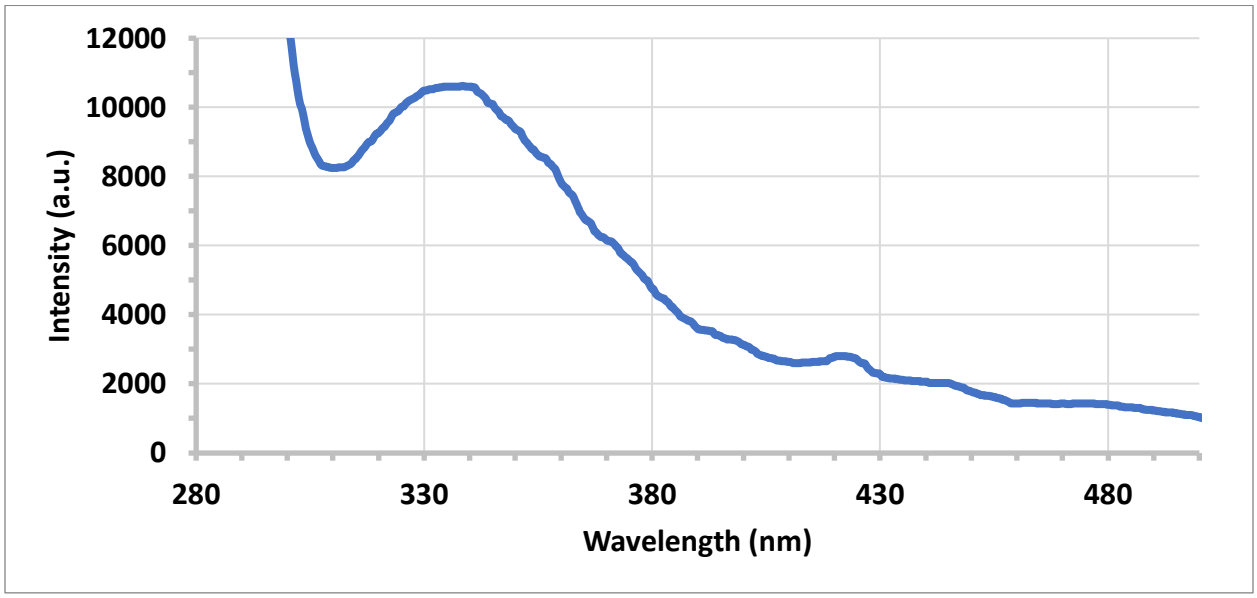

Figure 71: Fluorescence spectrum of *B. thuringiensis* recorded by portable instrument.

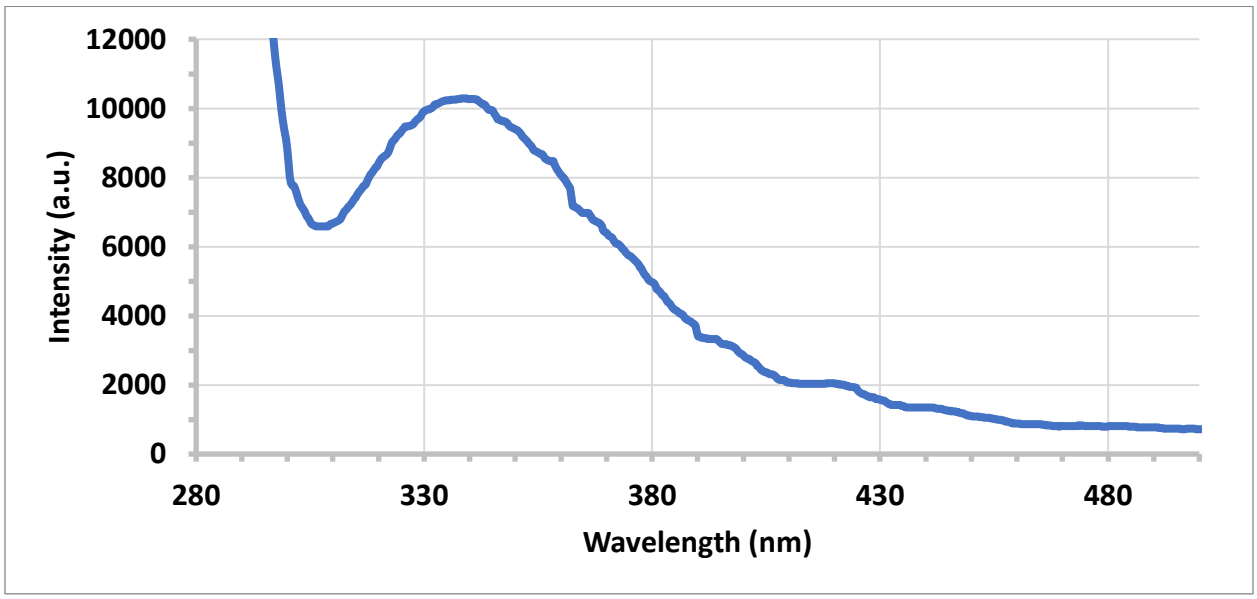

Figure 72: Fluorescence spectrum of *E. coli* recorded by portable instrument.

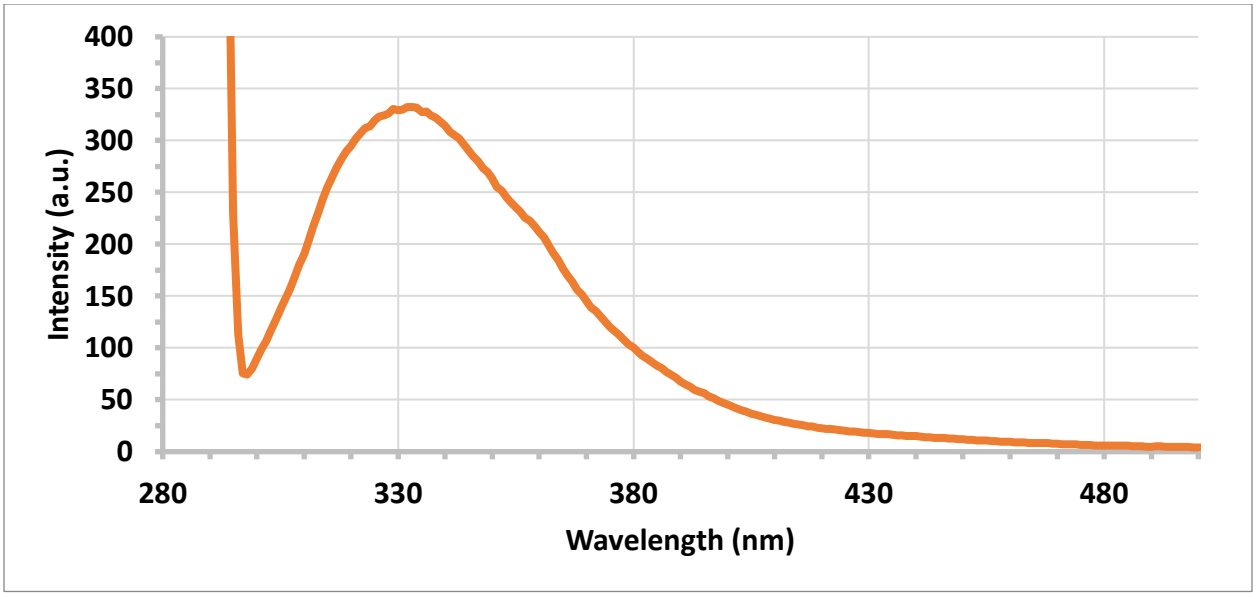

Figure 73: Fluorescence spectrum of *B. thuringiensis* recorded by benchtop instrument.

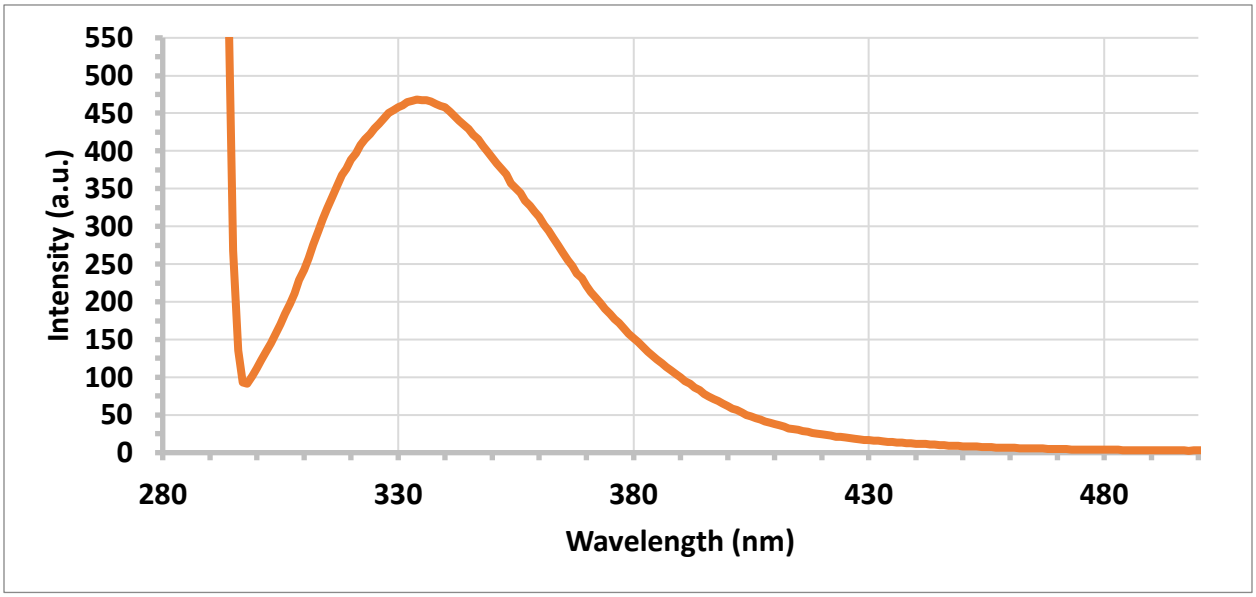

Figure 74: Fluorescence spectrum of *E. coli* recorded by benchtop instrument.

The initial high intensity, causing saturation of the detector, is due to Rayleigh (elastic) scattering of the excitation beam from the bacterial cells. As observed with tryptophan and tyrosine, the recorded spectra for *B. thuringiensis* and *E. coli* are practically identical with respect to the

fluorescence band shape and wavelength of peak intensity. The spectra recorded by the portable instrument were additionally compared against the literature [5–7, 17, 20–22] for further validation of their accuracy.

Excitation-Emission Matrix (EEM)

The excitation-emission matrices (EEMs) of *B. thuringiensis* and *E. coli* suspensions in water ($\sim 10^8 \frac{cells}{mL}$) were recorded over the excitation range of 260–310 nm with an excitation resolution of 2 nm (integration time: 30 seconds; averaging: 1 scan; median filter width: 50 points). The EEMs are provided as three-dimensional (3D) surface plots and two-dimensional (2D) contour plots for *B. thuringiensis* and *E. coli* in Figure 75 through Figure 78.

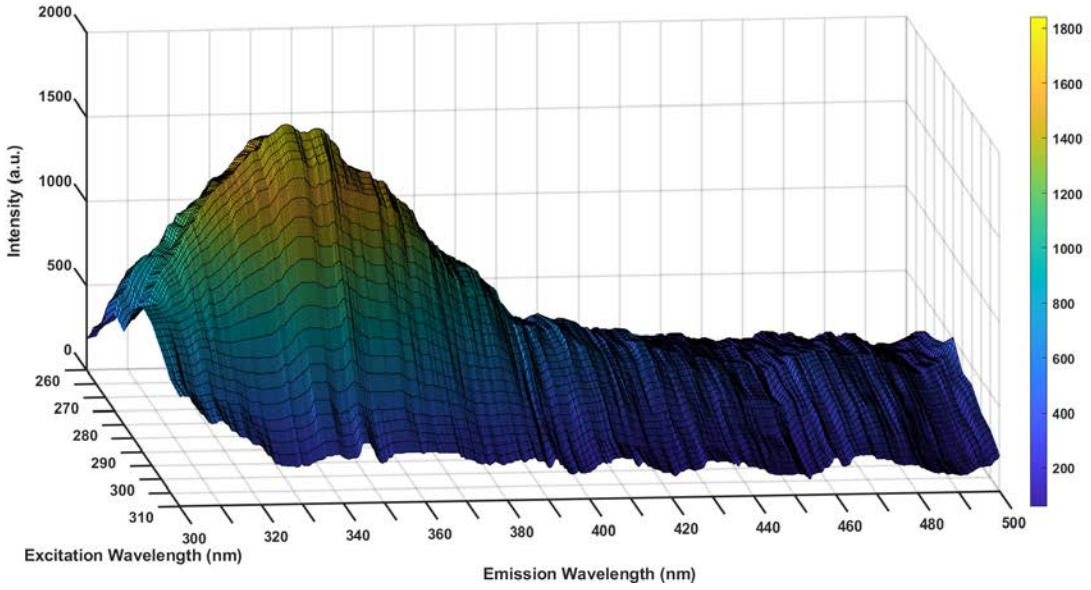

Figure 75: 3D surface plot of EEM for *B. thuringiensis* recorded by portable instrument.

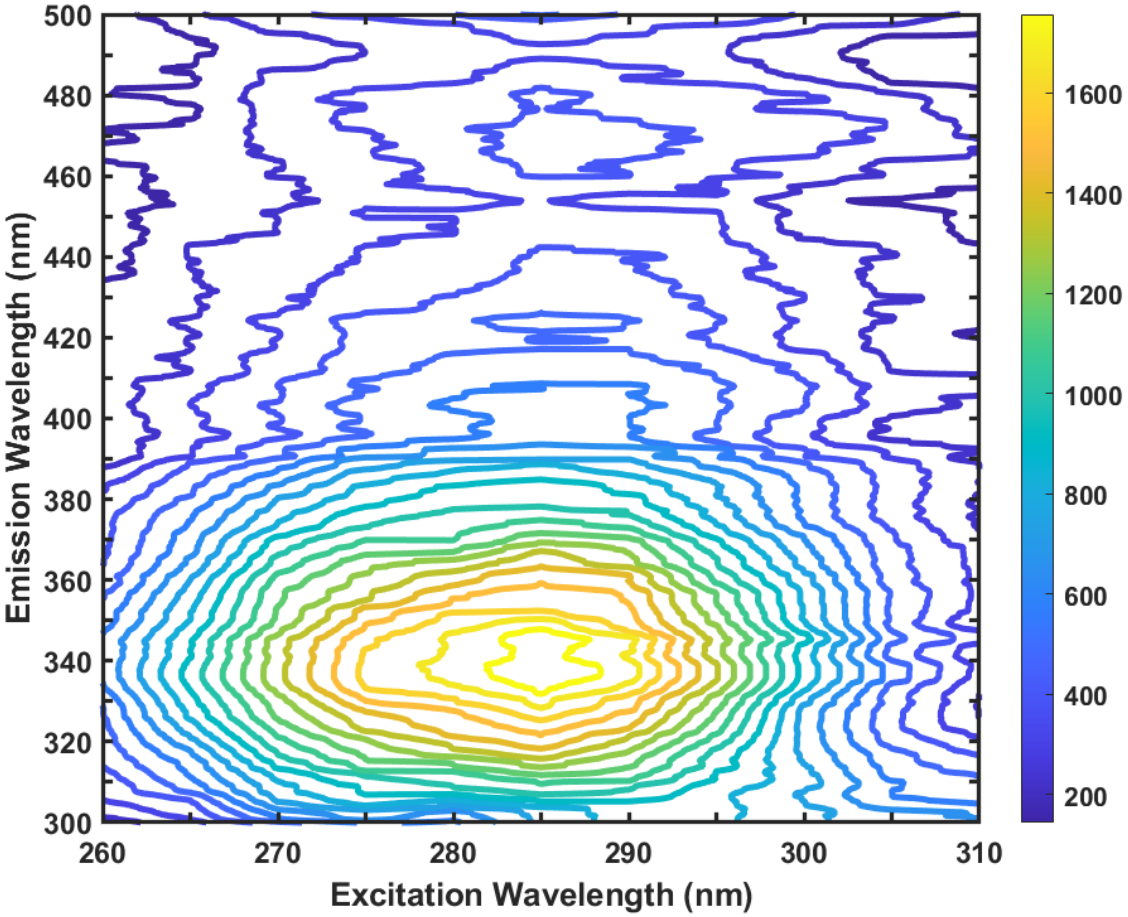

Figure 76: 2D contour plot of EEM for *B. thuringiensis* recorded by portable instrument.

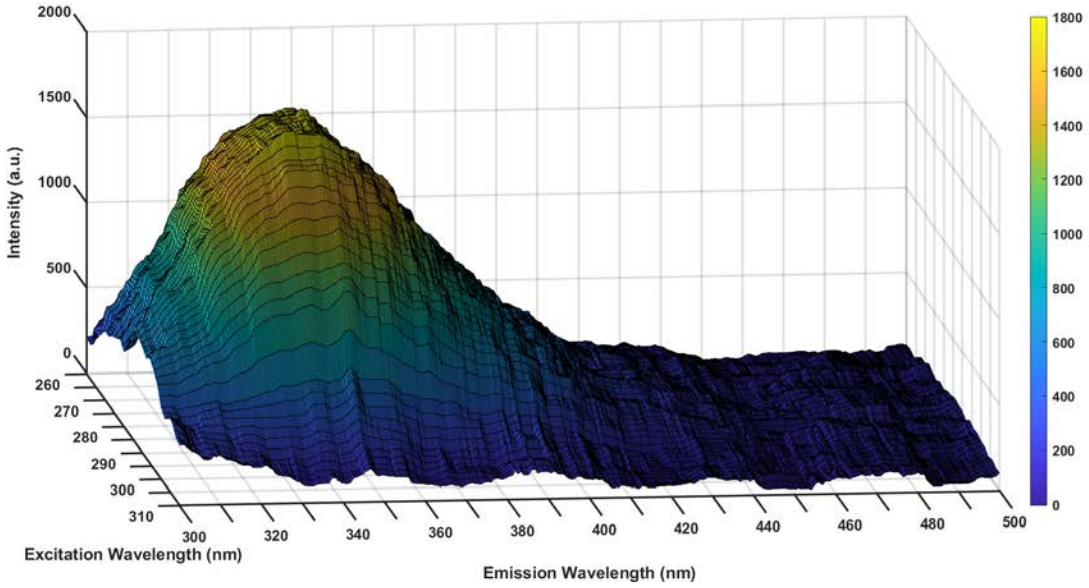

Figure 77: 3D surface plot of EEM for *E. coli* recorded by portable instrument.

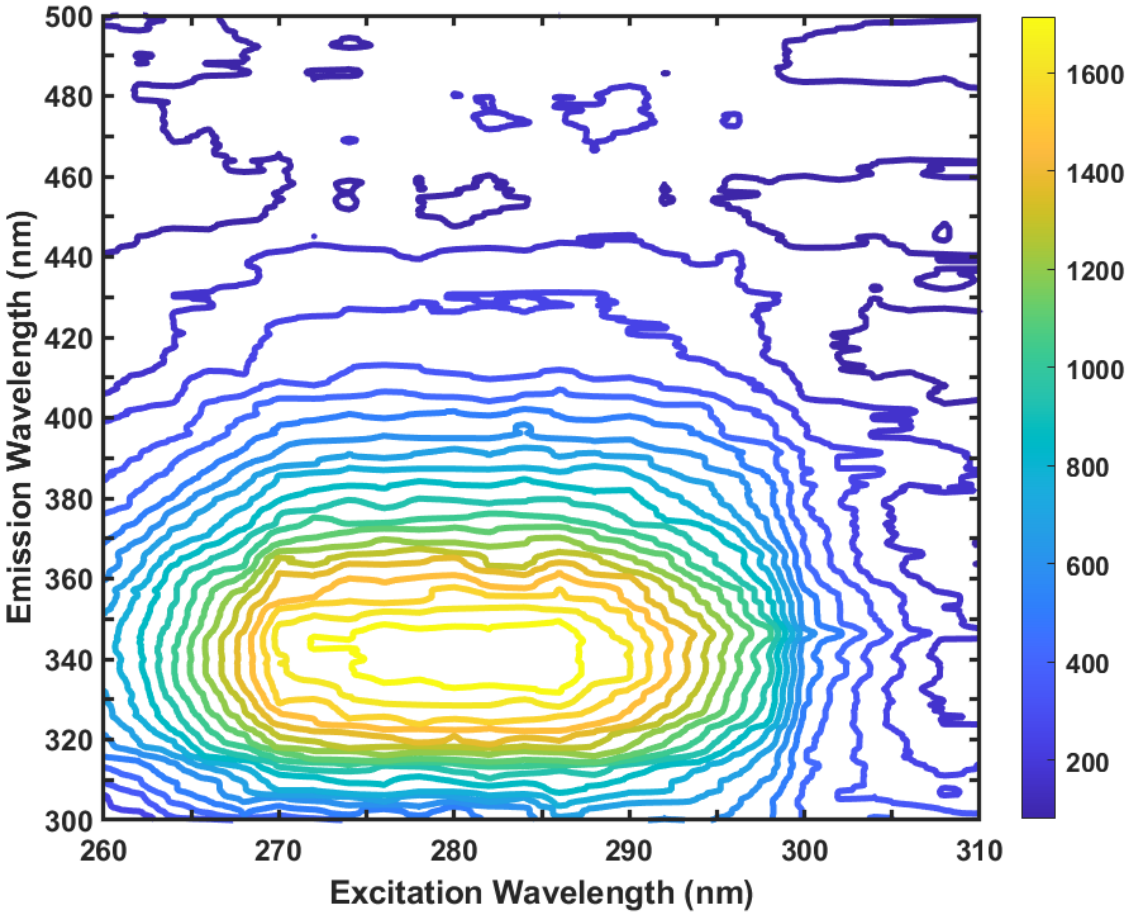

Figure 78: 2D contour plot of EEM for *E. coli* recorded by portable instrument.

An intense fluorescence band is observed in the EEM of both *B. thuringiensis* and *E. coli* with peak excitation at ~ 280–285 nm and peak emission at ~ 335–340 nm. This band is primarily assigned to tryptophan, which is known to be the most intensely absorbing and fluorescing component of bacterial cells [39, 73], and, to a lesser degree, tyrosine. It is worth noting that tryptophan and tyrosine do not exist as free molecules in bacterial cells but rather as components of membrane and cytoplasmic proteins. The locations of the excitation and emission band maxima are in good agreement with the literature [5, 17, 20–22].

Fluorescence and Synchronous Fluorescence Spectra

The fluorescence spectra of the *B. thuringiensis* and *E. coli* suspensions ($\sim 10^8 \frac{cells}{mL}$) at various excitation wavelengths, along with the synchronous fluorescence spectra of the tryptophan and tyrosine components, were extracted from the respective EEMs of the bacteria. The same set of $\Delta\lambda$ employed previously for the tryptophan and tyrosine mixture was utilized in this procedure. To that effect, the fluorescence spectrum at an excitation wavelength $\lambda_{EX} = 270$ nm, along with the synchronous fluorescence spectra of the tyrosine and tryptophan components extracted with $\Delta\lambda = 25$ nm and $\Delta\lambda = 65$ nm, respectively, are provided for *B. thuringiensis* and *E. coli* in Figure 79 and Figure 80, respectively. The corresponding fluorescence and synchronous fluorescence spectra recorded by the benchtop instrument are also provided in Figure 81 and Figure 82 for comparison.

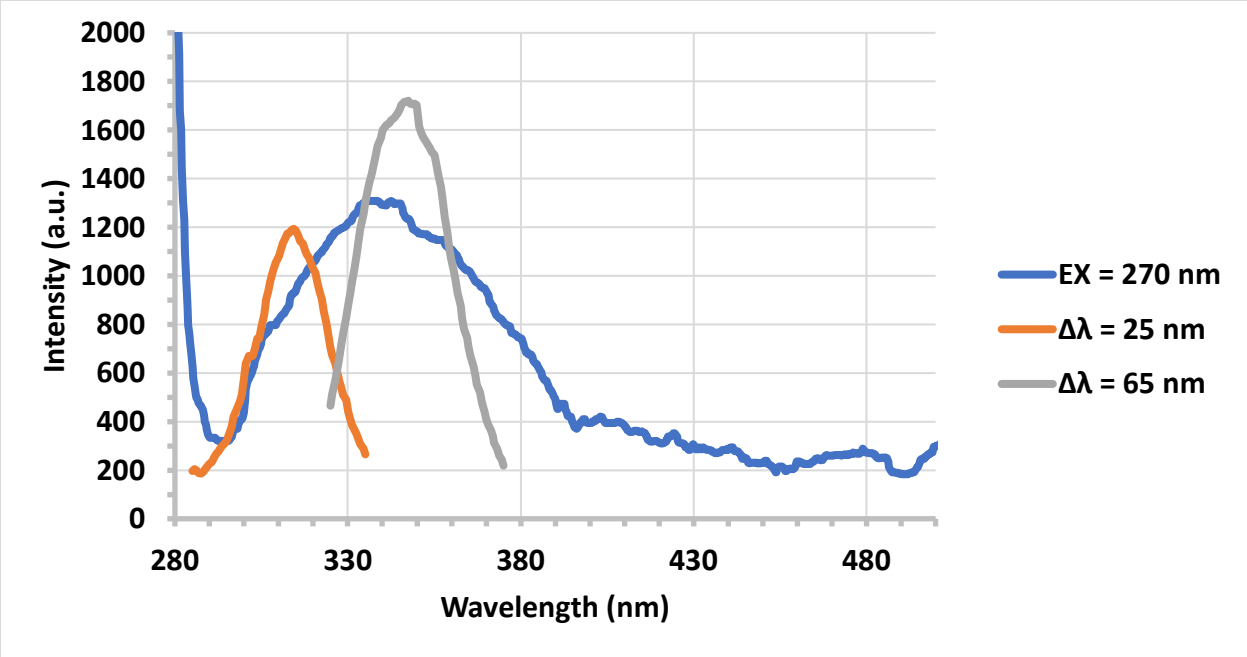

Figure 79: Fluorescence and synchronous fluorescence spectra of *B. thuringiensis* recorded by portable instrument.

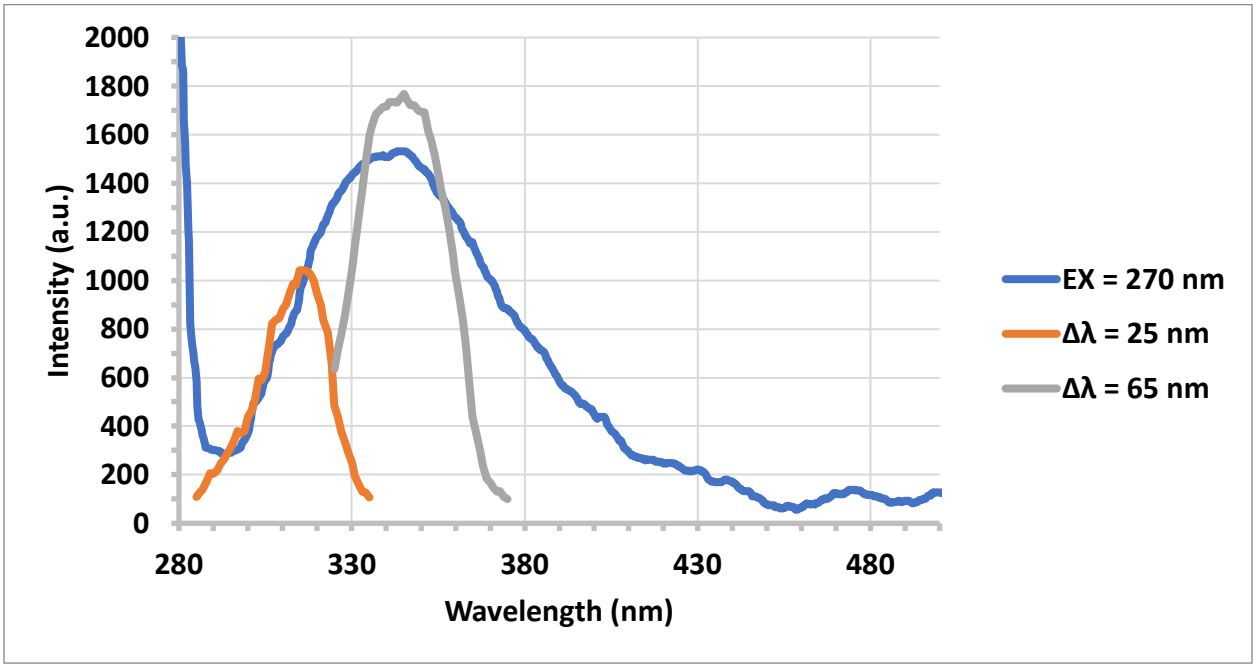

Figure 80: Fluorescence and synchronous fluorescence spectra of *E. coli* recorded by portable instrument.

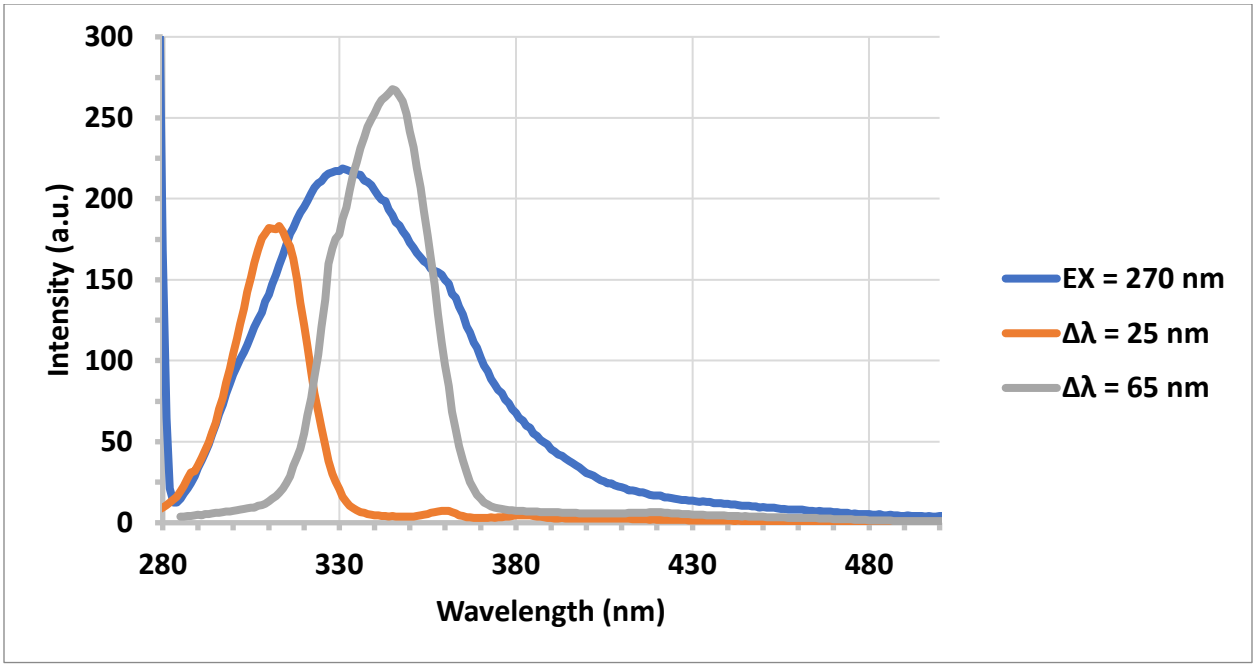

Figure 81: Fluorescence and synchronous fluorescence spectra of *B. thuringiensis* recorded by benchtop instrument.

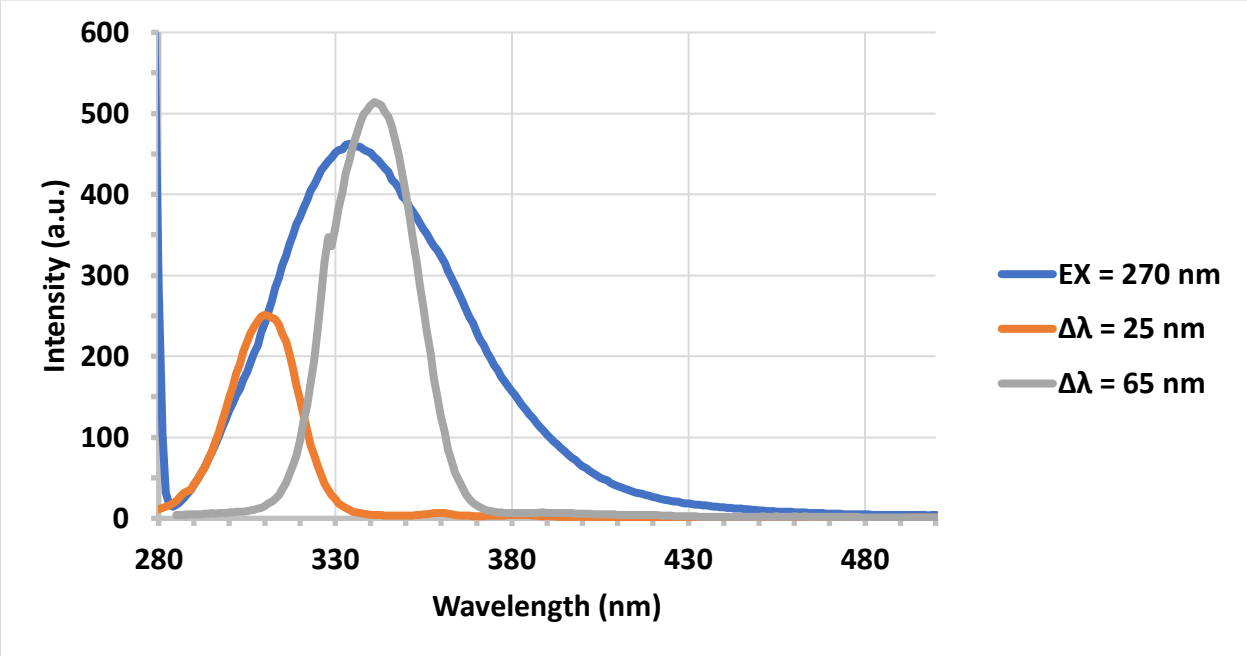

Figure 82: Fluorescence and synchronous fluorescence spectra of *E. coli* recorded by benchtop instrument.

The synchronous fluorescence spectra recorded for *B. thuringiensis* and *E. coli* are practically identical to those recorded for the mixture of tyrosine and tryptophan, revealing the tyrosine and tryptophan fluorescence band maxima at ~ 315 nm and 350 nm, respectively. This technique therefore provides a direct means of recording the fluorescence of individual cellular components in bacteria, in addition to observing the effects of UV radiation or other inactivating agents, such as antibiotics, on such components. Additionally, it may be possible to record similar information, *in-situ*, for other pathogens such as viruses. It is rather interesting to note that the tryptophan to tyrosine synchronous fluorescence intensity ratios recorded for *B. thuringiensis* and *E. coli* with the portable instrument, ~ 1.44 and ~ 1.70, respectively, are in reasonable agreement with those measured by the benchtop instrument, which are ~ 1.46 and ~ 2.05, respectively. These results suggest that *B. thuringiensis* and *E. coli* possess distinct synchronous fluorescence intensity ratios that may aid in identifying the respective bacterial strains. Further work is required in establishing the accuracy of this technique at various bacterial concentrations and extending it to include additional bacterial strains. We find that the data recorded by our portable instrument is practically identical to that provided in the literature and recorded by benchtop instruments [5, 17, 20–22, 39].

Fluorescence Decay

Suspensions of *B. thuringiensis* and *E. coli* in water ($\sim 10^8 \frac{cells}{mL}$) were irradiated by means of a mercury arc lamp and UV LED, integrated with our portable instrument in the disinfection unit, for various irradiation times ranging from 0 to 120 minutes. Fluorescence spectra were recorded by the portable instrument (integration time: 5 seconds; averaging: 5 scans; median filter width: 20 points) following each interval of irradiation. To that effect, Figure 83 through Figure 86 display the fluorescence spectra and peak fluorescence intensities of *B.*

thuringiensis and *E. coli* as a function of the irradiation time, respectively, using the mercury arc lamp.

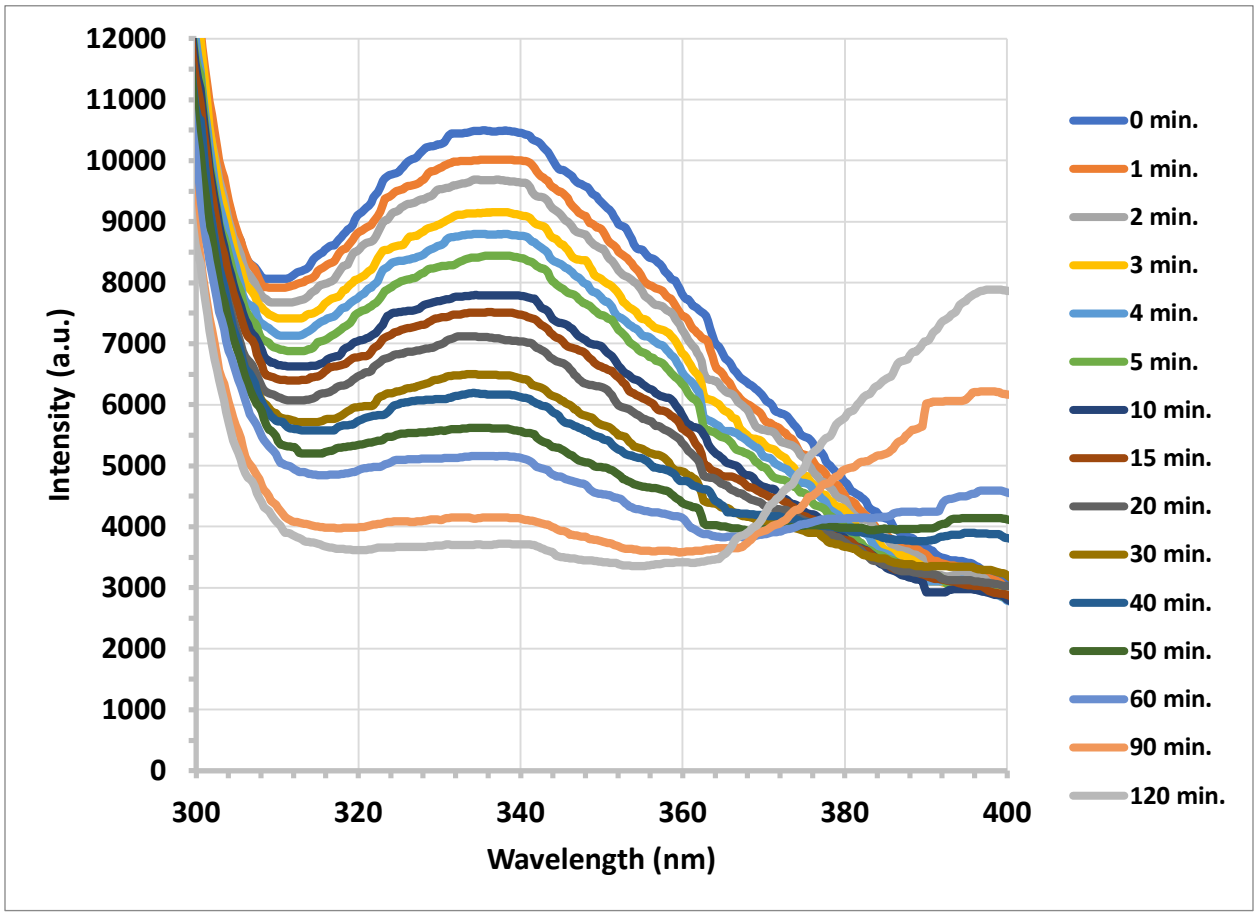

Figure 83: Fluorescence spectra of *B. thuringiensis* as a function of irradiation time using arc lamp.

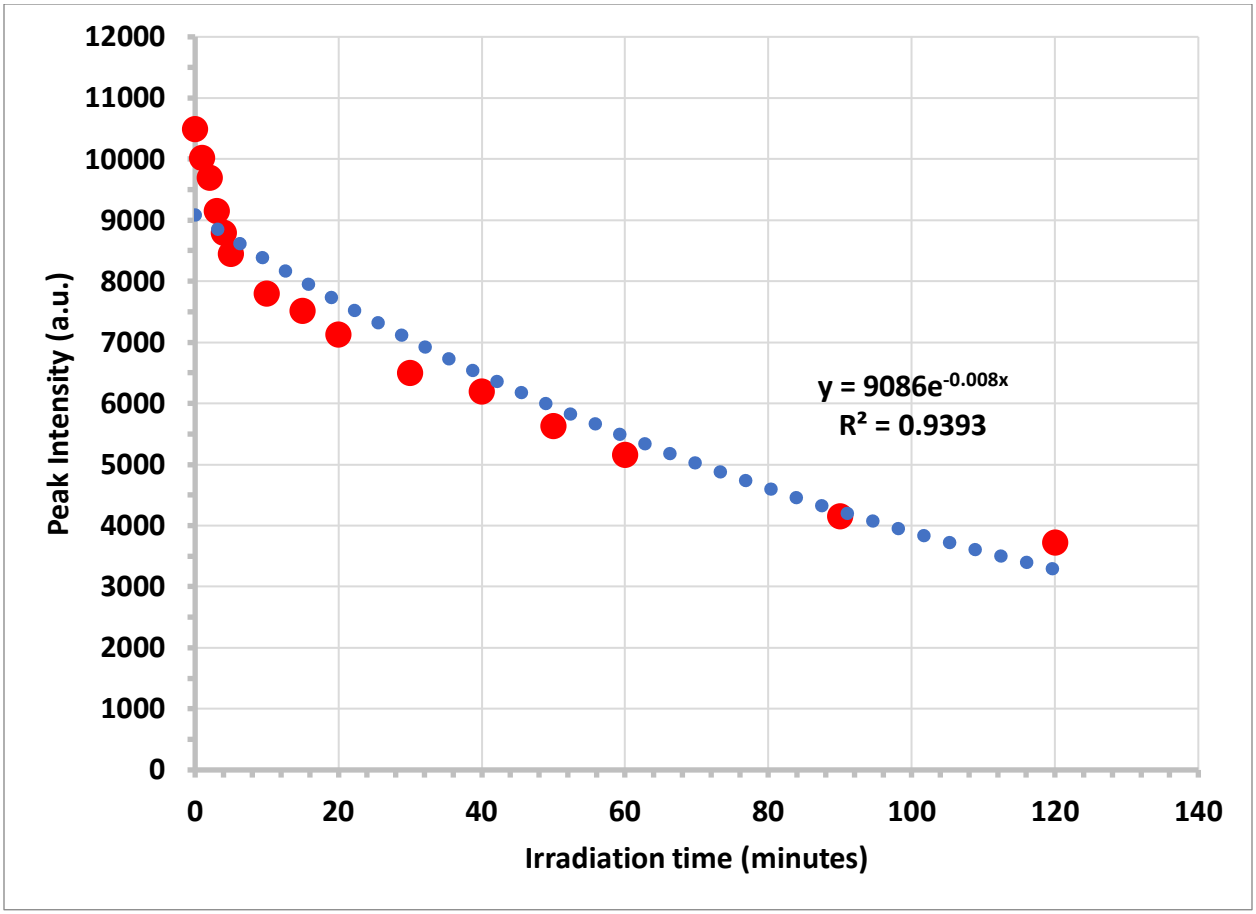

Figure 84: Peak intensity of *B. thuringiensis* as a function of irradiation time using arc lamp.

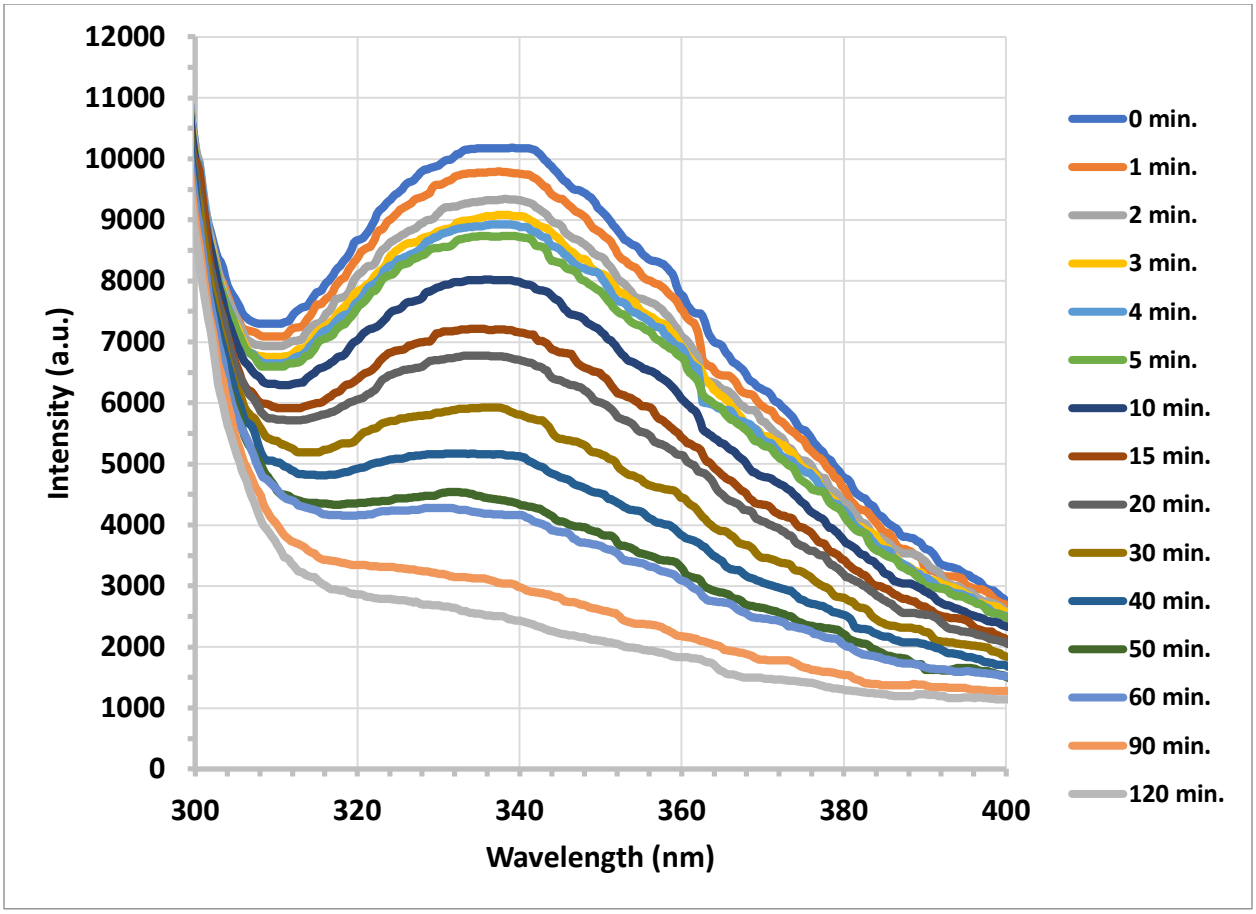

Figure 85: Fluorescence spectra of *E. coli* as a function of irradiation time using arc lamp.

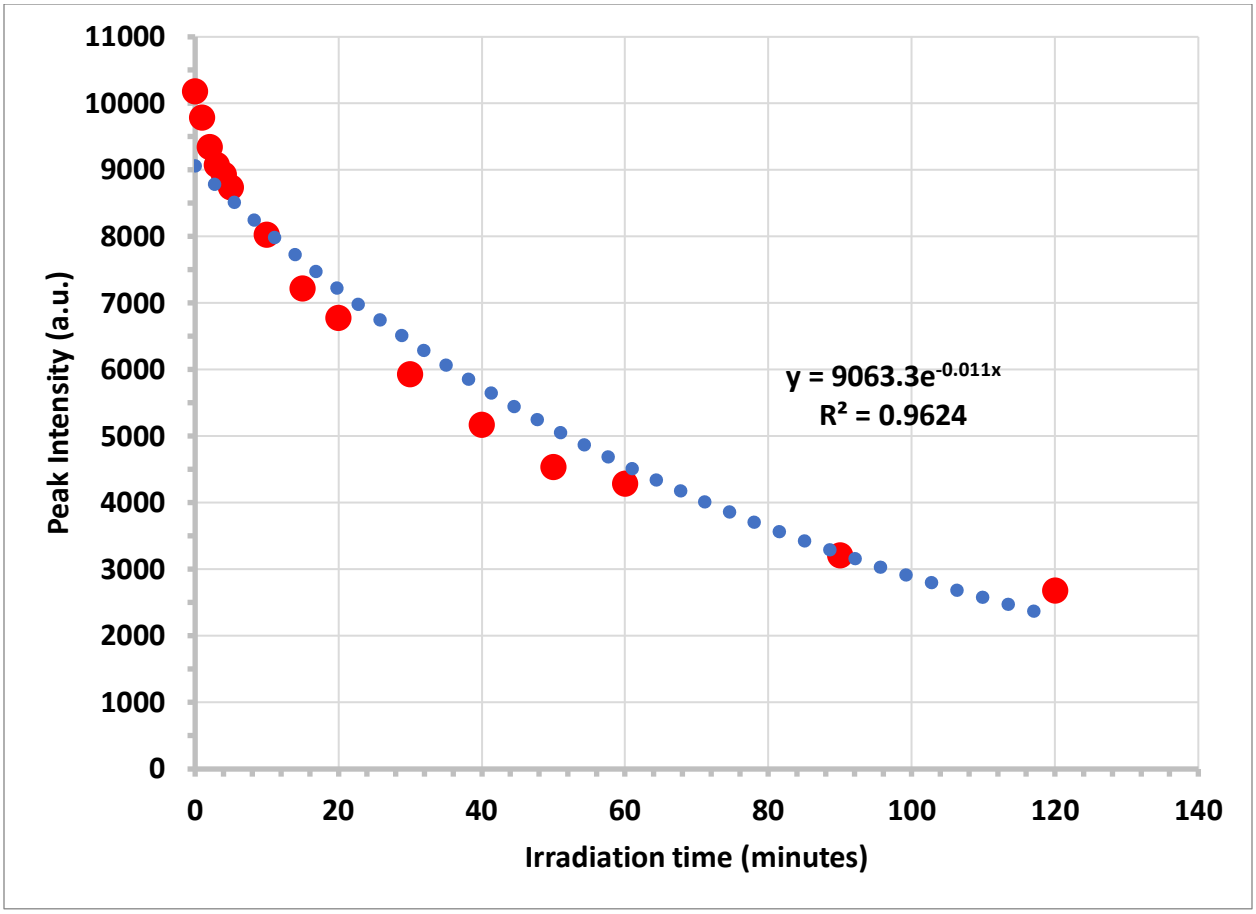

Figure 86: Peak intensity of *E. coli* as a function of irradiation time using arc lamp.

Figure 87 through Figure 90 similarly display the fluorescence spectra and peak fluorescence intensities of *B. thuringiensis* and *E. coli* as a function of the irradiation time, respectively, using the UV LED in the disinfection unit of the portable instrument.

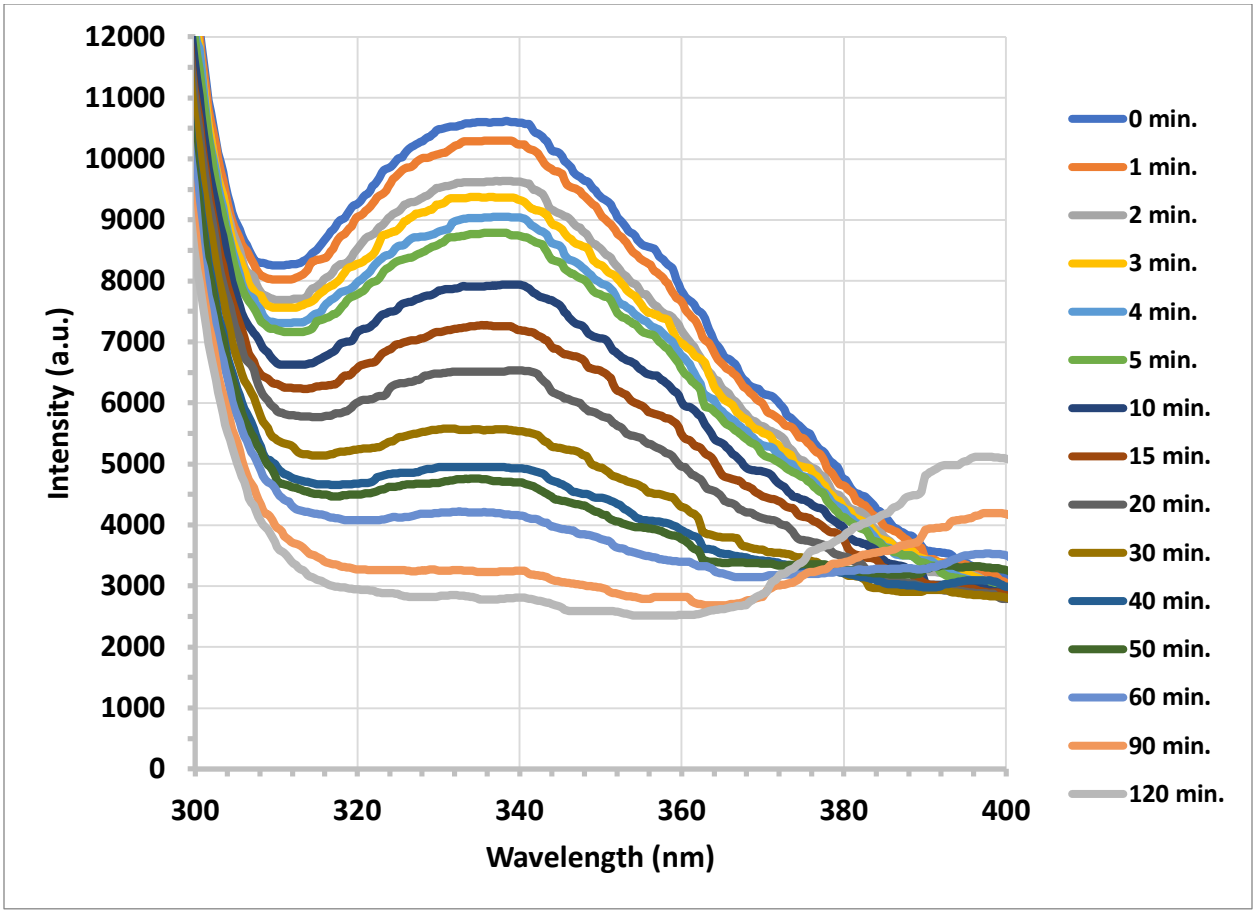

Figure 87: Fluorescence spectra of *B. thuringiensis* as a function of irradiation time using UV LED.

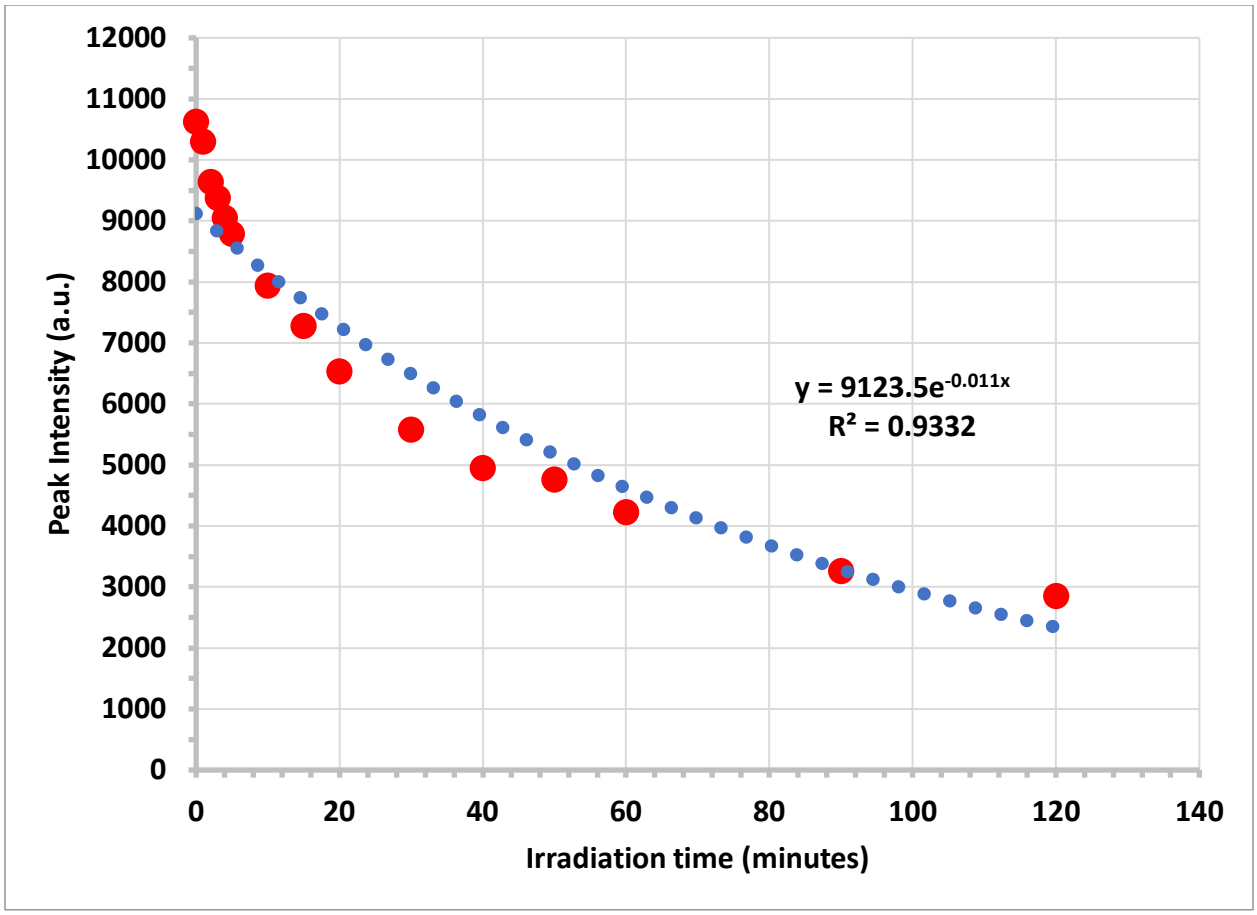

Figure 88: Peak intensity of *B. thuringiensis* as a function of irradiation time using UV LED.

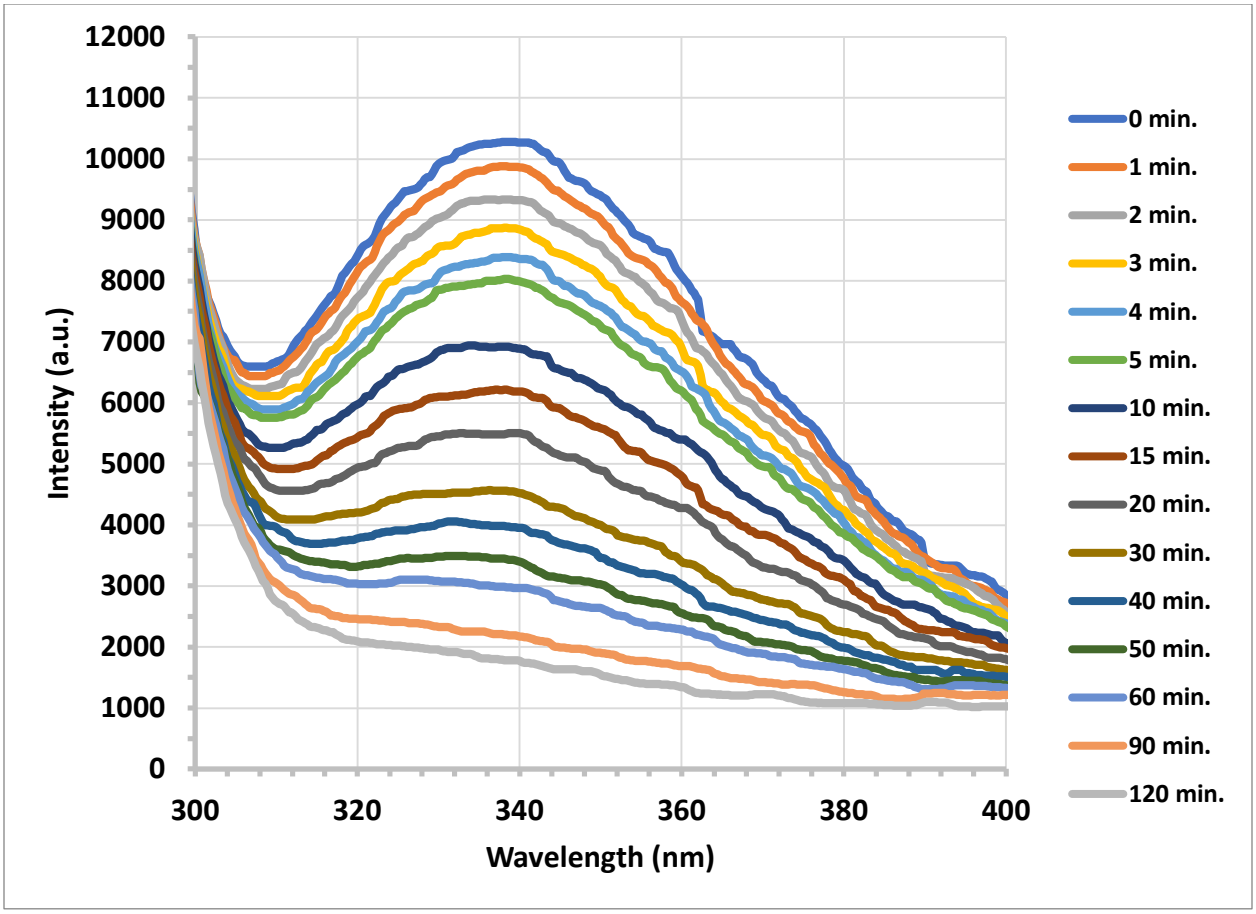

Figure 89: Fluorescence spectra of *E. coli* as a function of irradiation time using UV LED.

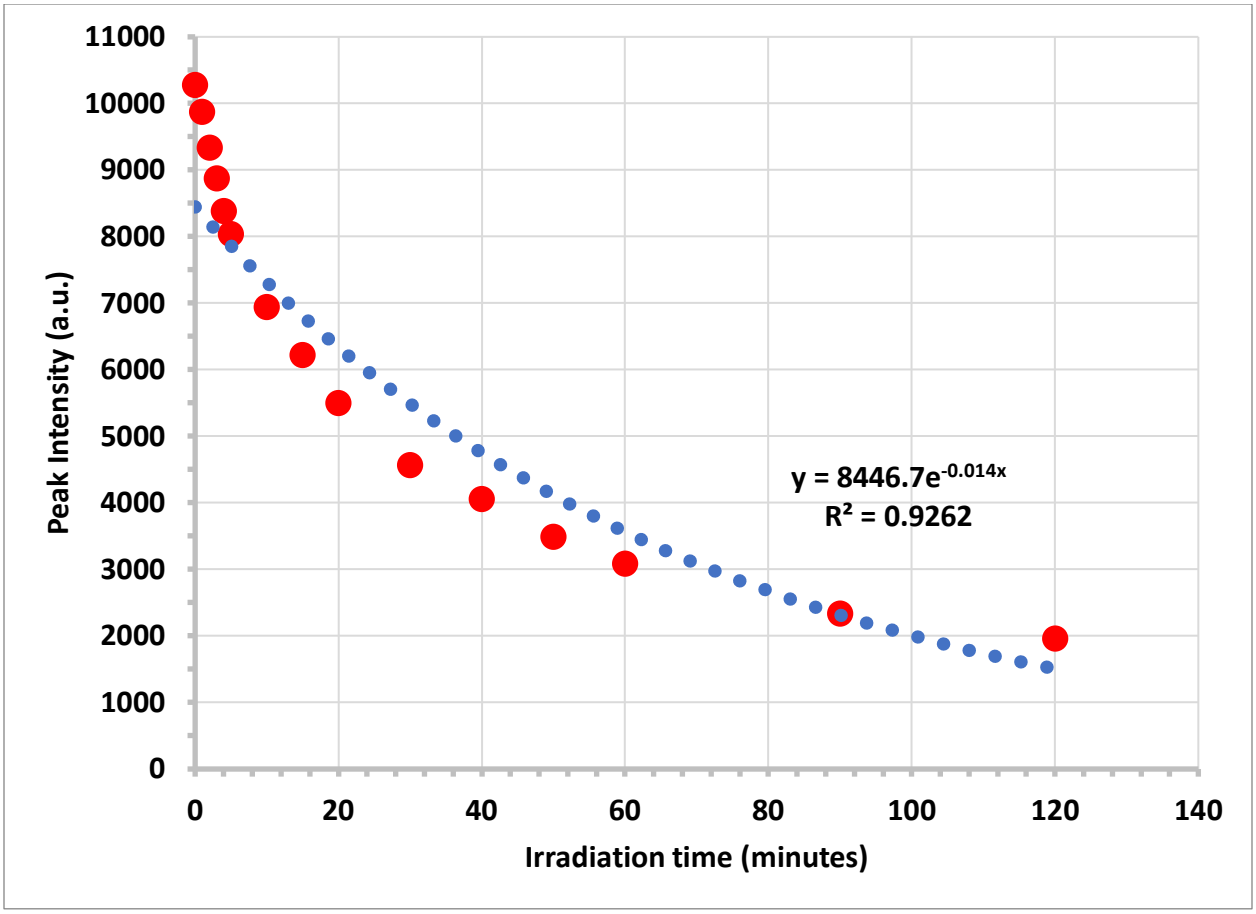

Figure 90: Peak intensity of *E. coli* as a function of irradiation time using UV LED.

The decrease in the fluorescence band intensities of *B. thuringiensis* and *E. coli* closely resembles the previously discussed decrease in the fluorescence of tryptophan and tyrosine solutions irradiated with UV light. This suggests that similar photodamage occurs to tryptophan and tyrosine residues within the bacterial cells. Moreover, it is well known that proteins denature upon illumination with UV light, thereby resulting in structural damage and loss of cellular function. It is worth noting, however, that the inactivation, or death, of a bacterium is strictly attributed to DNA damage, namely the formation of thymine dimers which prohibit cellular replication. Our previous studies [21, 23, 39] have demonstrated that protein damage, in addition to displaying a more intense fluorescence and Raman signature, precedes DNA dimerization.

This is due to the fact that proteins envelope the DNA in the cytoplasm and possess higher absorption than DNA, by orders of magnitude, in the UV region. We determined that protein damage, and the resulting changes in the fluorescence and Raman spectra, correlates with the inactivation of bacteria and may therefore differentiate between live and dead bacteria. We find that the results obtained with the portable instrument are consistent with our previous studies [20–22, 39].

Additionally, it is interesting to note that the fluorescence decay rate constants obtained using the mercury lamp and UV LED are comparable for both *B. thuringiensis* and *E. coli*, varying from ~ 0.008–0.014 minutes^{-1}, which suggests that the inactivation rates for each source are similar. This may be due to the fact that while the mercury lamp provides a higher net optical power, ~ 4–5 mW in these experiments, than the LED, ~ 1–2 mW, over the UV region, the efficiency of the LED in the UVB and UVC regions, where the absorption of proteins is at its maximum, is higher. Other studies have similarly demonstrated the advantage of UV LEDs over conventional mercury lamps in achieving disinfection [87–89].

Identification of live and dead bacteria

The fluorescence band maximum decrease of *B. thuringiensis* and *E. coli,* following irradiation by the UV LED, may be utilized in conjunction with PCA for distinguishing live and dead bacteria. To that effect, Figure 91 and Figure 92 display the PCA score plots for unirradiated (control) and irradiated *B. thuringiensis* as a function of the irradiation time. These score plots were obtained by subjecting fluorescence data in the range of ~ 300 to 400 nm to PCA, which resulted in the greatest variation between spectra. The data from at least three independent experiments were normalized to the fluorescence band maximum and utilized for the analysis.

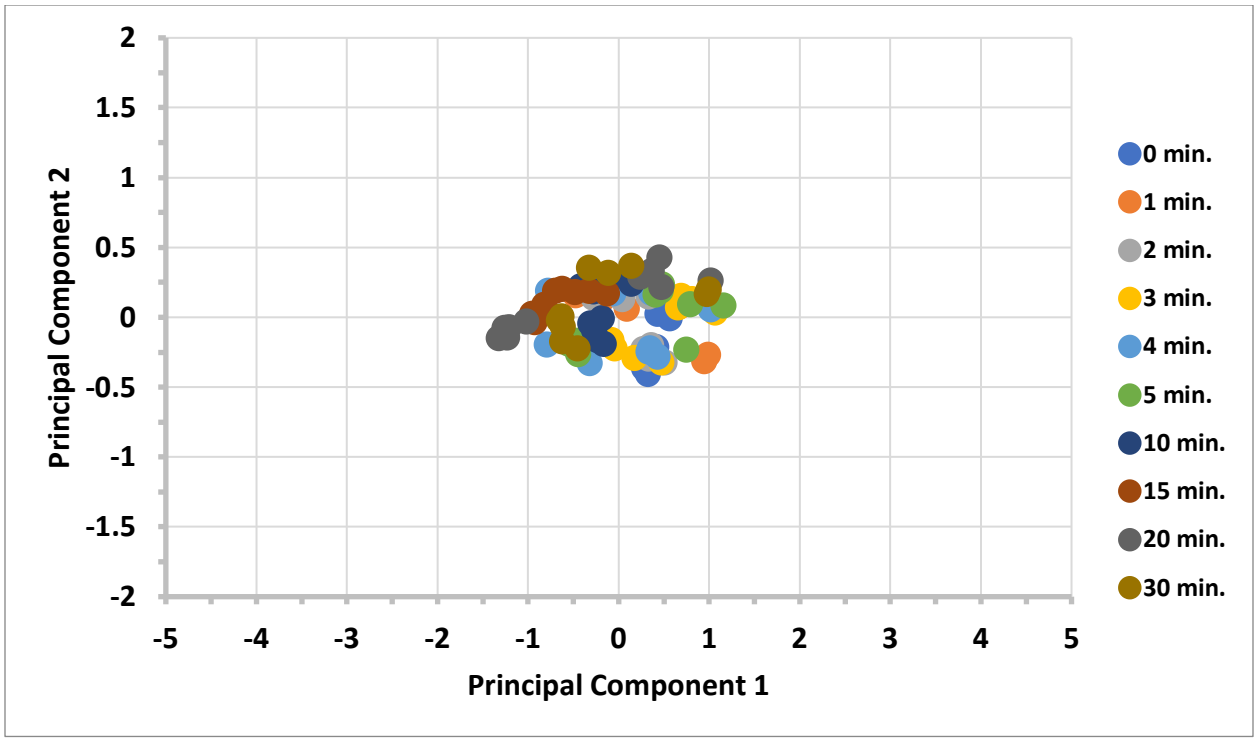

Figure 91: PCA score plot for non-irradiated (control) *B. thuringiensis*.

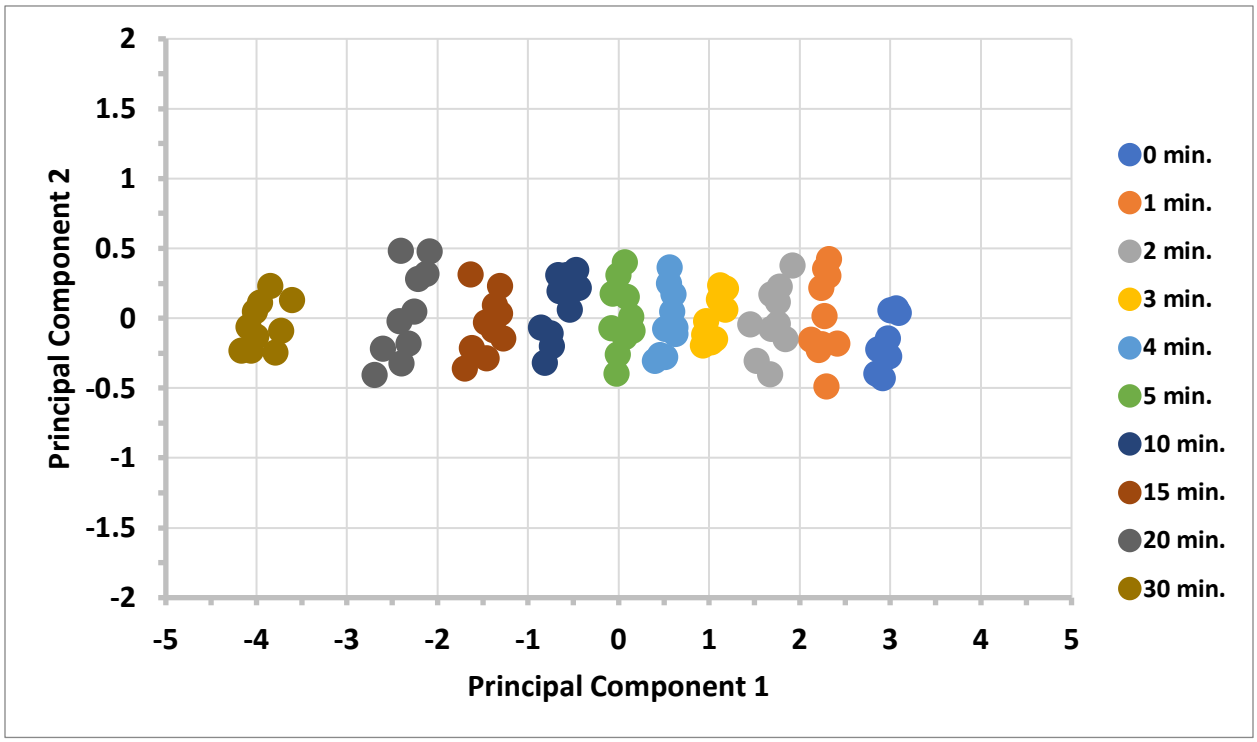

Figure 92: PCA score plot for irradiated *B. thuringiensis*.

While the score plot for non-irradiated (control) *B. thuringiensis* displays practically no variation with irradiation time, owing to the random scattering of PCA points, the score plot for irradiated *B. thuringiensis* displays a rather strong variation along the principal component 1 (PC1) axis as a function of the irradiation time. In particular, as the irradiation time increases, the PC1 score of the spectra decreases. The principal component 2 (PC2) score of the spectra, however, remains relatively constant. To that effect, the average PC1 and PC2 scores for each irradiation time, in addition to the principal component plot for PC1, are plotted in Figure 93 and Figure 94, respectively.

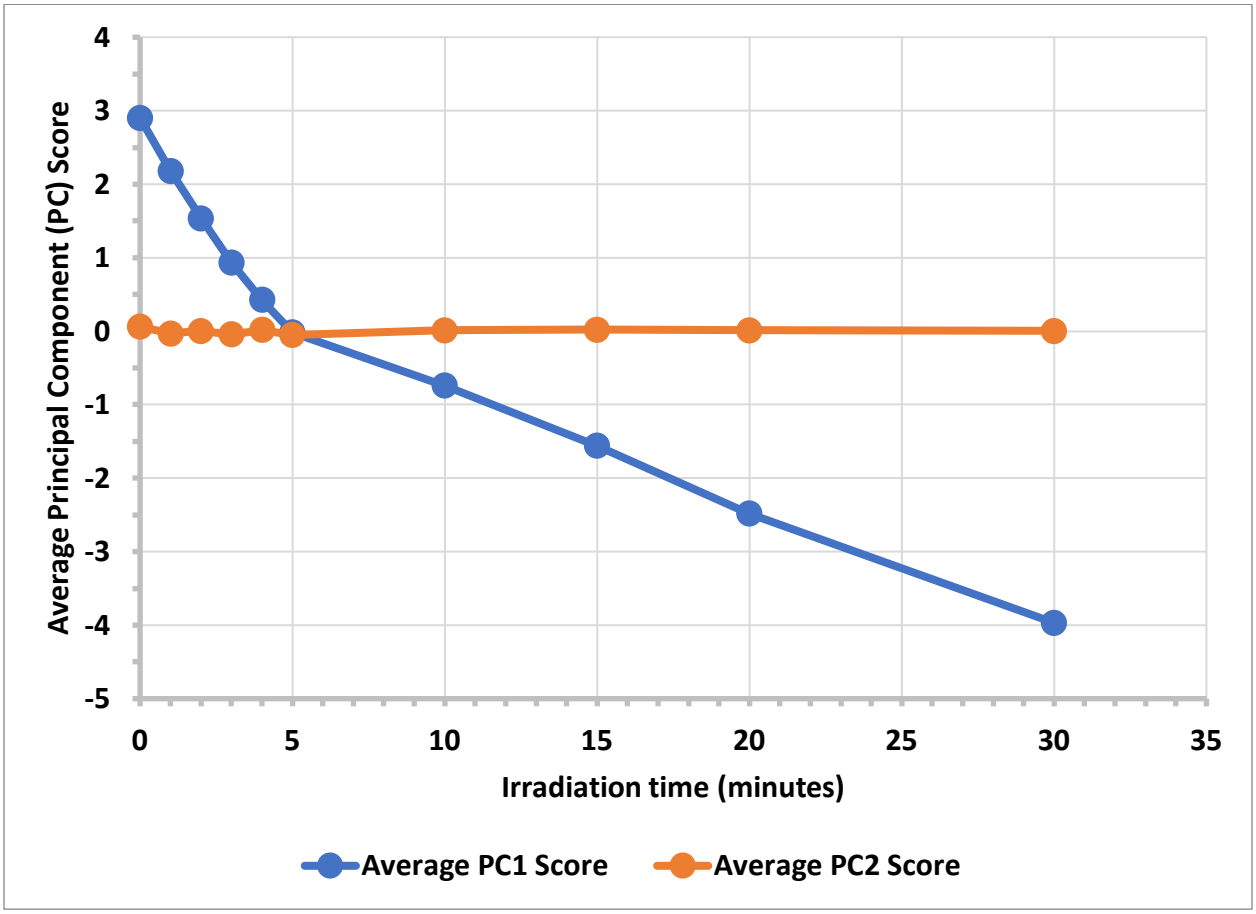

Figure 93: Average PC1 and PC2 scores as a function of irradiation time for *B. thuringiensis*.

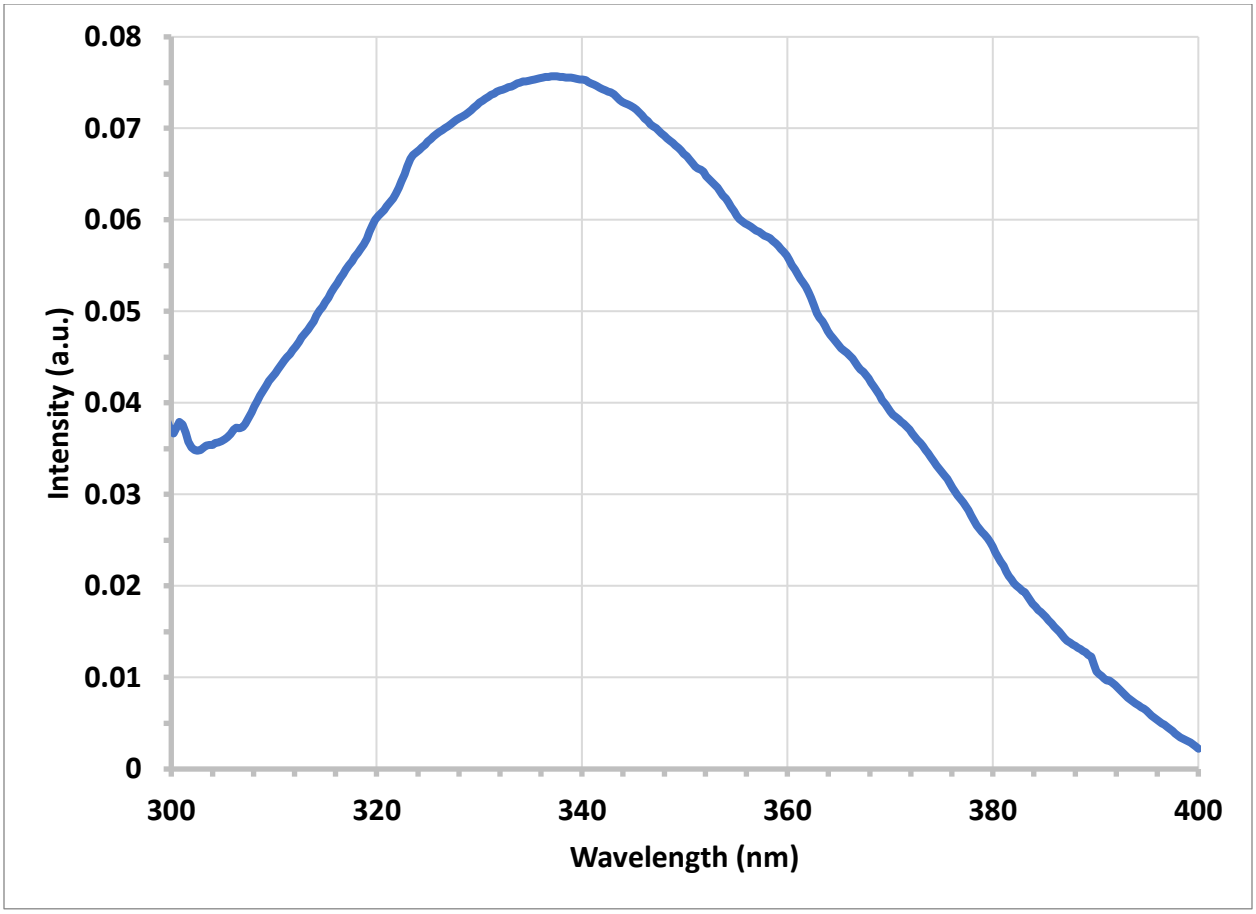

Figure 94: Plot of principal component 1 for *B. thuringiensis*.

A continuous decrease in the average PC1 score, as a function of the irradiation time, is observed, while the average PC2 score is practically constant. We may therefore consider all variation in the spectral data to be captured by PC1 alone. A close inspection of the PC1 plot reveals that this variation may essentially be attributed to the decrease of the fluorescence band, ~ 335 nm, maximum following UV irradiation. It is rather interesting to observe that the shape of the PC1 decrease closely resembles the decrease in the peak fluorescence intensity, which correlates with the number, or fraction, of bacteria inactivated following UV irradiation. Thus, the average PC1 score is an indication of the concentration of live bacteria. Our previous experimental data with a mercury lamp [20–21] demonstrated that a rather large fraction of

bacteria is inactivated within the first few minutes of UV irradiation, which is in good agreement with the separation displayed in the PCA plots recorded by our portable instrument. Additionally, we found that practically all bacteria were inactivated (dead) after ~ 10 to 20 minutes of irradiation, which also shows pronounced separation from the non-irradiated (live) bacteria on the score plots. Thus, our portable instrument possesses sufficient sensitivity for detecting variations in the number of live bacteria at concentrations comparable to those used with benchtop instruments. When calibrated with the culturing data obtained through traditional means, namely CFU counting, these procedures provide a practically instantaneous, *in-situ* determination of the number of live and dead bacteria following inactivation by UV light, antibiotics, or other methods.

The corresponding PCA score and principal component plots, along with the variation of PC1 as a function of the irradiation time, are provided for *E. coli* in Figure 95 through Figure 98. The PCA results for *E. coli* similarly demonstrate a clear separation between spectra, as a function of the irradiation time, along the PC1 axis.

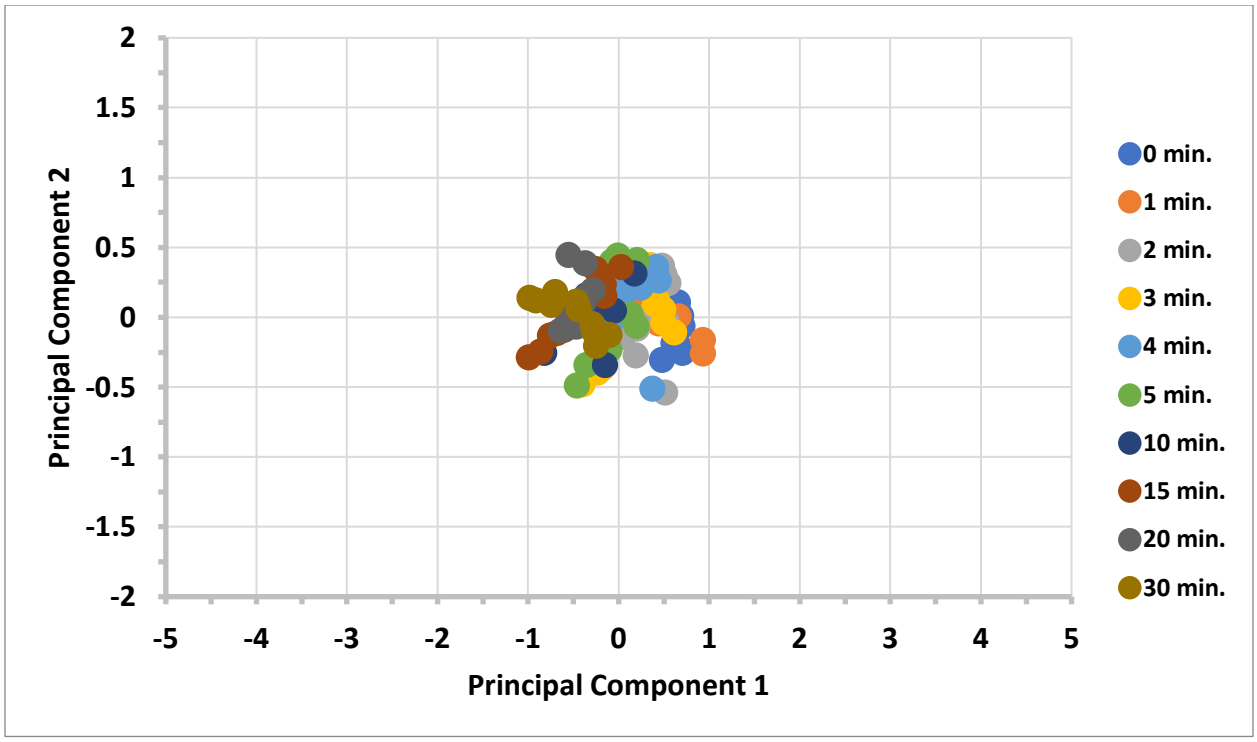

Figure 95: PCA score plot for non-irradiated (control) *E. coli*.

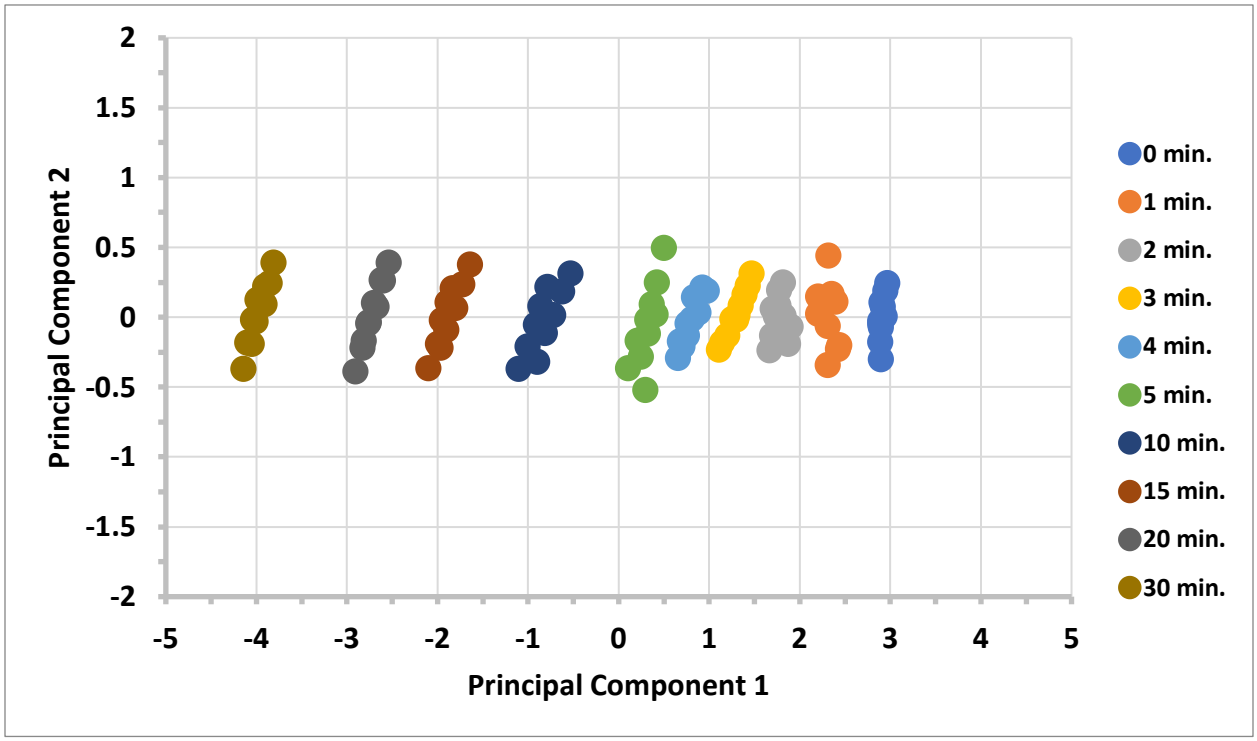

Figure 96: PCA score plot for irradiated *E. coli*.

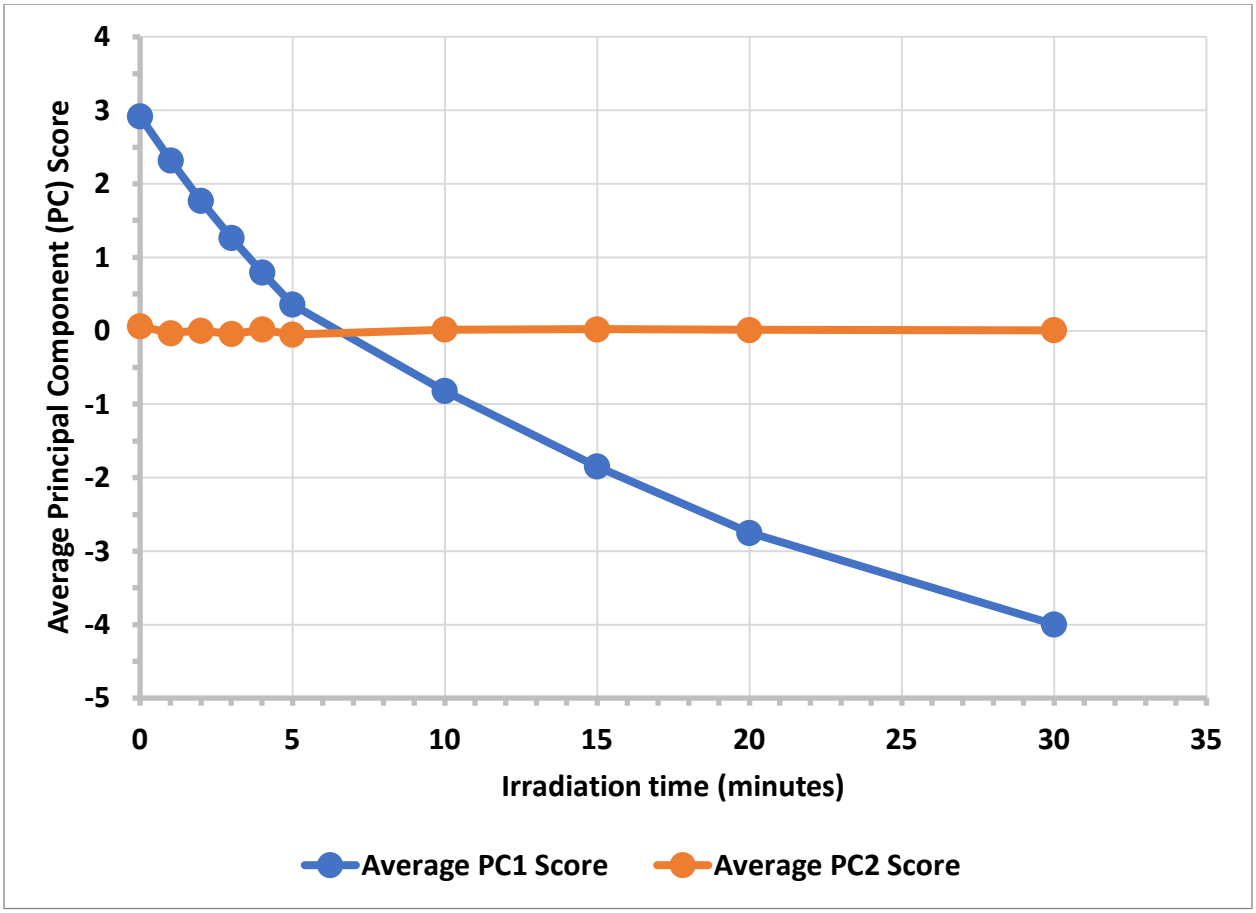

Figure 97: Average PC1 and PC2 scores as a function of irradiation time for *E. coli*.

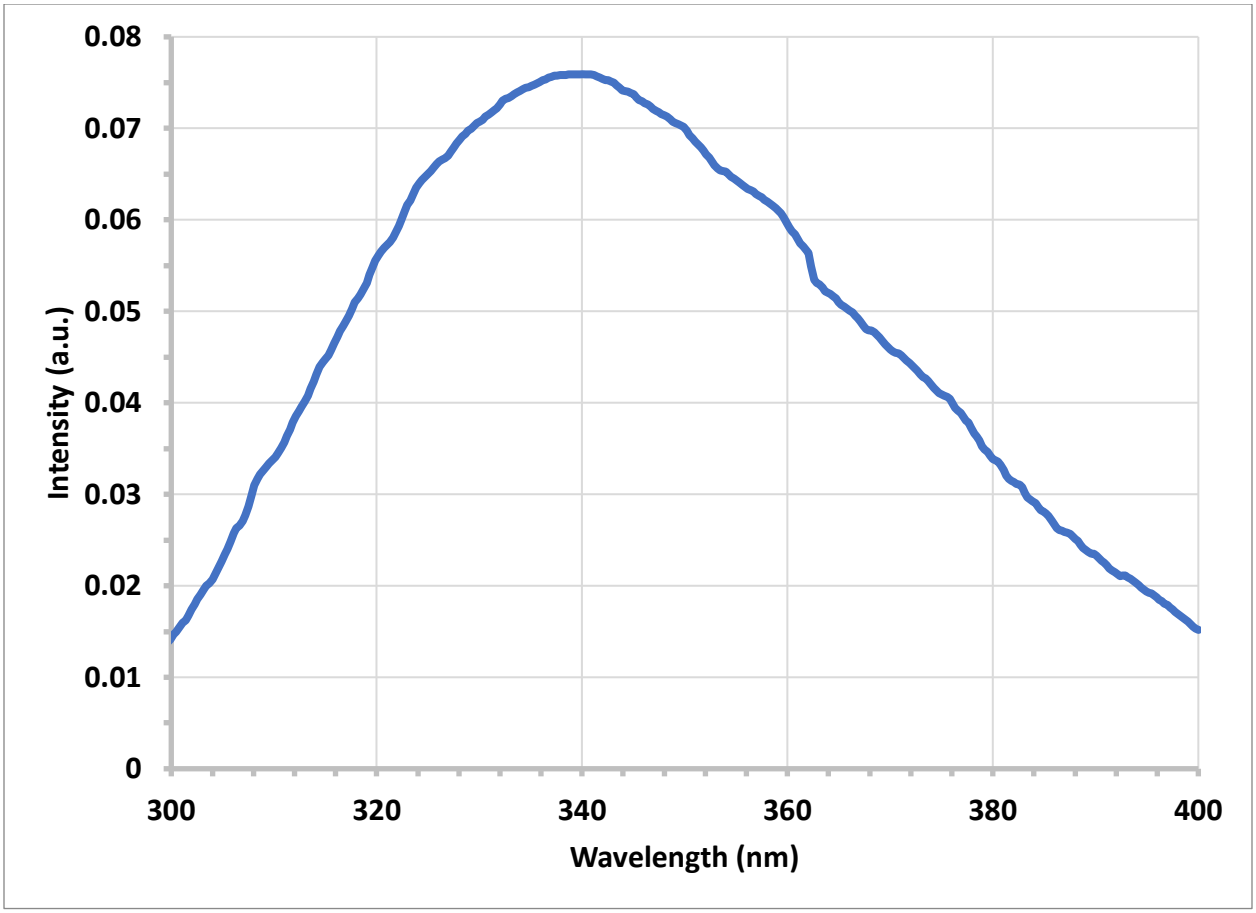

Figure 98: Plot of principal component 1 for *E. coli*.

Identification of bacterial strains

Our portable instrument may also enable the immediate identification of bacterial strains through PCA processing of the fluorescence spectra. To that effect, the fluorescence spectra of the bacterial strains *B. thuringiensis*, *E. coli*, and their mixture were recorded and subjected to PCA over the range of ~ 300 to 500 nm. The normalized fluorescence spectra and PCA score plot are provided in Figure 99 and Figure 100, respectively. The data from at least three independent experiments were normalized to the fluorescence band maximum and utilized for the analysis.

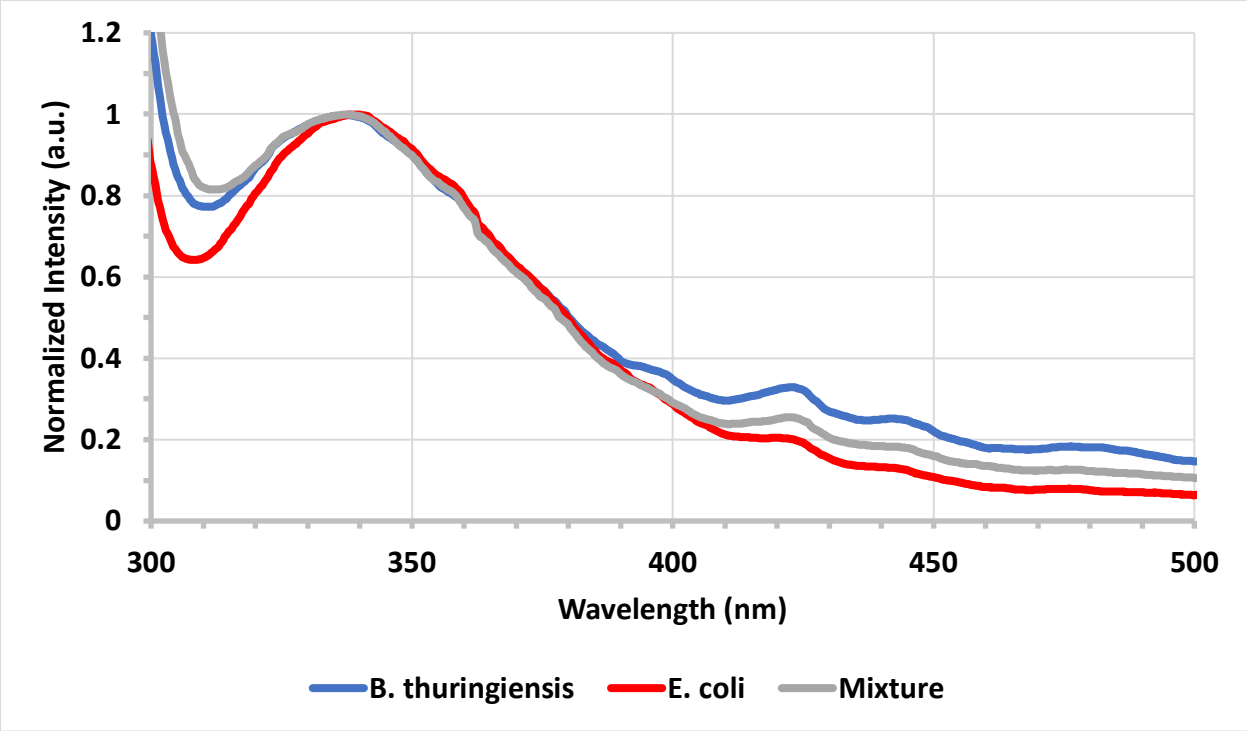

Figure 99: Normalized fluorescence spectra of *B. thuringiensis*, *E. coli*, and their mixture.

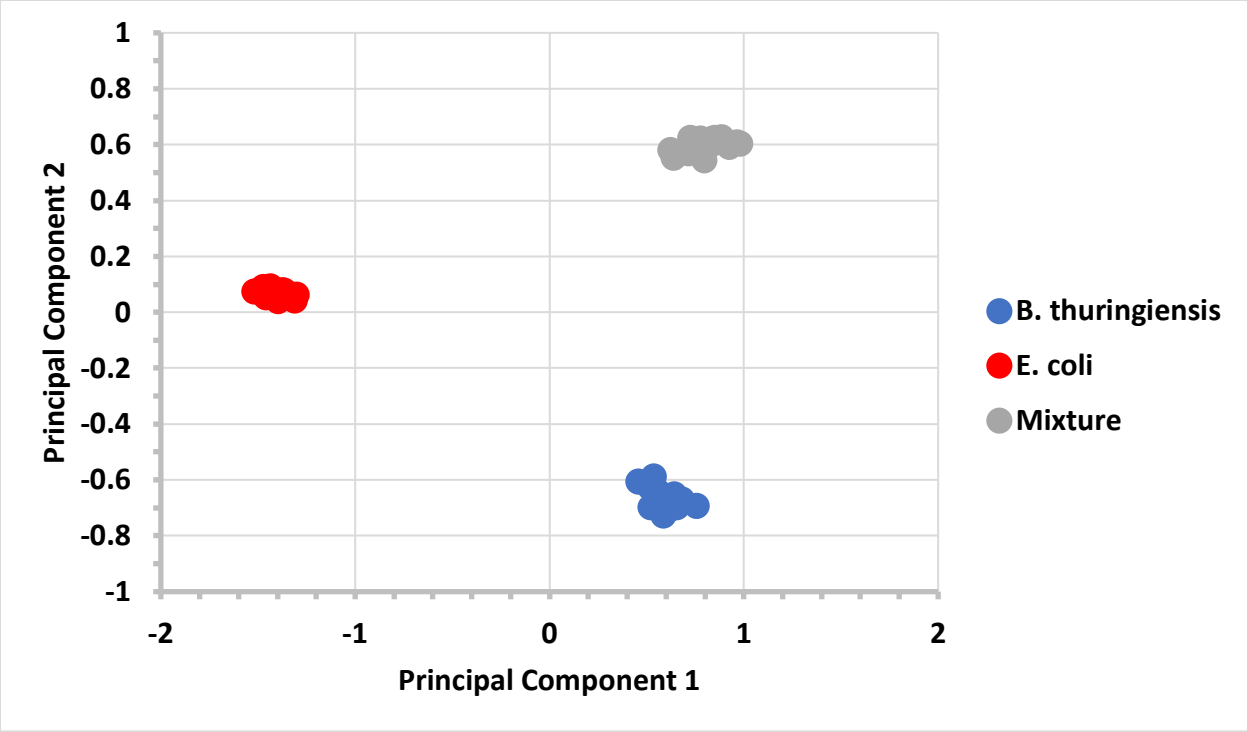

Figure 100: PCA score plot for identification of *B. thuringiensis*, *E. coli*, and their mixture.

Following PCA processing, a clear separation between *B. thuringiensis*, *E. coli*, and their mixture is observed in the score plot displayed in Figure 100. A close inspection of the normalized bacterial spectra in Figure 99 reveals differences between the spectra with respect to the wavelength of the fluorescence band maximum, along with the normalized fluorescence intensity in several regions. For example, *B. thuringiensis* displays a higher normalized fluorescence intensity than *E. coli* at longer wavelengths, ~ 400 to 500 nm, in addition to a somewhat shorter wavelength of peak fluorescence intensity. These changes are commensurate with the principal component plots of PC1 and PC2 provided in Figure 101.

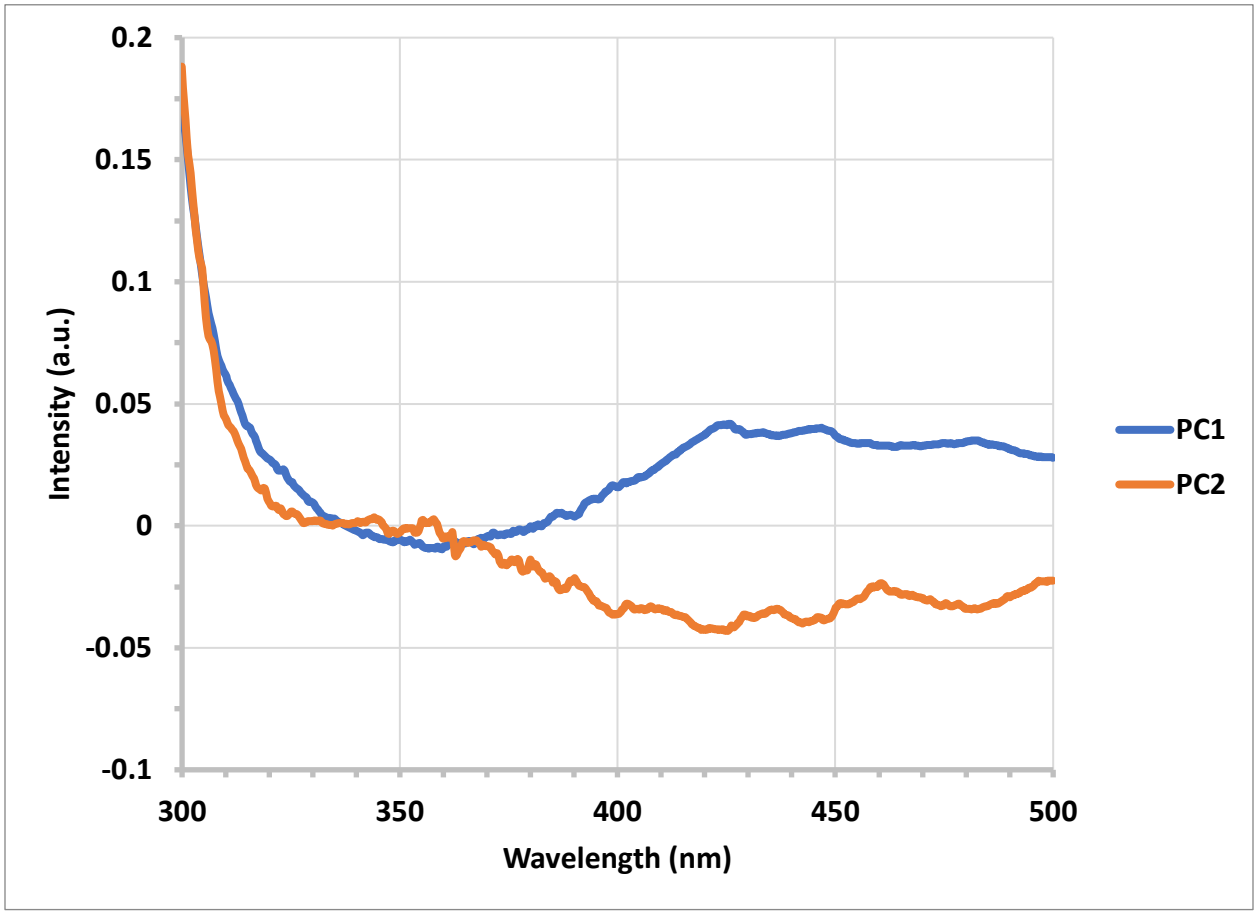

Figure 101: Plots of principal component 1 and 2 for bacterial strain identification.

The PCA results suggest that the fluorescence spectra of *B. thuringiensis* and *E. coli* possess detectable differences that may be utilized for the rapid, *in-situ* identification of each bacterial strain. Interestingly, these results additionally suggest that the fluorescence spectrum of the mixture is distinct from that of the constituent *B. thuringiensis* and *E. coli* strains. The ability to identify and distinguish various mixtures of bacteria, in addition to single strains, could prove to be very helpful in determining what inactivating agents, such as specific antibiotics, are the most effective for a given bacterial infection. Further work is required in recording the fluorescence and synchronous fluorescence spectra of additional bacteria and mixtures in order to assess the capabilities and limitations of this method.

Raman Spectra

Materials Identification

To validate the construction and operation of the Raman excitation module, we recorded the Raman spectra of several molecules with our portable instrument. This was achieved by coupling the emission monochromator and Raman excitation module subsystems. To that effect, the Raman spectra of water, methanol, ethanol, isopropanol, and acetone recorded by the portable instrument (integration time: 5 seconds; averaging: 10 scans), in addition to those recorded by the benchtop Raman spectrometer (integration time: 2 seconds; averaging: 5 scans), are shown in Figure 102 through Figure 111.

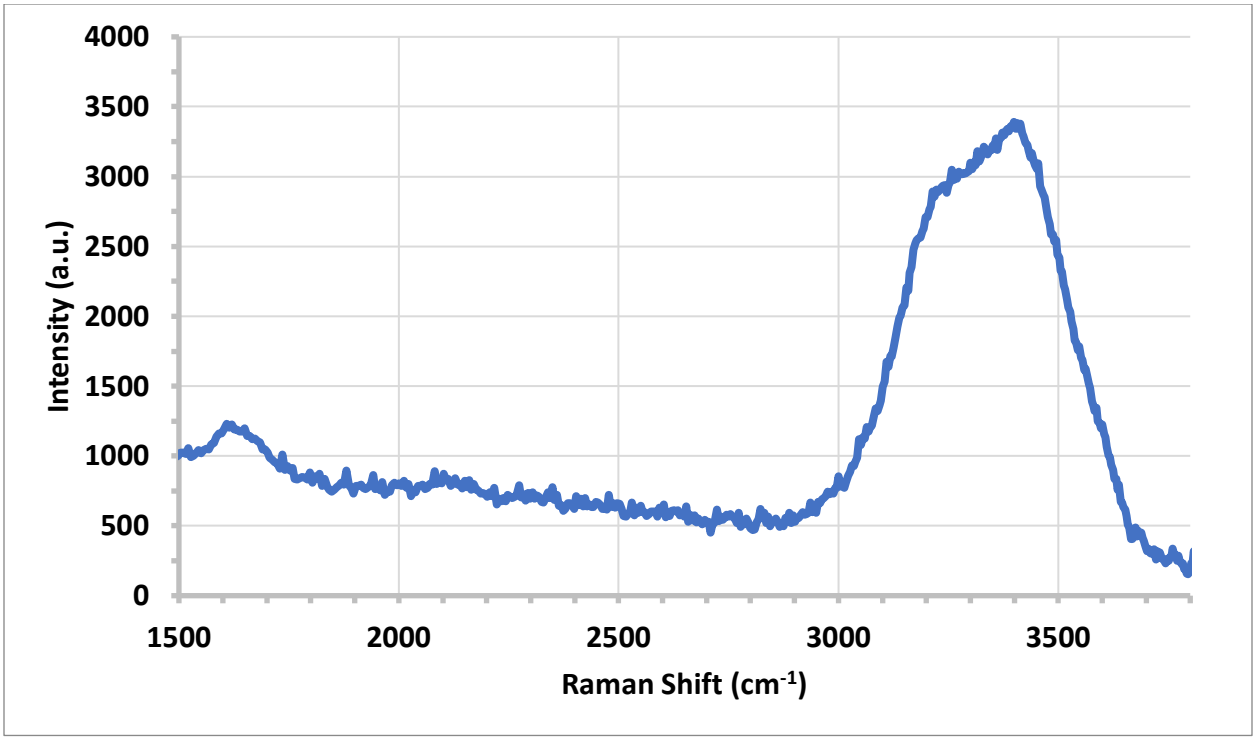

Figure 102: Raman spectrum of water (H_2O) recorded by portable instrument.

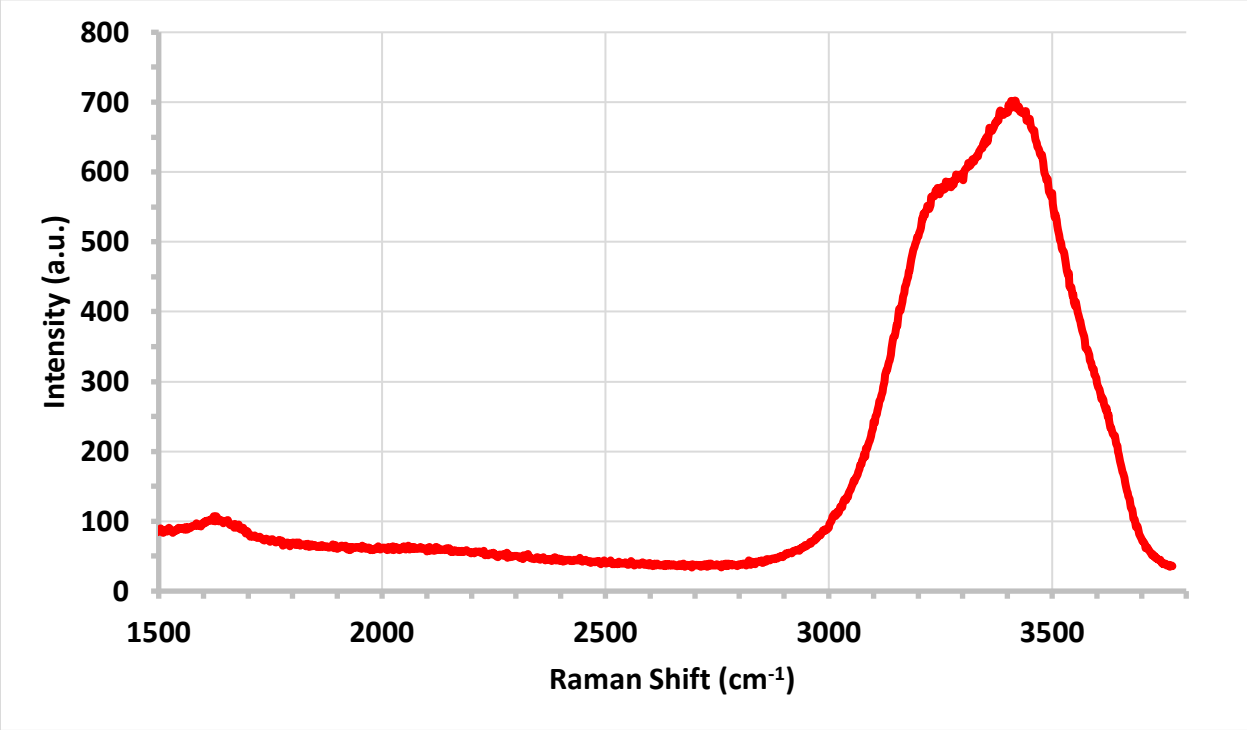

Figure 103: Raman spectrum of water (H_2O) recorded by benchtop instrument.

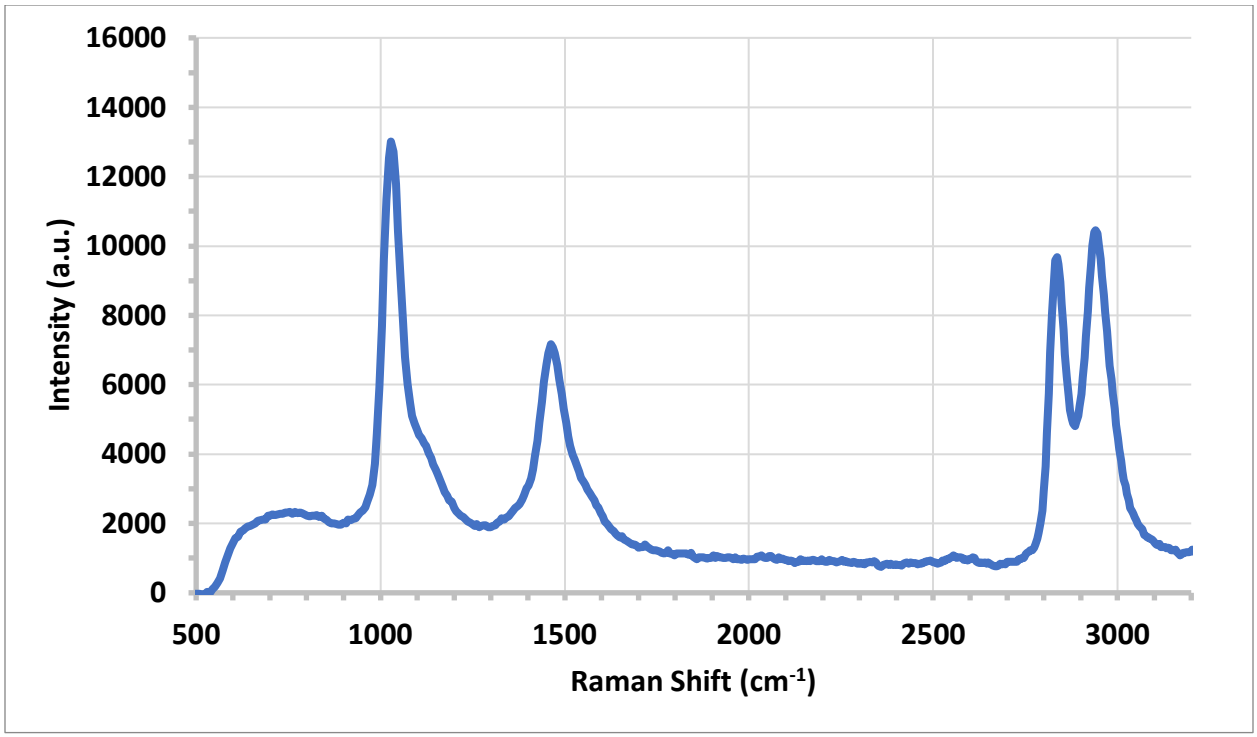

Figure 104: Raman spectrum of methanol (CH_3OH) recorded by portable instrument.

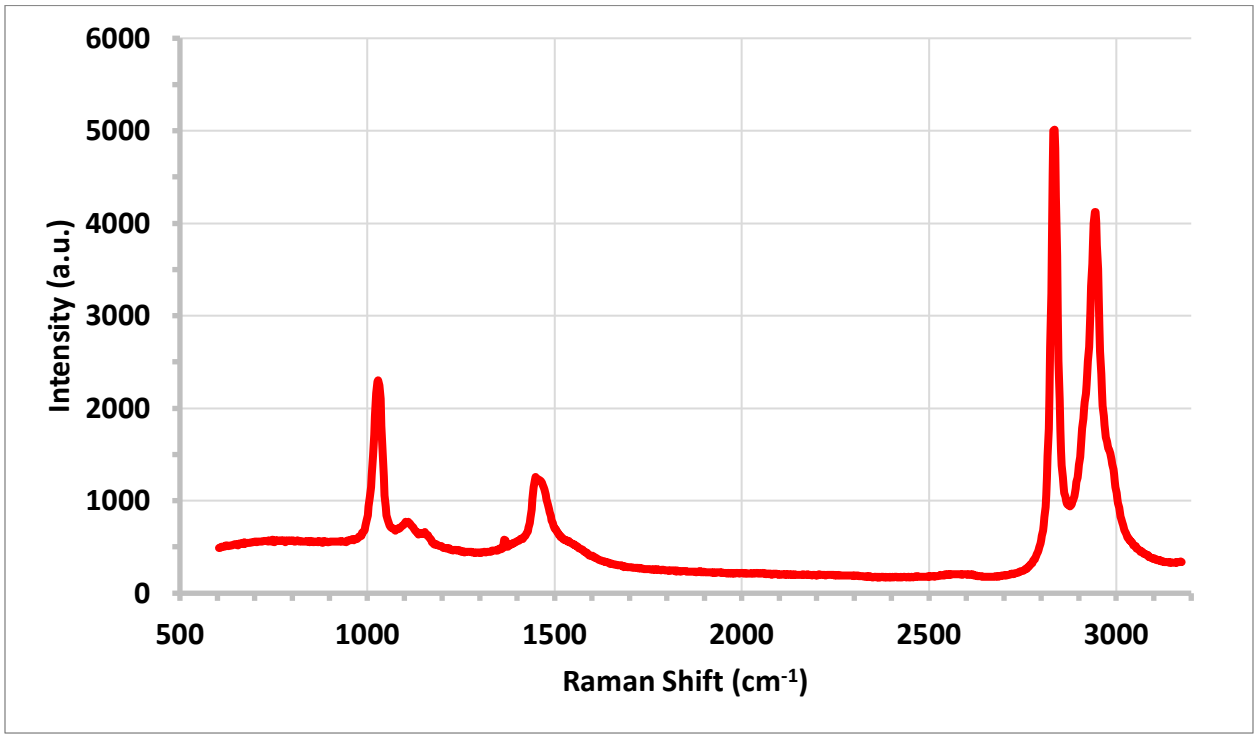

Figure 105: Raman spectrum of methanol (CH_3OH) recorded by benchtop instrument.

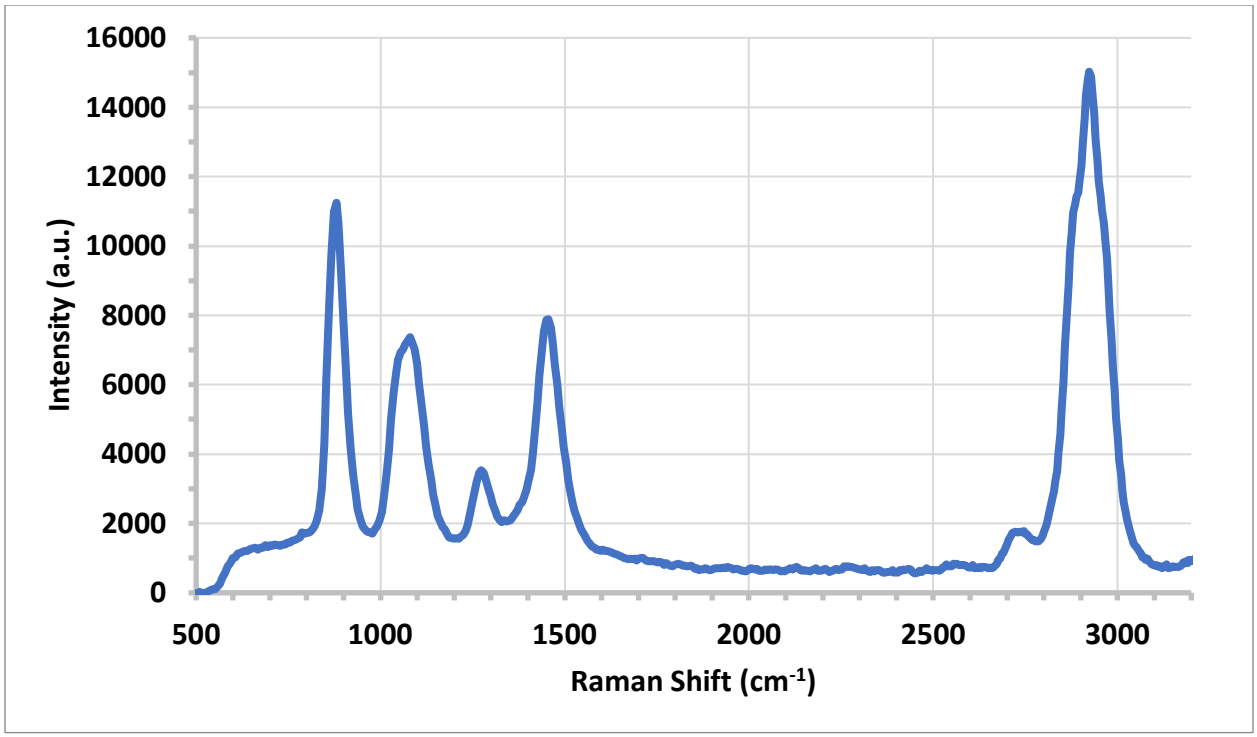

Figure 106: Raman spectrum of ethanol (C_2H_5OH) recorded by portable instrument.

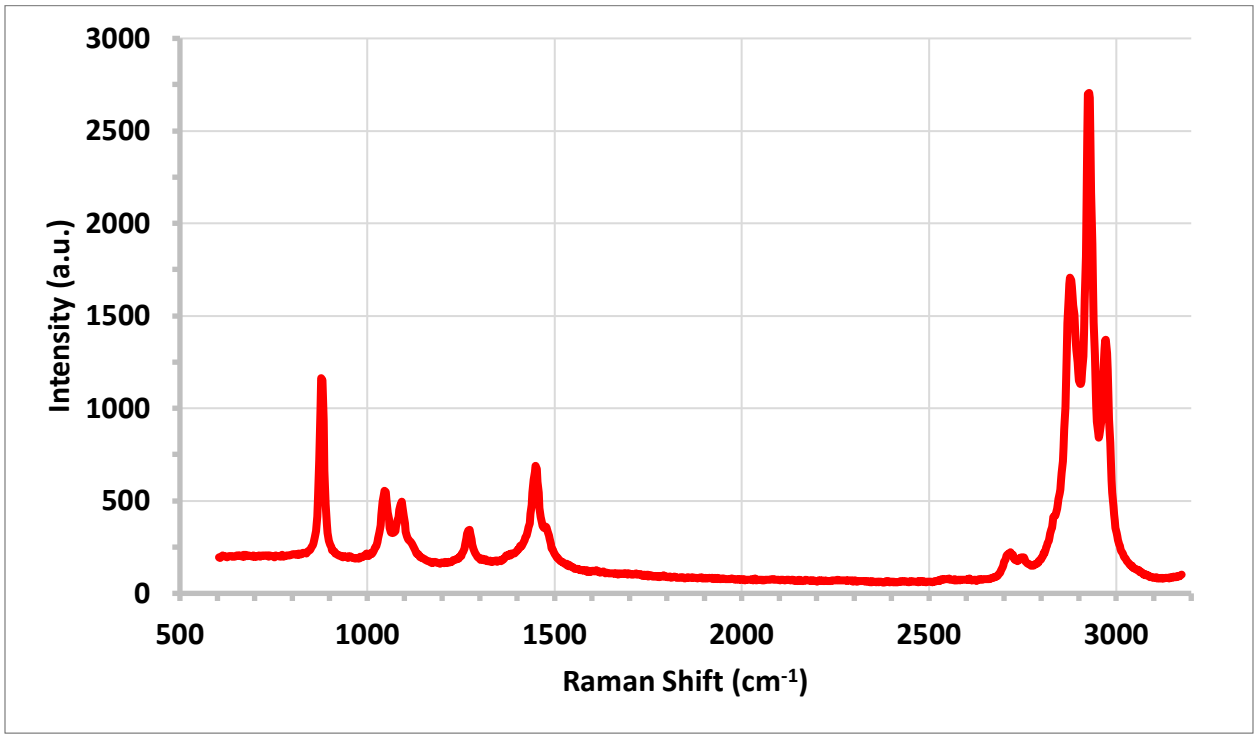

Figure 107: Raman spectrum of ethanol (C_2H_5OH) recorded by benchtop instrument.

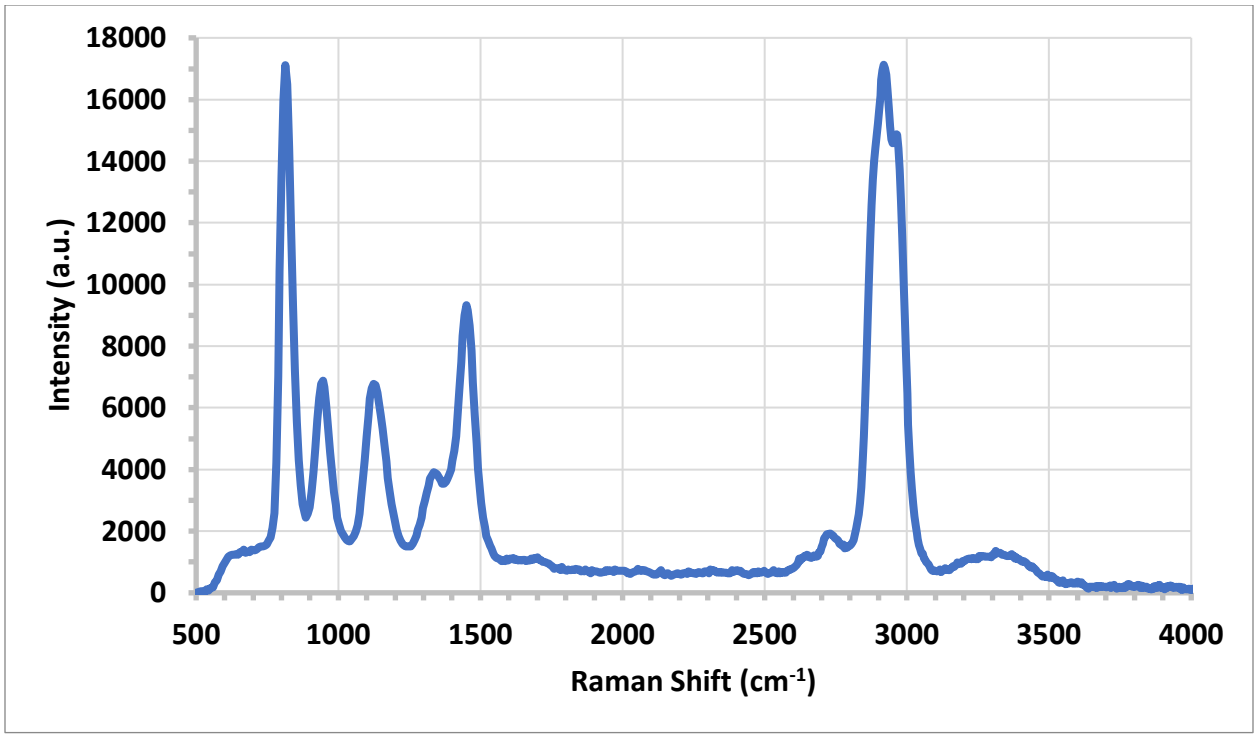

Figure 108: Raman spectrum of isopropanol (C_3H_8O) recorded by portable instrument.

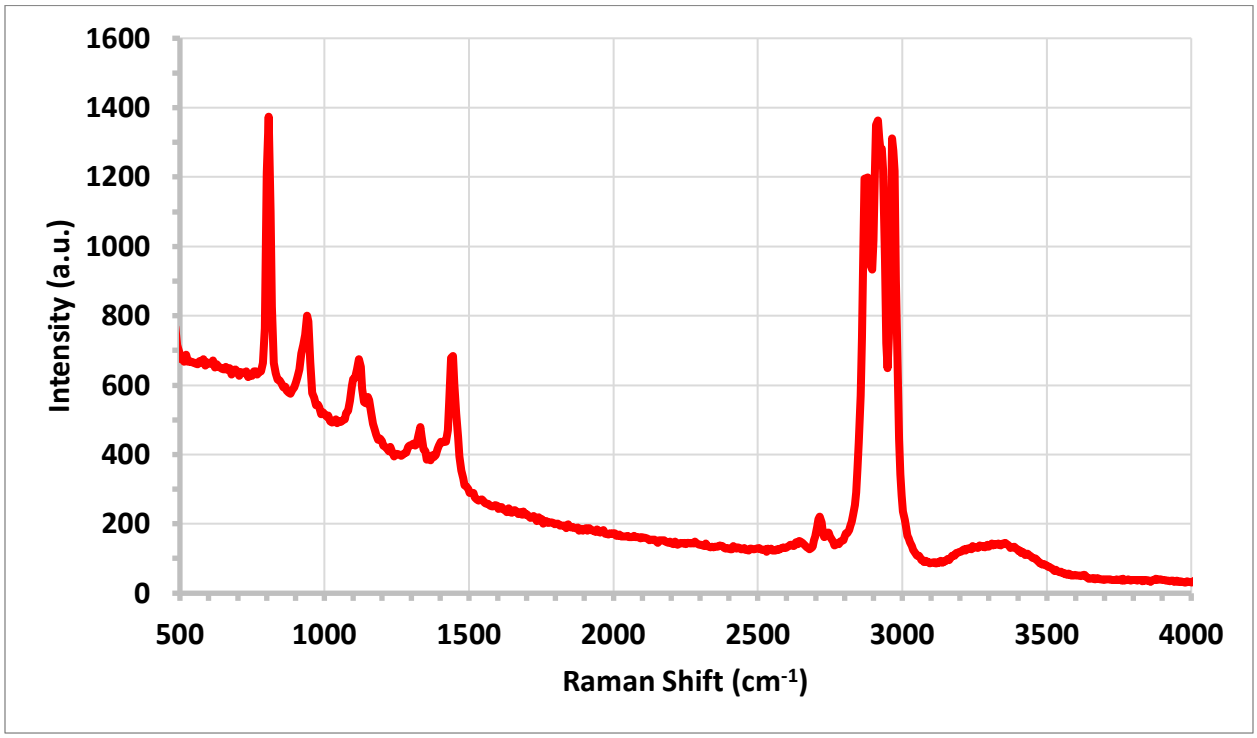

Figure 109: Raman spectrum of isopropanol (C_3H_8O) recorded by benchtop instrument.

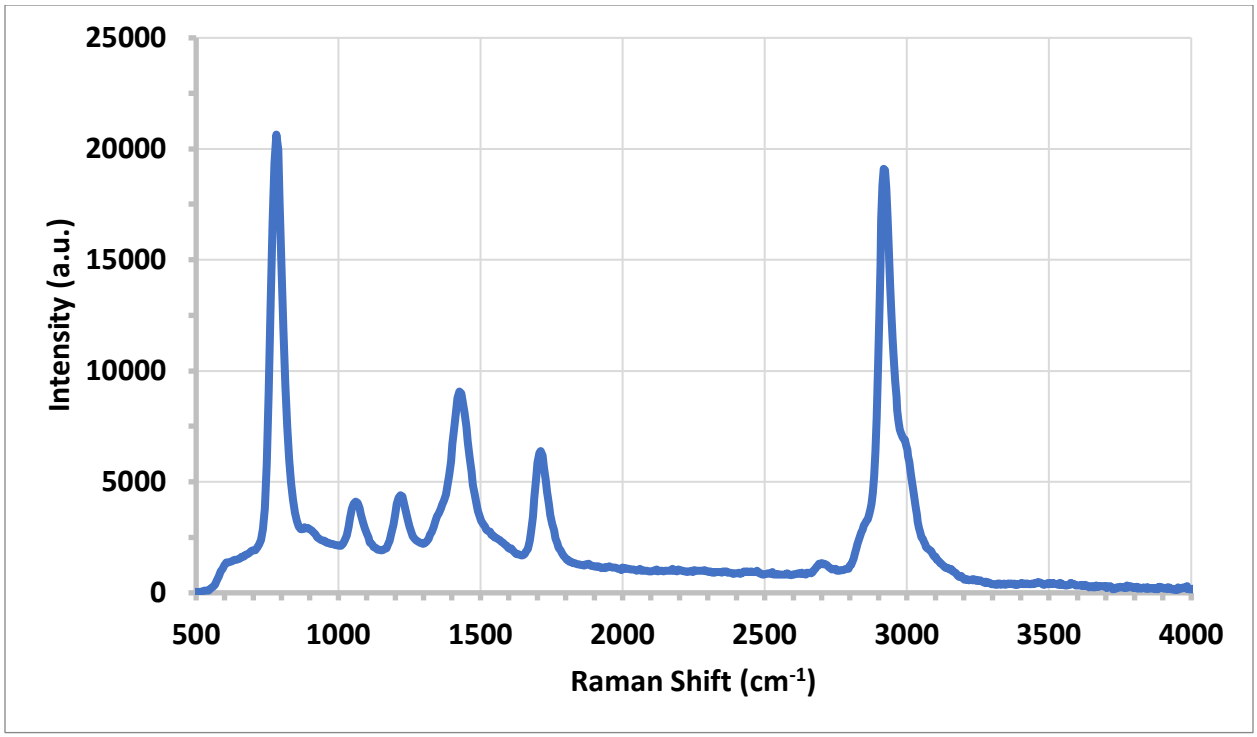

Figure 110: Raman spectrum of acetone (C_3H_6O) recorded by portable instrument.

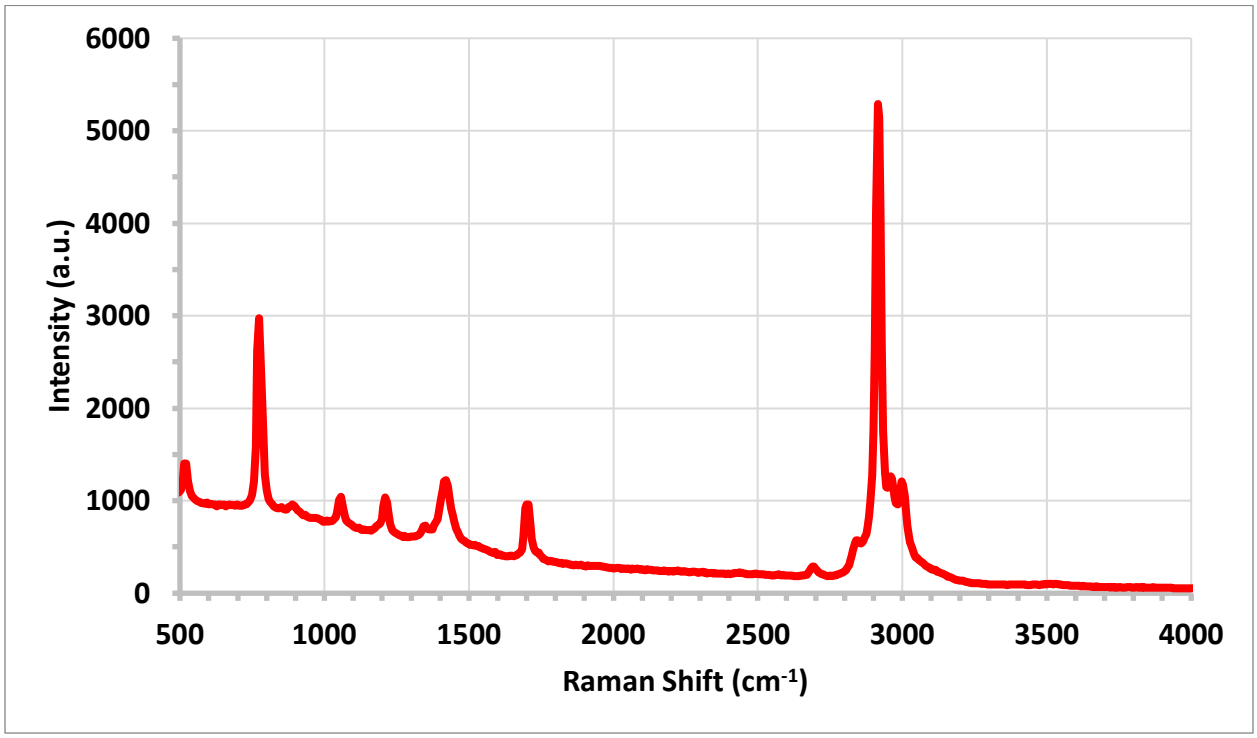

Figure 111: Raman spectrum of acetone (C_3H_6O) recorded by benchtop instrument.

The Raman spectra recorded by the portable and benchtop instruments are practically identical and display the characteristic vibrational bands of several chemical bonds and groups, including $-OH$ (hydroxyl), $C=O$ (carbonyl), $-CH_3$ (methyl), $C-C$, and $C-O$, among others. A more detailed assignment of these bands may be obtained through the literature or appropriate databases. It is worth noting that while the current resolution of the portable instrument ($dR \sim$ 70.4 cm^{-1}) prevents certain Raman bands from necessarily being resolved, the most prominent, intense Raman bands are clearly detected and distinguished between each of the molecules. These results demonstrate the utility of Raman spectroscopy in obtaining a unique chemical fingerprint for a molecule based on its vibrational modes.

To further investigate the application of Raman spectroscopy in materials identification, we subjected the Raman spectra of water, methanol, ethanol, isopropanol, and acetone to PCA over the range of $\sim$ 500 to 4000 cm^{-1}. The normalized Raman spectra for these chemicals, along with the 2D and 3D PCA score plots, are provided in Figure 112 through Figure 114. The data from at least ten independent measurements were background subtracted and normalized to the peak intensity for the analysis.

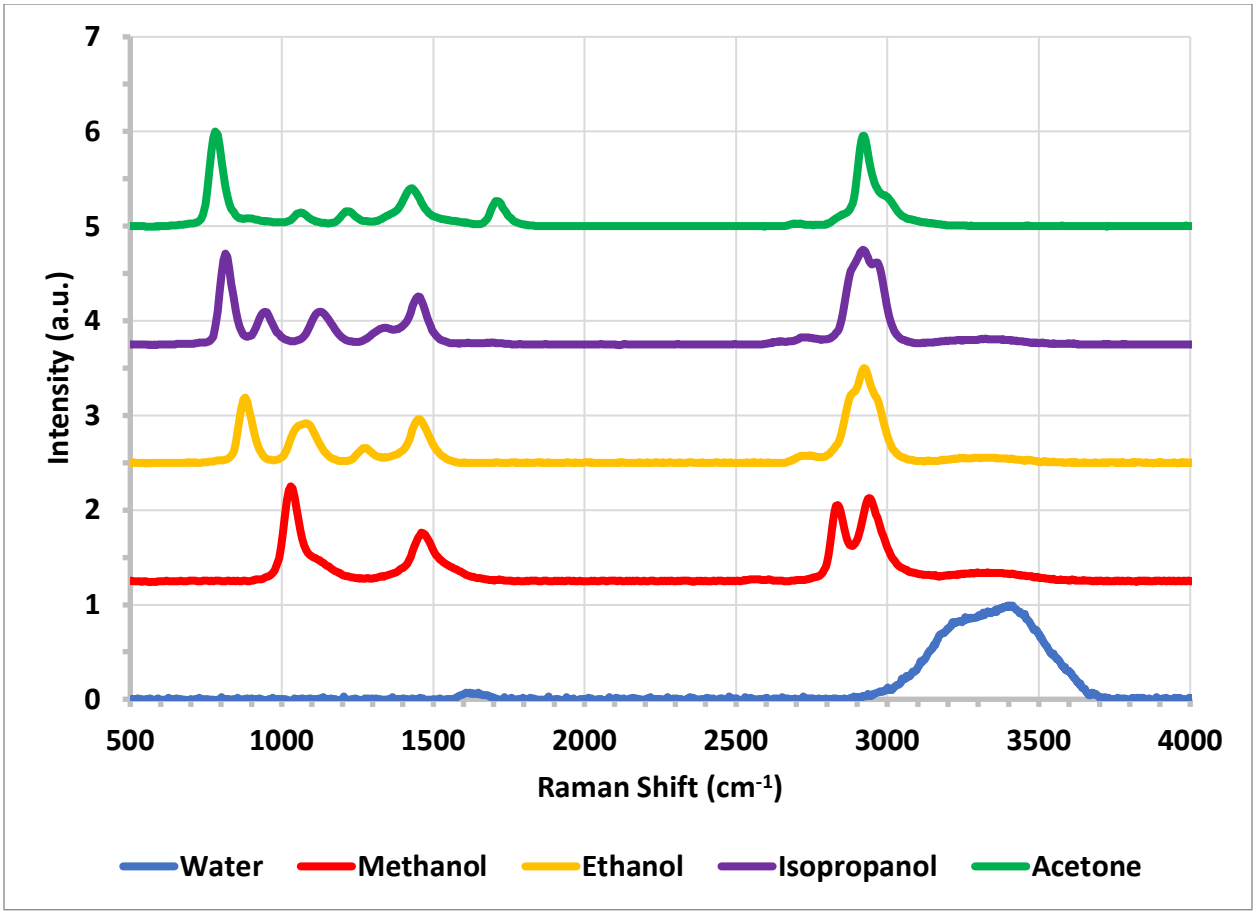

Figure 112: Normalized Raman spectra for performing materials identification.

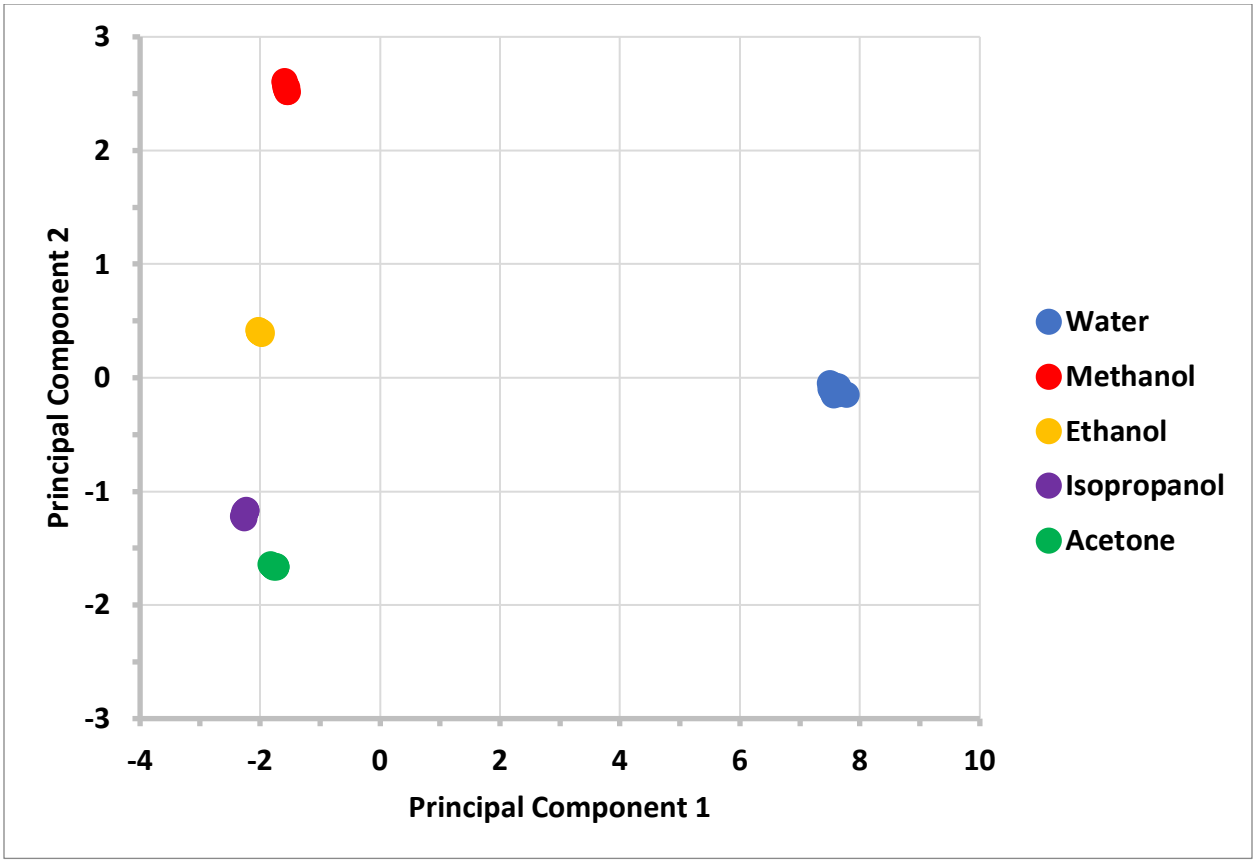

Figure 113: 2D PCA score plot of Raman spectra for materials identification.

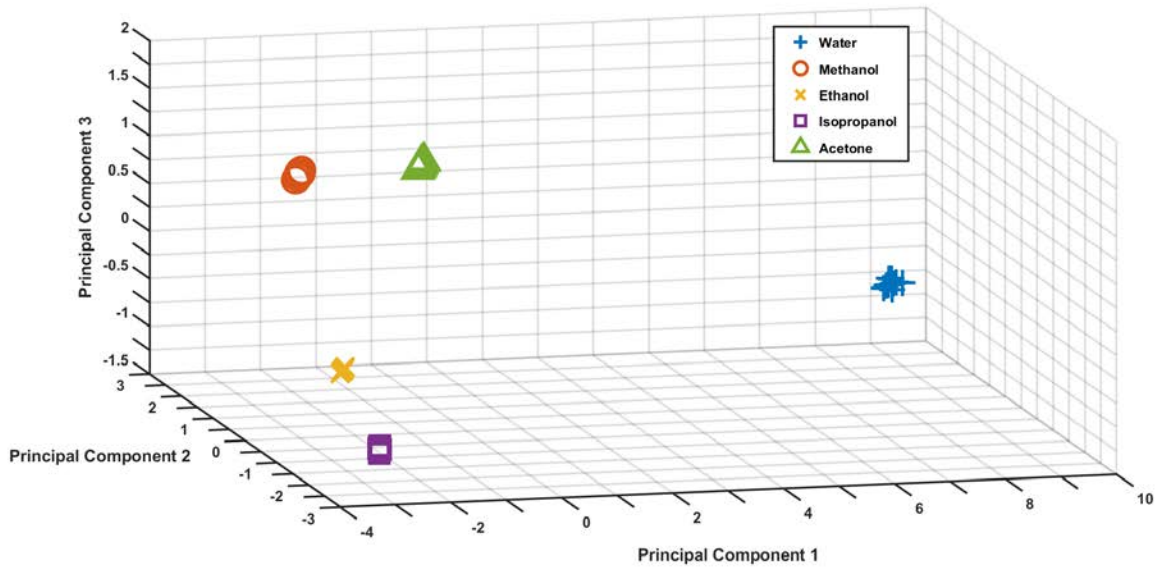

Figure 114: 3D PCA score plot of Raman spectra for materials identification.

A prominent separation between each chemical along the PC1 and PC2 axes is observed in the 2D PCA score plot. Additionally, plotting in three dimensions, with PC1, PC2, and PC3, resulted in more pronounced separation. In particular, the separation between acetone and isopropanol increased significantly in the 3D, compared to 2D, PCA score plot, owing to the additional variation captured along the PC3 axis. In fact, it was found that practically all variation in the original Raman spectra was attributed to as high as four principal components during this analysis. To that effect, the principal component plots for PC1, PC2, PC3, and PC4 are depicted in Figure 115 through Figure 118.

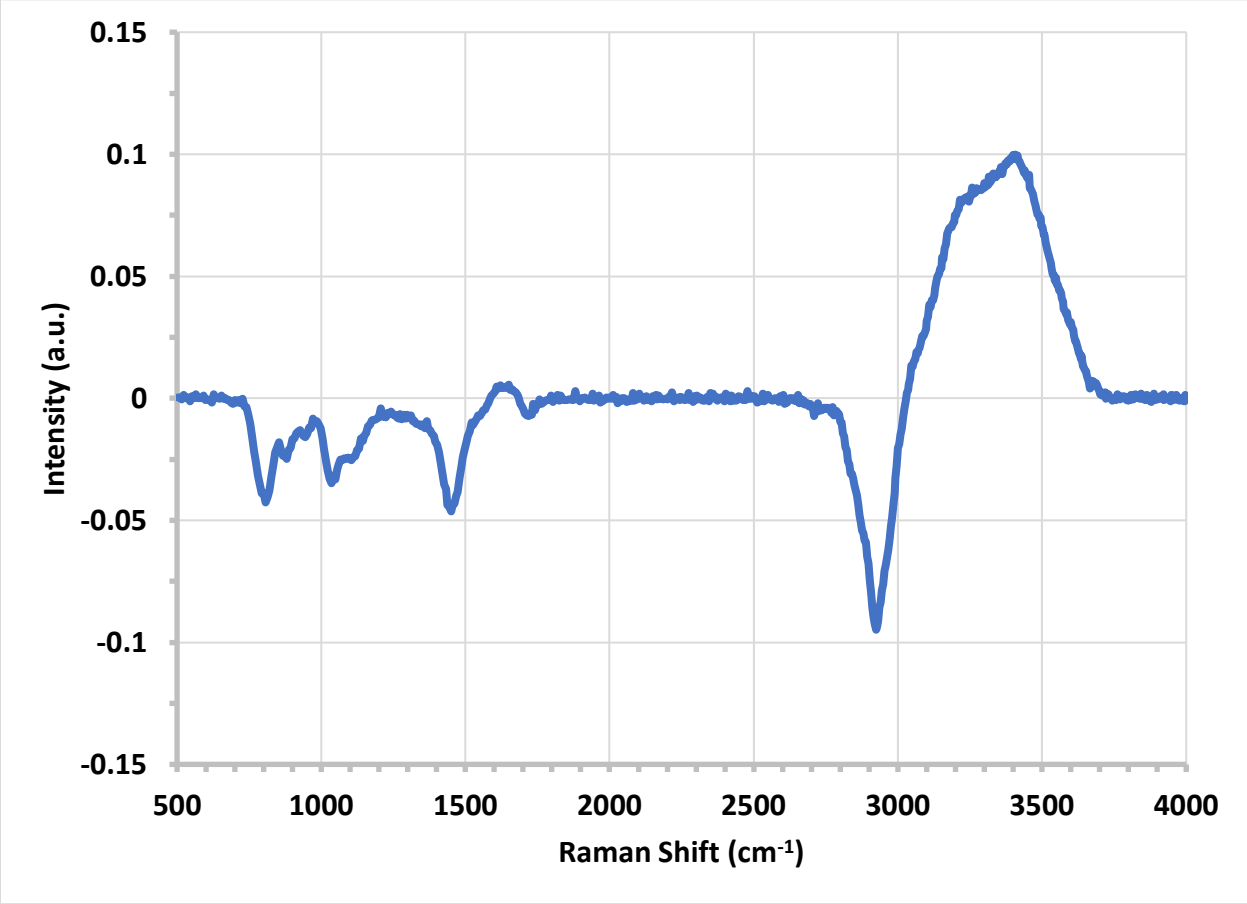

Figure 115: Plot of principal component 1 for materials identification.

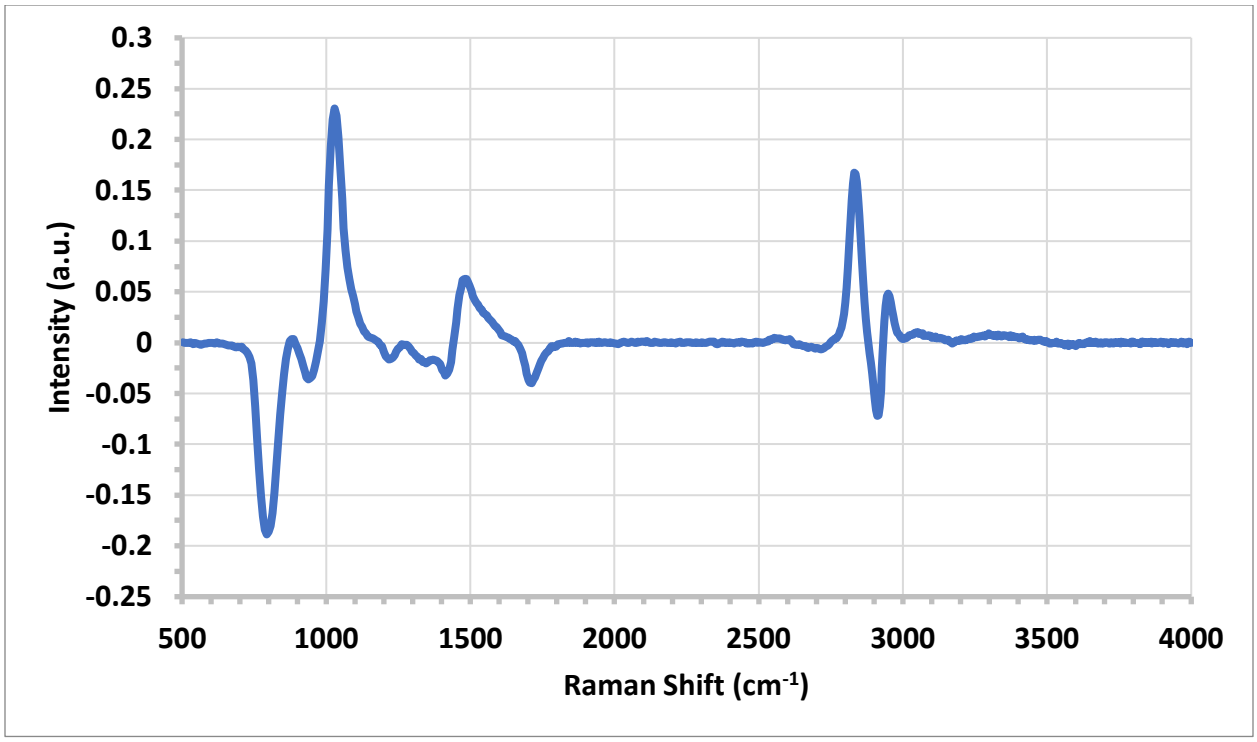

Figure 116: Plot of principal component 2 for materials identification.

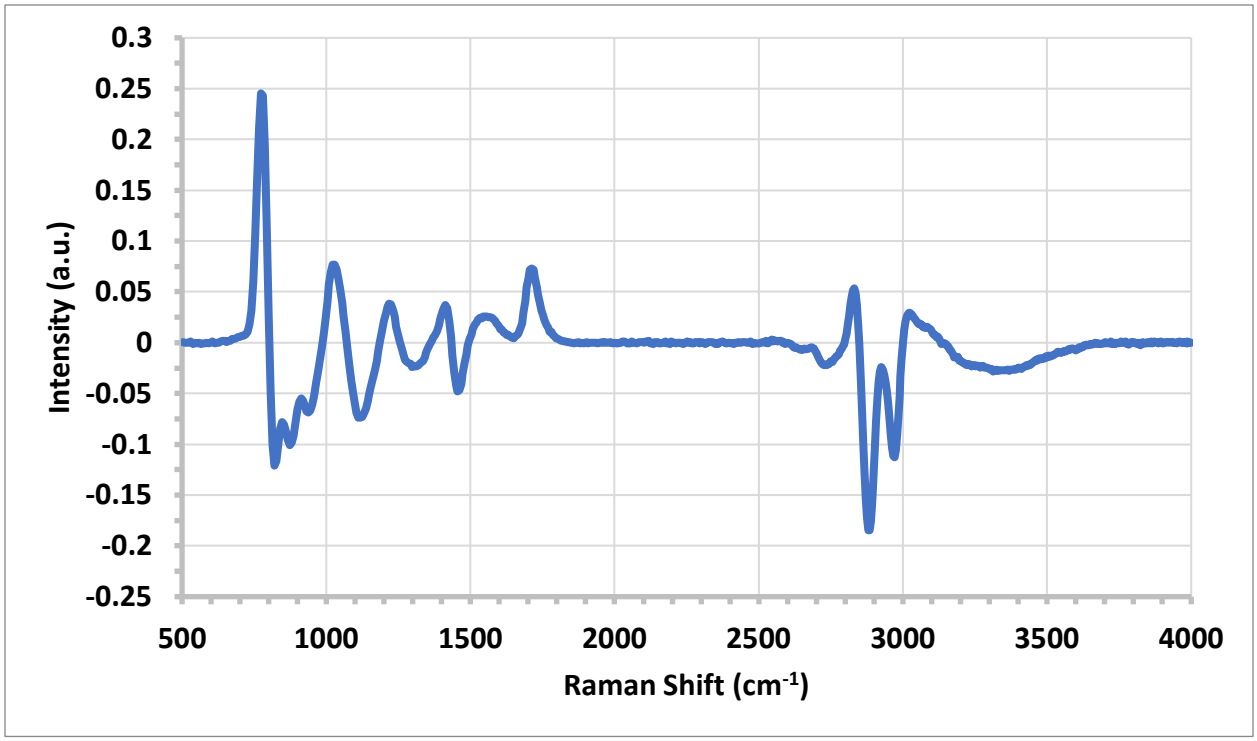

Figure 117: Plot of principal component 3 for materials identification.

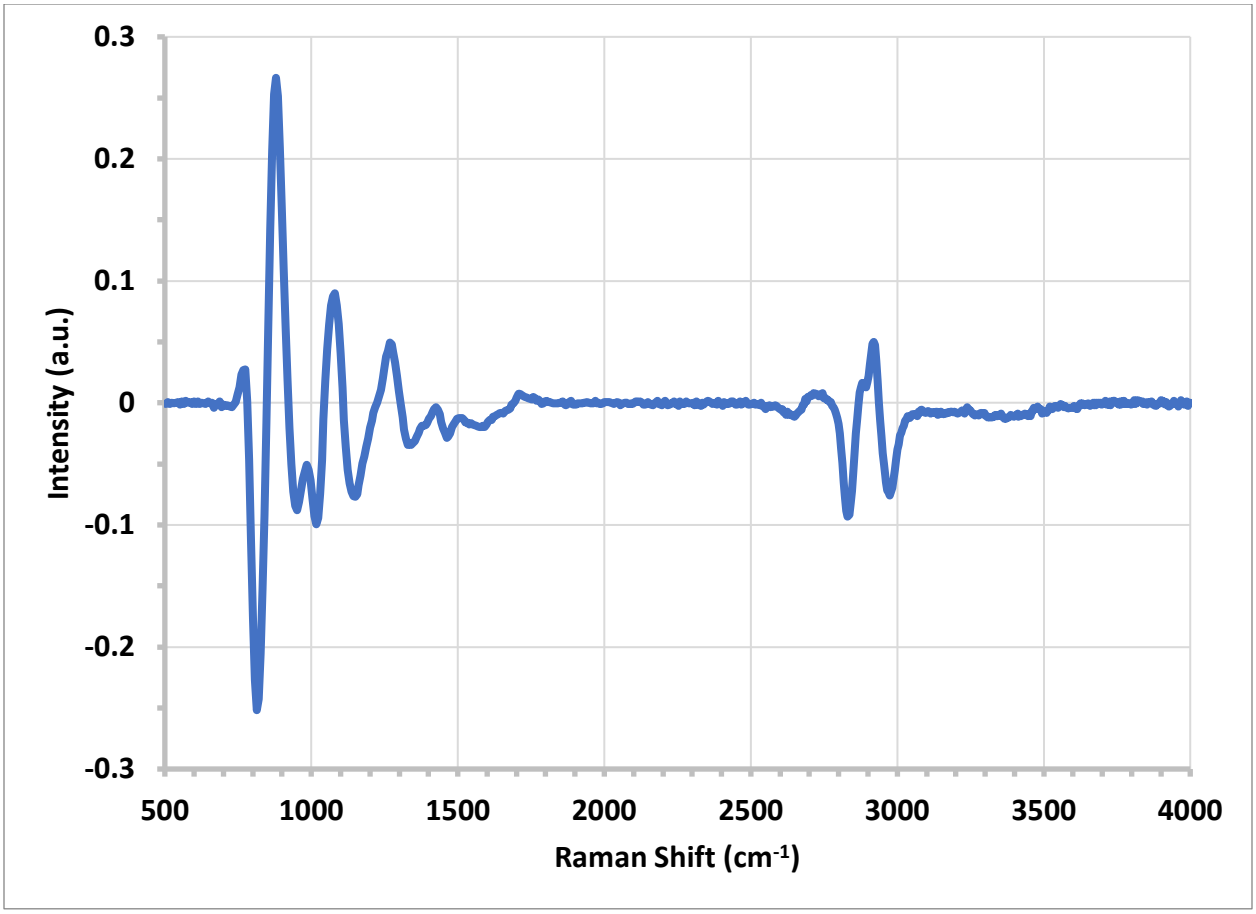

Figure 118: Plot of principal component 4 for materials identification.

These principal component plots provide additional information regarding the separation between each chemical in the 2D and 3D PCA score plots. Specifically, the regions of variation, or differences, in the Raman spectra, captured along each respective principal component axis, may be deduced. For example, the PC1 plot most prominently displays the rather broad $-OH$ stretching band at ~ 3400–3600 cm^{-1}, composed of symmetric and asymmetric vibrational modes [90], in addition to the CH_2 and CH_3 stretching modes at ~ 2800–3100 cm^{-1} [91]. Additional structural information is obtained by plotting PC2, whereupon the $C-C$ and $C-O$ stretching modes at ~ 787 cm^{-1} and ~ 1036 cm^{-1}, respectively, are clearly displayed [90, 92]. The PC3 and PC4 plots reveal additional low-frequency, ~ 700–1500 cm^{-1}, Raman bands, which

further differentiate each chemical. Whereas fluorescence spectra are relatively simple and generally unimodal distributions whose variation can be captured within a few principal components, Raman spectra may require a higher number of principal components in order to fully describe their variation. For molecules with many Raman bands, such PCA processing may require plotting various combinations of the principal components in both 2D and 3D principal component space to achieve useful separation. Consequently, Raman spectra possess a tremendous amount of molecular and structural information that, when coupled with PCA, may support the identification of various materials in the solid, liquid, or gas state of matter. These results suggest that our portable spectroscopic instrument may be utilized for rapid, *in-situ* materials identification with applications in the chemical, pharmaceutical, and food industry, among many others [93–94]. Such applications could involve creating an appropriate database of Raman spectra that is integrated with our portable instrument and PCA.

Bacterial Detection

The Raman capabilities of our portable instrument were further tested by recording the Raman spectrum of *S. marcescens*, which is a Gram-negative bacterium that produces the red pigment prodigiosin under certain growth conditions [67], thus causing the bacterial cells to be colored. The amount of pigmentation is a function of various growth and environmental factors [67, 95]. Prodigiosin ($C_{20}H_{25}N_3O$) is a large molecule with a high degree of conjugation and an absorption band maximum of $\sim$ 535 nm in neutral pH [67, 96–97]. The rather high absorption of prodigiosin in the visible region, $\sim$ 400–600 nm, results in its red pigmentation. This suggests that excitation in the green region, at a wavelength near the absorption band maximum of prodigiosin, may provide a resonant enhancement of its vibrational bands by orders of magnitude. Such an excitation range is rather ideal for our Raman excitation module, owing to

its laser source emitting at 532 nm. To that effect, the resonance Raman spectrum of red *S. marcescens* recorded by the portable instrument (integration time: 1 second; averaging: 20 scans), along with that recorded by the benchtop Raman spectrometer (integration time: 1 second; averaging: 10 scans), are shown in Figure 119 and Figure 120, respectively.

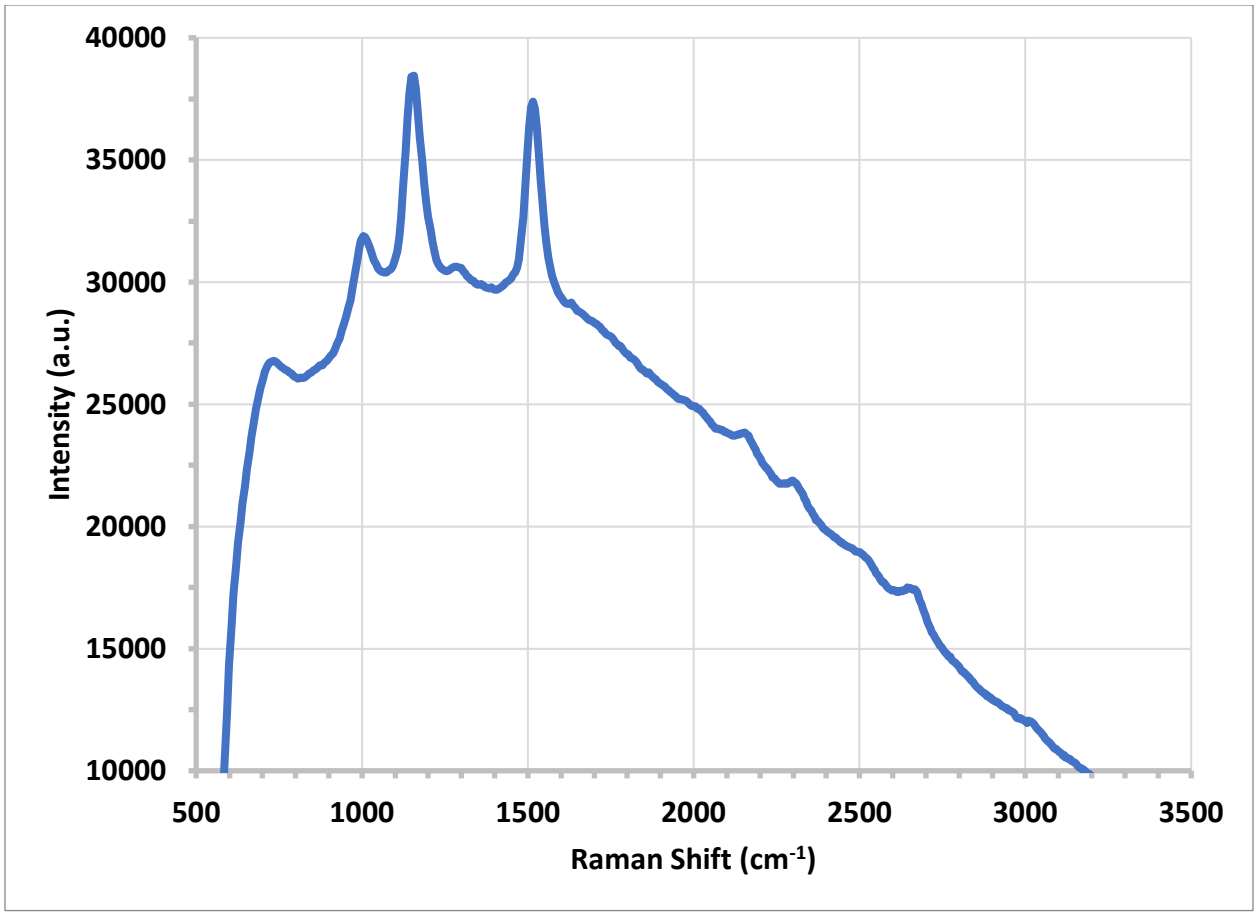

Figure 119: Resonance Raman spectrum of red *S. marcescens* recorded by portable instrument.

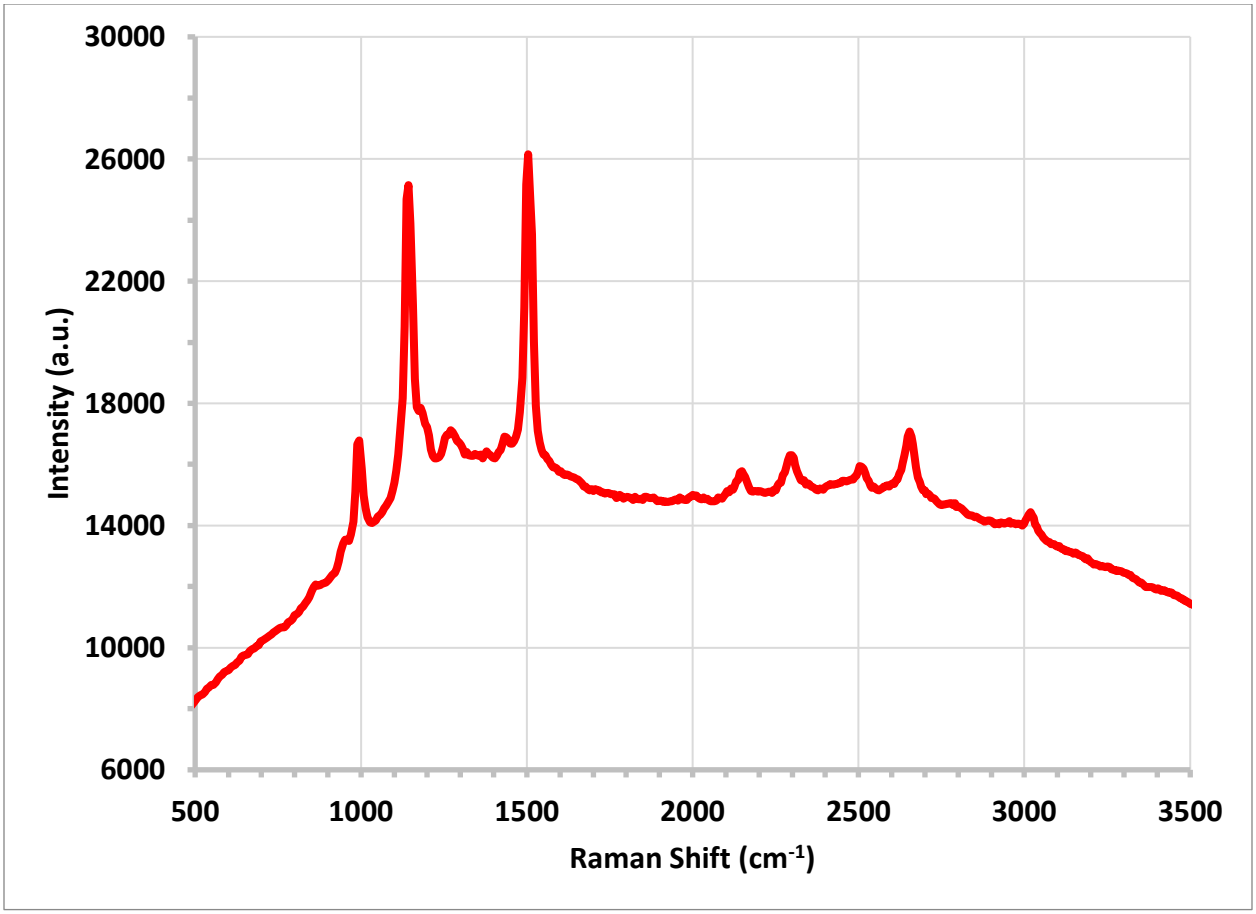

Figure 120: Resonance Raman spectrum of red *S. marcescens* recorded by benchtop instrument.

The vibrational bands of prodigiosin (~ 1016, 1156, and 1521 cm^{-1}) are clearly distinguishable in the resonance Raman spectra recorded by both the portable and benchtop instruments, which demonstrate the enhancement of its Raman signal under resonant conditions. It may be observed that the Raman spectra are superimposed on the fluorescence background of the pigment itself, which may be easily removed through background subtraction to obtain the corrected Raman band intensities. The most intense, ~ 1156 and 1521 cm^{-1}, bands may be assigned to the stretching modes of $C-C$ and $C=C$, which correspond to the conjugated chain in prodigiosin, while the weaker band at ~ 1016 cm^{-1} is due to the in-plane rocking modes of CH_3 groups attached to the conjugated chain [32–33]. It is rather interesting to note that several other

bacteria, including *Micrococcus luteus*, *Vibrio cholerae*, and *Staphylococcus aureus*, also produce pigments that serve as a defense mechanism against oxidative stress and UV light exposure, in addition to strengthening the integrity of the cell membrane [32, 68, 98–99]. It may even be possible that the inactivation of bacteria can be correlated with damage to its pigments [33]. Such pigments also possess broad absorption bands from the visible to UVA region, owing to their conjugation, which may be exploited via resonance Raman for the enhancement of their vibrational spectra. In fact, the wavenumber positions of the $C-C$ and $C=C$ vibrational bands depend on the conjugated chain length [32] and may therefore be an indicator of the pigment and the bacterial strain. To that effect, our portable spectroscopic instrument may enable the studies and identification of various pigmented bacteria, *in-situ* within minutes, by means of both fluorescence and resonance Raman spectroscopy. When modified with the appropriate laser source, longpass filter, and diffraction grating, this instrument may also permit the usage of additional enhancement mechanisms, including UV resonance Raman (UVRR) and surface-enhanced Raman spectroscopy (SERS) [100], for the selective enhancement of bacterial Raman bands.

CHAPTER VI

CONCLUSION

We have designed, constructed, and validated a portable spectroscopic instrument which is capable of recording the fluorescence, synchronous fluorescence, and Raman spectra of bacteria, biomolecules, and mixtures remotely. This instrument possesses the additional capabilities of UV disinfection and PCA processing of the recorded fluorescence and Raman spectra. We have employed this instrument to determine the mechanism of bacterial inactivation following UV irradiation by means of both a mercury lamp and UV LED. Fluorescence spectroscopy, synchronous fluorescence spectroscopy, and PCA were applied to identify bacterial strains and their components, in addition to distinguishing live and dead bacteria practically instantaneously, within minutes, compared to the days required using conventional procedures. In addition, Raman spectroscopy was utilized to record the vibrational spectra of chemicals and bacteria, which were subjected to PCA for rapid materials identification. To that effect, this instrument provides a novel, portable spectroscopic means for the detection and identification of live and dead bacteria *in-situ*.

REFERENCES

[1] Antibiotic Resistance: A Global Threat. (2018, September 19). Retrieved January 26, 2020, from https://www.cdc.gov/features/antibiotic-resistance-global/index.html

[2] Peleg, A. Y., & Hooper, D. C. (2010). Hospital-acquired infections due to gram-negative bacteria. *N Engl J Med, 362*(19), 1804-1813. doi:10.1056/NEJMra0904124

[3] McNamara, L. (2009). Health Care–Associated Infection. *American Journal of Critical Care, 18*(1), 41-41. doi:10.4037/ajcc2009483

[4] Hazan, R., Que, Y.-A., Maura, D., & Rahme, L. G. (2012). A method for high throughput determination of viable bacteria cell counts in 96-well plates. *BMC Microbiology, 12*(1), 259. doi:10.1186/1471-2180-12-259

[5] Sohn, M., Himmelsbach, D. S., Barton, F. E., 2nd, & Fedorka-Cray, P. J. (2009). Fluorescence spectroscopy for rapid detection and classification of bacterial pathogens. *Appl Spectrosc, 63*(11), 1251-1255. doi:10.1366/000370209789806993

[6] Leblanc, L., & Dufour, E. (2002). Monitoring the identity of bacteria using their intrinsic fluorescence. *FEMS Microbiol Lett, 211*(2), 147-153. doi:10.1111/j.1574-6968.2002.tb11217.x

[7] Ammor, S., Yaakoubi, K., Chevallier, I., & Dufour, E. (2004). Identification by fluorescence spectroscopy of lactic acid bacteria isolated from a small-scale facility producing traditional dry sausages. *J Microbiol Methods, 59*(2), 271-281. doi:10.1016/j.mimet.2004.07.014

[8] Helm, D., Labischinski, H., Schallehn, G., & Naumann, D. (1991). Classification and identification of bacteria by Fourier-transform infrared spectroscopy. *J Gen Microbiol, 137*(1), 69-79. doi:10.1099/00221287-137-1-69

[9] Zarnowiec, P., Lechowicz, L., Czerwonka, G., & Kaca, W. (2015). Fourier Transform Infrared Spectroscopy (FTIR) as a Tool for the Identification and Differentiation of Pathogenic Bacteria. *Curr Med Chem, 22*(14), 1710-1718. doi:10.2174/0929867322666150311152800

[10] Martak, D., Valot, B., Sauget, M., Cholley, P., Thouverez, M., Bertrand, X., & Hocquet, D.

(2019). Fourier-Transform InfraRed Spectroscopy Can Quickly Type Gram-Negative Bacilli Responsible for Hospital Outbreaks. *Frontiers in Microbiology, 10*(1440). doi:10.3389/fmicb.2019.01440

[11] Jarvis, R. M., & Goodacre, R. (2004). Discrimination of bacteria using surface-enhanced Raman spectroscopy. *Anal Chem, 76*(1), 40-47. doi:10.1021/ac034689c

[12] Strola, S. A., Baritaux, J. C., Schultz, E., Simon, A. C., Allier, C., Espagnon, I., . . . Dinten, J. M. (2014). Single bacteria identification by Raman spectroscopy. *J Biomed Opt, 19*(11), 111610. doi:10.1117/1.Jbo.19.11.111610

[13] Cozar, I. B., Colniţă, A., Szöke-Nagy, T., Gherman, A. M. R., & Dina, N. E. (2019). Label-Free Detection of Bacteria Using Surface-Enhanced Raman Scattering and Principal Component Analysis. *Analytical Letters, 52*(1), 177-189. doi:10.1080/00032719.2018.1445747

[14] Ho, C.-S., Jean, N., Hogan, C. A., Blackmon, L., Jeffrey, S. S., Holodniy, M., . . . Dionne, J. (2019). Rapid identification of pathogenic bacteria using Raman spectroscopy and deep learning. *Nature Communications, 10*(1), 4927. doi:10.1038/s41467-019-12898-9

[15] E., V. H. K., Johnson, W. C., & Ho, P. S. (2006). *Principles of Physical Biochemistry*. Upper Saddle River, NJ: Pearson/Prentice Hall.

[16] Vo-Dinh, T. (1978). Multicomponent analysis by synchronous luminescence spectrometry. *Analytical Chemistry, 50*(3), 396-401. doi:10.1021/ac50025a010

[17] Dartnell, L. R., Roberts, T. A., Moore, G., Ward, J. M., & Muller, J. P. (2013). Fluorescence characterization of clinically-important bacteria. *PLoS One, 8*(9), e75270. doi:10.1371/journal.pone.0075270

[18] Atif, M., AlSalhi, M. S., Devanesan, S., Masilamani, V., Farhat, K., & Rabah, D. (2018). A study for the detection of kidney cancer using fluorescence emission spectra and synchronous fluorescence excitation spectra of blood and urine. *Photodiagnosis Photodyn Ther, 23*, 40-44. doi:10.1016/j.pdpdt.2018.05.012

[19] Genova, T., Borisova, E., Penkov, N., Vladimirov, B., Zhelyazkova, A., & Avramov, L. (2016). Excitation–emission matrices and synchronous fluorescence spectroscopy for the diagnosis of gastrointestinal cancers. *Quantum Electronics, 46*(6), 510-514.

doi:10.1070/qel16112

[20] Li, R., Goswami, U., Walck, M., Khan, K., Chen, J., Cesario, T. C., & Rentzepis, P. M. (2017). Hand-held synchronous scan spectrometer for in situ and immediate detection of live/dead bacteria ratio. *Review of Scientific Instruments, 88*(11), 114301. doi:10.1063/1.4991351

[21] Li, R., Goswami, U., King, M., Chen, J., Cesario, T. C., & Rentzepis, P. M. (2018). In situ detection of live-to-dead bacteria ratio after inactivation by means of synchronous fluorescence and PCA. *Proceedings of the National Academy of Sciences, 115*(4), 668-673. doi:10.1073/pnas.1716514115

[22] Li, R., Dhankhar, D., Chen, J., Cesario, T. C., & Rentzepis, P. M. (2018). Determination of live:dead bacteria as a function of antibiotic treatment. *Journal of Microbiological Methods, 154*, 73-78. doi:https://doi.org/10.1016/j.mimet.2018.10.010

[23] Li, R., Dhankhar, D., Chen, J., Krishnamoorthi, A., Cesario, T. C., & Rentzepis, P. M. (2019). Identification of Live and Dead Bacteria: A Raman Spectroscopic Study. *IEEE Access, 7*, 23549-23559. doi:10.1109/ACCESS.2019.2899006

[24] Vidyasagar, A. (2019, April 25). What Are Bacteria? Retrieved January 26, 2020, from https://www.livescience.com/51641-bacteria.html

[25] Brazier, Y. (2019, February 12). Bacteria: Types, characteristics, where they live, hazards, and more. Retrieved January 26, 2020, from https://www.medicalnewstoday.com/articles/157973.php

[26] Bailey, R. (2019, October 30). What Are Prokaryotic Cells? Structure, Function, and Definition. Retrieved January 26, 2020, from https://www.thoughtco.com/prokaryotes-meaning-373369

[27] Difference Between Gram Positive and Gram Negative Cell Wall. (2018, June 7). Retrieved January 26, 2020, from https://www.differencebetween.com/difference-between-gram-positive-and-gram-negative-cell-wall/

[28] Situ, A. J., Kang, S. M., Frey, B. B., An, W., Kim, C., & Ulmer, T. S. (2018). Membrane Anchoring of alpha-Helical Proteins: Role of Tryptophan. *J Phys Chem B, 122*(3), 1185-1194.

doi:10.1021/acs.jpcb.7b11227

[29] Kachel, K., Asuncion-Punzalan, E., & London, E. (1995). Anchoring of Tryptophan and Tyrosine Analogs at the Hydrocarbon-Polar Boundary in Model Membrane Vesicles. *Biochemistry, 34*(47), 15475-15479. doi:10.1021/bi00047a012

[30] Wen, Z. Q., & Thomas, G. J., Jr. (1998). UV resonance Raman spectroscopy of DNA and protein constituents of viruses: assignments and cross sections for excitations at 257, 244, 238, and 229 nm. *Biopolymers, 45*(3), 247-256. doi:10.1002/(sici)1097-0282(199803)45:3<247::Aid-bip7>3.0.Co;2-r

[31] Rösch, P., Harz, M., Schmitt, M., Peschke, K.-D., Ronneberger, O., Burkhardt, H., . . . Popp, J. (2005). Chemotaxonomic Identification of Single Bacteria by Micro-Raman Spectroscopy: Application to Clean-Room-Relevant Biological Contaminations. *Applied and Environmental Microbiology, 71*(3), 1626-1637. doi:10.1128/aem.71.3.1626-1637.2005

[32] Jehlička, J., Edwards, H. G. M., & Oren, A. (2014). Raman spectroscopy of microbial pigments. *Applied and Environmental Microbiology, 80*(11), 3286-3295. doi:10.1128/AEM.00699-14

[33] Kumar B. N, V., Kampe, B., Rösch, P., & Popp, J. (2015). Characterization of carotenoids in soil bacteria and investigation of their photodegradation by UVA radiation via resonance Raman spectroscopy. *Analyst, 140*(13), 4584-4593. doi:10.1039/C5AN00438A

[34] Gupta, A., Avci, P., Dai, T., Huang, Y.-Y., & Hamblin, M. (2013). Ultraviolet Radiation in Wound Care: Sterilization and Stimulation. *Advances in wound care, 2*, 422-437. doi:10.1089/wound.2012.0366

[35] Randive, R. (2016, March 1). Improved POU disinfection with UVC LEDs. Retrieved January 26, 2020, from https://www.watertechonline.com/wastewater/article/15549943/improved-pou-disinfection-with-uvc-leds

[36] Pattison, D. I., & Davies, M. J. (2006). Actions of ultraviolet light on cellular structures. *Exs*(96), 131-157. doi:10.1007/3-7643-7378-4_6

[37] Sinha, R. P., & Häder, D.-P. (2002). UV-induced DNA damage and repair: a review.

Photochemical & Photobiological Sciences, 1(4), 225-236. doi:10.1039/B201230H

[38] Mouret, S., Baudouin, C., Charveron, M., Favier, A., Cadet, J., & Douki, T. (2006). Cyclobutane pyrimidine dimers are predominant DNA lesions in whole human skin exposed to UVA radiation. *Proceedings of the National Academy of Sciences, 103*(37), 13765-13770. doi:10.1073/pnas.0604213103

[39] Li, R., Dhankhar, D., Chen, J., Cesario, T. C., & Rentzepis, P. M. (2019). A tryptophan synchronous and normal fluorescence study on bacteria inactivation mechanism. *Proceedings of the National Academy of Sciences, 116*(38), 18822-18826. doi:10.1073/pnas.1909722116

[40] Chelala, C. A., & Margolin, P. (1983). Bactericidal photoproducts in medium containing riboflavin plus aromatic compounds and MnCl2. *Can J Microbiol, 29*(6), 670-675. doi:10.1139/m83-109

[41] Yoakum, G. H. (1975). Tryptophan photoproduct(s): sensitized induction of strand breaks (or alkali-labile bonds) in bacterial deoxyribonucleic acid during near-ultraviolet irradiation. *J Bacteriol, 122*(1), 199-205.

[42] Craggs, J., Kirk, S. H., & Ahmad, S. I. (1994). Synergistic action of near-UV and phenylalanine, tyrosine or tryptophan on the inactivation of phage T7: Role of superoxide radicals and hydrogen peroxide. *Journal of Photochemistry and Photobiology B: Biology, 24*(2), 123-128. doi:https://doi.org/10.1016/1011-1344(94)07014-8

[43] Lever, J., Krzywinski, M., & Altman, N. (2017). Principal component analysis. *Nature Methods, 14*(7), 641-642. doi:10.1038/nmeth.4346

[44] Jolliffe, I. T., & Cadima, J. (2016). Principal component analysis: a review and recent developments. *Philosophical Transactions of the Royal Society A: Mathematical, Physical and Engineering Sciences, 374*(2065), 20150202. doi:doi:10.1098/rsta.2015.0202

[45] Silfvast, W. T. (2009). *Laser Fundamentals*. Cambridge, UK: Cambridge University Press.

[46] Definition of Monochromators. (n.d.). Retrieved January 27, 2020, from https://www.chemicool.com/definition/monochromators.html

[47] Diem, M. (2015). *Modern Vibrational Spectroscopy and Micro-Spectroscopy: Theory, Instrumentation and Biomedical Applications*: Wiley.

[48] Vitha, M. F. (2018). *Spectroscopy: Principles and Instrumentation*: Wiley.

[49] Manoharan, R., Ghiamati, E., Dalterio, R. A., Britton, K. A., Nelson, W. H., & Sperry, J. F. (1990). UV resonance Raman spectra of bacteria, bacterial spores, protoplasts and calcium dipicolinate. *Journal of Microbiological Methods, 11*(1), 1-15. doi:https://doi.org/10.1016/0167-7012(90)90042-5

[50] Gaus, K., Rosch, P., Petry, R., Peschke, K. D., Ronneberger, O., Burkhardt, H., . . . Popp, J. (2006). Classification of lactic acid bacteria with UV-resonance Raman spectroscopy. *Biopolymers, 82*(4), 286-290. doi:10.1002/bip.20448

[51] Myers, J. A., Curtis, B. S., & Curtis, W. R. (2013). Improving accuracy of cell and chromophore concentration measurements using optical density. *BMC Biophysics, 6*(1), 4. doi:10.1186/2046-1682-6-4

[52] MTSM285UV-F1120S. (n.d.). Retrieved March 1, 2020, from https://marktechopto.com/marktech-emitters/high-power-smd-uv-emitters/

[53] DCB 241. (n.d.). Retrieved March 1, 2020, from http://stepcontrol.com/dc_dcb241/

[54] Spectrometer Command Set for BTC110/BRC100/BRC110/BTC200. (n.d.). Retrieved March 1, 2020, from http://www.bwtek.com/

[55] RVXP4-280-SM-077132. (n.d.). Retrieved March 1, 2020, from https://rayvio.com/xpseries/

[56] Mini-Chrom Monochromators & Accessories. (n.d.). Retrieved March 1, 2020, from https://www.dynasil.com/knowledge-base/mini-chrom-monochromators/

[57] SDMC1-02. (n.d.). Retrieved March 1, 2020, from https://www.dynasil.com/catalog/mini-chrom-monochromators/scanning-digital-mini-chrom-monochromator/scanning-digital-monochromator-200-800-nm/

[58] Diffraction Grating Selection Guide. (n.d.). Retrieved March 1, 2020, from https://www.newport.com/g/diffraction-grating-selection-guide

[59] SONY-ILX511B. (n.d.). Retrieved March 1, 2020, from https://www.spectrecology.com/price-lists-technical-documents/sony-ilx511b/

[60] Lumogen F. (n.d.). Retrieved March 1, 2020, from http://www2.basf.us/additives/pdfs/lumred300.pdf

[61] Ahmed, H., Kennedy, M., Doran, J., & McCormack, S. J. (2013). *Characterisation of Luminescent Down-Shifting Materials for the Enhancement of Solar Cell Efficiency*.

[62] Efficiency Curve 060R. (n.d.). Retrieved March 1, 2020, from https://www.newport.com/p/33025FL01-060R

[63] Diffraction Grating Physics. (n.d.). Retrieved March 1, 2020, from https://www.newport.com/t/grating-physics

[64] Part 5: Spectral Resolution. (n.d.). Retrieved March 1, 2020, from https://bwtek.com/spectrometer-part-5-spectral-resolution/

[65] Compact Fluorescent Lights for Calibration of Spectrometers. (2018, September 22). Retrieved March 1, 2020, from https://stargazerslounge.com/topic/322690-compact-fluorescent-lights-for-calibration-of-spectrometers/

[66] Spectrum of Fluorescent Light. (n.d.). Retrieved March 1, 2020, from http://www.bealecorner.org/best/measure/cf-spectrum/

[67] Andreeva, I. N., & Ogorodnikova, T. I. (2015). [Pigmentation of Serratia marcescens and spectral properties of prodigiosin]. *Mikrobiologiia, 84*(1), 43-49.

[68] Saviola, B. (2014). Pigments and Pathogenesis. *Mycobacterial Diseases, 04*. doi:10.4172/2161-1068.1000168

[69] FL05532-10. (n.d.). Retrieved March 1, 2020, from https://www.thorlabs.com/thorproduct.cfm?partnumber=FL05532-10

[70] DMLP550T. (n.d.). Retrieved March 1, 2020, from https://www.thorlabs.com/thorproduct.cfm?partnumber=DMLP550T

[71] Hecht, E. (2017). *Optics*: Pearson Education, Incorporated.

[72] FELH0550. (n.d.). Retrieved March 1, 2020, from https://www.thorlabs.com/thorproduct.cfm?partnumber=FELH0550

[73] Ghisaidoobe, A. B. T., & Chung, S. J. (2014). Intrinsic tryptophan fluorescence in the detection and analysis of proteins: a focus on Förster resonance energy transfer techniques. *International journal of molecular sciences, 15*(12), 22518-22538. doi:10.3390/ijms151222518

[74] Teale, F. W., & Weber, G. (1957). Ultraviolet fluorescence of the aromatic amino acids. *The Biochemical journal, 65*(3), 476-482. doi:10.1042/bj0650476

[75] Yang, H., Xiao, X., Zhao, X., & Wu, Y. (2015). *Intrinsic Fluorescence Spectra of Tryptophan, Tyrosine and Phenyloalanine*.

[76] McCormick, J. P., & Thomason, T. (1978). Near-ultraviolet photooxidation of tryptophan. Proof of formation of superoxide ion. *Journal of the American Chemical Society, 100*(1), 312-313. doi:10.1021/ja00469a068

[77] Reid, L. O., Roman, E. A., Thomas, A. H., & Dántola, M. L. (2016). Photooxidation of Tryptophan and Tyrosine Residues in Human Serum Albumin Sensitized by Pterin: A Model for Globular Protein Photodamage in Skin. *Biochemistry, 55*(34), 4777-4786. doi:10.1021/acs.biochem.6b00420

[78] Pirie, A. (1972). Fluorescence of N'-formylkynurenine and of protein exposed to sunlight. *The Biochemical journal, 128*(5), 1365-1367. doi:10.1042/bj1281365

[79] FUKUNAGA, Y., KATSURAGI, Y., IZUMI, T., & SAKIYAMA, F. (1982). Fluorescence Characteristics of Kynurenine and N′ -Formylkynurenine, Their Use as Reporters of the Environment of Tryptophan 62 in Hen Egg-White Lysozyme 1. *The Journal of Biochemistry,*

92(1), 129-141. doi:10.1093/oxfordjournals.jbchem.a133909

[80] Heinecke, J. W., Li, W., Daehnke, H. L., 3rd, & Goldstein, J. A. (1993). Dityrosine, a specific marker of oxidation, is synthesized by the myeloperoxidase-hydrogen peroxide system of human neutrophils and macrophages. *J Biol Chem, 268*(6), 4069-4077.

[81] Aeschbach, R., Amado, R., & Neukom, H. (1976). Formation of dityrosine cross-links in proteins by oxidation of tyrosine residues. *Biochim Biophys Acta, 439*(2), 292-301. doi:10.1016/0005-2795(76)90064-7

[82] Malencik, D. A., & Anderson, S. (2004). Dityrosine as a product of oxidative stress and fluorescent probe. *Amino acids, 25,* 233-247. doi:10.1007/s00726-003-0014-z

[83] Mayer, F., Propper, S., & Ritz-Timme, S. (2014). Dityrosine, a protein product of oxidative stress, as a possible marker of acute myocardial infarctions. *Int J Legal Med, 128*(5), 787-794. doi:10.1007/s00414-014-1015-z

[84] Grigoryan, K., & Shilajyan, H. (2017). Fluorescence 2D and 3D spectra analysis of tryptophan, tyrosine and phenylalanine. *Chem Biol, 51,* 3-7.

[85] Píš, Ľ., Májek, P., & Sádecká, J. (2011). Synchronous Fluorescence Spectroscopy for Differentiating Between Brandies and Wine Distillates. *Acta Chimica Slovaca, 4*(1), 47-58.

[86] Vekshin, N. L. (2013). *Photonics of Biopolymers*: Springer Berlin Heidelberg.

[87] Woo, H., Beck, S. E., Boczek, L. A., Carlson, K., Brinkman, N. E., Linden, K. G., . . . Ryu, H. (2019). Efficacy of inactivation of human enteroviruses by dual-wavelength germicidal ultraviolet (UV-C) light emitting diodes (LEDs). *Water, 11*(6), 1-1131. doi:10.3390/w11061131

[88] Beck, S. E., Ryu, H., Boczek, L. A., Cashdollar, J. L., Jeanis, K. M., Rosenblum, J. S., . . . Linden, K. G. (2017). Evaluating UV-C LED disinfection performance and investigating potential dual-wavelength synergy. *Water research, 109,* 207-216. doi:10.1016/j.watres.2016.11.024

[89] Chatterley, C., & Linden, K. (2010). Demonstration and evaluation of germicidal UV-LEDs for point-of-use water disinfection. *Journal of water and health, 8,* 479-486.

doi:10.2166/wh.2010.124

[90] Shimanouchi, T. (1972). *Tables of Molecular Vibrational Frequencies*: National Bureau of Standards.

[91] Yu, Y., Lin, K., Zhou, X., Liu, S., & Ma, X. (2007). New C-H Stretching Vibrational Spectral Features in the Raman Spectra of Gaseous and Liquid Ethanol. *J. Phys. Chem. C, 111*. doi:10.1021/jp0675781

[92] Vaskova, H., & Tomeček, M. (2018). Rapid spectroscopic measurement of methanol in water-ethanol-methanol mixtures. *MATEC Web of Conferences, 210*, 02035. doi:10.1051/matecconf/201821002035

[93] Li, Y.-S., & Church, J. S. (2014). Raman spectroscopy in the analysis of food and pharmaceutical nanomaterials. *Journal of Food and Drug Analysis, 22*(1), 29-48. doi:https://doi.org/10.1016/j.jfda.2014.01.003

[94] Buckley, K., & Ryder, A. G. (2017). Applications of Raman Spectroscopy in Biopharmaceutical Manufacturing: A Short Review. *Applied Spectroscopy, 71*(6), 1085-1116. doi:10.1177/0003702817703270

[95] Williams, R. P. (1973). Biosynthesis of prodigiosin, a secondary metabolite of Serratia marcescens. *Applied microbiology, 25*(3), 396-402. Retrieved from https://pubmed.ncbi.nlm.nih.gov/4572893

[96] Narayan, D., & Krishnan, M. (2016). Prodigiosin inhibits motility and activates bacterial cell death revealing molecular biomarkers of programmed cell death. *AMB Express, 6*. doi:10.1186/s13568-016-0222-z

[97] Monk, G. W. (1957). Spectral absorption of prodigiosin in intact cells. *Journal of bacteriology, 74*(1), 71-74. Retrieved from https://pubmed.ncbi.nlm.nih.gov/13462962

[98] Saviola, B. (2018). Pigments of pathogenic bacteria. *Journal of Microbiology & Experimentation, 6*. doi:10.15406/jmen.2018.06.00198

[99] Azman, A. S., Mawang, C. I., & Abu Bakar, S. (2018). Bacterial pigments: The bioactivities

and as an alternative for therapeutic applications. *Natural Product Communications, 13*, 1747-1754.

[100] Popp, J., & Bauer, M. (2015). *Modern Techniques for Pathogen Detection*: Wiley.